Hydration Effects on Defect Chemistry of LiSCN and $Li_2Sn_2S_5$

Von der Fakultät Chemie der Universität Stuttgart
zur Erlangung der Würde eines

Doktors der Naturwissenschaften

(Dr. rer. nat.) genehmigte Abhandlung

vorgelegt von

Markus Joos

aus Geislingen b. Balingen, Deutschland

Hauptberichter:	Prof. Dr. J. Maier
Mitberichter:	Prof. Dr. R. Niewa
Prüfungsvorsitzender:	Prof. Dr. F. Giesselmann

Tag der Einreichung:	24.11.2021
Tag der mündlichen Prüfung:	02.02.2022

Max-Planck-Institut für Festkörperforschung
Stuttgart
2021

Erkärung über die Eigenständigkeit der Dissertation

Ich versichere, dass ich die vorliegende Arbeit mit dem Titel

Hydration Effects on Defect Chemistry of LiSCN and $Li_2Sn_2S_5$

selbstständig verfasst und keine anderen als die angegebenen Quellen und Hilfsmittel benutzt habe; aus fremden Quellen entnommene Passagen und Gedanken sind als solche kenntlich gemacht.

Declaration of Authorship

I hereby certify that the dissertation entitled

Hydration Effects on Defect Chemistry of LiSCN and $Li_2Sn_2S_5$

is entirely my own work except where otherwise indicated. Passages and ideas from other sources have been clearly indicated.

Name/name: Markus Joos

Unterschrift/signature: _____

Datum/date: Stuttgart, 17.11.2021

Table of Contents

7   Lithium Tin Sulphide $Li_2Sn_2S_5$

8   Discussion

9   Conclusion

A   Symbols and Abbreviations

B   Supplemental

C   References

Acknowledgements

1 | Zusammenfassung

Diese Doktorarbeit untersucht den Einfluss der Hydratation auf die elektrochemischen Eigenschaften zweier ionischer Materialien mit Li$^+$-Kationen: Lithiumthiocyanat (LiSCN) und Lithiumzinnsulfid (Li$_2$Sn$_2$S$_5$). Beide Materialien sind hygroskopisch, aber der Einfluss auf den Ionentransport und die Defektchemie bei der Hydratation (Einbau von undissoziierten Molekülen) ist sehr unterschiedlich.

LiSCN ist ein sehr stabiles ionisches Salz, das aus Lithiumkationen Li$^+$ und Thiocyanatanionen SCN$^-$ besteht. Das Anion hat eine lineare Struktur, wobei Li$^+$-Kationen entweder an das Schwefel- oder Stickstoffatom binden, und entspricht einem molekularen Liganden. Wasserfreies LiSCN bildet Schottkydefekte mit Lithiumleerstellen als dominante mobile Ladungsträger. Die Leerstellenkonzentration und die Mobilität sind gering, was dieses Material bei 25 °C (10^{-13} S/cm) zu einem schlechten Ionenleiter macht. Diese geringe Leitfähigkeit wird dem SCN$^-$ Anion zugeschrieben, das sowohl über den Stickstoff als auch über den Schwefel an Lithium koordiniert, allerdings mit sehr unterschiedlichen Bindungsstärken. Ein Li$^+$-Sprung erfordert eine wesentliche strukturelle Relaxation der Umgebung, die den langreichweitigen Ionentransport verlangsamt. Nahe dem Schmelzpunkt kommen Defekt-Defekt-Wechselwirkungen ins Spiel, und die Leerstellenkonzentration sowie die Leitfähigkeit sind vergleichsweise hoch (10^{-5} S/cm). Im Fall von LiSCN $\cdot$ x H$_2$O genügen Wassergehalte von $x \approx 1000$ ppm aus um die Leitfähigkeit um $\sim$3 Grössenordnungen zu erhöhen. In diesen niederstöchiometrischen Mengen wirkt Wasser als Donor-Dotiersubstanz (H$_2$O$_{SCN}^{\cdot}$) und erhöht somit die Konzentration von Lithiumleerstellen. Im Gegensatz zu anderen Dotiersubstanzen erhöht der Einbau von H$_2$O auch die Beweglichkeit von Lithiumleerstellen, sogar bei sehr geringen Wasserkonzentrationen. Bei tiefen Temperaturen wird die Leitfähigkeit in H$_2$O-dotiertem LiSCN durch die Assoziation von eingebautem Wasser mit Lithiumleerstellen behindert, die erst bei höheren Temperaturen dissoziieren und freie Ladungsträger bilden. Ein umfassendes chemisches Defektmodell wurde abgeleitet, einschliesslich Defektbildungsenthalpien und Migrationsbarrieren. Wenn der Hydratationsgrad auf stöchiometrische Werte erhöht wird, bilden sich das Mono- und Dihydrat. Im Zweiphasenregime von trockenem LiSCN und Monohydrate als auch bei reinem Monohydrat wird der Ionentransport durch Defektas-

soziate bestimmt, was zu einer aussergewöhnlich hohen Aktivierungsenthalpie führt. Aufgrund des niedrigen Schmelzpunktes des Dihydrats (38 °C) und dessen Unterkühlung, wird die Leitfähigkeit von zweiphasigen Gemischen aus Mono- und Dihydrat durch perkolierendes geschmolzenes Dihydrat determiniert. Dies führt zu Leitfähigkeiten von bis zu 7×10^{-4} S/cm bei 25 °C.

$Li_2Sn_2S_5$ hat eine Schichtstruktur, die aus negativ geladenen Zinnsulfidschichten besteht, wobei sich die Li^+-Kationen innerhalb der Zwischenschichtgalerie befinden. Das mehratomige $Sn_2S_5^{2-}$-Netzwerk bildet die strukturellen Einheiten dieses Materials. Li^+-Kationen koordinieren nicht direkt an die anionischen Schichten, sondern sind zwischen den Schichten verteilt und wechselwirken nur über vergleichsweise schwache coulombsche Bindungen. Da die Li^+-Kationen zwischen den Schichten nur zu 38 % besetzt sind, ist das Li^+-Untergitter bereits bei Raumtemperatur vollständig ungeordnet mit annähernd konstanter Ladungsträgerkonzentration, was sich durch die geringe Aktivierungsenthalpie äussert.

In $Li_2Sn_2S_5 \cdot x\,H_2O$ kann der Hydratationswert viel höher sein als in LiSCN, da eine geschichtete Struktur flexibler ist und mehr Wasser bis zu $x \approx 10$ aufnehmen kann. Auch bei kleinen Wassergehalten wird H_2O nicht substituierend eingebaut, sondern additiv (d.h. im Zwischengitter). Die H_2O Moleküle sitzen zwischen den Zinnsulfidschichten und koordinieren an die Li^+-Kationen, wobei sich der Schichtabstand gegenüber der wasserfreien Situation vergrössert. Mit Röntgenbeugung wurden zwei kristallographisch unterschiedliche Hydratphasen von $Li_2Sn_2S_5$ entdeckt, die im Vergleich zu den LiSCN-Hydraten viel breitere Phasenbreiten im Salz − Wassersystem aufweisen. Die Leitfähigkeit nimmt mit der Hydratation monoton zu, während die Aktivierungsenthalpie annähernd konstant bleibt. Das heisst, der präexponentielle Faktor der Mobilität ist entscheidend. Dieser Anstieg ist auf die coulombsche Abschirmwirkung von Wasser für die Li^+-Kationen zurückzuführen, die sich mit der Menge des eingebauten Wassers verstärkt. In vollständig hydratisiertem $Li_2Sn_2S_5$ besitzen die Kationen eine vollständige Hydratationshülle, die einen flüssigkeitsähnlichen schnellen Ionentransport mit einer Li^+-Leitfähigkeit bei Raumtemperatur von bis zu 2×10^{-2} S ermöglicht. Dieser Transportmechanismus weist eine gewisse Ähnlichkeit mit dem oben erwähnten LiSCN-Komposit aus Mono- und Dihydrat auf, beinhaltet jedoch eine grössere Hydratationshülle für Li^+. Insgesamt schlagen diese Ergebnisse neue Wege bei der Suche nach festen Li^+-Elektrolyten für Batterie- oder andere elektrochemische Anwendungen vor.

2 | Abstract

This thesis explores the impact of hydration on the electrochemical properties of two ionic materials with Li^+ cations: lithium thiocyanate (LiSCN) and lithium tin sulfide ($Li_2Sn_2S_5$). Both materials are hygroscopic, yet the impact on ion transport and defect chemistry upon hydration (incorporation of undissociated molecules) is very different.

LiSCN is a very stable ionic salt composed of lithium cations Li^+ and thiocyanate SCN^- anions. The anion has a linear structure where Li^+ cations directly bond to either the sulphur or nitrogen atom, and represents a molecular ligand. Anhydrous LiSCN forms Schottky defects with lithium vacancies as the dominant mobile charge carriers. The vacancy concentration and mobility are low, making this material a poor ionic conductor at 25 °C (10^{-13} S/cm). This low conductivity is attributed to the SCN^- anion, coordinating to lithium both via the nitrogen and sulphur atom, but with very different bonding strengths. Thus a Li^+ jump requires substantial structural relaxation of the environment, which slows down long-range transport. Near the melting point defect-defect interactions come into play, and the concentration of vacancies as well as the conductivity are fairly high (10^{-5} S/cm). In case of LiSCN $\cdot x\,H_2O$, water contents of $x \approx 1000$ ppm suffice to raise the conductivity by $\sim$3 orders of magnitude. In these substoichiometric amounts water acts as a donor dopant ($H_2O_{SCN}^{\cdot}$) and increases the concentration of lithium vacancies. In contrast to other doping agents, the incorporation of H_2O also increases the mobility of lithium vacancies even at very low water concentrations. At low temperatures the conductivity in H_2O-doped LiSCN is impeded by the association of incorporated water with lithium vacancies, which become free carriers only at higher temperatures. A comprehensive defect chemical model is derived, including defect formation enthalpies and migration barriers. When the hydration level is increased to stoichiometric values, the mono- and dihydrate form. Within the two-phase regime of dry LiSCN plus the monohydrate as well as for the pure monohydrate, ion transport is determined by defect associates, causing an exceptionally high activation enthalpy. Given the low melting point of the dihydrate (38 °C) and the possibility of supercooling, the conductivity of two-phase mixtures of mono- and dihydrate is determined by percolating molten dihydrate, giving rise to conductivities as high as 7×10^{-4} S/cm at 25 °C.

$Li_2Sn_2S_5$ has a layered structure, which consists of negatively charged tin sulfide sheets while the Li^+ cations reside within the interlayer gallery. The polyatomic $Sn_2S_5{}^{2-}$ network forms the structural units of this material. Li^+ cations do not directly coordinate to the anionic layers, but are distributed between the sheets and interact only via comparably weak Coulombic bonds. As the interlayer Li^+ sites are only 38 % occupied, already at room temperature the material is fully disordered with an approximately constant charge carrier concentration as indicated by the low activation enthalpy.

In $Li_2Sn_2S_5 \cdot x\,H_2O$, hydration levels can be much higher than in LiSCN, since a layered structure is more flexible and can accommodate more water up to $x \approx 10$. Even for small water contents, H_2O is not incorporated substitutionally but additively (i.e. interstitially). The H_2O molecules reside between the tin sulphide sheets, coordinate to the Li^+ cations, and the interlayer distance has increased with regard to the water free situation. X-ray diffraction showed two distinct hydrate phases of $Li_2Sn_2S_5$, which possess much broader phase widths in the salt − water system compared to the LiSCN hydrates. The conductivity increases monotonically with hydration while the activation enthalpy stays approximately constant, meaning the pre-exponential factor of the mobility is determining. This increase is due to the Coulombic shielding effect of water for the Li^+ cations, which intensifies with the amount of incorporated water. In fully hydrated $Li_2Sn_2S_5$ the cations have a complete hydration shell, which enables liquid-like fast ion transport with a room temperature Li^+ conductivity of up to 2×10^{-2} S/cm. This transport mechanism bears some similarity to the LiSCN composite of mono- and dihydrate mentioned above, but involves a larger hydration shell for Li^+. Overall, these results suggest new avenues in the search of solid Li^+ electrolytes for battery or other electrochemical applications.

3 | Introduction

3.1 Motivation

With the rising importance of renewable energy technologies and the progressive shift away from fossil fuels, materials that contain lithium have received strongly increasing interest, which is mostly related to the science of lithium ion batteries. Unfortunately, since industrial application is the key motivator, fundamental research in this field is rare, and in-depth analyses of "less useful materials" may easily get lost in the sheer volume of research on "promising candidates" as Li^+ electrolyte for solid state batteries. Since water is incompatible and damaging for most battery systems, research on hydrated Li^+ ion conductors is less frequent[1]. Even though understandable, this strong polarisation in research limits new perspectives and innovative avenues to be explored, which is detrimental for future developments. It is therefore desired to conduct a fundamental study on ion transport in hydrated Li^+ conducting materials to expand the knowledge of defect chemistry in hydrates, and propose new concepts in the research of electrolyte systems, which have not been considered yet.

3.2 Materials

Lithium Thiocyanate LiSCN

Metal thiocyanate salt systems have been known for decades, and over time an extended data base of crystal structures and chemical / physical properties of these materials has been collected (Figure 3.1). One common attractive property is their high ability to form various coordination compounds,[1–9] attributed to the bidental coordination capability of the thiocyanate anion SCN^- to bond via nitrogen or sulphur. Naturally, the most common coordination compounds are hydrates, and various thiocyanate salt hydrate systems have already been reported.[10–21]

---

[1]For example, web search of key words "hydrated Li ion conductor" compared to "Li ion conductor" yields results of < 1 % (*Web of Science*) and $\sim$10 % (*Google Scholar*) as of 9th September, 2021.
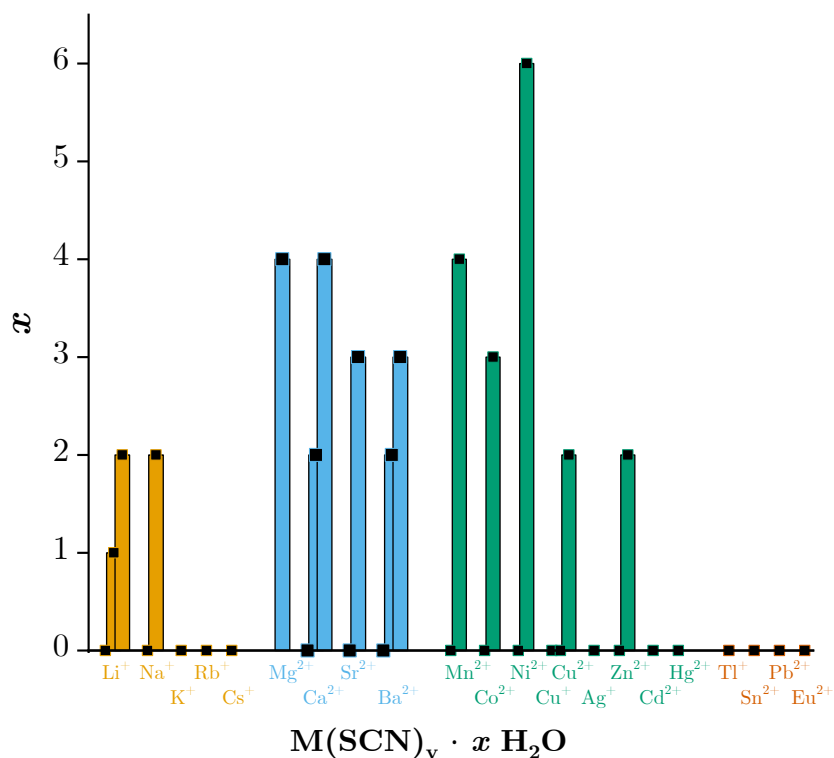
Figure 3.1: Overview of known metal thiocyanate salt systems with their respective hydrates: alkali,[14, 22–24] alkaline earth,[9, 13, 15, 18, 19, 25, 26] transition,[2, 8, 11, 16, 17, 21, 27–34] main group,[35–37] and lanthanide[25] metal thiocyanate salts.

One of the first thorough investigations of LiSCN was done by Nikolaev in 1928.[10] Later contributions to this material were much less impactful,[38–42] until almost 6 decades later the first proper electrochemical study was published by Poulsen in 1985.[43] Only after nearly 3 more decades its crystal structure was solved by Reckeweg et al. in 2014.[22] Besides the investigation by Poulsen, other work about LiSCN related to electrochemistry focused on liquid systems[41, 42, 44] or on using LiSCN as an additive.[45–50] As shown later in this thesis, the extreme hygroscopy of anhydrous LiSCN complicates investigations of the anhydrous material as well as of specific hydrated states, and the impact that hydration has on ionic conductivity had previously been underestimated.[43] Since LiSCN is essentially a pseudo-binary system, it is interesting to explore how its defect chemistry compares to regular binary systems such as lithium halides or chalcogenides. Given its ability to easily and reversibly form hydrates, this material was identified as an interesting candidate for studies regarding Li^+ ion transport as a function of hydration.

Lithium Tin Sulphide Li$_2$Sn$_2$S$_5$

Within the ternary system Li-Sn-S, several phases have been reported such as semiconducting mixed-valent Sn$^{2+/4+}$ LiSnS$_2$[51] or ionically conducting Li$_{4z}$Sn$_{1-z}$S$_2$ ($z = 0.2, 0.33$ and 0.5) with formally Sn^{4+}.[52–55] Regarding the phase diagram shown in Figure 3.2, these compounds are located between Li$_2$S, SnS and SnS$_2$.

In this work, the material of interest is Li$_2$Sn$_2$S$_5$ ($z = 0.2$), which is — as the previous compound — a promising candidate for hydration studies. In an earlier work, Li$_2$Sn$_2$S$_5$ was identified as a layered material consisting of partially Li-substituted tin sulphide sheets which are held together by ionic bonds to interlayer Li$^+$ ions (Figure 3.3a).[52] The material exfoliates when immersed in water by reducing the ionic interaction strength of Li$^+$ ions with the layers, and a suspension of monolayer tin sulphide sheets is formed. This investigation suggested that any incorporated H$_2$O molecules would be situated in the interlayer galleries in the vicinity of the interlayer Li$^+$ ions, in accordance with the expected Li$^+$ coordination chemistry (Figure 3.3b). The solved crystal structure of anhydrous Li$_2$Sn$_2$S$_5$ later revealed that 75 % of the Li$^+$ ions are on interlayer Li sites (occupancy of 38 %), while the remaining 25 % of Li$^+$ ions have a mixed occupancy with Sn^{4+} ions on sites within the layers, i.e. (Li,Sn)S$_2$-sheets.[53] After exfoliation, these sheets react sensitively to the environmental humidity by uptake or release of H$_2$O. When they are incorporated in a Bragg stack, the accompanied changes in optical response can be used as a humidity sensor signal.[56] These previous reports are a strong motivation to explore the hydration mechanism of Li$_2$Sn$_2$S$_5$ via the gas phase without exfoliating the material, and to study the resulting impact on ion transport.
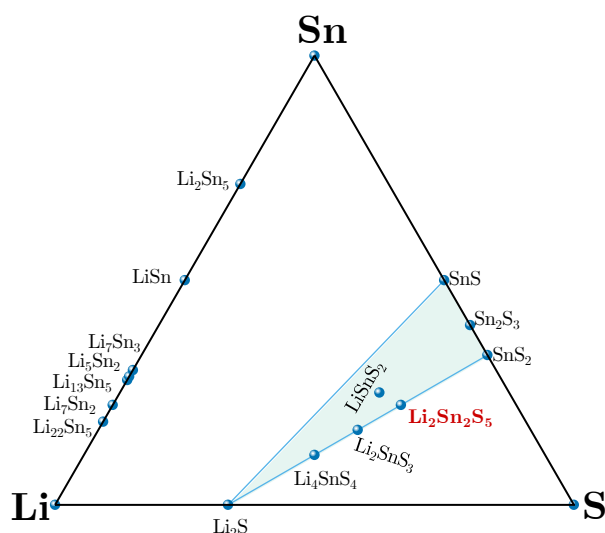

Figure 3.2: Ternary phase diagram of the system Li-Sn-S.[51–55, 57–60] The green shaded field shows the area where lithium tin sulphides can form.
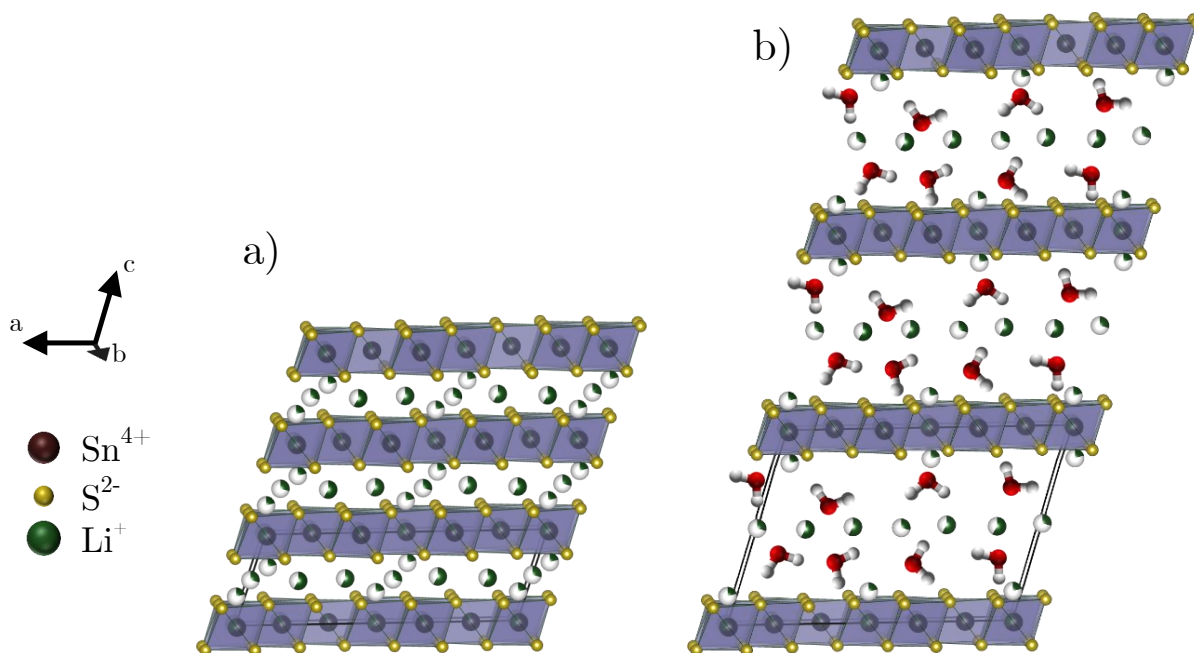
Figure 3.3: a) Crystal structure of anhydrous $Li_2Sn_2S_5$; b) schematic structure of $Li_2Sn_2S_5 \cdot x\,H_2O$. The partially filled Li^+ spheres indicate a partial occupancy of 38 %.

3.3 Outline

This work investigates the effects molecular hydration has on Li^+ conductivity and defect chemistry in lithium thiocyanate LiSCN and lithium tin sulfide $Li_2Sn_2S_5$, by comparing ion transport properties of the anhydrous material with the hydrates. It will be shown that in LiSCN water can act as dopant, which not only increases the concentration of the mobile defect, but also its mobility. Stoichiometric hydration produces low melting hydrate phases, which show distinctly different conductivities compared to the anhydrous situation. Composites of these phases form highly conducting samples, in which ion transport is dominated by the intergranular network. In contrast, the layered structure of $Li_2Sn_2S_5$ allows for higher degrees of hydration, which enables fast, liquid-like transport in the solid material. Interlayer Li^+ ions coordinate to H_2O molecules forming a hydration shell, which weakens Coulombic interactions to the tin sulfide sheets and increases the mobility of the Li^+ cations. Electrochemical impedance spectroscopy is used as primary investigation method, and occasionally complemented by nuclear magnetic resonance. Various analysis techniques are used for further support. The results of both materials are compared to emphasize the diversity of ion transport mechanisms in hydrated systems.

4 | Literature Background

4.1 Defect Chemistry of Lithium Halides LiX

Lithium halides are well known materials, since they are easy to synthesize, stable and crystallise exclusively in the rock salt structure.[61] They have all been identified as Schottky defective materials, in which lithium vacancies are the mobile carrier.[62, 63] The comparison of their defect formation and migration enthalpies (Table 6.3, p. 37) reflects the Pearson concept.[64] The larger the difference in electronegativity, size and polarisability between cation and anion, the weaker are the ionic bonds (i.e. lower lattice energies, cf. Table 6 in [62]) and the better conducting is the material (Figure 6.8). This is obviously a simplistic concept, but it is appropriate for chemically closely related systems such as the lithium halides. A characteristic feature is that the defect formation enthalpies are consistently higher than the migration barriers, which emphasizes the high lattice energy of the rock salt structure. The defect chemistry of these compounds serves as a good starting point for lithium thiocyanate, as LiSCN is regarded as pseudo-halide and behaves in many ways similar to the halides.[10]

4.2 Hydration Behaviour and Ion Transport in Hydrated Li$^+$ Conductors

In general, there are three basic mechanisms for the interaction of gaseous water with solid materials that do not suffer from hydrolysis: Surface adsorption (e.g. on CeO_2[65] and ZrO_2[66]), dissociative incorporation (formation of protonic defects $OH_O^{\cdot}$, e.g. in Y-doped $BaZrO_3$),[67] and molecular incorporation, which occurs e.g. in Li$^+$ ion conductors and will be discussed here. The driving force is always the formation of favourable Li-OH_2 bonds, which is the stronger the lower the lattice energy of the parent material is. Lithium salts are prone to form hydrates, as in many LiX systems the Li-O bond with water is preferred to the bond with the anion.[10, 43, 68–75] Another material class known for its ability to intercalate molecular water are mineral clays, many of which are predom-

inantly known as proton conductors; here the mobile cation can be ion exchanged.[76–83] As shown in Figure 4.1, the conductivities of hydrated systems can differ strongly, even among different hydrates of the same material. Nonetheless, overall trends in the Li^+ (or Na^+) ion transport in hydrated materials shown here can be summarized accordingly:

(i) Hydrated lithium salts have mostly higher conductivities and lower activation enthalpies compared to their anhydrides, which is typically attributed to higher defect concentrations and/or lower migration barriers. Ion transport occurs via defect migration, where mobile defects might interact with the structural water molecules.

(ii) In hydrated mineral clays with a layered (2D) structure, the cation present in the interlayer gallery coordinates to the H_2O molecules, forms a hydration shell, and has a liquid-like mobility. All present carriers are mobile and the activation enthalpy directly relates to the migration barrier. Ion conduction only occurs within the layers (anisotropic transport), and conductivities are higher compared to most other hydrate systems.

However, there are exceptions to the above trends, e.g. seen in $LiBr \cdot 1\,H_2O$,[69] $LiI \cdot 2\,H_2O$[72, 73] and $LiBH_4 \cdot 1\,H_2O$,[75] which show unusually high activation enthalpies. Possible reasons are phase transition, irreversible changes, or defect interactions as will be shown in this thesis. These materials serve as reference systems for the here investigated hydrated Li^+ ion conductors $LiSCN \cdot x\,H_2O$ and $Li_2Sn_2S_5 \cdot x\,H_2O$.

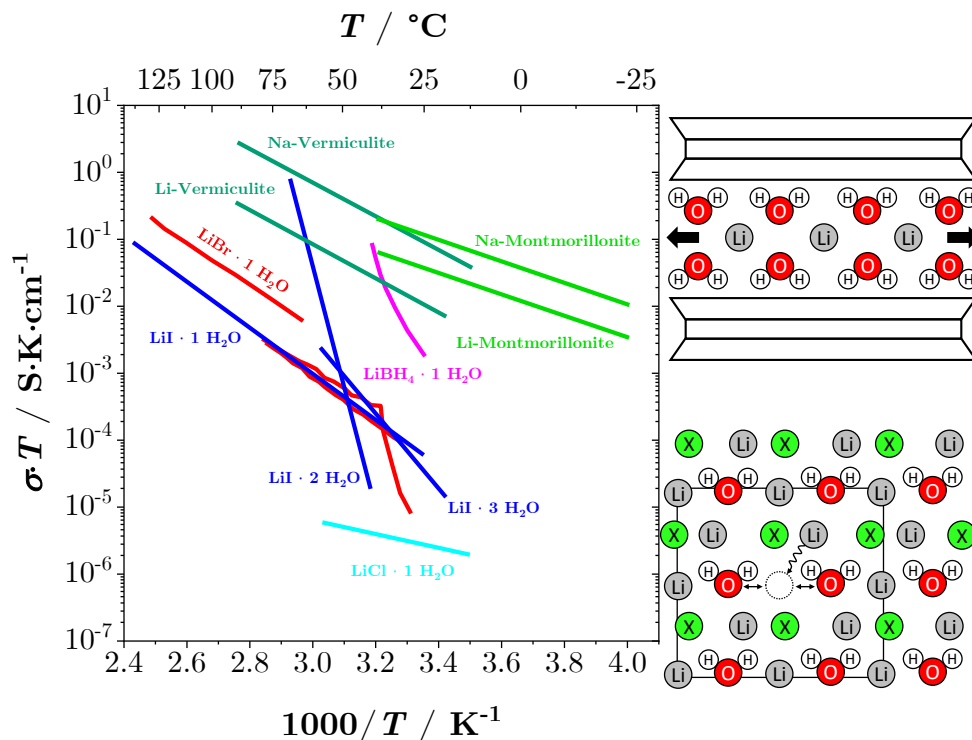Figure 4.1: Literature conductivity data of various hydrated materials: $LiCl \cdot 1\,H_2O$,[69] $LiBr \cdot 1\,H_2O$,[69, 70] $LiI \cdot z\,H_2O$ ($z = 1, 2, 3$),[73] $LiBH_4 \cdot 1\,H_2O$[75] as well as fully hydrated (Li,Na)-modifications of vermiculite and montmorillonite minerals.[80] The right hand side schematically shows hydrated lithium halides (bottom) and layered minerals (top).

5 | Experimental Methods

The following experimental methods were used in this thesis:
Thermogravimetric Analysis (TGA), equilibrium water partial pressure (p_{H_2O}) measurements, differential scanning calorimetry (DSC), X-ray powder diffraction (XRPD), single crystal X-ray diffraction (SXRD), X-ray photoelectron spectroscopy (XPS), energy dispersive X-ray (EDX) analysis, Raman and infrared (IR) spectroscopy, inductively coupled plasma optical emission spectroscopy (ICP-OES), scanning electron microscopy (SEM), solid state nuclear magnetic resonance (ssNMR), pulsed field gradient (PFG) NMR, electrochemical impedance spectroscopy (EIS) and direct current (DC) measurements.

5.1   Preparation and Measurement Conditions

Anhydrous samples of LiSCN and $Li_2Sn_2S_5$ were prepared, handled, and measured under dry inert gas (Ar or N_2 with < 1 ppm H_2O) or dynamic vacuum. Hydrated samples were sealed in containers with a small dead volume to minimize water loss, in which they could be stored for months. Due to their hygroscopy, the samples could not be handled at air, as they would take up additional water from atmosphere. Even though hydrated samples loose water at prolonged exposure to a dry Ar or N_2 atmosphere (cf. Figure B.20a in the supplementary), the samples were handled and stored inside a glove box to keep the experimental uncertainty systematic. Therefore, throughout this thesis the degree of hydration x (defined as $n(H_2O)/n(\text{material})$, i.e. average amount of incorporated water) has to be regarded as an approximate value. In $Li_2Sn_2S_5 \cdot x\,H_2O$, x was determined and verified gravimetrically with an average error of 0.5 or less. In case of $LiSCN \cdot x\,H_2O$, mass changes were too small to be resolved by weighing, yet based on infrared spectroscopy and X-ray powder diffraction, the error in x was typically in the order of 10 % or less. Apart from their sensitivity to water partial pressure p_{H_2O}, both materials appeared to be stable at air (no decomposition by oxidation was observed). Some transfer steps required exposing anhydrous or hydrated samples to air for a short time, on the order of seconds (indicated at the respective paragraphs).

5.2 Synthesis

Lithium Thiocyanate LiSCN

Anhydrous LiSCN was obtained from purchased $LiSCN \cdot x\,H_2O$ (*Sigma Aldrich*, Germany). The material was first pre-dried at 50 °C, then heated stepwise to 150 °C under dynamic vacuum for 24 hours, and then fully dried at 200 °C for at least another 24 hours. The final anhydrous LiSCN was a white, highly hygroscopic powder. This procedure was done by Maurice Conrad.

Hydrated LiSCN $\cdot\, x\,H_2O$ was synthesized from the anhydrous material mentioned above. For solid samples ($x < 2$), the powder was weighed (typically 1-2 g) inside a glove box, filled into a small vial, and afterwards placed into a Schlenk tube. A second empty vial with the same dimensions was then placed on top, and the respective calculated amount of water x to produce $LiSCN \cdot x\,H_2O$ was injected into the upper vial with a syringe under argon back flow. If necessary (usually for $x \approx 1.0$), a desiccator was used instead of the Schlenk tube and the anhydrous LiSCN powder filled into a wide bowl to provide more surface area and avoid inhomogeneity problems. The samples remained inside the grease sealed containers until hydration via the gas phase was finished and equilibration was reached (at least 2 weeks).

For $x \approx 2$, the final sample consistency at room temperature was close to or completely liquid, and water was directly added to the respective amount of dry LiSCN. If x was greater than 2, commercially available $LiSCN \cdot x\,H_2O$ was directly used, by first assessing x with TGA ($x \approx 2.2$) and then calculating the necessary additional amount of H_2O to obtain the wanted concentration (cf. Figure B.42b). The synthesis was done in a volumetric flask with double-distilled water at 21 °C, to obtain also the densities of the respective solutions (Figure B.43b). The synthesis and preparation were done with the support of Maurice Conrad.

$Mg(SCN)_2 \cdot 4\,H_2O/THF$ for use as dopant had to be synthesized, since the synthesis of anhydrous $Mg(SCN)_2$ is yet unknown.[9] $Mg(SCN)_2 \cdot 4\,H_2O$ was synthesized via cation exchange. A column was filled with hydrogen-form Amberlite IR-120 (*Fluka*, Switzerland) and loaded with Mg^{2+} cations using an aqueous solution of $MgCl_2$ (400 g in 1800 ml, 99 % *Grüssing*). The column was washed thoroughly with deionized water, and then a solution of KSCN (4.5 g in 150 mL deionized water, p.a. *Merck*) was passed through. Most water was removed with a rotary evaporator and the remaining slurry was put into a desiccator over dry silica gel, yielding colourless, transparent crystals of pure $Mg(SCN)_2 \cdot 4\,H_2O$.

For the synthesis of $Mg(SCN)_2 \cdot 4\,THF$ (THF, tetrahydrofuran) $MgCl_2 \cdot 6\,H_2O$ (99.995 % *Aldrich*; 99.999 % *Alfa Aesar*) was dissolved in dry ethanol ($\geq$ 99.8 % *Roth*, $\leq$ 2000 ppm H_2O; for 1 g of $MgCl_2 \cdot 6\,H_2O$ about 50 ml of ethanol were used) and KSCN ($\geq$ 99.0 %

Sigma-Aldrich) was added stepwise in the corresponding stoichiometric amount while stirring. KCl started to precipitate quickly and the solution was left stirring for ∼0.5-2 h (the precipitate was confirmed to be KCl by XRPD). The precipitated KCl was filtered off (vacuum filtering or without suction) and the ethanol was mostly removed with a standard laboratory rotary evaporator set-up. About 50 ml of THF ($\geq$ 99.9 % *Roth*; anhydrous $\geq$ 99.9 % inhibitor free, *Sigma-Aldrich*) were added to the slurry, and the solution was again stirred for ∼0.5-1 h. All THF was removed with the rotary evaporator until a yellow powder precipitated (mixture of $Mg(SCN)_2 \cdot 2\,H_2O \cdot 2\,THF$ and $Mg(SCN)_2 \cdot 4\,THF$). The powder was redissolved in ∼80 ml of dry THF under argon atmosphere and left stirring for ∼12 h (some powder remained undissolved). To remove the remaining H_2O, a three-neck flask containing the solution was connected to a Schlenk line and a Dimroth condenser, and the mixture was refluxed for ∼20 minutes at 90 °C under constant argon flow. Afterwards the THF was directly removed at room temperature with the vaccum of the Schlenk line, and the flask was transferred into a glove box. The yellow powder was confirmed to be phase pure $Mg(SCN)_2 \cdot 4\,THF$ (∼2 wt.-% KCl contamination). This synthesis was performed with the assistance of Maurice Conrad.

$Zn(SCN)_2$ for use as dopant was synthesized according to literature.[84] $Ba(OH)_2 \cdot 8\,H_2O$ (2 g, $\geq$ 98 %, *Roth*) was mixed with the respective amount of NH_4SCN (99.99 %, *Sigma-Aldrich*) and dissolved in ∼110 ml of deionized H_2O. Even after stirring at 50 °C (1.5 h), 75 °C (0.5 h), 80 °C (1 h) and the addition of 50 ml methanol MeOH ($\geq$ 99.9 % p.a., *Roth*), the solution remained turbid. 1.14 g of $ZnSO_4 \cdot 1\,H_2O$ (99 %, *Acros Organics*) was added and $BaSO_4$ instantly precipitated. The solution was vacuum filtered, cooled with an ice bath, and remnants of $BaSO_4$ were removed by a second filtration. The solvent was removed with a rotary evaporator and a white (slightly yellow) powder precipitated, which was fully dried at the Schlenk line. To remove residual $Ba(SCN)_2$, confirmed by XRPD, the powder was re-dissolved in deionized water and carefully titrated with a saturated solution of $ZnSO_4$. After analysing the sample (XRPD and IR Figure B.6, SEM-EDX and ICP-OES Figure B.7, DSC Figure B.8a), it was determined that α-$Zn(SCN)_2$ was successfully synthesized, with a small contamination of $ZnSO_4$ hydrates.

$Mg_{1+\varsigma}Li_{4-2\varsigma}(SCN)_6$ ($\varsigma = 0.02$) resulted as a secondary phase when doping beyond the solubility limit (∼5.0 mol%) of Mg^{2+} in LiSCN. The synthesis procedure was analogous to the method used for doping with $Mg(SCN)_2 \cdot 4\,H_2O$ (cf. section 5.3), using slower stepwise heating and more steps up to 230 °C. It was observed multiple times that some of the nominally employed amount of $Mg(SCN)_2$ was lost (Figure B.12b), possibly due to the formation of volatile decomposition products. Using an excess of $Mg(SCN)_2 \cdot 4\,H_2O$ (up to 60 mol%) had to be done with care, as an additional, unknown side phase would start to form. Numerous attempts to produce a phase pure sample of $Mg_{1+\varsigma}Li_{4-2\varsigma}(SCN)_6$ were unsuccessful, including various heating and cooling cycles with different rates, longer

synthesis times (up to 44 days), higher temperatures (up to 270 °C) and using a different precursor (Mg(SCN)$_2 \cdot 4$ THF). The highest achieved purity was around 81 % (Figure B.4).

Lithium Tin Sulphide Li$_2$Sn$_2$S$_5$

Anhydrous Li$_2$Sn$_2$S$_5$ was synthesized from SnS$_2$ (SnS$_2$ was synthesized by heating a stoichiometric amount of Sn (99.8 %, *Acros*) and S$_8$ (99.998 %, *Sigma Aldrich*) with a slight excess of sulphur to 680 °C (12 h, 2 K/min)) and Li$_2$S (99.9 %, *Alfa Aesar*). A small amount of excess sulphur was added to the stoichiometric mixture to ensure a sulphur rich atmosphere during the reaction. The mixture was manually ground and mixed by mortar and pestle, pressed into pellets, and transferred into a glassy carbon crucible inside a quartz ampoule. The ampoule (17 mm diameter, 12 cm length) was flame sealed under low vacuum and annealed (650 °C, 48 h, 2 K/min). A shiny violet powder was obtained. During cooling, residual sulphur condensed at the cold end of the ampoule and was discarded. The synthesis was done by Christian Schneider.[85]

Hydrated Li$_2$Sn$_2$S$_5 \cdot x$ H$_2$O with specific values of x was prepared by sealing anhydrous Li$_2$Sn$_2$S$_5$ powder in a glass container next to (but not in contact with) the desired amount of deionized water. The system was then allowed to equilibrate at 25 or 50 °C for at least 1-2 days. In one occasion, the synthesis was performed in a thermogravimetric analyser (TGA) (cf. section 5.4). Another preparation method employed saturated salt solutions for humidification with defined p_{H_2O}. Samples were placed in a custom-built desiccator containing the solution, a small fan as well as a sensor (SHT35, *Sensirion AG*) to measure both humidity and temperature. The samples were kept in the humid atmosphere for sufficient time to ensure equilibration at the respective humidities. The synthesis was done with the aid of Christian Schneider.[85]

Electrode Material Li$_7$Ti$_5$O$_{12}$ (LTO7) was synthesized according to literature.[86] The synthesis was done in an Ar filled glove box by filling 1 g of Li$_4$Ti$_5$O$_{12}$ (LTO4, *Nanomyte* BE-10) into a round bottom flask and adding 20 ml of n-hexane ($\geq$ 99 % p.a., *Sigma-Aldrich*). Afterwards a 2.3 M solution of n-butyllithium (in cyclohexane/hexane, *Acros Organics*) was added drop-wise while the solution in the flask was permanently agitated with a Vortex mixer or a stirring bar. The white LTO4 almost immediately turned dark blue. The solution was stirred / agitated for 2 days, after which the blue powder was filtered off, washed several times with n-hexane and left to dry inside the glove box.

5.3 Sample Preparation

Compaction Procedure

Lithium Thiocyanate LiSCN

Anhydrous LiSCN was compacted by uniaxial pressing in hardened steel dies to produce dense pellets for electrochemical measurements. Cold pressing was the most efficient compaction method for this material. With a pellet diameter and thickness of 6 and 2.5 mm, the optimum pressing force was 15 kN (5.2 kbar) to produce on average 89 % dense pellets determined from mass and volume. A minimum pressure of 3.5 kbar had to be used to achieve sufficiently dense pellets, which were on average 86 % dense. Smaller pressures yielded densities < 80 %. Higher pressures of up to 18 kbar did not improve the density significantly. Pellets were pressed with thicknesses between 1.0-4.0 mm, however, thicknesses of up to 16 mm were achievable. Occasionally the pellets were polished with Al_2O_3 lapping paper (9MIC, *3M Lapping Film*) to remove any residue from the pressing tools. Various, yet unsuccessful sintering procedures were attempted to improve the density further:
- heating with 5 K/min to 80 °C, dwell for 12 h, cooling with 10 K/min
- heating with 10 K/min to 150 °C, dwell for 12 h, cooling with 10 K/min
- heating with 1 K/min to 180 °C, dwell for 12 h, cooling with 10 K/min
- heating with 10 K/min to 200 °C, dwell for 12 h, cooling with 10 K/min

The sintering was done under vacuum ($\sim10^{-6}$ mbar) in glassy carbon crucibles (*SIGRADUR G*) inside flame sealed quartz ampoules. The pellets were surrounded and covered with sacrificial LiSCN powder. Depending on the temperature, the white powder / pellets could turn brown, grey or even black.

Another attempt was uniaxial hot-pressing (*P/O/WEBER*, Germany). The material was pressed with a 5 mm hardened steel die under 13 kN (6.6 kbar), 15 kN (7.6 kbar) or 25 kN (12.7 kN) force and heated to 110 °C, 130 °C or 180 °C for 12 h. However, this method was inferior to cold pressing, since the obtained pellet densities were comparable to those of cold pressed ones, and the pellet would stick to the inside of the pressing die and could not be recovered unscathed.

"Spark plasma sintering" (SPS, HP D 5 SPS, *FCT Systems* GmbH, Germany) of 500 mg of dry LiSCN in a 10 mm graphite die produced fully densified pellets (up to 95 % relative density), applying a force of 8 kN (1 kbar) and heating to 240 °C for 1 min (heating and cooling rate 20 K/min). The LiSCN powder and resulting pellet were exposed to air for $\sim$30 s during transfer steps. Thereafter, the pellet was cleaned with SiC paper and polished with Al_2O_3 lapping paper in a glove box. SPS pressing was performed with the aid of Armin Sorg.

LiSCN single crystals or re-crystallised melts were also tried for conductivity measurements. LiSCN powder was melted in a glassy carbon crucible (typically heated to 350 °C) and then either slowly cooled (1 K/h) to 100 °C (in a quartz ampoule under vacuum in a furnace) or quenched quickly to room temperature (on a hot-plate inside a glovebox). Neither method produced single crystals, and the obtained crystallites were very porous with densities < 80 %. Crystal growth attempts were conducted with the help of Masahiko Isobe.

Hydrated LiSCN $\cdot x\,$H$_2$O samples with $x \approx 0.001$-1.0 were compacted like the anhydrous material by uniaxial cold pressing. For a pellet diameter of 5 mm, a pressing force of 10 kN (5.1 kbar) was used (lower or higher pressures yielded similar results), and thicknesses of 1.3-4.8 mm were attained. With this method relative densities of at least 86 % on average were achieved, determined from mass and volume (for two-phase mixture pellets $0.001 < x < 1.0$, the density represents only an estimate).

Lithium Tin Sulphide Li$_2$Sn$_2$S$_5$

Anhydrous Li$_2$Sn$_2$S$_5$ pellets were uniaxially pressed with a 5 mm diameter (10-20 kN (5-10 kbar), 1-5 min) at 25 °C. In one case a 5 mm square die was used. The resulting pellets had thicknesses in the range 0.5-7.3 mm and were about 87 % dense as determined from mass and volume. In order to further densify samples of Li$_2$Sn$_2$S$_5$, different heat treatments were conducted (sintering under vacuum either in Al$_2$O$_3$ or glassy carbon crucibles inside quartz ampoules):
• Pellet pressed with 10 kN (5 kbar), heated to 300 °C with 5 K/min, dwelled for 0.3 h, cooled to room temperature with 5 K/min; relative density of 92.5 %
• Pellet pressed at 25 °C with 10 kN (5 kbar), heated to 400 °C with 1 K/min in a S$_8$ flux, dwelled for 72 h, heated to 520 °C with 1 K/min, dwelled for 3 h, cooled to room temperature with 5 K/min; relative density of 86.7 %
• Pellet pressed at 25 °C with 15 kN (7.5 kbar), heated to 700 °C with 2 K/min in a S$_8$ rich atmosphere, dwelled for 48 h, cooled to room temperature with 2 K/min (similar to synthesis conditions); relative density of 87.8 %

Hydrated Li$_2$Sn$_2$S$_5$ $\cdot x\,$H$_2$O was compacted by uniaxial cold pressing (5 or 10 mm diameter, 0.1-1 min, 1.0-2.9 mm thickness). The material became softer with increasing water content, so the pressing force was decreased to 7-10 kN (3.5-5 kbar) for $0 < x \leq 3.0$ and 0.1-1 kN (0.05-0.1 kbar) for $x \geq 4.0$. For samples with $x \geq 4.0$, pressing forces above this range were avoided, since they seemed to squeeze water out of the material. The relative density of the resulting compacts was estimated to be at least 79 % for $0 < x \leq 3.0$, at least 72 % for $x \approx 4.0$, and at least 61 % for $x \approx 8.0$.

Drying Procedure

Undoped and doped samples of anhydrous LiSCN had to be dried right before any electrochemical measurement. Drying (as well as doping, see below) was conducted while using electrochemical impedance spectroscopy (EIS) to monitor the process (cf. section 5.6). The samples were thoroughly dried at temperatures between 230 °C and 250 °C under dynamic high vacuum ($< 10^{-3}$ mbar) in the respective EIS measurement cell (Figure 5.1) in which the sample was already strapped in with Pt contacts. One exception were measurements above 270 °C, which were dried and measured under Ar or N_2 flow, since they would start to sublimate under vacuum. The drying was monitored by EIS over the course of at least 2-3 days. This rigorous, yet necessary drying procedure explains the discrepancy between the here reported conductivities of anhydrous, undoped LiSCN compared to a previous study (Figure B.15a).[43]

Doping Procedure

Doping of anhydrous LiSCN was conducted by thoroughly mixing LiSCN with the doping agent, pressing the powder into a pellet as described for anhydrous LiSCN, and then heating the pellet stepwise to either 230 or 250 °C under dynamic high vacuum ($< 10^{-3}$ mbar) while monitoring its impedance. The densities of doped pellets were comparable to those of undoped material.

In case of Mg^{2+}-doping, the pellet consisting of an intimately mortar-ground mixture of LiSCN and $Mg(SCN)_2 \cdot 4\,H_2O$ had to be heated up slowly, to first remove the crystal water and avoid the formation of hydroxides or oxides (within the solubility limit of LiSCN for Mg^{2+}, $Mg(SCN)_2 \cdot 4\,H_2O$ was used as dopant). $Mg(SCN)_2 \cdot 4\,H_2O$ melts at 144 °C and decomposes at 167 °C.[9] To avoid any liquefaction and remove the H_2O first, the pellets were heated stepwise to 80 °C, 100 °C, 120 °C, 150 °C, 180 °C and 230 °C under high vacuum directly in the EIS measurement cell (Figure 5.1). The dwell time at each temperature step was typically at least 2-3 h.

The thermal properties of $Zn(SCN)_2$ and $Co(SCN)_2$ (99.9 %, *Aldrich*) were investigated by DSC (Figure B.8) as well as by visual inspection. $Zn(SCN)_2$ is stable up to 200 °C, after which the material decomposes. In contrast, $Co(SCN)_2$ did not show any signs of melting or decomposition until 333 °C. The doping procedure with both $Zn(SCN)_2$ and $Co(SCN)_2$ required less temperature steps compared to $Mg(SCN)_2 \cdot 4\,H_2O$, since both could be obtained in their anhydrous forms:

$Zn(SCN)_2$: 25 °C → 30 °C → 150-170 °C → 190 °C → 230-250 °C

$Co(SCN)_2$: 25 °C → 150 °C → 200 °C → 250 °C

Dwell times on each temperature step varied between 1.5 h and >100 h. Acceptor doping with Li_2S (99.98 %, *Sigma-Aldrich*) and Li_2SO_4 (99.99 %, *Sigma-Aldrich*) was attempted,

either by the same method as for donor doping or by solidification after melting, but was ultimately unsuccessful (Figure B.15b).

Doping with H$_2$O was conducted by exposing a pellet of dry LiSCN to various $p_{\text{H}_2\text{O}}$ at different temperatures. The pellet was prepared by uniaxial cold pressing (see above), contacted by sputtering (cf. section 5.6) and put into cell 1 (Figure 5.1) which was connected to a humidifier. The humidifier consisted of a single-walled glass container which was immersed in a thermostat (F 25, *Julabo*) to regulate its temperature (range between 2-18 °C). The humidifier contained deionized water through which dry N$_2$ was flushed to humidify the carrier gas. The humidified N$_2$ was mixed with dry N$_2$ close to the measurement cell (range of flow rates; dry 0-144 ml/min, humidified 2-77 ml/min). EIS measurements were done isothermally at 80 °C, 120 °C and 160 °C while applying various $p_{\text{H}_2\text{O}}$ between 0.1-4.3 mbar (relative humidities RH 0.02-0.9 %), 0.4-20.6 mbar (RH 0.02-1.0 %) and 0.4-20.6 mbar (RH 0.01-0.3 %) respectively. Lower measurement temperatures at 30 and 50 °C were also attempted, but due to the extreme hygroscopy of LiSCN were too unstable for doping the material. Before the initial exposure to $p_{\text{H}_2\text{O}}$ as well as after every temperature change, the pellet was fully dried as described above to ensure the same starting conditions. The sample temperature was constantly monitored with the dedicated thermocouple next to the pellet. The exhaust gas humidity after the measurement cell was checked with a humidity (*Rototronic*) and dew point (EE355-PA1, *E+E Elektronik*) sensor (Figure B.31a). Gas flows were adjusted with flow controllers and the complete set-up was leak checked (helium leak detector, UL 200 dry, *Oerlikon Leybold Vacuum*).

5.4   Sample Characterization

Thermogravimetric Analysis (TGA)

The amount of incorporated water was measured on powder samples (70-600 mg) in quartz crucibles. In this thesis, two different TGA set-ups were employed, and for both the sample was exposed to atmosphere for approx. 30 s during transfers.
The first TGA set-up was a *Netzsch* STA 449 instrument with a protective N$_2$ gas flow (< 10 ppm H$_2$O including trace leaks, 60 ml/min). For LiSCN samples, the powder was first heated at 120-180 °C under dry N$_2$ flow to remove any surface water, and then exposed to various $p_{\text{H}_2\text{O}}$ (1.4-17.1 mbar) at temperatures between 70-200 °C (RH of 0.009-2.3 %). In case of Li$_2$Sn$_2$S$_5$, measurements were done in a temperature range of 27-100 °C and $p_{\text{H}_2\text{O}}$ range of 1.4-17.1 mbar (RH range of 0.4-48.2 %). The humidity was set by mixing dry and humidified N$_2$ in different ratios (0-60 ml/min dry or wet N$_2$). The N$_2$ gas was humidified by bubbling dry N$_2$ gas through deionized water in a thermostatic

double-walled glass container, operated at 5-18 °C. The flow rates were sufficiently low that saturation could be assumed, such that the humidity is given by the water saturation pressure at the thermostat setpoint. The TGA exhaust gas was analysed by a *Balzers* Prisma quadrupole mass spectrometer. If necessary, a buoyancy correction was performed by subtraction of respective mass changes of an empty crucible.

The second TGA set-up, used for synthesis of $Li_2Sn_2S_5 \cdot x\,H_2O$, employed a balance (*Mettler AT20*) magnetically coupled (*Rubotherm*) to a quartz glass crucible containing the sample powder, which allows one to use high p_{H_2O} up to pure steam. The sample chamber (double-walled brass container) was connected to a transfer stage, which was directly attached to a humidifier (double-walled glass container). The sample chamber, humidifier and transfer stage were temperature controlled within an accuracy of $\pm\,0.05$ K. A wobble piston pump dropwise feeds enough water into the humidifier to obtain the desired p_{H_2O}. N_2 was used as protective and carrier gas ($<$ 10 ppm H_2O including trace leaks, 40 ml/min) and after passing the sample the humidified gas escapes through a heated (180 °C) capillary-exhaust at the top of the sample chamber. The recorded weight gain was corrected using a two-dimensional (T and p_{H_2O}) buoyancy correction parameterized for the empty crucible. The TGA measurements were performed with the aid of Rotraut Merkle, Klaus-Dieter Kreuer and Udo Klock.

Equilibrium Water Partial Pressure (p_{H_2O}) Measurements

The measurements were conducted on single phase samples of $LiSCN \cdot x\,H_2O$ ($x = 1$ and 2). $LiSCN \cdot 1\,H_2O$ was freshly synthesized as described in section 5.2 via gas phase hydration, and then filled into a custom made glass crucible. $LiSCN \cdot 2\,H_2O$ was synthesized directly inside the crucible by adding the respective amount of water with an *Eppendorf* pipette, and then heated with a hot air blower until the sample was completely liquid and homogeneous. The crucible was sealed with a silicone septum to avoid losses of H_2O. In both cases typical sample amounts were around 2-3 g. The glass crucible was connected to a humidity sensor (Hygroclip HK40, *Rotronic*) which was attached by gas-tight rubber seals. The filling height was chosen accordingly for minimal distance between the sample and humidity sensor. Temperatures were set and monitored with a modified drying oven (*Heraeus*) and an integrated thermocouple, as well as an additional thermocouple next to the humidity sensor.

Differential Scanning Calorimetry (DSC)

Anhydrous and hydrated samples were measured with a DSC 214 Polyma (*Netzsch*) (40 ml/min protective, 60 ml/min purging N_2 gas). The samples were weighed inside a glove box and filled into aluminium pans, which were sealed by cold welding with aluminium

caps. Heating and cooling rates varied between 2, 5 and 10 K/min. The employed reference was an empty, pierced aluminium pan. In case of hydrated samples, the cold welded seal prevented water losses up to ∼70 °C, after which dehydration or decomposition occurred. In addition, anhydrous LiSCN was also measured with a *Setaram* DSC 121 (CS92 controller, Tian-Calvet sensors) up to 700 °C in a stainless steel container (cold welded Ni O-ring seal), which was flushed with 10 ml/min of argon.

X-Ray Powder Diffraction (XRPD)

Phase Analysis was conducted by sealing powder samples, pellets or electrodes under dry inert gas in a polycarbonate dome (*PANalytical*). The sample holder provides sufficient protection from atmosphere for ∼24 h. Alternatively, powder samples were flame sealed in 0.5-0.7 mm capillaries (*Hilgenberg*, glass no. 14) in Ar atmosphere, which were fixated on zero-background XRPD sample holders (amorphous Si, *PANalaytical*). The patterns were measured at room temperature (*PANalytical* Empyrean Series 2 diffractometer, Bragg-Brentano configuration, Cu-K$_\alpha$, PIXcel 3D detector), and analysed using HighScore Plus 3.0e (*PANalytical*). The measurements were performed by Helga Hoier. For Li$_2$Sn$_2$S$_5 \cdot x$ H$_2$O, XRPD measurements were acquired using a *Stoe* StadiP diffractometer (curved Ge (111) monochromater, *DECTRIS* Mython2R 1K detector, Debye-Scherrer geometry, Mo-K$_{\alpha 1}$). Powder samples with lower x values (0-4.0) were packed in borosilicate capillaries (*Hilgenberg*, 0.3 mm diameter) and flame sealed under argon. Due to their soft and sticky consistency, samples at higher x values (4.0-10.0) were prepared in Kapton tubes of 0.8 mm diameter. These data were analysed using WinXPow (*Stoe*). The measurements were performed by Christian Schneider.[85]

Temperature Dependent *in situ* XRPD on LiSCN and LiSCN – Mg$_{1+\varsigma}$Li$_{4-2\varsigma}$(SCN)$_6$ composites were performed on a D8-Advance diffractometer (*Bruker*, Cu-K$_{\alpha 1}$ radiation from primary Ge(111)-Johann-type monochromator, Lynx Eye position sensitive detector) in Debye-Scherrer geometry using a water cooled furnace (mri capillary heater, 25-1000 °C) for heating the capillary. Within the respective temperature ranges, LiSCN had to be filled in quartz capillaries (*Hilgenberg*, 0.5 mm) to avoid fracturing, while LiSCN – Mg$_{1+\varsigma}$Li$_{4-2\varsigma}$(SCN)$_6$ composites could be measured in glass capillaries (*Hilgenberg*, glass no. 14). XRPD patterns of LiSCN were collected in a 2θ range from 5.0° to 40.0° applying a total scan time of 2 h. The patterns were recorded in 20 K steps, and in 5 K steps close to the melting point. Prior to each measurement a delay time of 10 minutes was applied to ensure thermal equilibration. XRPD patterns of LiSCN – Mg$_{1+\varsigma}$Li$_{4-2\varsigma}$(SCN)$_6$ composites were collected in a 2θ range from 5.0° to 90.0° applying a total scan time of 6 h.
XRPD patterns of LiSCN $\cdot$ 1 H$_2$O for *in situ* measurements were also recorded in Debye-Scherrer geometry on a laboratory powder diffractometer (Stadi-P diffractometer *Stoe*,

Cu-K$_{\alpha 1}$ radiation from primary Ge(111)-Johann-type monochromator, triple array of Mythen 1 K detectors, *Dectris*). The capillary samples were spun during the measurements. The experiments were performed using a hot and cool air blower (Cobra 700, *Oxford Cryosystems*). Heating and cooling rates were 5 K/min with 10 K steps and an equilibration time of 5 minutes. The patterns were recorded within 0° to 110° 2θ applying a total scan time of 30 minutes for each. The measurements were conducted by Sebastian Bette.

Water Partial Pressure Dependent *in situ* XRPD was performed on LiSCN in Bragg-Brentano configuration in the same set-up as described for phase analysis. Sample powder was filled into a modified polycarbonate dome (*PANalytical*), to which gas connectors had been attached for the hydration experiment. To change the p_{H_2O}, a water evaporator immersed in a thermostat (4-15 °C) for accurate temperature control was used. Humidified nitrogen gas was mixed with dry gas close to the measurement cell to set low partial pressures of water in the range of 0-1.5 mbar (dry N_2 gas flow 30-50 ml/min, wet N_2 gas flow 0-3 ml/min). The XRPD measurements were done isothermally at 27 °C (RH 0-4.4 %). Patterns were collected continuously between 10°-40° 2θ with a total scan time of 15 minutes. The patterns were measured by Helga Hoier, and analysed with the assistance of Sebastian Bette.

Crystal Structure Refinement

XRPD patterns for structure determination were collected at the respective temperature in the same set-up as described above for temperature dependent *in situ* measurements (Stadi-P diffractometer *Stoe*, 2θ range 0° to 110° with 30 min ($Mg_{1+\varsigma}Li_{4-2\varsigma}(SCN)_6$) or 4 h ($LiSCN \cdot 1\,H_2O$) scan time). The program TOPAS 6.0[87] was used to determine and refine the crystal structures of $Mg_{1+\varsigma}Li_{4-2\varsigma}(SCN)_6$ ($\varsigma = 0.02$), α- and β-$LiSCN \cdot 1\,H_2O$. In case of $Mg_{1+\varsigma}Li_{4-2\varsigma}(SCN)_6$, only the high temperature phase above 62 °C (cf. Figure 6.1) could be indexed and its crystal structure solved with the Rietveld method. The low temperature phase was highly disordered, and since pure phase samples could not be obtained, a precise indexing and solution of the crystal structure were not possible. If possible, phases were indexed by an iterative use of singular value decompositions (LSI).[88] This led to a *F*-centered cubic unit cell with $Fd\overline{3}m$ as most probable space group for $Mg_{1+\varsigma}Li_{4-2\varsigma}(SCN)_6$, a *C*-centered monoclinic unit cell with $C2$, Cm and $C2/m$ as most probable space groups for α-$LiSCN \cdot 1\,H_2O$, and a primitive orthorhombic unit cell with $Pnam$ or $Pna2$ as the most probable space groups for β-$LiSCN \cdot 1\,H_2O$, derived from systematic reflection absences. The peak profile and the precise lattice parameters were determined by LeBail using the fundamental parameter approach of TOPAS.[89, 90] The background was modelled by employing 6th order Chebychev polynomials and convergence was reached quickly. During the refinement of $Mg_{1+\varsigma}Li_{4-2\varsigma}(SCN)_6$, the presence of additional peaks attributed

to LiSCN was observed. Hence, the crystal structure of LiSCN was included into the refinement,[22] and into the subsequent process of crystal structure determination. The refinement of the XRPD patterns and solution of the crystal structures were performed by Sebastian Bette.

Single Crystal X-Ray Diffraction (SXRD)

For single crystal measurements, a suitable, transparent crystal ($\sim 10 \times 10 \times 5\,\mu m^3$) was picked in grease (*Dow Corning*) under a microscope in a glove box. The crystal was mounted using grease on a 0.3 mm capillary (*Hilgenberg*, glass no. 14), inserted in a 0.5 mm capillary, and sealed with a hot wire under argon. Diffraction data were then collected at room temperature (*Bruker* AXS diffractometer, graphite-monochromated Mo-K$_\alpha$, SMART-APEX-II detector) and analysed (*Bruker* Suite software, precession module).[91] The SXRD data was collected and analysed with the aid of Jürgen Nuss.

X-Ray Photoelectron Spectroscopy (XPS)

XPS spectra were recorded on a *Kratos* Axis Ultra spectrometer using a monochromatic Al-K$_\alpha$ X-ray source (1486.6 eV, 15kV, 10 mA). Survey and analysis spectra were recorded using either 80 or 20 eV as pass energy, respectively. The spectra were evaluated using the software CasaXPS. In case of S 2p peaks, the distance between 2p$_{3/2}$ and 2p$_{1/2}$ was constrained to 1.18 eV and the ratio of the peak areas was fixed to 2:1. XPS measurements and analysis were conducted by Kathrin Küster.

Raman and Infrared (IR) Spectroscopy

Raman spectra were taken with a Jobin Yvon Typ V 010 LabRAM single grating spectrometer, equipped with a double super razor edge filter and a Peltier cooled CCD camera (1 cm^{-1} resolution). Samples were measured as loose powder packed and hot-wire sealed in capillaries (*Hilgenberg*, glass no. 14) under argon. Spectra were taken in quasi-backscattering geometry using the linearly polarised 632.817 nm line of a He/Ne gas laser with power less than 1 mW, focused to a 10 µm spot through a 50x microscope or 20 µm spot through a 20x microscope objective on to the top surface of the sample. For heating experiments, the setup was equipped with a heating microscope stage (THMS600, controlled, Linkam TMS 94). Heating and cooling rates were 5 K/min under nitrogen atmosphere. The measurements were performed by Armin Schulz.

IR spectroscopy was conducted with a *Bruker* ALPHA II FT-IR (Fourier transform infrared) spectrometer using both attenuated total reflection (ATR) and diffuse reflectance infrared Fourier transform spectroscopy (DRIFTS) under argon atmosphere in a glove

box. The spectra were analysed with the software OPUS from *Bruker*. In general, a total of 24 scans were collected for each measurement within the range 400-4000 cm^{-1} and the resolution 4 cm^{-1}.

Inductively Coupled Plasma Optical Emission Spectroscopy (ICP-OES)

Samples for ICP-OES were prepared by dissolving finely ground powder in double-distilled water either under neutral conditions or by adding 5 vol.-% HNO_3 (65 % conc.). The measurements were performed on a Spectro Ciros ICP-OES spectrometer (*Spectro Analytical Instruments* GmbH, Germany). ICP-OES measurements were done by Samir Hammoud.

Scanning Electron Microscopy (SEM) and Energy Dispersive X-Ray (EDX) analysis

Samples were placed on carbon tape and coated with ∼6 nm carbon (ACE600, *Leica*). Micrographs were acquired by a *Zeiss* microscope (Merlin) using SE2 (Everhart-Thomley type) and/or in-lens detectors. EDX spectra were recorded with an Ultim Extreme EDX detector (*Oxford Instruments*). When the sample was sensitive to atmosphere, transfer steps were performed under high vacuum and inert gas, with no air exposure. SEM-EDX was conducted with the aid of Annette Fuchs, Bernhard Fenk and Ulrike Waizman.

5.5 Nuclear Magnetic Resonance

Solid State Nuclear Magnetic Resonance (ssNMR)

Powder samples were filled in a Pyrex magic angle spinning (MAS) rotor insert (*Rototec*) under argon. The insert was custom fitted with a ground glass joint for transfers. The sample bottom part of the insert was immersed in liquid nitrogen, and under slight static vacuum (∼0.5 bar) the insert was flame sealed. Spectra were acquired on a *Bruker* Avance III 400 MHz instrument (magnetic field of 9.4 T) at Larmor frequencies of 400 MHz (^{1}H), 155.5 MHz (^{7}Li), 149.15 MHz (^{119}Sn) and 58.8 MHz (^{6}Li), using a *Bruker* BL4 double resonance MAS probe and 4 mm outer diameter ZrO_2 spinners. The MAS spectra for all nuclei were acquired with a simple Bloch decay experiment (i.e. pulse-acquisition), and acquisition delays sufficiently long for a complete magnetization recovery. The ^{7}Li experiments were performed using central transition selective 90° pulses (the non-selective liquid 90° pulses were scaled by a factor of $(I + 0.5) - 1 = 0.5$).[92, 93] ^{7}Li and ^{6}Li variable temperature spin-lattice T_1 relaxation time measurements were performed both on spinning and non-spinning samples using the saturation-recovery method. Experiments with static measurements were performed with a *Bruker* static double resonance PE400

probe with a horizontal 5 mm coil. When more sample amount for higher signal intensity was needed than available with the rotor inserts, powder samples were first compacted (4 mm diameter, 10 kN (8 kbar), cf. section 5.3), several compacts filled into a NMR glass capillary (*Deutero*, D400) equipped with a ground glass joint, and consequently flame sealed under slight static vacuum. 8 to 64 scans were commonly averaged for a good signal-to-noise ratio. The temperature in the probes was regulated with a *Bruker* BVT3000 temperature controller. Actual temperature of the sample was calibrated on ^{207}Pb signal of powdered Pb(NO$_3$)$_2$.[94] Chemical shifts were referenced externally relative to tetramethylsilane (^{1}H, δ_{iso} = 0.0 ppm), to tetramethyltin (^{119}Sn, δ_{iso} = 0.0 ppm), using SnO$_2$ as a secondary standard (-603 ppm), and to 1 M LiCl solution (^{6,7}Li, δ_{iso} = 0.0 ppm).[95] ssNMR measurements were done by Igor Moudrakovski and analysed with his assistance.

Pulsed Field Gradient (PFG) NMR

PFG NMR was used to investigate the long-range diffusion of ions in samples of LiSCN $\cdot$ x H$_2$O and Li$_2$Sn$_2$S$_5$ $\cdot$ x H$_2$O. The technique probes the diffusion of ions by relating the attenuation of spin-echo signals to the translational motion of the targeted nuclei (details about this technique are well described by Price 1997).[96] Solid anhydrous and hydrated powder samples were densified (4 mm diameter, 10 kN (8 kbar), cf. section 5.3) and packed under argon at one end of a NMR glass capillary (*Deutero*, D400) equipped with ground joints, and a solid glass rod that matched the capillary inner diameter was inserted to reduce the dead volume (in case of anhydrous samples, the glass rod was omitted). The capillary was then flame sealed under slightly reduced pressure ($\sim$0.5 bar) of inert gas. Water loss during the sealing was found to be negligible. In case of liquid hydrates, a syringe was used to fill the sample directly at the bottom part of the NMR capillary at air, after which it was sealed. For LiSCN $\cdot$ 2 H$_2$O, sample and equipment were first heated to ensure the sample remains liquid during handling. Capillaries prepared in this way were installed in the NMR instrument (*Bruker* Avance III 400) equipped with either a diff60 gradient probe (max. 2900 G/cm, specialized RF inserts for ^{1}H and ^{7}Li) or a double resonance broad band probe (max. 1750 G/cm, BBO 400 MHz W1/S2 5 mm with Z-gradient) with tuneable frequency for different nuclei. The sample end of the capillary was stepwise heated or cooled between 25-180 °C (cooling with N$_2$ gas flow), or initially cooled down to -40 °C (cooling with liquid N$_2$) and then stepwise heated up again. After a $\sim$0.5 h effective dwell time at each temperature for equilibration, NMR measurements were acquired. At all temperatures the intent was to preserve the water content in the powder. However, above room temperature some water condensation was visible at the protruding cold (non-sample) end of the capillary, suggesting the samples underwent a small (and reversible) amount of water loss during heating. In case of Li$_2$Sn$_2$S$_5$ $\cdot$ 8 H$_2$O,

the capillary sealing was modified to essentially eliminate the dead volume of gas, and no condensation was observed. Data were acquired using a stimulated echo sequence with spoiler gradients. Various diffusion times in the range 6-100 ms were used, with effective gradient durations of 0.8-3 ms. Remagnetization dwell times D_1 were chosen to be 4 to 5 times higher than the spin-lattice relaxation time T_1. The measured echo-signal attenuation peaks were phase corrected, and the integrated areas were used to extract the diffusivities. The main analysis approach assumed isotropic (3D) diffusion for LiSCN $\cdot x\,H_2O$,[96] and anisotropic (2D) diffusion with negligible out-of-plane diffusivity for $Li_2Sn_2S_5 \cdot x\,H_2O$.[97] Measurements and analysis of PFG NMR were conducted with the assistance of Andreas Münchinger.

5.6 Electrochemical Measurements

Electrochemical Impedance Spectroscopy (EIS) was employed to measure the conductivity of the dominant charge carrier(s). EIS induces a small, frequency dependent voltage perturbation to yield a linear current response which is mathematically translated to the complex impedance (details about this technique can be found in references [98] and [99]). The measurements were conducted with a *Novocontrol* Alpha-A analyzer (2-wire measurement, 10^6 to $10^0 - 10^{-2}$ Hz, 0.1 V amplitude). Typically, two spectra were acquired at each condition to confirm reproducibility, with an average equilibration and dwell time of 1 h for anhydrous and 0.5 h for hydrated samples. When necessary, the stray impedance of the measurement setup was measured separately (by short-circuiting the electrodes at the respective temperatures) and pointwise subtracted out. Impedance spectra were fitted using Zview (*Scribner*, Version 3.5.c) by a respective equivalent circuit consisting of resistors (R), capacitors (C) and/or constant phase elements (CPE). The conductivity σ and dielectric constant ε_r were extracted using the standard relations $\sigma = L/(R \cdot A)$ and $\varepsilon_r = (C_{\text{eff}} \cdot L)/(\varepsilon_0 \cdot A)$, where R is resistance, L is sample thickness, A is cross-sectional area, ε_0 is the electrical permittivity of free space, and C_{eff} is the effective capacitance when employing a CPE calculated from $C_{\text{eff}} = Q^{n^{-1}} \cdot R^{(n^{-1}-1)}$, where Q and n are the magnitude and exponent of the CPE.

Direct Current (DC) Measurements were used for galvanostatic polarisation or electromotive force (EMF) measurements. Currents and voltages were set and measured either with a sourcemeter (*Keithley*, 2400 Sourcemeter) or with a battery analyzer (*Arbin Instruments*, BT Pulse).

Measurement Cells and Set-Up

Various measurement cell designs were used (Figure 5.1) which are briefly described here. Solid pellets of anhydrous samples were measured either under constant flow of inert gas (Ar or N_2, typically 50-100 ml/min) or under dynamic high vacuum. The anhydrous compacts were installed next to a thermocouple in an enclosed quartz holder and contacted with electrodes (Pt foil for cells 1, 3, 4, 6, and stainless steel for 2 and 5) under a slight spring pressure (cf. cell 1). To avoid water loss, pellets of hydrated samples were installed in a Teflon-lined tube fitting (*Swagelok*) and contacted by two rods that sealed to the fitting using Teflon ferrules (cell 2). This cell was installed in a quartz tube next to a thermocouple, similar to the one as shown for cell 1. Measurements intended to observe a solid to liquid phase transition had to use a different cell design (cell 3-5). Anhydrous samples were filled as loose powder in a quartz crucible equipped with Pt electrodes, and EIS was measured under inert gas flow or vacuum (cell 3). If humidified N_2 gas was used, cell 4 was employed to observe the transition point. The phase transition of hydrated samples was measured in a closed cell, by filling sample powder in a Teflon crucible, which was sealed with a PEEK plug inside a modified Swagelok cell with Teflon ferrules (cell 5). Cell 5 was also put into a quartz tube next to a thermocouple and contacted accordingly. For liquid systems, measurements were done in a U-shaped cell with inserted Pt electrodes, which was sealed with plastic screw caps (cell 6). Except for cell 6, all
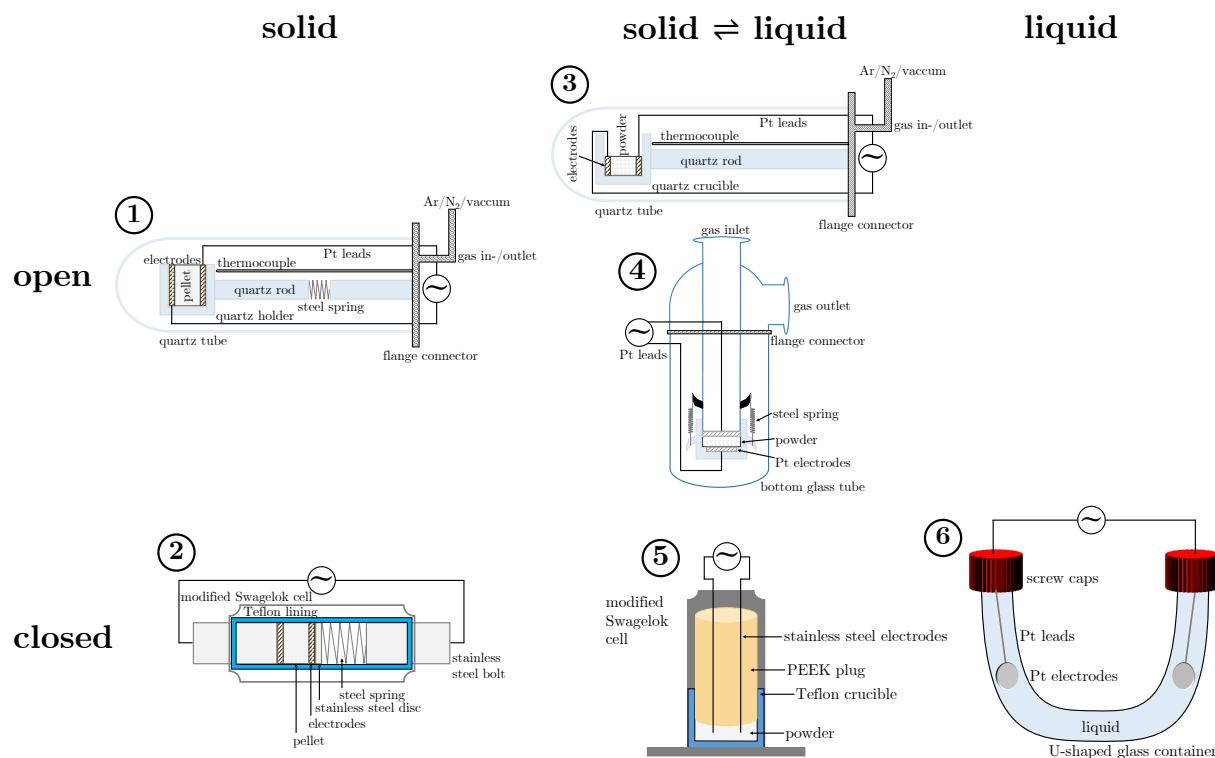
Figure 5.1: Measurement cell designs used for electrochemical measurements in this thesis. The cells were designed and built with the aid of Florian Kaiser.

measurement cells were leak-checked using a helium leak detector (UL 200 dry, *Oerlikon Leybold Vacuum*).

Measurements above room temperature were conducted in tube furnaces with either *Eurotherm* or *JUMO* temperature controllers (cell 1-3 and 5), a silicone oil filled *Julabo* thermostat (cell 4) or a modified *Heraeus* drying furnace (cell 6). Below room temperature, anhydrous samples were measured with a cryostat (*LH Leybold*, RDK 10-320, He cooling) under dynamic high vacuum, and hydrated samples by immersing the quartz tube containing cell 2 in a thermostat-controlled silicone oil bath (thermostat FP90, silicone oil Thermal HY, *Julabo*).

Measurements by Christian Schneider shown in this thesis were performed on a different set-up: TSC Battery closed cell (*rhd instruments*) in which pellet samples were contacted directly by steel electrodes under a constant pressure of 0.3 bar in a Microcell HC cell stand (1 h equilibration time).[85]

AC/DC measurements with Li$^+$ blocking electrodes

All measurements of anhydrous LiSCN below 270 °C, except for H_2O-doping, had to be measured under high dynamic vacuum ($< 10^{-3}$ mbar) to avoid any water (cell 1 in Figure 5.1). Dry Ar or N_2 flow were insufficient. For measurements above 270 °C (cell 3), a dynamic vacuum could not be used due to sublimation of the sample. However, at these high temperatures, dry Ar or N_2 flows could be used. LiSCN $\cdot\, x\, H_2O$ samples were measured either while varying p_{H_2O} (cell 1 and 4) or in a closed system (cell 2, 5 and 6). Anhydrous $Li_2Sn_2S_5$ could be measured without problems under flowing Ar or N_2 gas (cell 1) and hydrated $Li_2Sn_2S_5 \cdot\, x\, H_2O$ pellets were measured under closed conditions (cell 2).

Anhydrous samples of LiSCN and $Li_2Sn_2S_5$ were contacted by sputtering both sides of the pellets with $\sim$400 nm thick ruthenium metal (99.95 %, *Lesker*) applied by DC sputtering (*Emitech* K575X, 100 mA current, 4 min sputter time) in a glove box. During sputtering, the samples were exposed to high vacuum for several minutes, and the temperature increased to $\sim$50 °C as measured by an adjacent thermocouple. A mask was used to prevent metal deposition on the sides of each sample.

Hydrated samples of LiSCN $\cdot\, x\, H_2O$ and $Li_2Sn_2S_5 \cdot\, x\, H_2O$ had to be prepared for measurements depending on x. Sputtering with Ru as described above was used for $x \approx$ 0.01-0.1 (LiSCN $\cdot\, x\, H_2O$) and $x \leq 3.0$ ($Li_2Sn_2S_5 \cdot\, x\, H_2O$), though the sputtering time was reduced to 2 min. LiSCN $\cdot\, x\, H_2O$ did not show any evident signs of H_2O losses for these x values during sputtering, while in $Li_2Sn_2S_5 \cdot\, x\, H_2O$, x typically decreased by $\sim$0.5, as determined by weighing. To assure that x was preserved, other methods for contacting pellets of LiSCN $\cdot\, x\, H_2O$ were employed such as; (i) direct wet-bonding with the stainless steel bolts in cell 2 in an initial heating run to $\sim$150 °C ($x \approx$ 0.001-0.75), or (ii) uniaxial co-

pressing of graphite or indium foil electrodes with the sample powder (cf. section 5.3, $x \approx$ 0.1-1.0). For $Li_2Sn_2S_5 \cdot x\,H_2O$ compacts with $x \geq 4.0$, electrical contact with the stainless steel bolts in cell 2 from the spring pressure was sufficient without adding electrodes, so further preparation steps were omitted. Liquid samples of $LiSCN \cdot x\,H_2O$ ($x \gtrsim 2.0$) were directly filled into cell 6 and sealed with Pt electrodes containing screw caps.

AC/DC measurements with Li$^+$ reversible electrodes

Li metal (99.9 %, *Alfa Aesar*), LiAl (> 99.5 %, *ELSAindustries SAS*) and $Li_7Ti_5O_{12}$ (LTO7) (section 5.2) were used for conductivity and/or EMF measurements. Li metal electrodes were made by punching disks out of Li foil with a diameter according to the pellet size. To make electrodes, the synthesized LTO7 powder (1.1 g) was mixed with 0.15 g of polyvinylidene fluoride (PVDF) binder as well as 0.22 g of carbon black (ratio 15:2:3) and dispersed in 6.8 ml of n-methyl-2-pyrrolidone (99.0+ %, *Alfa Aesar*) by stirring for $\sim$16 h. The obtained slurry was cast on commercial Cu-foil with a doctor blade and dried at 80 ℃ on a hot plate. Electrodes were obtained with a 10 mm punch and tested against Li metal in a standard battery set-up (*Whatman* separator, 1 M LiPF$_6$ in EC:DEC (1:1) electrolyte *Sigma-Aldrich*). The cell showed a stabile voltage response of 1.56 V under open circuit condition. Both Li metal and LTO7 electrodes could be contacted to pellets by soft pressing with a hand crank, while LiAl powder had to be co-pressed with the sample material (cf. section 5.3). For $Li_2Sn_2S_5 \cdot x\,H_2O$ with $x \geq 4.0$, LiAl was pressed separately and contacted afterwards. Measurements were performed either in an Ar filled glove box with stainless steel contacts, under constant Ar flow (100 ml/min) in cell 1, for which protective molybdenum discs were used to avoid alloying of the Pt electrodes, or with commercial Swagelok battery cells in case of hydrated samples.

6 | Lithium Thiocyanate LiSCN

This chapter presents the collected results on defect chemistry and ionic conductivity of anhydrous LiSCN and hydrated LiSCN $\cdot\, x\,H_2O$. The first section focuses on anhydrous LiSCN, which was studied by aliovalent donor doping and identified as Schottky defective material with lithium vacancies as dominant mobile defects. The derived defect model reveals that the resulting conductivity depends on the employed dopant. The second subsection discusses the observed frequency dependent conductivity. Fast Li^+ ion transport occurs locally at high frequencies, while low frequency long-range transport is very slow. This behaviour is attributed to the long relaxation time of the SCN^- anion lattice when a cation jump occurs. A physical model is formulated and brought into context with the jump relaxation mechanism described by K. Funke.[100] The last subsection on anhydrous LiSCN discusses its defect chemistry close to the melting point (premelting regime) using the cube-root law approach.[101]

The second section presents the hydrated material, where the first part focuses on the structure and hydration behaviour of all LiSCN $\cdot\, x\,H_2O$ phases ($x = 0$, 1 and 2). Together with data from literature[10, 38] an updated phase diagram is constructed. The subsequent subsection focuses on using H_2O as a dopant. Doping with H_2O promotes anion lattice relaxation, which therefore not only increases the defect concentration, but also the defect mobility. A defect model for H_2O-doped LiSCN is constructed and compared to the anhydrous material. The final subsection presents ion transport data of stoichiometric hydrates LiSCN $\cdot\, x\,H_2O$ with $x \gtrsim 0.01$ covering all one- and two-phase regions in the $LiSCN - H_2O$ system. A comparison with literature data suggests broadly valid connections between $Li^+ - H_2O$ coordination chemistry and ion transport mechanism: In certain hydrates ion migration might be severely inhibited by the formation of strong associates. The present investigations on crystal structure, hydration behaviour and ion transport in the $LiSCN - H_2O$ system nicely depict the complexity of the SCN^- ligand coordination, the manifold effects hydration can have on a material, and provide deeper insights into (hydrated) ion conductors with complex anions.

6.1 Anhydrous LiSCN

6.1.1 Defect Chemistry

Ion transport investigations of anhydrous LiSCN are challenging, since trace amounts of water ($\leq$ 1000 ppm) can have an immense impact on conductivity and capacitance (cf. section 6.2). The difficulty to prepare anhydrous LiSCN was already noticed in previous investigations.[10, 39] However, in the first report on ion transport the impact of H_2O was underestimated,[43] which is why the previously reported conductivity data deviate from the present work (Figure B.15a). After performing various analyses including XRPD, Raman spectroscopy and DSC measurements at high temperatures (Figure B.1 and B.2), it was concluded that the material is stable beyond its melting point, and can be melted and recrystallised reversibly. Electrochemical investigations (galvanostatic DC polarisation and EMF measurement, Figure B.3) showed that LiSCN is, as expected, a Li^+ ion conductor with negligible electronic contributions. The EMF measurement indicates that LiSCN does not decompose (i.e. become reduced) or form percolating electronic pathways when in contact with reversible Li^+ electrodes, although it is expected that the material is only kinetically stable (formation of a stable SEI consisting of Li_2S, Li_3N, ...). The estimated ionic transference number was $\langle t_{Li+}\rangle \geq 0.99$.
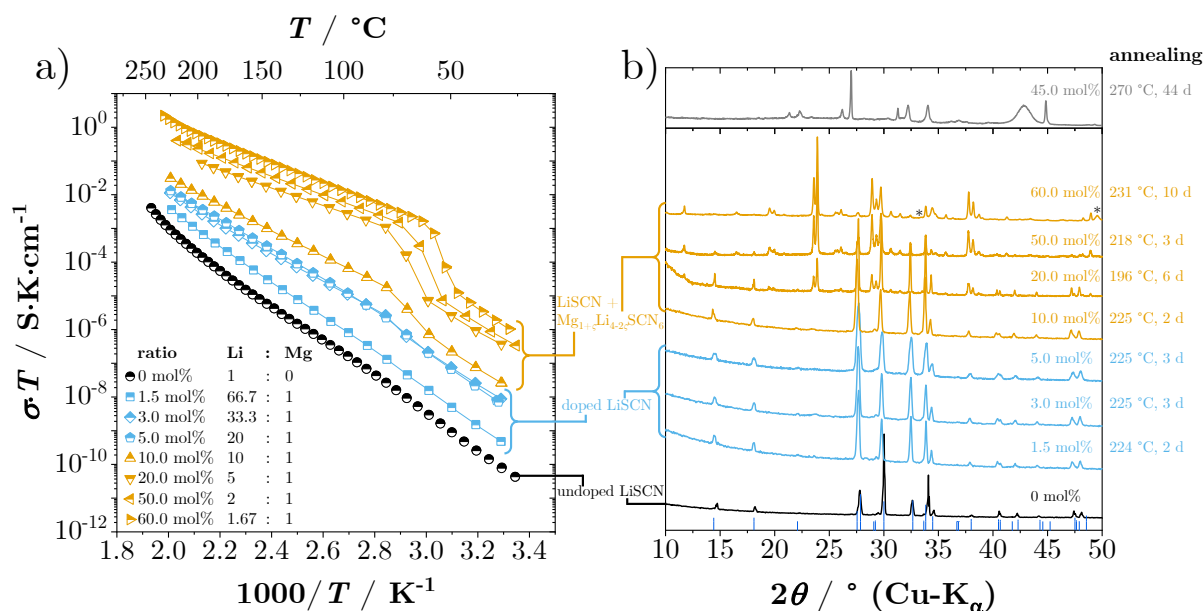
Figure 6.1: a) Conductivity and b) XRPD patterns of various LiSCN and $Mg(SCN)_2$ reaction products after heating: Anhydrous LiSCN (black), Mg^{2+}-doped LiSCN (blue), and mixtures of LiSCN and $Mg_{1+\varsigma}Li_{4-2\varsigma}(SCN)_6$ with $\varsigma = 0.02$ (orange). Blue bars in (b) correspond to the XRPD pattern of dry LiSCN from literature,[22] and peaks marked with an asterisk as well as the top grey pattern belong to unknown decomposition products.
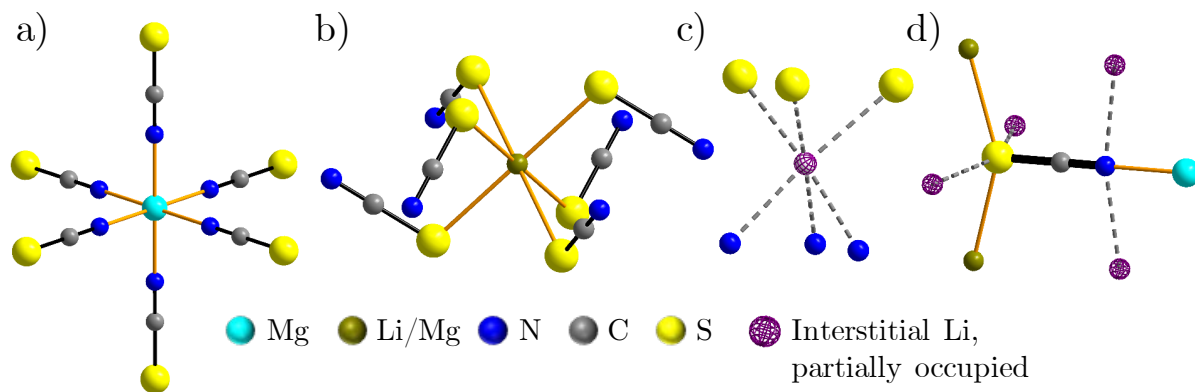
Figure 6.2: Coordination spheres in $Mg_{1+\varsigma}Li_{4-2\varsigma}(SCN)_6$ ($\varsigma = 0.02$) showing the coordination of; a) Mg sites, b) Li/Mg mixed sites, c) interstitial Li sites (partially occupied) and d) S and N sites in the SCN^- anion.

To identify the mobile defect in this material and investigate its defect chemistry, a doping study was conducted using aliovalent donor doping of cations with similar sizes as Li^+ (0.76 Å); Mg^{2+} (0.72 Å), Zn^{2+} (0.74 Å) and Co^{2+} (0.75 Å).[102] Figure 6.1a shows the conductivity for different Mg^{2+}-doping concentrations. Starting at around 10 mol% nominal Mg^{2+} concentration, a secondary phase was observed (Figure 6.1b), which was later identified as new compound $Mg_{1+\varsigma}Li_{4-2\varsigma}(SCN)_6$ with $\varsigma = 0.02$ based on Rietveld refinement (Figure B.4).

This new material $Mg_{1+\varsigma}Li_{4-2\varsigma}(SCN)_6$ showed a reversible phase transition at $\sim$47-62 °C, leading to cubic symmetry ($Fd\bar{3}m$, $Z = 8$, $V_{UC} = 3348.9(2)$ Å^3), and strongly increasing the conductivity. As can be seen in coordination compounds of Mg and Li thiocyanates,[9, 103] the cation-sulphur bonds are unfavourable, and the disfavour is higher for Mg^{2+} compared to Li^+. This bonding trend is nicely reflected in the structure of $Mg_{1+\varsigma}Li_{4-2\varsigma}(SCN)_6$ (Figure 6.2), in which (almost) all Mg atoms are exclusively coordinated via the nitrogen atom in SCN^-, while most of the Li atoms have to coordinate with the sulphur. This systematic arrangement of SCN^- is most likely the reason for the increase in conductivity, as discussed later in more detail. The crystal structure of the low temperature modification of this new phase could not be solved, owing both to the impurity of available samples, and the high degree of disorder in it. Numerous attempts to produce a pure phase were unsuccessful, and longer synthesis times even led to decomposition products (cf. Figure 6.1b, grey pattern).

To avoid secondary phases, doping concentrations of 5 mol% were not exceeded. Figure 6.3 shows exemplary impedance spectra of undoped and donor doped LiSCN. For both the complex modulus representation revealed an additional signal at higher frequencies (Figure 6.3b and B.11). The nature of this signal will be discussed in detail
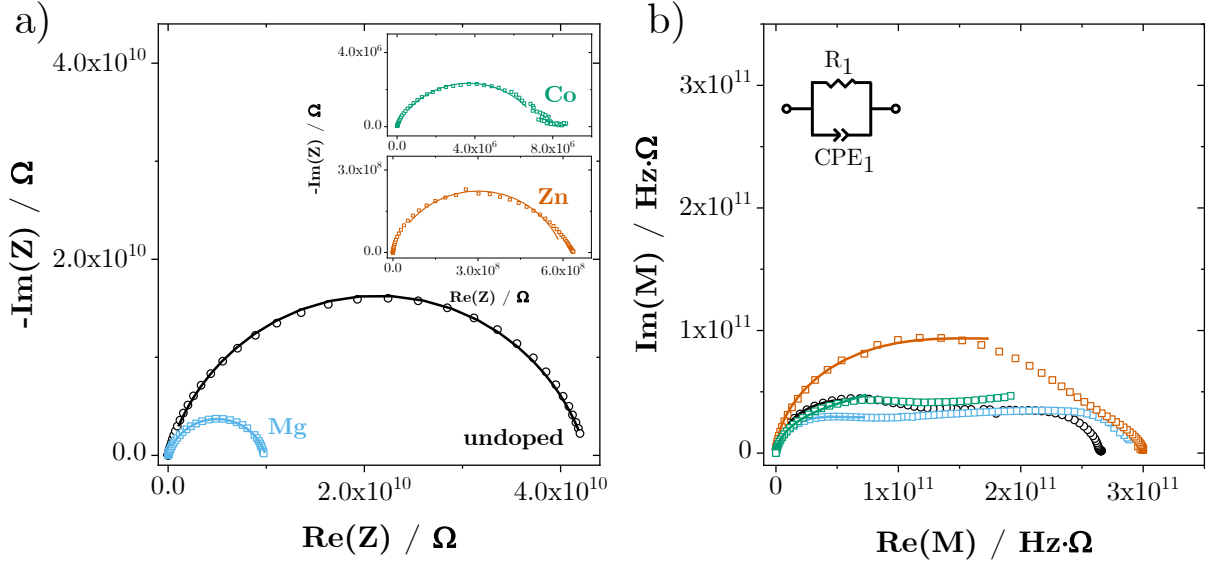
Figure 6.3: Exemplary a) impedance and b) modulus spectra of undoped (black) and 1.5 mol% doped (Mg^{2+} blue, Zn^{2+} red and Co^{2+} green) LiSCN at 68-69 °C, fitted with the equivalent circuit shown in (b).

in subsection 6.1.2[2]. However, for the analysis of the defect chemistry, only the "DC conductivity" at low frequency is relevant, and accordingly the following conductivity data in this subsection were extracted from the low frequency end of the impedance arc. Anion acceptor doping using Li_2S and Li_2SO_4 was attempted, however, turned out to be unsuccessful (Figure B.15b).

The conductivity of undoped LiSCN is shown in Figure 6.4a. Even though the changes in slope are subtle, the activation energy changes from low to high temperature, which can be classified into three different regimes: I intrinsic regime at high temperatures, II extrinsic regime at intermediate temperatures, and III association regime at low temperatures. This classification is similar to many ionic conductors (e.g. LiH[104] and Li_2S[105]). Donor doping increased the conductivity for all dopants (Figure 6.4b). One can therefore conclude that lithium vacancies V'_{Li} are the mobile defects in LiSCN. Since all lithium halides are known to be Schottky defective,[62, 63] and LiSCN classifies as a pseudo-halide, one can expect the formation of Schottky defect pairs as intrinsic defects:

$$Li^x_{Li} + SCN^x_{SCN} \rightleftharpoons V'_{Li} + V^{\cdot}_{SCN} + LiSCN_{surface} \tag{6.1}$$
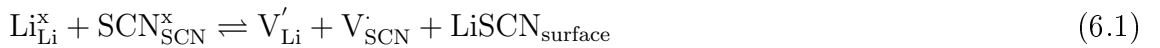
Donor doping increases the concentration of lithium vacancies according to:

$$2\,Li^x_{Li} + D(SCN)_2 \rightarrow D^{\cdot}_{Li} + V'_{Li} + 2\,LiSCN_{surface} \tag{6.2}$$

in which D stands for Mg, Zn and Co. Thus the defect concentration in the extrinsic

---

[2]$Mg_{1+\varsigma}Li_{4-2\varsigma}(SCN)_6$ did not show any additional high frequency signal (Figure B.5), which will also be explained in subsection 6.1.2.
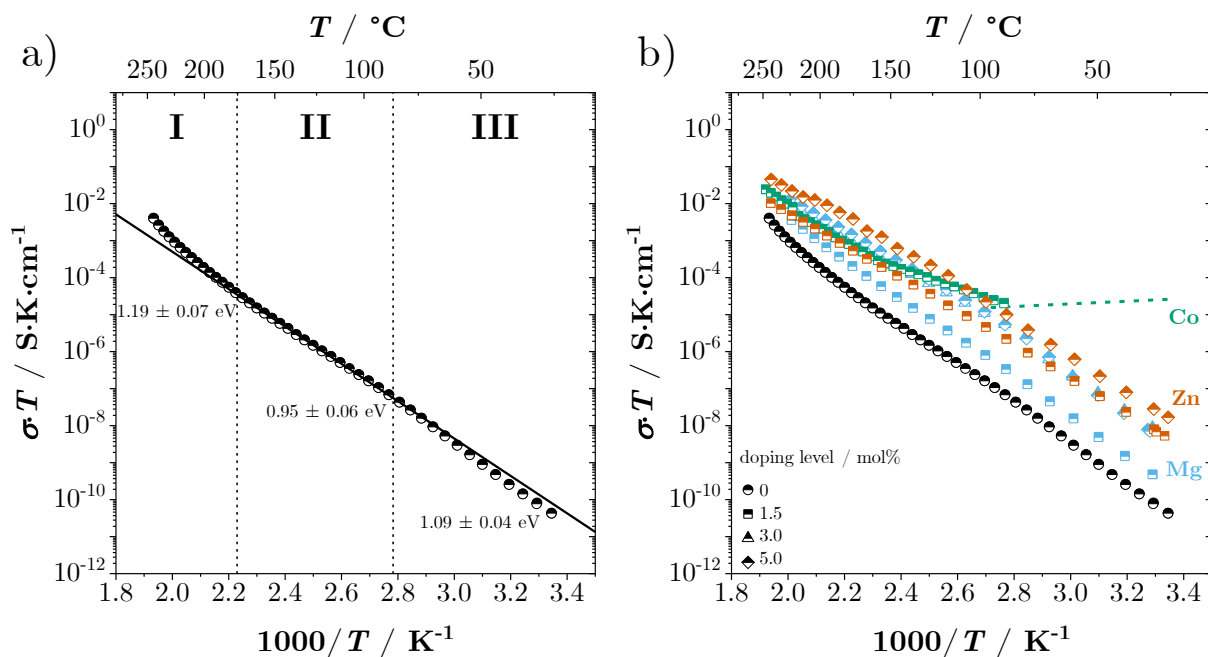
Figure 6.4: a) Conductivity of anhydrous, undoped LiSCN marking the regimes for association (III), extrinsic (II) and intrinsic (I) behaviour with the respective activation energies. b) Comparison of conductivities for undoped and donor doped LiSCN. The green dashed line shows where the Co^{2+}-doped material became electronically conducting.

regime is fixed to the nominal dopant concentration (assuming ideal solution behaviour)[3]. However, the concentration of mobile defects is lowered when the temperature is decreased as defect associates start to form:

$$D_{Li}^{\cdot} + V_{Li}^{'} \rightleftharpoons (D_{Li}V_{Li}) \tag{6.3}$$

Equations 6.1-6.3 nicely explain the observed changes in activation energy for the conductivity of LiSCN. Interestingly, the behaviour of donor doped LiSCN depends on the actual dopant (Figure 6.4b). Mg^{2+}-doped LiSCN showed the same regimes as the nominally undoped material (intrinsic to extrinsic transition at 180 °C, extrinsic to association transition at 88 °C). In case of Zn^{2+}-doping no noticeable defect association was observed, and Co^{2+}-doping even leads to dominant electronic conductivity at low temperatures (Figure B.10). This dopant dependent defect chemical behaviour distinguishes LiSCN from other ionic systems, and a possible explanation for this behaviour is discussed below. Except for undoped and 1.5 mol% Mg^{2+}-doped LiSCN, the intrinsic regime was not observed for the doped samples. This is not surprising given that the intrinsic regime of a Schottky defective material is expected to be small, and doping usually lowers the melting point. A possible explanation for the dopant-specific conductivity behaviour can be found in the

---

[3]In nominally undoped LiSCN the extrinsic regime is created by one or more contaminants, typically common elements such as Mg^{2+} or Fe^{2+}.

differences in coordination chemistry. As mentioned above, Mg^{2+} has a high tendency to avoid Mg-S bonds with the SCN^- anion, which is reflected in the fact that anhydrous $Mg(SCN)_2$ is as of yet unknown, and the tetrahydrate does not show any Mg-S bonds.[9] This disfavour for sulphur also applies to LiSCN and NaSCN. It has been related to both the size and polarisability mismatch of cation and anion,[106] well in accord with the hard and soft acid and bases (HSAB) concept of Pearson.[64] In contrast, both $Zn(SCN)_2$ and $Co(SCN)_2$ show cation to sulphur bonds in their crystal structures,[2, 32] indicating a more favourable Zn- / Co-S interaction. Since the defect $Mg^{\cdot}_{Li}$ in the crystal structure of anhydrous LiSCN is coordinated as $[Mg^{\cdot}_{Li}(NCS)_3(SCN)_3]$, it has a much stronger tendency to form associates with V'_{Li} than $Zn^{\cdot}_{Li}$ or $Co^{\cdot}_{Li}$.

The same idea explains the structural features in $Mg_{1+\varsigma}Li_{4-2\varsigma}(SCN)_6$, and one can now go one step further to understand its conduction behaviour. As shown in Figure 6.1a, $Mg_{1+\varsigma}Li_{4-2\varsigma}(SCN)_6$ displayed a much higher conductivity than highly doped LiSCN, and the conductivity even increased with the phase transition. If it is reasonably assumed that lithium vacancies are also the mobile defects in $Mg_{1+\varsigma}Li_{4-2\varsigma}(SCN)_6$, the increased conductivity is most likely related to an increase in defect concentration due to a lowering of the formation enthalpy. Since all Li atoms are exclusively coordinating with the sulphur of SCN^-, the formation of vacancies is favoured (the coordination $V'_{Li} - SCN^{x}_{SCN}$ is assumed to be stabilising). This is already reflected in the electron density map of the Rietveld refinement, which showed a severely lowered occupancy of Li atoms on their respective sites (but keeping in mind the low sensitivity of XRPD for Li atoms)[4]. These differences in metal cation to thiocyanate anion coordination chemistry can explain the experimental observations, i.e. the higher conductivity in $Mg_{1+\varsigma}Li_{4-2\varsigma}(SCN)_6$, the association or trapping of V'_{Li} for Mg^{2+}-doping, and the negligible tendency to form associates in Zn^{2+}- and Co^{2+}-doped LiSCN.

To quantify the defect formation thermodynamics in LiSCN, one can formulate the mass action constants of the respective regimes and derive the temperature dependences of the concentrations for all dominant defects. For the intrinsic regime according to equation 6.1:

$$K_S = [V'_{Li}][V^{\cdot}_{SCN}] = N_{Li}N_{SCN} \cdot \exp\left(\frac{\Delta_S S^\circ}{k_B}\right) \exp\left(-\frac{\Delta_S H^\circ}{k_B T}\right) \tag{6.4}$$

where K_S is the Schottky reaction equilibrium constant, $[V'_{Li}]$ and $[V^{\cdot}_{SCN}]$ are the respective defect concentrations (expressed in cm^{-3}), $N_{Li} = N_{SCN} = 4/V_{UC}$ are the number of available sites in the lattice ($V_{UC} = 240.56\,\text{Å}^3$ unit cell volume),[22] $\Delta_S S^\circ$ and $\Delta_S H^\circ$ are the standard entropy and enthalpy of Schottky defect formation, and k_B and T are Boltzmann's constant and temperature. In the extrinsic regime the defect concentration is

---

[4]A possible kinetic effect for the increase in conductivity for $Mg_{1+\varsigma}Li_{4-2\varsigma}(SCN)_6$ will be discussed in the next subsection 6.1.2 .

constant and independent of temperature (electroneutrality condition neglecting minority species):

$$[V'_{Li}] = [D_{Total}] \tag{6.5}$$

in which $[D_{Total}]$ is the total concentration of the dopant.

At lower temperatures the defect concentrations are affected by the formation of associates (cf. equation 6.3):

$$K_A = \frac{[(D_{Li}V_{Li})]}{[D^{\cdot}_{Li}][V'_{Li}]} = \frac{N_A}{N_D N_{Li}} \cdot \exp\left(\frac{\Delta_A S^\circ}{k_B}\right) \exp\left(-\frac{\Delta_A H^\circ}{k_B T}\right) \tag{6.6}$$

K_A being the association equilibrium constant, $[(D_{Li}V_{Li})]$, $[D^{\cdot}_{Li}]$, and $[V'_{Li}]$ the concentrations of associates, dopants and lithium vacancies, and $\Delta_A S^\circ$ and $\Delta_A H^\circ$ the standard entropy and enthalpy of association. Since doping occurs only on the Li sites, the number of available lattice sites for dopants N_D equals N_{Li}, and every Li has two other Li atoms as nearest neighbours, meaning $N_A = 2N_{Li}$ for the associates. One can express the total dopant concentration as (mass balance):

$$[D_{Total}] = [(D_{Li}V_{Li})] + [D^{\cdot}_{Li}] \tag{6.7}$$

Considering overall electroneutrality ($[D^{\cdot}_{Li}] + [V^{\cdot}_{SCN}] = [V'_{Li}]$), respective Brouwer approximations for all dopants and regimes can be formulated as listed in Table 6.1.[98, 105] With the equations in Table 6.1 the temperature dependences of all defects can be derived using equations 6.4-6.6, and are shown in Figure 6.5.

Table 6.1: Overview of the Brouwer approximations used to derive the defect chemical model of anhydrous LiSCN.

	Mg	Zn	Co
regime I intrinsic	$[V'_{Li}] = \sqrt{K_S} = [V^{\cdot}_{SCN}]$ $[Mg^{\cdot}_{Li}] = [D_{Total}] > [(Mg_{Li}V_{Li})]$ $[(Mg_{Li}V_{Li})] = K_A\sqrt{K_S}[D_{Total}]$	$[V'_{Li}] = \sqrt{K_S} = [V^{\cdot}_{SCN}]$ $[Zn^{\cdot}_{Li}] = [D_{Total}]$	$[V'_{Li}] = \sqrt{K_S} = [V^{\cdot}_{SCN}]$ $[Co^{\cdot}_{Li}] = [D_{Total}]$
regime II extrinsic	$[V'_{Li}] = [D_{Total}] = [Mg^{\cdot}_{Li}]$ $[V^{\cdot}_{SCN}] = K_S/[D_{Total}]$ $[(Mg_{Li}V_{Li})] = K_A[D_{Total}]^2$	$[V'_{Li}] = [D_{Total}] = [Zn^{\cdot}_{Li}]$ $[V^{\cdot}_{SCN}] = K_S/[D_{Total}]$	$[V'_{Li}] = [D_{Total}] = [Co^{\cdot}_{Li}]$ $[V^{\cdot}_{SCN}] = K_S/[D_{Total}]$
regime III association	$[V'_{Li}] = \sqrt{[D_{Total}]/K_A} = [Mg^{\cdot}_{Li}]$ $[V^{\cdot}_{SCN}] = K_S\sqrt{K_A/[D_{Total}]}$ $[(Mg_{Li}V_{Li})] = [D_{Total}]$		
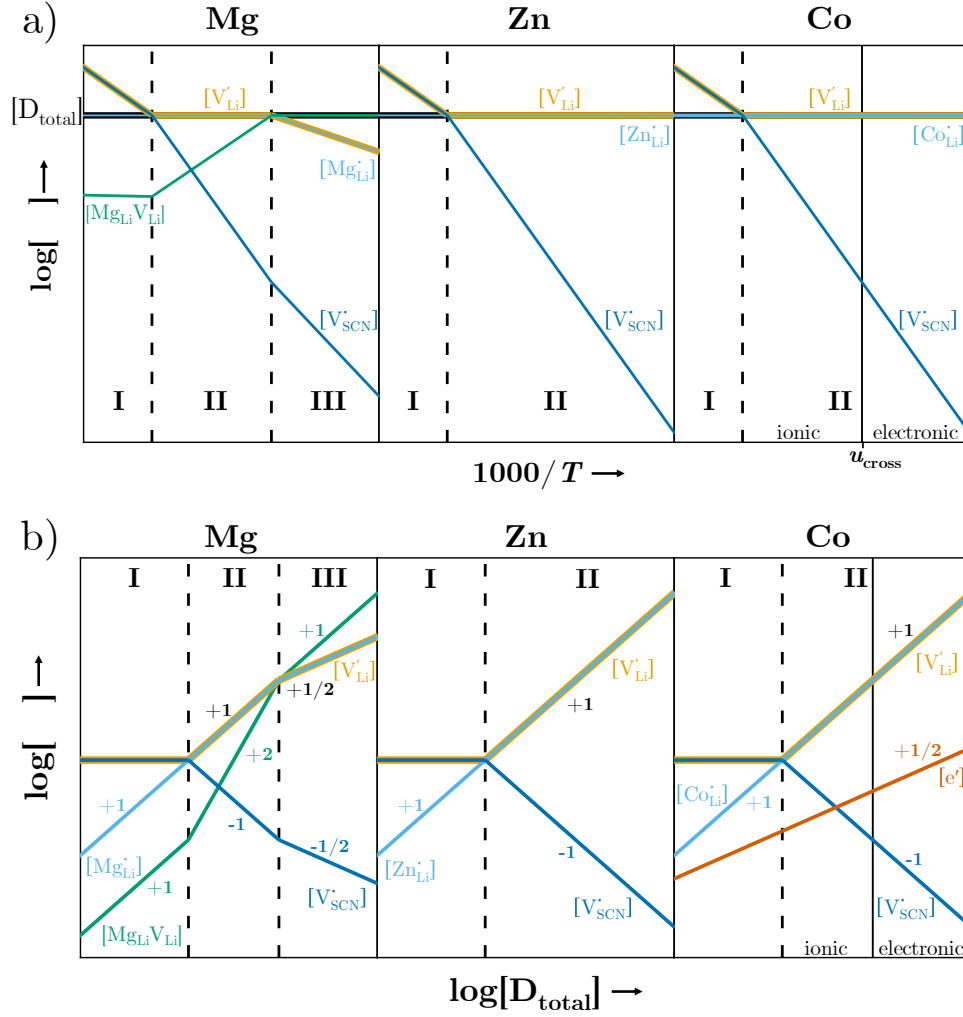
Figure 6.5: Defect concentrations as a function of a) temperature and b) dopant concentration (Brouwer diagram) indicating the different regimes by the respective changes in slopes. In case of Co^{2+}-doping, an additional line marks the transition from predominantly electronic to ionic conduction.

In case of Co^{2+}-doping, some additional considerations for electronic charge carriers are necessary. In Figure 6.5, the extrinsic regime for Co^{2+}-doped LiSCN is subdivided to mark the electronic and ionic parts. However, the type of electronic defect (electrons e' or holes $h^{\cdot}$) is unknown, but it is likely that the concentration of electrons is increased with donor doping. Looking at the redox chemistry of Co^{2+} in liquid systems, it is clear that the reduction/oxidation potential is influenced by the ligands,[107] and the coordination with SCN^- was suggested to lower the potential for the redox pair Co^{2+}/Co^{3+}.[108] It is therefore assumed that the mobile electronic defects are electrons, which are generated by:

$$Co_{Li}^{\cdot} \rightleftharpoons Co_{Li}^{\cdot\cdot} + e' \tag{6.8}$$

with the corresponding equilibrium constant of electronic disorder K_e:

$$K_e = \frac{[Co_{Li}^{\cdot\cdot}][e']}{[Co_{Li}^{\cdot}]} \tag{6.9}$$

Since dominant electronic conduction was measured at a doping concentration as low as 1.5 mol%, it is possible that the SCN^- anion is involved in the hopping mechanism of the electrons[5]. It is reasonable to assume that only a fraction of $Co_{Li}^{\cdot}$ is dissociated into $Co_{Li}^{\cdot\cdot}$ and e'. The concentrations of $Co_{Li}^{\cdot\cdot}$ and e' are higher than the background concentration of electronic defects, yet considering the electronic structure of LiSCN, they are nonetheless very low compared to the concentrations of other ionic defects. This means that $[Co_{Li}^{\cdot}] \gg [Co_{Li}^{\cdot\cdot}]$ and $[Co_{Li}^{\cdot\cdot}] = [e']$. One can therefore approximate $[Co_{Li}^{\cdot}] \approx [D_{Total}] = $ constant, and the following Brouwer approximation can be formulated:

$$[e'] = \sqrt{K_e[D_{Total}]} \tag{6.10}$$

Using the standard expression for conductivity σ, the mobility of vacancies $u_{V_{Li}'}$ can be calculated according to:

$$u_{V_{Li}'}T = \frac{\sigma_{V_{Li}'}T}{z_{V_{Li}'}e \cdot [V_{Li}']} \tag{6.11}$$

since the concentration $[V_{Li}']$ is constant in the extrinsic regime ($z_{V_{Li}'}$ and e are the charge number of V_{Li}' (equal to 1) and charge of an electron). Figure 6.6 shows the mobilities of lithium vacancies calculated by inserting the conductivity data from the extrinsic regimes of all dopants into equation 6.11 and dividing by the respective values of $[D_{Total}]$. The mobility term $u_{V_{Li}'}T$ is given by:

$$u_{V_{Li}'}T = \frac{r_{Li}^2 e}{Nk_B}\nu_0 \cdot \exp\left(\frac{\Delta_m S_{V_{Li}'}}{k_B}\right)\exp\left(-\frac{\Delta_m H_{V_{Li}'}}{k_B T}\right) \tag{6.12}$$

where $r_{Li} = 3.16$ Å is the distance to a neighbouring available site of V_{Li}', $N = 2$ is the number of neighbouring sites and $\nu_0 \approx 10^{13}$ Hz is the typical jump attempt frequency.[98, 105] The linear fits in Figure 6.6 were averaged and used to derive the following expression for the mobility of lithium vacancies:

$$u_{V_{Li}'}T = 10^{(5.1\pm0.4)}\exp\left(-\frac{(0.89\pm0.08)\,eV}{k_B T}\right)\frac{cm^2 K}{Vs} \tag{6.13}$$

---

[5]If homogeneous doping of 1.5 mol% $Co_{Li}^{\cdot}$ is assumed, one Co atom would sit between 33-34 Li atoms in the octahedra chains in b direction, which means a Co-Co hopping distance of $\sim$100 Å.

[6]For Co^{2+}-doped LiSCN only data above 153 °C were used for the fitting.
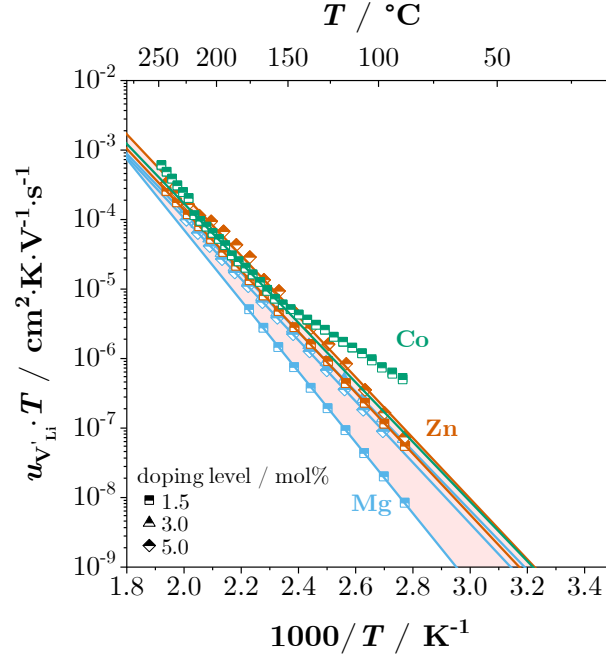
Figure 6.6: Calculated mobilities of lithium vacancies V'_{Li} from the extrinsic regime (II) in donor doped LiSCN (cf. Figure 6.4). Solid lines are linear fits[6].

Since the concentration of electrons is unknown, one can only define a lower bound for the electron mobility by linearly fitting the conductivity data of Co^{2+}-doped LiSCN below 84 °C (cf. Figure 6.4b, green dashed line), setting $[e'] = [D_{Total}]$ and inserting them into equation 6.11[7]:

$$u_{e'}T \geq 10^{(-7.5)} \exp\left(-\frac{(-0.074)\,\text{eV}}{k_B T}\right) \frac{\text{cm}^2\text{K}}{\text{Vs}} \tag{6.14}$$

With the mobility of V'_{Li} known, one can derive expressions for K_S and K_A using the conductivity data in Figure 6.4 and the Brouwer approximations in Table 6.1[8]. Fitting regime I in Figure 6.4a and inserting $[V'_{Li}] = \sqrt{K_S}$ with equation 6.13 into equation 6.11 yields:

$$K_S = 10^{(45\pm2)} \exp\left(-\frac{(0.6\pm0.3)\,\text{eV}}{k_B T}\right) \text{cm}^{-6} \tag{6.15}$$

Fitting regime III of Mg^{2+}-doped LiSCN in Figure 6.4b and inserting $[V'_{Li}] = \sqrt{[D_{Total}]/K_A}$ with equation 6.13 into equation 6.11 yields:

$$K_A = 10^{(-25\pm3)} \exp\left(-\frac{(-0.3\pm0.2)\,\text{eV}}{k_B T}\right) \text{cm}^3 \tag{6.16}$$

---

[7]The real value of $\Delta_m H_{e'}$ is most certainly positive yet very small, and due to experimental uncertainty, the linear fit yielded a negative value.

[8]A value of K_e is not given because of too large uncertainties.

Since all equilibrium constants were derived, Brouwer diagrams could be constructed in which the respective defect concentrations are shown as a function of total dopant concentration (Figure 6.5). The concentration $[e^{'}]$ was defined to be lower than $[Co_{Li}^{\cdot}]$, i.e. it represents an upper bound. By combining equations 6.13, 6.15 and 6.16 with 6.4, 6.6 and 6.12, the respective entropies can be calculated and are included in Table 6.2. Having the thermodynamic and kinetic data of defect formation and migration at hand, charge carrier concentrations in anhydrous LiSCN can be obtained, here shown for 1.5 mol% of Mg^{2+}-doping (Figure 6.7).

Table 6.2: Enthalpies and entropies of defect formation, migration and association of the Schottky defective material LiSCN.

Schottky disorder	$\Delta_{S}H^{\circ}$ / eV	0.6 ± 0.3
	$\Delta_{S}S^{\circ}$ / k_{B}	$5 \pm 2^{\dagger}$
$V_{Li}^{'}$ migration	$\Delta_{m}H_{V_{Li}^{'}}$ / eV	0.89 ± 0.08
	$\Delta_{m}S_{V_{Li}^{'}}$ / k_{B}	7.7 ± 0.9
$(Mg_{Li}V_{Li})$ association	$\Delta_{A}H^{\circ}$ / eV	-0.3 ± 0.2
	$\Delta_{A}S^{\circ}$ / k_{B}	-8 ± 6

†Values of different samples could deviate more than this estimated error.

Figure 6.8 compares the DC conductivity of anhydrous LiSCN with the reported data of comparable Li^{+} ion conductors. One can immediately notice that Li^{+} ion transport
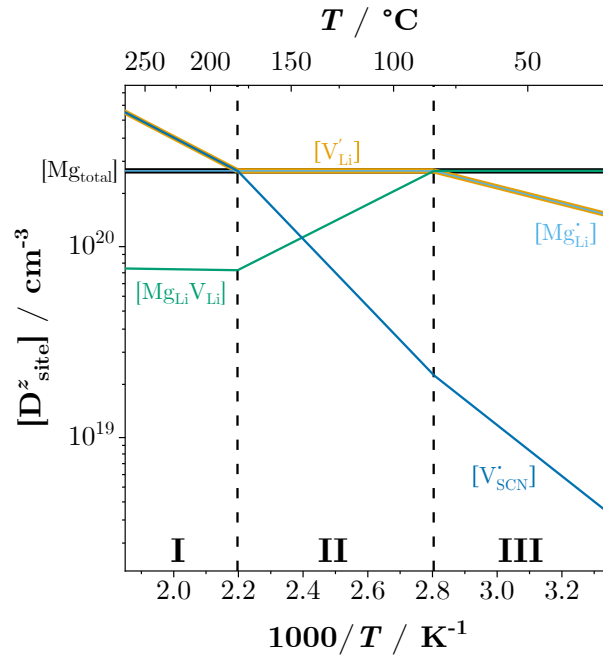
Figure 6.7: Calculated concentrations of various defects in 1.5 mol% Mg^{2+}-doped LiSCN.
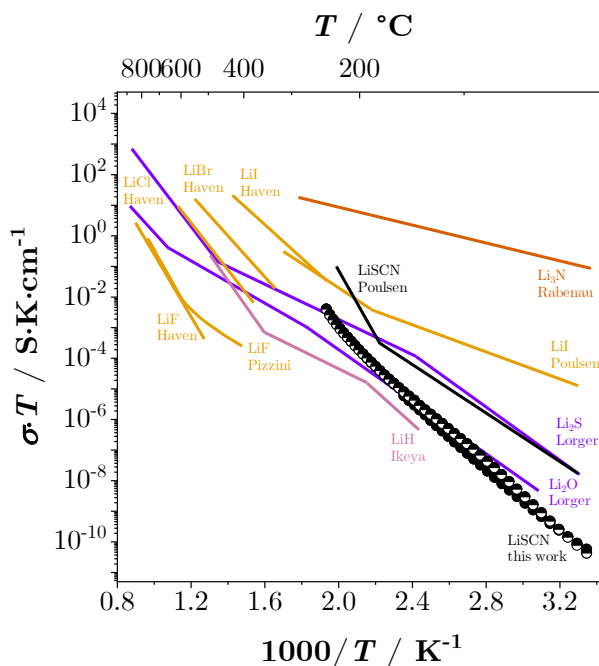
Figure 6.8: Comparison of the DC conductivity of anhydrous, undoped LiSCN with literature values[43] as well as with chemically similar binary Li$^+$ ion conductors: lithium hydride LiH,[104] lithium halides LiX (X = F,[62, 63] Cl,[62] Br,[62] I[62, 74]), lithium chalcogenides Li$_2$Cn (Cn = O,[109] S[105]) and lithium nitride Li$_3$N.[110]

is rather poor compared to these other materials, which at a first glance is unexpected. Judging from the crystal structure, one might initially expect the conductivity of LiSCN to be somewhere between Li$_2$S and Li$_3$N, which, however, is evidently inaccurate. Judging from cation to anion relative size and chemical behaviour, Li$^+$ ion transport in LiSCN should be similar to LiI, but this comparison does also not apply. This surprising result can be explained by reviewing the thermodynamic and kinetic quantities of defect formation and migration of other Schottky defective materials (Table 6.3). The observed trend for the enthalpies in the lithium halides correlates with the differences in electronegativity and ion size. Even though LiH does not quite fit into this series, it nonetheless shows similar transport characteristics, i.e. a high defect formation enthalpy and a low migration enthalpy. LiSCN indeed shows a very low defect formation enthalpy (and a comparable entropy), which fits into this trend for the lithium halides. However, its migration enthalpy is much higher than one would expect, exceeding even the values of LiF. The evident difference between LiSCN and these LiX compounds is the anion, which in the former consists of an anisotropic bidental ligand, that forms both Li-S and Li-N bonds. As shown in detail in the next subsection, the anisotropic and slow local motion of the SCN$^-$ anion causes a frequency dependence of the Li$^+$ ion transport. This impedes long-range Li$^+$ ion migration, lowers the conductivity drastically, and leads to a high migration enthalpy. Such a mechanism does not occur in the LiX phases.

Table 6.3: Comparison of thermodynamic and kinetic data of LiSCN obtained in this work with various LiX (X = H, F, Cl, Br, I) compounds from literature.

compound		$\Delta_S H°$ / eV	$\Delta_S S°$ / k_B	$\Delta_m H_{V'_{Li}}$ / eV	$\Delta_m S_{V'_{Li}}$ / k_B	$\Delta_A H°$ / eV	$\Delta_A S°$ / k_B	reference
LiH	experimental	2.3 ± 0.3		0.54 ± 0.02		-0.50 ± 0.05 (Mg$_{Li}$V$_{Li}$)		[104]
LiF	experimental	2.6 ± 0.2		0.67 ± 0.02				[63, 111–113]
	DFT	2.2-2.9		0.6				[114]
LiCl	experimental	2.12		0.41				[63, 111]
LiBr	experimental	1.80		0.39				[63, 111]
LiI	experimental	1.2 ± 0.1	4.5	0.41 ± 0.03	4.9			[63, 111, 115]
LiSCN	experimental	0.6 ± 0.3	5 ± 2	0.89 ± 0.08	7.7 ± 0.9	-0.3 ± 0.2 (Mg$_{Li}$V$_{Li}$)	-8 ± 6 (Mg$_{Li}$V$_{Li}$)	this work

6.1.2   Frequency Dependence of Ion Transport

As mentioned in the previous subsection, undoped (and doped) anhydrous LiSCN consistently showed two relaxation processes in the impedance spectra, more clearly depicted in Figure 6.9 below. A characteristic feature of these two processes was their strong convolution, making them less discernable in the complex impedance representation (Figure 6.9a), but more so in the complex modulus (Figure 6.9b). With increasing temperature the low frequency process ω_2 becomes gradually less distinguishable, until only the high frequency process ω_1 remains (Figure 6.9c). Various experiments were undertaken to determine the nature of these two signals, which will briefly be listed here:
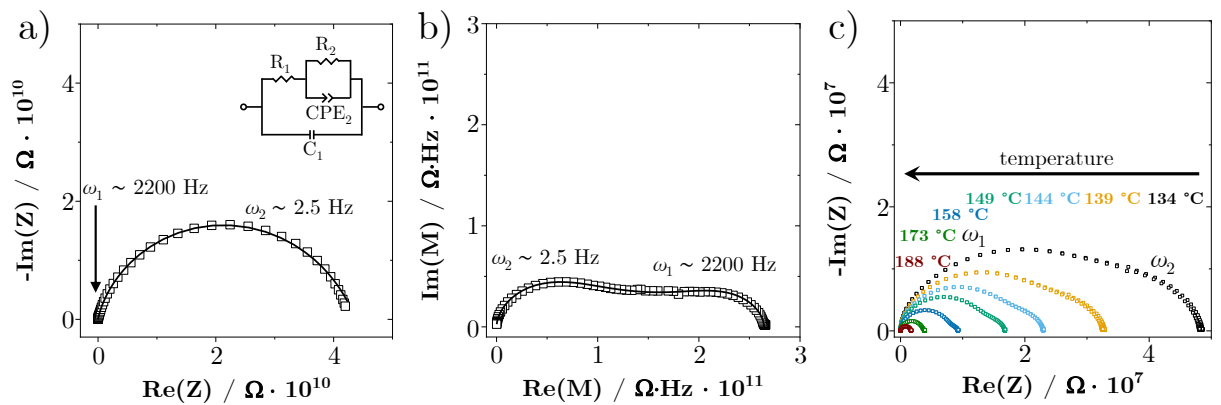
Figure 6.9: a) Impedance and b) complex modulus spectrum at 69 °C, and c) impedance spectra at various temperatures of anhydrous, undoped LiSCN. All spectra were fitted with the equivalent circuit shown in (a).

- The resistances of various samples for both ω_1 and ω_2 were measured as a function of the pellet thickness. Figure B.16 demonstrates that both resistances scale with sample thickness.

- To exclude possible porosity effects or artefacts from current constriction, cold pressed samples were compared with a fully densified sample (relative density 94 %) made by SPS. Both types of samples are shown in Figure 6.10, exhibiting the same conductivities and dielectric constants within the experimental error.

- The dielectric constants of ω_1 and ω_2 typically differed by less than one order of magnitude (Figure 6.10). With an average grain size of $\sim$10-50 µm (cf. Figure B.14a) and thickness of grain-boundary regions in the nanometre range, blocking grain-boundary capacitances should be at least three orders of magnitude higher compared to the bulk response. It would also be rather unexpected to observe a blocking grain-boundary response for a chemically "soft" ionic salt such as LiSCN (cf. Figure B.14b). For example, LiI does not show any blocking features before the Warburg diffusion tail (Figure B.17b).

- Given their chemical similarity, a pellet of LiI was measured for comparison (Figure B.17). LiI did not show any additional high frequency process ($\varepsilon_\mathrm{r} \sim$30), which suggests that the ω_1 signal in LiSCN is related to some specific properties of the SCN$^-$ anion.

The circuit in Figure 6.9a can better describe the data than a serial connection consisting of two parallel R-C-units (Ser{Par[R$_\mathrm{bulk}$,C$_\mathrm{bulk}$],Par[R$_\mathrm{GB}$,C$_\mathrm{GB}$]} circuit), which is often used for strongly blocking grain-boundaries (in the limiting case of C$_\mathrm{GB} \gg$ C$_\mathrm{bulk}$ the circuits become equivalent). Having clarified that both ω_1 and ω_2 are part of the sample response in LiSCN, the nature of these signals is now discussed. Figure 6.10 shows that around 150 °C ω_1 and ω_2 become indistinguishable. Only the high frequency process remains ($\varepsilon_\mathrm{r} = 23 \pm 8$), which continues with the same activation energy of 1.2 ± 0.2 eV as ω_2 at lower temperatures. The dielectric behaviour of ω_2 is attributed to an induced polarisation effect which decreases at higher temperatures, and considering the above analysis, it can be related to the SCN$^-$ anion lattice.

To understand the underlying physical mechanism, the impedance results are discussed in the context of the jump relaxation model (JRM) introduced by K. Funke.[100] Within this model, ion transport is analysed as a function of frequency, for which three regimes are classified:

Regime I: High Frequency Plateau, where all mobile ions hop to neighbouring sites in correlated forward-backward motions. On a short time scale, i.e. high frequency, backward jumps are highly favoured because the environment of the final site has not yet
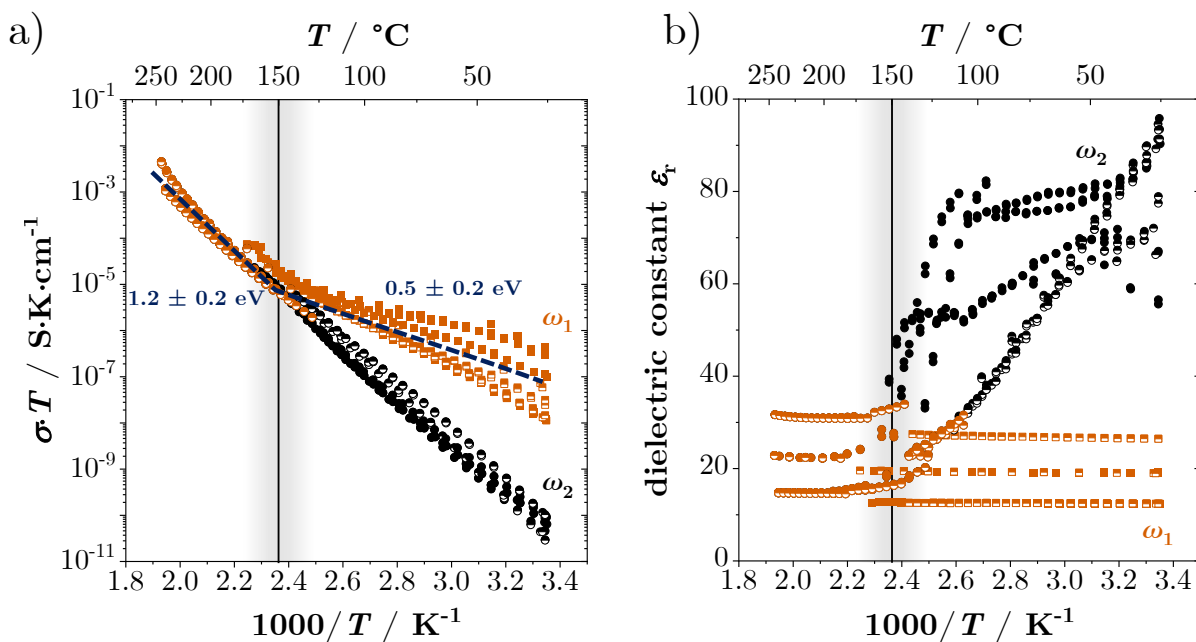
Figure 6.10: a) Conductivity and b) dielectric constant ε_r of both the high (ω_1 red) and low (ω_2 black) frequency signals. Full symbols correspond to heating, half-filled symbols to cooling cycles.

adjusted to the presence of the hopped ion. Since all mobile defects are involved in this hopping, the conductivity approaches a plateau.

Regime II: Dispersive Regime, in which probability determines whether a jump is successful and migration continues (long-range motion), or the jump is unsuccessful and the ion hops back (local motion). Since the success rate decreases for a longer waiting time, the conductivity decreases as a function of frequency in this regime.

Regime III: Low Frequency DC Plateau, at which only the successful jumps remain (including slow relaxation of the environment) and the frequency independent DC conductivity of the material is reached (low frequency intersection with the real axis in the complex impedance plot).

These three regimes were identified in LiSCN and are shown together with the dielectric response in Figure 6.11 ($\varepsilon_\perp(\omega)$ corresponds to the Warburg diffusion, which was omitted in Figure 6.9c for clarity).

Frequency dependence of ion transport is a universal feature, as every material must in principle have all three regimes. However, for the vast majority of materials the high frequency plateau near room temperature occurs at frequencies in the gigahertz range or higher, which are accessible only with microwave techniques[9].[100, 116, 117] It is therefore astonishing and exceptional to observe the high frequency plateau in a material at room temperature, making LiSCN a fascinating candidate to study local ion hopping phenom-

---

[9]An alternative method is to cool the sample to subzero temperatures in order to shift the frequency in the megahertz range, provided that the conductivity is still measurable.
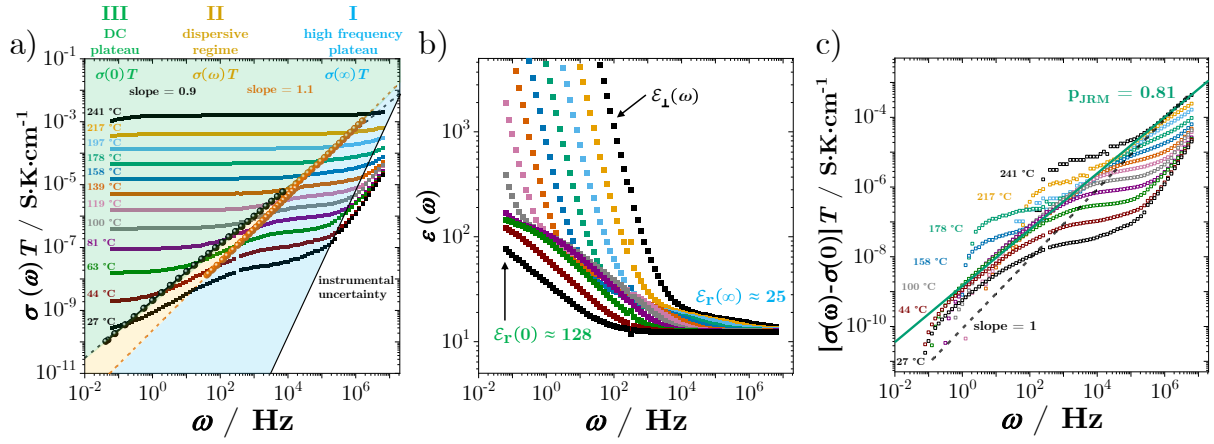
Figure 6.11: Frequency dependent a) conductivity and b) dielectric constant ε_r of anhydrous LiSCN. Solid spheres in (a) correspond to the respective relaxation times $\omega_n = 1/\tau_n$ with $n = 1$ (red) and $n = 2$ (black). c) Frequency dependent conductivity shifted by the DC plateau value $\sigma(0)$. The solid line corresponds to a linear fit of the data.

ena in solids. The overall idea of the JRM is that an ion hop from the initial site to the next available one will induce local structural changes in the environment. This creates an energetic asymmetry between the initial and final ion sites, which relaxes on a time scale longer than the initial ion jump. The transition from dispersive behaviour to long-range motion (regime II to III) follows $[\sigma(\omega) - \sigma(0)] \propto \omega^p$, in which the exponent p describes the energetic asymmetry[10]. The signals ω_1 and ω_2 therefore correspond to local, short-range ion hopping and global, long-range ion migration, respectively.

In addition to the results from EIS, ^{7}Li solid state NMR measurements were conducted
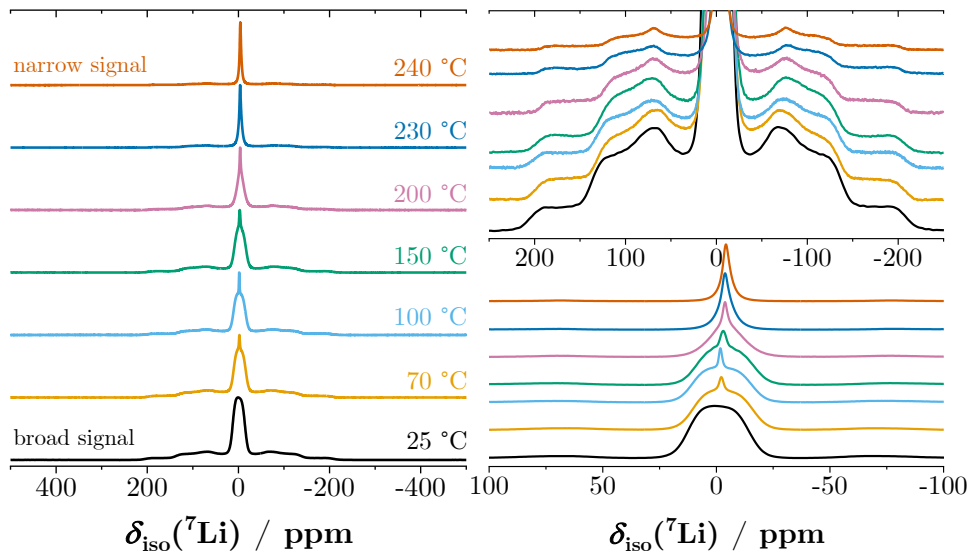
Figure 6.12: ^{7}Li ssNMR measurements of anhydrous LiSCN at various temperatures. The left hand side shows the complete spectra, while the right side magnifies selected regions.

---

[10]This is analogous to the phenomenological expression of Jonscher's power law.[118]

to corroborate the above explanation based on the JRM (Figure 6.12). At lower temperatures the central transition consists of a broad signal, yet with increasing temperature an additional, narrow signal starts to manifest, which increases in intensity until at 150-200 °C a transition occurs and only the narrow signal remains. The extracted line widths (FWHM) in Figure 6.13a reflect very nicely the sharp transition starting at ~150 °C. The results from ssNMR are analogous to the observations from EIS, i.e. two relaxation processes occur in the transport mechanism of LiSCN, one occurring fast on a local scale (narrow signal, ω_1), and one occurring slowly on a long-range scale (broad signal, ω_2). The empirically derived activation energy in Figure 6.13a matches reasonably well with the one of ω_1 in Figure 6.10. The T_1 relaxation times of the broad signal (Figure 6.13b) are astonishingly long (compared to e.g. KSCN),[119] which is in accord with the observations from EIS. The ssNMR measurements show that the hopping mechanism in the intrinsic regime corresponds to only ω_1.

At this point it can be summarized that the transport mechanism is affected by the SCN$^-$ anion, that ω_1 and ω_2 represent short- and long-range ion hopping, and that the hopping mechanism changes at ~150 °C. The defect chemical analysis from the previous sections showed that V'_{Li} are the mobile defects in LiSCN with a migration enthalpy $\Delta_m H_{V'_{Li}}$ of 0.89 eV. The next step is to formulate a physical model for V'_{Li} migration in LiSCN, which can explain the experimental observations. The model proposed here is centred around the role of the SCN$^-$ anion, i.e. slow processes of SCN$^-$ causes the long relaxation
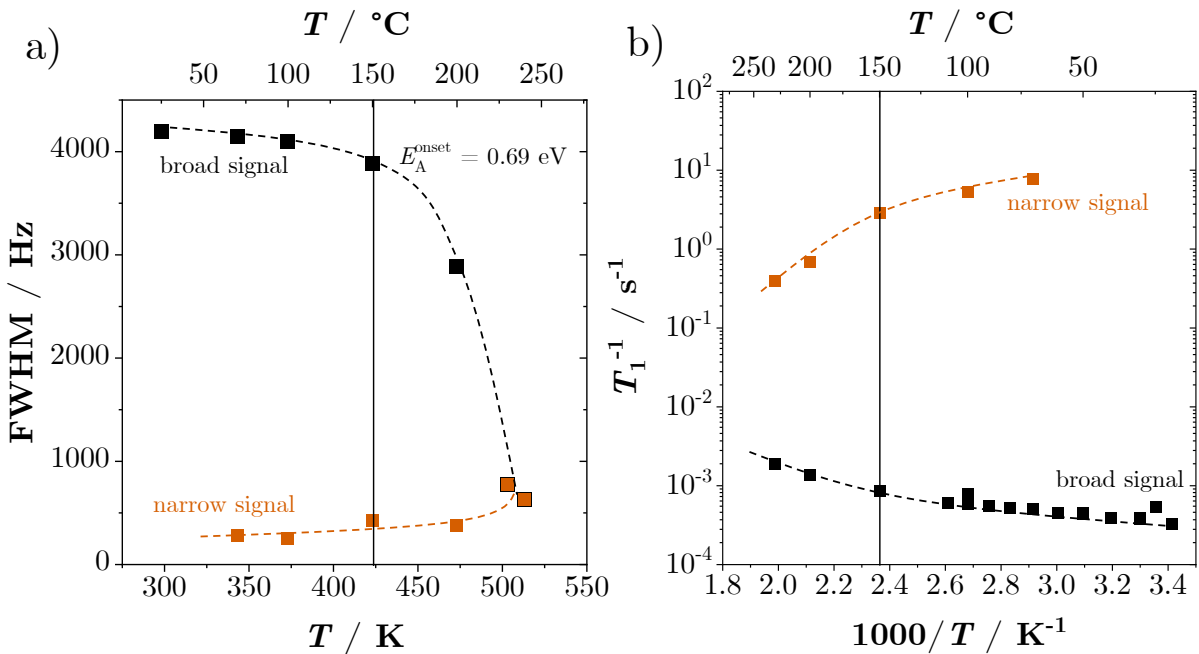
Figure 6.13: a) Full width at half maximum (FWHM) and b) inverse relaxation time T_1^{-1} of the central transition signals shown in Figure 6.12. The activation energy E_A^{onset} was calculated empirically according to $E_A^{\text{onset}} = 1.617 \times 10^{-3}\,\text{eV} \cdot T_c/\text{K}$, T_c being the onset temperature of motional narrowing.[120, 121]

time of ω_2 and the low long-range conductivity of V'_{Li}. A suitable reference system is KSCN, which was already thoroughly investigated.[119] This material undergoes a structural phase transition at 142 °C, at which point the SCN⁻ anions become completely rotationally disordered, changing the structure from orthorhombic to tetragonal. Such a transition, in which the anion becomes fully rotationally disordered (also called rotor phase transition), has been observed for various material systems with complex anions (e.g. Li_2SO_4, Li_3PO_4, Li_2WO_4, $Na_2S_2O_3$). It was the subject of numerous investigations related to the strong, non-linear increase in ionic conductivity (often in the context of the "paddle-wheel mechanism" or "percolation model").[122–134] However, it is unclear if the SCN⁻ anion can fully rotate in LiSCN, considering the much less spacious structure and highly asymmetric bonding tendency in contrast to KSCN.

Therefore, two models are proposed: (i) the SCN⁻ anion cannot fully rotate, but only slightly tilt and shift to relax the structure (and/or the anion is to a certain degree flexible[135]). If this process is fast, ion hopping is expected to occur only between regular Li sites for vacancy transport, and a frequency dependence is not observed. However, if the rearrangement between neighbouring sites occurs very slowly, the ion might first jump to an empty, interstitial position, and afterwards returns to the regular site. In such a limiting case lithium vacancy transport is mediated via empty tetrahedral interstitial sites (Figure 6.14). (ii) The SCN⁻ anion can fully rotate, however, only in the vicinity of
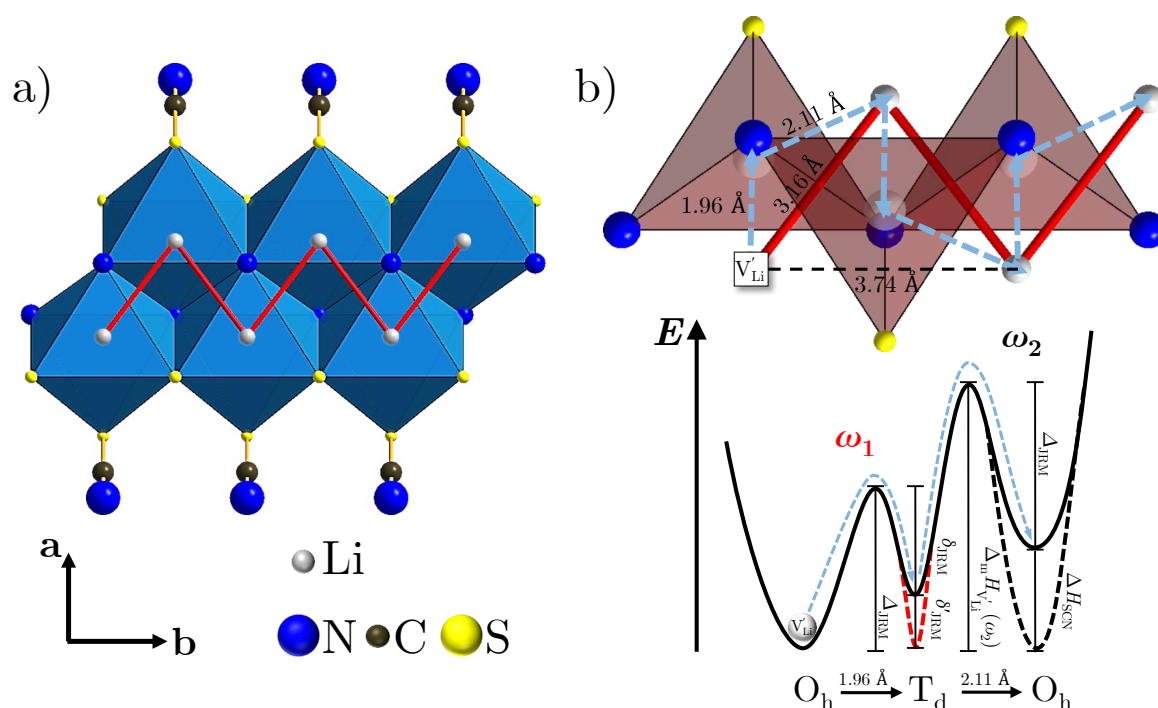
Figure 6.14: a) Nearest neighbour migration path (red line) of lithium vacancies V'_{Li} in the structure of anhydrous LiSCN. b) Possible transport mechanism of V'_{Li} mediated by tetrahedrally coordinated interstitial vacancies [V_iN_3S]. The corresponding energy diagram is shown below (symbols are explained in the main text).

a lithium vacancy, which drags the rotational SCN^- disorder along while moving through the lattice (analogous to polaron hopping, Figure 6.15).

The first mechanism is depicted in Figure 6.14. Within the 1D octahedra chains in b direction, lithium vacancies can move in a "zigzag" fashion between the nearest neighbours (3.16 Å) along the chains (red line in Figure 6.14a). Between these octahedra are empty tetrahedral sites, which the Li^+ ion could occupy before reaching the neighbouring octahedral site (Figure 6.14b). In these interstitial tetrahedral sites the Li^+ cation is coordinated as $[Li_iN_3S]$, corresponding to a metastable site (tetrahedral coordination with a higher concentration of Li-N-bonds vs. an octahedral coordination with a higher coordination number but lower Li-N-bond concentration), which is a reason for this hopping mechanism to be feasible. The energy diagram in Figure 6.14b schematically depicts this. ω_1 reflects local forward-backward hopping to a tetrahedral interstitial site until relaxation occurs, and ω_2 represents the final long-range motion with the total energy requirement $\Delta_m H_{V'_{Li}}(\omega_2)$, which includes the slow rearrangement of the SCN^- anion (ΔH_{SCN}). A similar mechanism has been proposed for Li_2SO_4[133] and β-Li_3PS_4.[117]
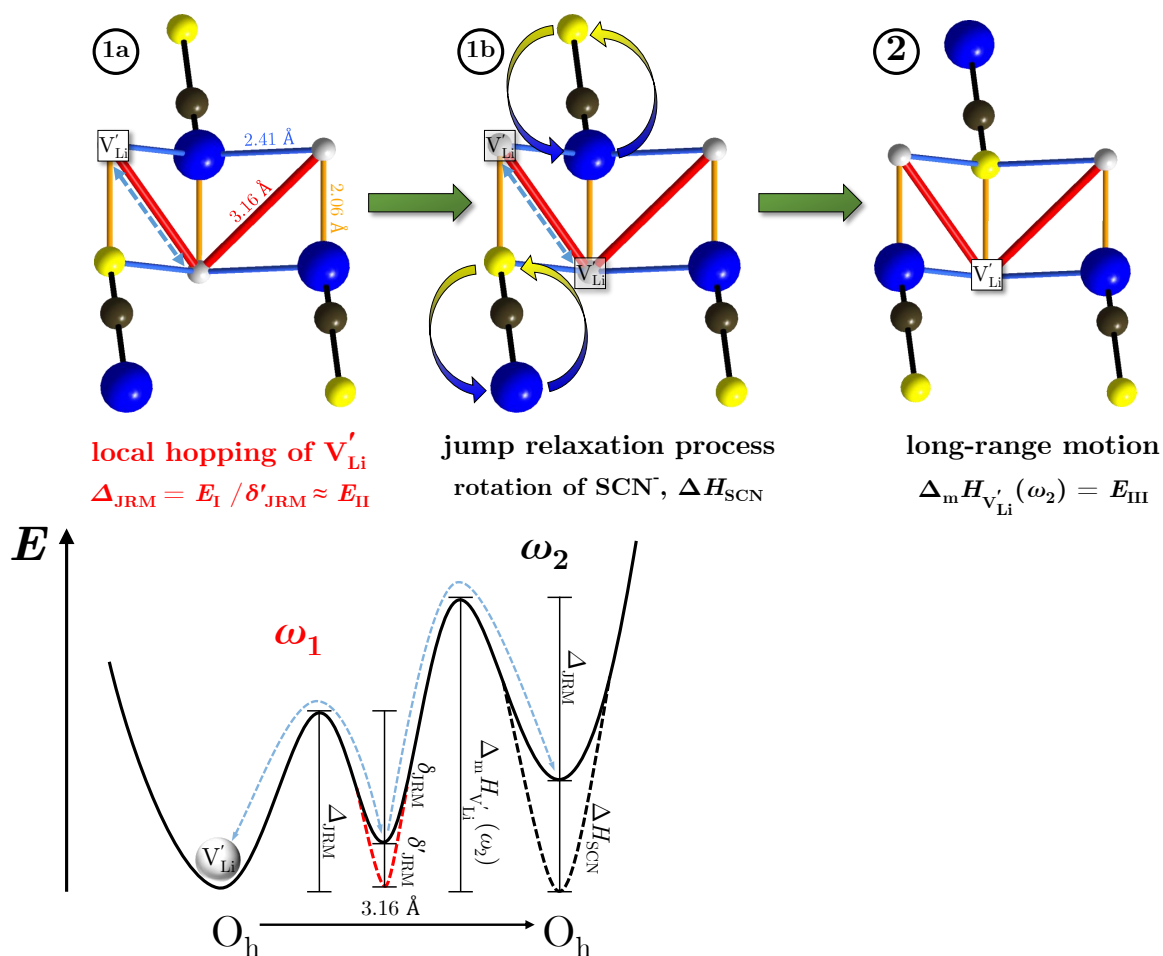
Figure 6.15: Possible migration mechanism of V'_{Li} in anhydrous LiSCN allowing for local, rotational disorder of the SCN^- anion in the lattice. A representative energy diagram is shown below (symbols are explained in the main text).

The second mechanism, which allows for full SCN$^-$ rotational disorder, is depicted in Figure 6.15. As discussed in the previous subsection, the coordination polyhedra in $Mg_{1+\varsigma}Li_{4-2\varsigma}(SCN)_6$ (Figure 6.2) indicate that lithium vacancies V'_{Li} are stabilized by a $V'_{Li} - SCN^x_{NCS}$ coordination. This idea was used for the vacancy formation shown in Figure 6.15, with one reoriented SCN$^-$ anion per V'_{Li} (1a). The vacancy then first locally jumps with correlated forward-backward hops between the neighbouring octahedral sites (1b), until the next SCN$^-$ anion fully rotates, the lattice relaxes, and the long-range hopping to the octahedral site is successful (2).

With the proposed models, the energy requirements for the various processes in the energy diagrams can be specified. The energy for high frequency local hopping $E_I = \Delta_{JRM} = \Delta_m H_{V'_{Li}}(\omega_1)$ is obtained from the low temperature part of ω_1 (cf. Figure 6.10). The equilibrium defect concentration is independent of frequency, and can reasonably be estimated by inserting the conductivity data of undoped LiSCN in the extrinsic regime (Figure 6.4a) together with equation 6.13 into equation 6.11. The high frequency mobility corresponding to ω_1 is obtained from the conductivity data in Figure 6.10a and equation 6.11 (Figure 6.16):

$$u_{V'_{Li}}(\omega_1)T = 10^{(2\pm1)} \exp\left(-\frac{(0.6 \pm 0.1)\,\mathrm{eV}}{k_B T}\right) \frac{\mathrm{cm^2 K}}{\mathrm{Vs}} \tag{6.17}$$

The entropy $\Delta_m S_{V'_{Li}}(\omega_1)$ was calculated with equation 6.12 using the same parameters as for $\Delta_m S_{V'_{Li}}(\omega_2)$ in subsection 6.1.1. The resulting entropy is close to zero and within the experimental error. The energetic asymmetry between V'_{Li} and the next available site
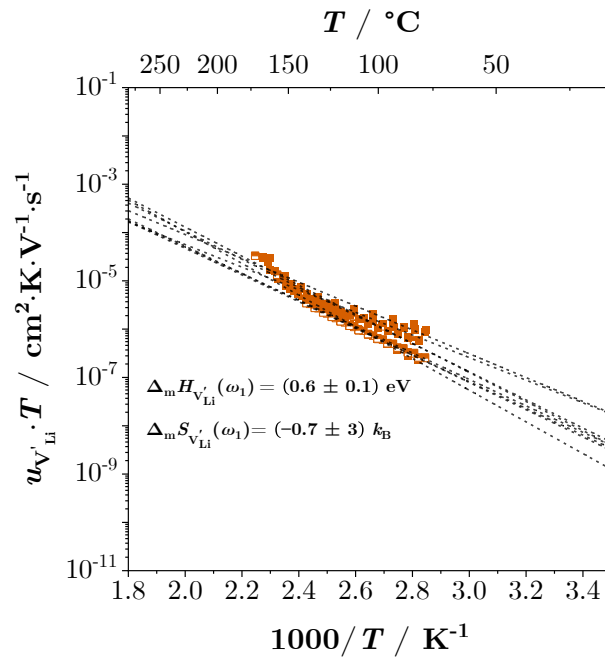
Figure 6.16: Calculated mobilities of the high frequency process ω_1 reflecting local ion hopping in LiSCN. Dashed lines are linear fits.

(model 1; T_d, model 2; O_h) is denoted as δ_{JRM}, with the related relaxation energy δ'_{JRM}. According to the JRM,[100, 136] the overall energy requirement for long-range ion motion corresponding to the low frequency DC plateau (ω_2) is defined as $E_{III} = E_I + 2A(E_I - \delta_{JRM})$, in which A is a constant close to unity. Since $E_{III} = \Delta_m H_{V'_{Li}}(\omega_2) = (0.89 \pm 0.08)$ eV and $E_I = \Delta_{JRM} = \Delta_m H_{V'_{Li}}(\omega_1) = (0.6 \pm 0.1)$ eV, it follows that $\Delta H_{SCN} = 2A(E_I - \delta_{JRM}) = (0.3 \pm 0.1)$ eV and $\delta_{JRM} = (0.5 \pm 0.1)$ eV. The relaxation process δ'_{JRM} is the energy required to match the site energies of the initial jump (i.e. energetic mismatch of neighbouring sites post jump event), which is represented by the dispersive regime and can be approximated with $\delta'_{JRM} \approx E_{II} = (1-p)E_{III} = (0.17 \pm 0.02)$ eV. The energy difference between the first maximum and the relaxed intermediate state is then (0.7 ± 0.1) eV, virtually identical to $\Delta_m H_{V'_{Li}}(\omega_1)$ within the experimental error. The jump mechanisms of model 1 and 2 can be formulated in the following equations (the respective barriers are given above the arrows):

$$\text{Model 1}: V'_{Li} + V_i + Li^x_{Li} \xrightleftharpoons{0.6\,eV} V'_{Li} + Li^{\cdot}_i + V'_{Li} \xrightleftharpoons{0.89\,eV} Li^x_{Li} + V_i + V'_{Li} \tag{6.18}$$

$$\text{Model 2}: V'_{Li} + SCN^x_{NCS} + Li^x_{Li} \xrightleftharpoons{0.6\,eV} V'_{Li}/Li^x_{Li} + SCN^x_{NCS} + Li^x_{Li}/V'_{Li} \xrightleftharpoons{0.89\,eV} Li^x_{Li} + NCS^x_{NCS} + V'_{Li} \tag{6.19}$$
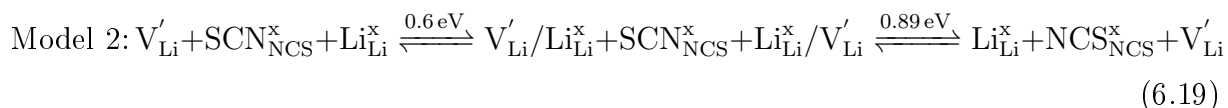
Above 150 °C long-range transport becomes dominant and local ion hopping can no longer be perceived in the megahertz frequency range. The reason is a higher SCN^- anion mobility provided with the more spacious lattice from thermal expansion (Figure 6.18), such that relaxation processes can occur much faster.

To support the validity of these kinetic models, one can compare to LiSCN the conductivity behaviour of other materials with complex and/or anisotropic counter ions. The first example is the newly found phase $Mg_{1+\varsigma}Li_{4-2\varsigma}(SCN)_6$ shown in subsection 6.1.1. This material has a more spacious structure than LiSCN, and since essentially all Li atoms coordinate to sulphur atoms, the formation of vacancies is facilitated (Figure 6.2). The shallow slope of the conductivity after the phase transition (cf. Figure 6.1a) suggests that not only is the formation of mobile defects promoted, but also that the SCN^- rearrangement, i.e. jump relaxation, occurs much faster. This conclusion matches with the observation from EIS, which showed only one relaxation process with negligible depression (Figure B.5a), and similar to LiI, the dielectric constant was nearly independent of temperature with a value of $\sim$30 (Figure B.5b).

A comparison with other ion conductors with complex anions from literature yields substantial evidence that the ionic conductivity behaviour depends on the transition point where anion lattice relaxation becomes fast, and that local ion hopping occurs in the

microwave frequency range or higher. Fast room temperature ion conductors have their transition points at very low temperatures, and one could even argue that the lower the respective temperature is, the higher ionic conductivity could be. Examples are found in various materials: (i) β-Li_3PS_4 shows a similar feature in ssNMR spectra as seen in LiSCN (Figure 6.12), however, at -74 °C (Figure 8a in ref. [117]). (ii) Li_6SbS_5I shows two semi-circles in EIS spectra at -78 °C (Figure 3 in ref. [141]). (iii) Li_6PS_5Cl with similar EIS spectra at -100 °C (Figure 4b in ref. [142]). In the last two examples, the appearance of two semi-circles in the impedance response was attributed to bulk and blocking grain-boundary signals based on the brick-layer model.[98] However, given that the capacitances differed by less than one order of magnitude, the same arguments as given above for LiSCN suggest that both signals actually correspond to the bulk response, showing local (high frequency) and long-range (low frequency) ion hopping. These materials are all comparatively good ion conductors at room temperature, with the transition from slow to fast anion lattice relaxation occurring at subzero temperatures. The differences in conductivity (or transition point) between different materials can be related with the (local) mobility of the anion, i.e. the higher the anion mobility, the faster jump relaxation occurs[11]. This has been shown to apply for the $PS_4{}^{3-}$ and $SbSe_4{}^{3-}$ anions in $Na_{11}Sn_2PnX_{12}$ (Pn = P, Sb and X = S, Se)[144] as well as for OH^- in Li_2OHCl.[145]
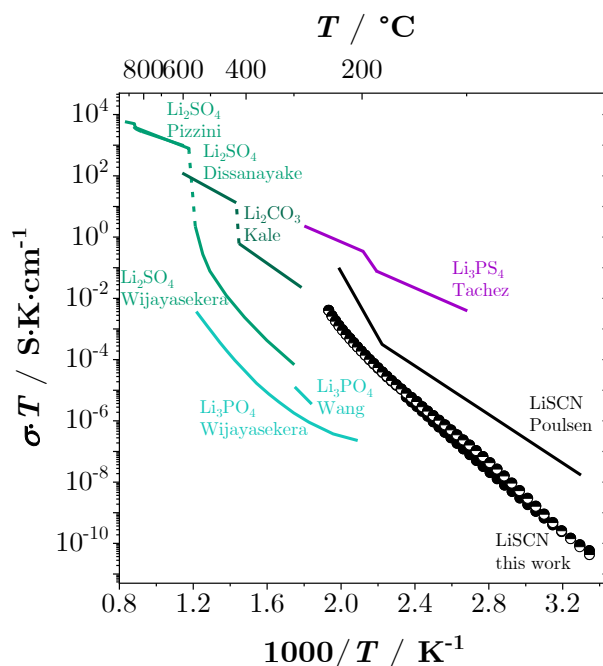
Figure 6.17: Comparison of the DC conductivity of anhydrous LiSCN from a previous study[43] and this work with other Li^+ ion conductors which possess complex anions (lithium carbonate Li_2CO_3,[137] lithium sulfate Li_2SO_4,[63, 130, 138] lithium phosphate Li_3PO_4,[138, 139] lithium thiophosphate Li_3PS_4[140]).

---

[11]E.g. in Figure 8 of ref. [143], this was pointed out with the connected flattening of the potential landscape, referred to as increasing anharmonicity.

Using this concept, one can now understand the observed DC conductivity data of LiSCN compared to other Li$^+$ ion conductors with complex anions (Figure 6.17). It can be noted that materials with oxygen containing anions $AO_x{}^{n-}$ have either lower or comparable conductivities as LiSCN, while the one containing sulphur anions $AS_x{}^{n-}$ is a far better conductor. The SCN$^-$ anion encompasses both the coordination of hard cation − hard anion, i.e. Li-N bond, and hard cation − soft anion, i.e. Li-S bond, making LiSCN a hybrid case of $AO_x{}^{n-}$ and $AS_x{}^{n-}$ systems. Therefore its transport data are located in between.

Finally, together with the thermodynamic results from the previous section (Table 6.4), one can understand the complete transport mechanism for lithium vacancies in LiSCN. The generation of V'_{Li} occurs rather facile due to the rearrangement of SCN$^-$ with a relatively small energetic cost (0.6 eV). Then, the lithium vacancy attempts to hop to the next position (0.6 eV), yet is hindered by the slow relaxation process of SCN$^-$ (0.3 eV), which creates a delay and results in a comparatively high total energy cost (0.89 eV) for long-range transport. The consequence is a low formation, but high migration enthalpy and overall low DC conductivity. If the anion can freely rotate within the lattice, as is the case for the Li_2SO_4 rotor phase, the migration enthalpy is severely lowered (0.36 eV) and ion transport is much faster.

Table 6.4: Summary of the thermodynamic and kinetic data of LiSCN from subsection 6.1.1 and 6.1.2, comparing the long-range migration enthalpy and the enthalpy for local hopping in LiSCN with the measured migration enthalpy in the high temperature rotor phase of Li_2SO_4.[63]

compound	$E_{III} =$ $\Delta_m H_{V'_{Li}}(\omega_2)$ / eV	$\Delta_m S_{V'_{Li}}(\omega_2)$ / k_B	$E_{II} \approx$ δ'_{JRM} / eV	$E_I = \Delta_{JRM} =$ $\Delta_m H_{V'_{Li}}(\omega_1)$ / eV	$\Delta_m S_{V'_{Li}}(\omega_1)$ / k_B	ΔH_{SCN} / eV
Li_2SO_4	0.36					
LiSCN	0.89 ± 0.08	7.7 ± 0.9	0.17 ± 0.02	0.6 ± 0.1	-0.7 ± 3	0.3 ± 0.1

6.1.3 Superionic Phase Transition

Often ionic materials are measured and investigated in their so-called dilute state, in which defect concentrations are low compared to atoms on regular lattice sites (Boltzmann statistics apply)[12]. However, near a phase transition (e.g. melting (first order) or structural transition (polymorphism, first or second order)), defect concentrations start

---

[12]An easy way to emphasize this statement is provided with the Gibbs-Duhem equation: $G(T,p,n) = \Sigma_k n_k \mu_k = \Sigma_{atoms} n_i \mu_i + \Sigma_{defects} n_j \mu_j \approx \Sigma_{atoms} n_i \mu_i$.[98]

a)

b)
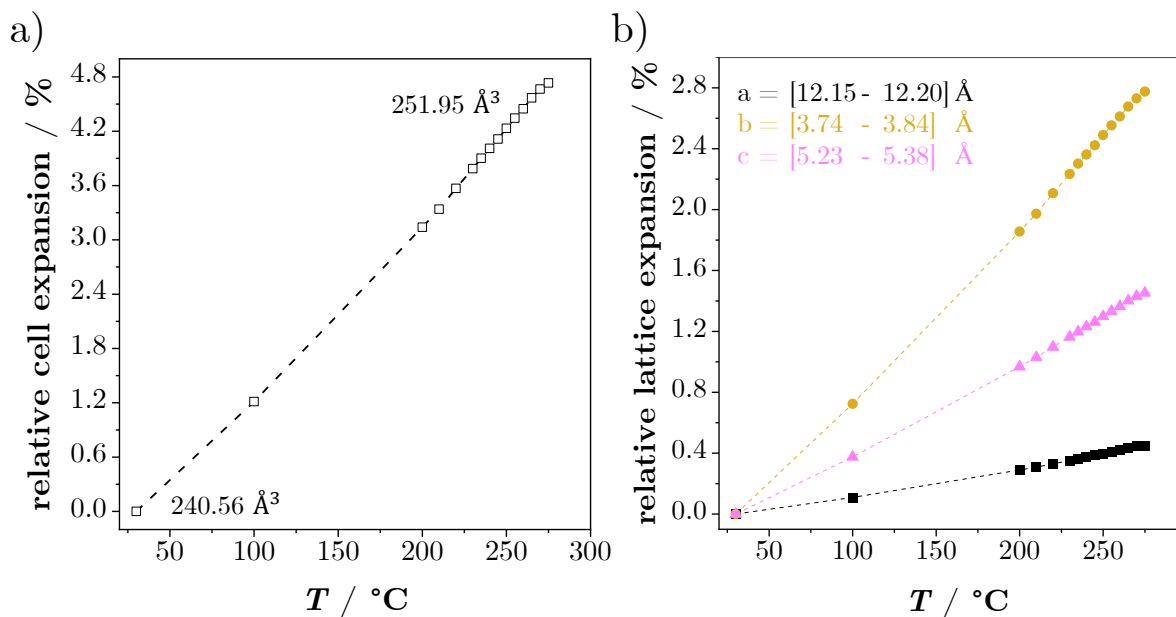
Figure 6.18: Temperature dependent a) volume expansion, and b) expansion of the individual lattice parameters in anhydrous LiSCN measured by XRPD.

to become stoichiometric, and the system is no longer dilute. Then Fermi-Dirac statistics apply, and additional effects of non-dilute defects must be considered, in particular when defects are charged. This corresponds to a change from linear (dilute) to non-linear behaviour (concentrated), which can be seen in various physical properties, e.g. volume expansion or conductivity.[98, 101, 116, 119, 146–149] When a system reaches a very high concentration of mobile defects (close to the maximum), the concentration can approximately be considered as constant and the temperature dependence of the conductivity arises mainly from the mobility. If attractive Coulombic defect-defect interactions are very stabilizing, to the point where no energy is required anymore for defect formation, the material can be regarded as superionic, and non-linear behaviour in the Arrhenius plot of the conductivity is observed.

Since strong and anisotropic volume expansion is common in thiocyanates as the rotational motion of SCN^- requires more space compared to a symmetric ligand,[9, 119] LiSCN was measured with *in situ* temperature dependent XRPD and the expansion analysed with Rietveld refinement (Figure 6.18). Even though LiSCN indeed shows a comparatively strong volume expansion, it remains linear within the measured temperature range. The observed anisotropic expansion is related to the interconnectivity of octahedral units, as octahedra in b direction are edge-sharing and closely stacked (1D chains), while they are only corner-sharing with greater distance in a and c directions.[22]

It is important to correctly classify a material to see which behaviour one can expect. In an (anti-) Frenkel defective material, defects are formed only on one sublattice, which means structural units are always retained and polymorphism is possible even close to the melting point.[101] A structural transition can of course also occur in Schottky defec-

tive materials (e.g. KSCN is assumed to be Schottky defective),[119] yet to be observable, the transition has to occur below the melting point as no structural units retain when defect concentrations are high. The more dense structure of LiSCN compared to KSCN does not allow for polymorphism below the melting point. Since it is Schottky defective, its intrinsic regime is small (cf. subsection 6.1.1) and it will enter into the premelting regime without major structural changes. Conductivity measurements are very sensitive for non-dilute behaviour, since they directly probe modified defect concentrations and/or mobilities. In order to investigate the defect chemistry in the premelting regime, the cube-root law approach was applied,[98, 101, 147, 149, 150] and the employed mathematical procedure will briefly be shown here.

In equation 6.4, the number of available lattice sites N_{Li} is defined as $N_{\mathrm{Li}} = g_{\mathrm{Li}} \cdot \alpha_{\mathrm{Li}}$, with g_{Li} being the degeneracy of vacancy sites and α_{Li} the number of occupiable vacancy sites (the definition can be per unit cell, i.e. $N_{\mathrm{Li}} = 1 \cdot 4$ with $Z = 4$, or per Li atom, i.e. $N_{\mathrm{Li}} = 1 \cdot 1$). For high defect concentrations, the exhaustibility of lattice sites has to be accounted for (Fermi-Dirac statistics), and the maximum number of available lattice sites reads:[101, 147]

$$N_{\mathrm{Li}} = g_{\mathrm{Li}}(\alpha_{\mathrm{Li}} - \sqrt{K_{\mathrm{S}}}) \tag{6.20}$$

within the Brouwer approximation $\sqrt{K_{\mathrm{S}}} = [\mathrm{V}'_{\mathrm{Li}}] = [\mathrm{V}^{\bullet}_{\mathrm{SCN}}]$. When the system is in the concentrated state, defects are close enough to each other that their Coulombic interactions are perceptible. Since a defect pair is oppositely charged, this interaction stabilizes the total energy of the system. This means that a second minimum appears in the free enthalpy curve at high defect concentrations, which becomes more pronounced with increasing temperature (Figure 6.19). Therefore, the free enthalpy for the formation of a Schottky pair $\Delta_{\mathrm{S}}G^{\circ}$ is modified by including a Coulombic interaction term $\mu_{\mathrm{int}}(c_{\mathrm{E}})$, with $c_{\mathrm{E}} \equiv \sqrt{K_{\mathrm{S}}}$ being the equilibrium defect concentration:

$$\Delta_{\mathrm{S}}G^{\circ} = \Delta G^{\circ} + \mu_{\mathrm{int}}(c_{\mathrm{E}}) = \Delta G^{\circ} - J c_{\mathrm{E}}^{1/3} \tag{6.21}$$

The parameter J is the Coulombic interaction parameter, which quantifies the defect-defect interaction in the system. This approach assumes that the Coulombic defect-defect interaction increases with defect concentration according to a cube-root law $c_{\mathrm{E}}^{1/3}$. This corresponds to a Madelung energy between the charged defects. The final expression then reads:

$$\frac{c_{\mathrm{E}}^2}{g_{\mathrm{Li}}^2(\alpha_{\mathrm{Li}} - c_{\mathrm{E}})^2} = \exp\left(-\frac{\Delta G^{\circ} - J c_{\mathrm{E}}^{1/3}}{k_{\mathrm{B}}T}\right) \tag{6.22}$$
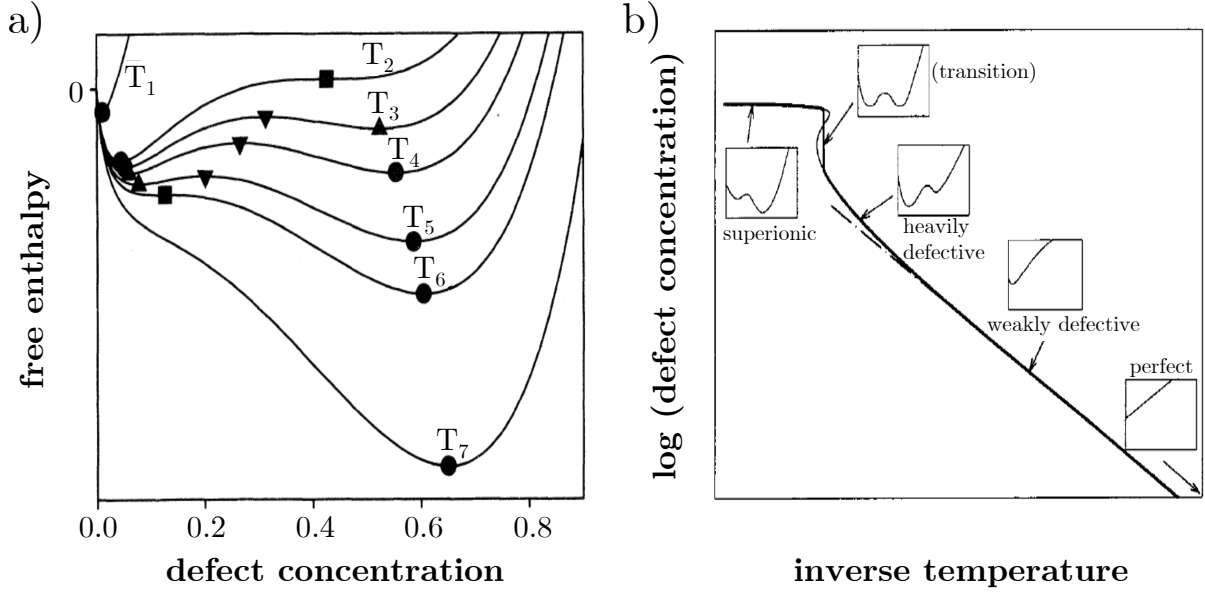
Figure 6.19: a) Generation of a second minimum in the total free enthalpy curve with increasing defect concentration (from ref. [101]), and b) the respective temperature dependent behaviour of the defect concentration (from ref. [147]).

This equation was used to calculate the defect concentration of V'_{Li} in LiSCN between 174-270 °C, in which non-linearity of the conductivity Arrhenius plot (Figure 6.20a) is observed for 242-270 °C in the premelting regime.

Since the equation is implicit, it had to be solved numerically with Matlab (*Mathworks*, Version R2017a) using the *vpasolve*-function to solve the equation at every temperature step (using $\Delta H°$, $\Delta S°$ and J as parameters). The resulting defect concentrations were converted into units of cm^{-1} with $c'_E = c_E \cdot (4/V_{UC})$. The mobility was calculated with equation 6.12 (using $\log_{10}(\nu_{V'_{Li}}) = \log_{10}\{(r_{Li}^2 e\,\nu_0)/(Nk_B) \cdot \exp(\Delta_m S_{V'_{Li}}/k_B)\}$ and $\Delta_m H_{V'_{Li}}$ as parameters) and together with the calculated defect concentration were inserted into equation 6.11 to fit the measured conductivity data (Figure 6.20). These calculations were set into a function handle, which was used by the *lsqnonlin*-function to fit the data. This fitting function was chosen, as it allows the usage of boundaries for the five employed parameters: $\Delta H°$, $\Delta S°$, J, $\log_{10}(\nu_{V'_{Li}})$ and $\Delta_m H_{V'_{Li}}$. With this approach J had a value of 0.61 eV (Figure 6.20b, dark blue line), and measured conductivity data up to 261 °C could be fitted (Figure 6.20a, dashed dark blue line).

Given the strong lattice expansion seen by XRPD (Figure 6.18), in the premelting regime Coulombic defect-defect interactions might perceptibly weaken by the increasing distance to the neighbouring defects. Therefore, a second approach including the lattice expansion in LiSCN was explored. According to the XRPD data in Figure 6.18, the volume expansion $\Delta V(T)$ of LiSCN reads:

$$\Delta V(T) = 4.60 \cdot 10^{-26}\,\frac{\text{cm}^3}{\text{K}} \cdot T - 2.27 \cdot 10^{-22}\,\text{cm}^3 \tag{6.23}$$
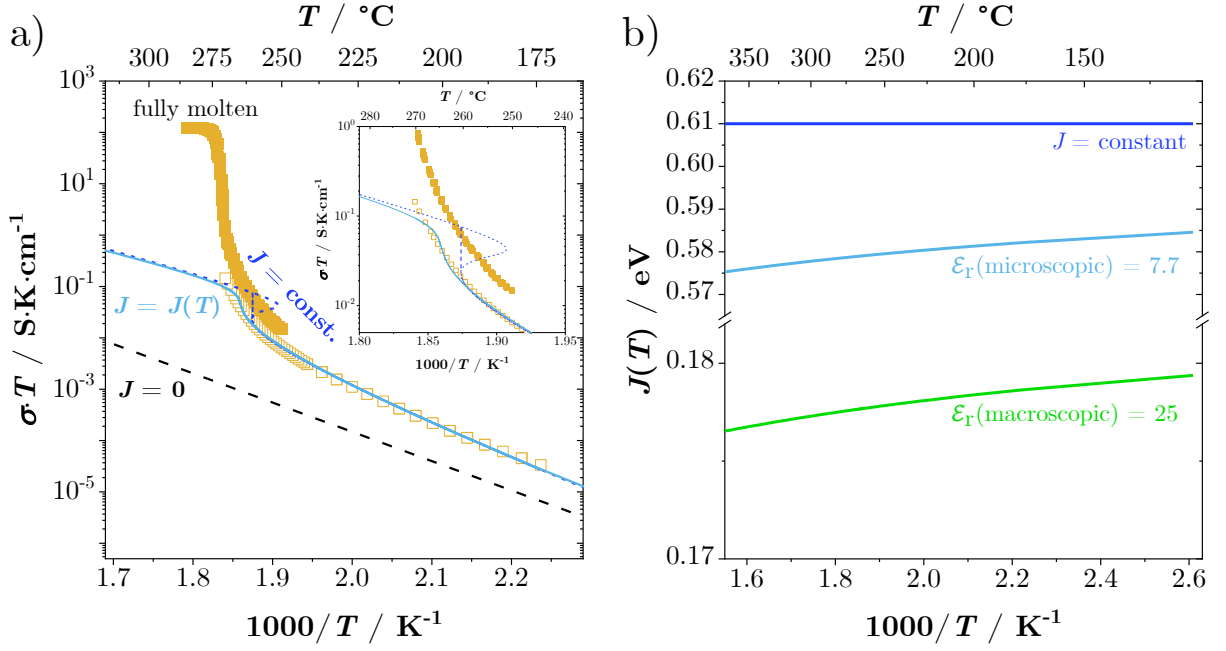
Figure 6.20: a) Measured conductivity of anhydrous LiSCN in the premelting regime and after melting (open squares correspond to measurements with cell 1, closed squares to cell 3, cf. Figure 5.1). The premelting regime was fitted by either neglecting Coulombic defect-defect interactions ($J = 0$), by using J as a parameter ($J = $ const.), or by including a temperature dependence ($J = J(T)$). b) Coulombic defect-defect interaction parameter J: (i) constant parameter J (dark blue), (ii) temperature dependent $J(T)$ calculated with the macroscopic dielectric constant ε_r(macroscopic) (green), and (iii) with the microscopic dielectric constant ε_r(microscopic) (bright blue).

The volume expansion was taken to be isotropic for the calculations. Since Coulombic interaction of nearest neighbours can be expressed by the Madelung energy U_M, J can be directly calculated according to:[147, 148]

$$J = \frac{4}{3\,\varepsilon_r} \cdot U_M \cdot \frac{f_d}{f} = \frac{e}{3\pi\varepsilon_0\varepsilon_r} \cdot f_d \cdot \frac{1}{b} \tag{6.24}$$

in which f_d is the effective Madelung constant of the defect superlattice (~ 0.73),[148] f is the Madelung constant, e is the charge of an electron, ε_0 and ε_r are the dielectric constants of free space and LiSCN, and b is the distance between nearest neighbours. Even though the lattice of LiSCN is orthorhombic, for simplicity it is approximated here as pseudo-cubic, which means $b_{pc}(T) = \sqrt[3]{\Delta V(T)}/2$. The Coulombic interaction consequently includes the volume expansion and decreases with increasing temperature:

$$J(T) = \frac{e}{3\pi\varepsilon_0\varepsilon_r} \cdot f_d \cdot \frac{1}{b_{pc}(T)} \tag{6.25}$$

which is shown in Figure 6.20b as green line. However, the resulting values for J were far too low to describe the Coulombic defect-defect interaction in LiSCN. These low values

result from the relatively high (macroscopic) dielectric constant ε_r(macroscopic) measured by impedance (Figure 6.10b). The average value used for ε_r(macroscopic) was $\sim$25, similar to the permittivity of LiI ($\sim$30) and characteristic for a soft, highly polarisable anion lattice. Yet for the premelting regime, one has to consider that polarisability effects of the SCN$^-$ anion are lower for the defect lattice at short distances[13]. Thus, a microscopic dielectric constant ε_r(microscopic) has to be employed, which rather reflects a less polarisable lattice (e.g. LiF, $\varepsilon_r \approx 9$).[152] Therefore, ε_r in equation 6.25 was included into the fitting as a parameter, using a total set of 5 parameters; ΔH°, ΔS°, $\log_{10}(\nu_{V'_{Li}})$, $\Delta_m H_{V'_{Li}}$, ε_r(microscopic), and calculating $J(T)$ directly with the equation[14]:

$$J(T) = \frac{e}{3\pi\varepsilon_0\varepsilon_r(\text{microscopic})} \cdot f_d \cdot \frac{2}{\sqrt[3]{\Delta V(T)}} \tag{6.26}$$

$J(T)$ is shown in Figure 6.20b as bright blue line. The corresponding fit is displayed in Figure 6.20a as bright blue solid line (labelled $J = J(T)$). With the inclusion of the volume expansion and ε_r(microscopic), the fitting in the premelting regime became smoother, and conductivity data up to 270 °C could be fitted without fail. For both approaches discussed above, reasonable boundaries had to be used to control the fitting procedure[15]:

- $\Delta H^\circ = [0.6 - 0.9]$ eV
- $\Delta S^\circ = [2 - 15]\, k_B$
- $\log_{10}(\nu_{V'_{Li}}) = [1 - 7]$
- $\Delta_m H_{V'_{Li}} = [0.7 - 0.9]$ eV
- excluding volume expansion; $J = [0.2 - 0.8]$ eV
- including volume expansion; ε_r(microscopic) $= [5 - 30]$

The final fits showed low residual sum of squares of about $\sim$0.1 or smaller.

Although the observed transition in LiSCN is clearly of first order, one can quantify the order of a transition with the expressions reported in ref. [101]; $\gamma = J/\Delta H^\circ$ and $\gamma_{crit} = 4^{1/3}/(1 + \ln(3)/4 + \Delta S^\circ/(8\, k_B))$ with the classifications:

- $\gamma > \gamma_{crit}$: first order phase transition

- $\gamma = \gamma_{crit}$: second order phase transition

- $\gamma < \gamma_{crit}$: diffuse phase transition

---

[13]This correction of polarisability effects was also used in e.g. PbF$_2$[150] and SrTiO$_3$[151].

[14]$J(T)$ was consequently also included in the function handle for the *lsqnonlin*-function.

[15]At least one fitting parameter would run into a boundary during a calculation. Without boundaries parameters would often become non-physical and the calculation would fail.

This relation indicates for both approaches a first order phase transition (cf. Table 6.5)[16]. There are some examples in literature which have used the cube-root model for the pre-melting regime (Figure 6.21 and Table 6.5). Although reports on superionic transition can be found for many different materials (Figure B.18), it is often challenging to derive defect concentrations from the used measurement techniques (e.g. Raman spectroscopy, neutron diffraction, ...), or the premelting regime has simply not been investigated. From the reported values in Table 6.5, one can directly see that $\Delta H°$ and J are linked. The differences in defect formation enthalpies nicely reflect the chemistry of the materials. Regarding the first order transitions of β-AgI and LiSCN in Figure 6.21, the extent of the discontinuous jump in conductivity after the superionic transition is much higher than what could be predicted with the cube-root law fitting. Since both transitions are connected with liquefaction (β-AgI, cation sublattice becomes quasi-molten; LiSCN, complete lattice becomes molten), a change in ion mobility is expected to occur, which is not considered in the model.
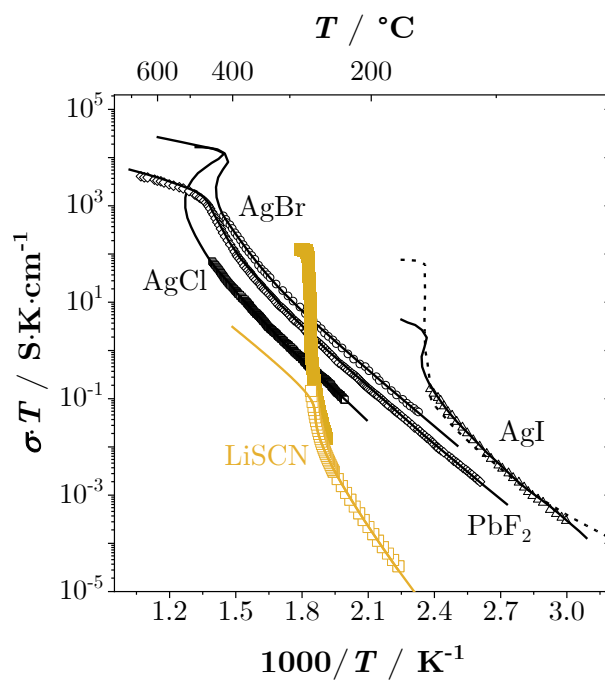
Figure 6.21: Application of the cube-root law approach to LiSCN (Schottky defects), silver halides AgX (X = Cl, Br, I) (Frenkel defects), and PbF$_2$ (anti-Frenkel defects). Black symbols and solid lines belong to reference [101], and the dashed line to reference [116].

---

[16]Note that for the second approach with $J(T)$, values of γ and γ_{crit} were almost identical, and the choice of decimal position could decide which one of the two would be greater. The calculated values of γ and γ_{crit} are therefore taken to be less significant than experimental observation.

[17]In reference [101], the pre-exponential factor ν_0 in Table 1 was reported 2 orders of magnitude larger than the actual values.

Table 6.5: Comparison of the cube-root law fitting data for the superionic transition in Schottky defective LiSCN with (anti-) Frenkel defective materials from literature[17]. The index j refers to the mobile defect in the respective material. In PbF$_2$ $\Delta H°$ and $\Delta_m H_j$ refer to the formation and migration of anion interstitials, in AgX to cation interstitials, in Bi$_{0.75}$Pr$_{0.25}$O$_{1.5}$ to V$_O^{\cdot\cdot}$, and in LiSCN they refer to V$'_{Li}$.

compound		$\Delta H°$ / eV	$\Delta S°$ / k_B	$\Delta_m H_j$ / eV	$\log_{10}[\nu_j$ / (cm^{2}K$\cdot$s^{-1}V^{-1})]	J / eV	$\gamma = J/\Delta H°$	γ_{crit}	reference
PbF$_2$	cube-root	1.08	8.48	0.18	2.94	0.75	0.694	0.779	[101]
AgCl	cube-root	1.48	9.73	0.045	2.48	1.03	0.696	0.580	[101]
AgBr	cube-root	1.15	7.67	0.145	3.22	0.803	0.698	0.646	[101]
β-AgI	cube-root	0.82	11.77	0.244	1.60	0.497	0.606	0.578	[101]
Bi$_{0.75}$Pr$_{0.25}$O$_{1.5}$	cube-root	1.51	5.78	0.90 0.48	2.01	1.78	1.179	1.340	[149]
LiSCN	experimental cube-root J cube-root $J(T)$	0.6 ± 0.3 0.6 0.8	5 ± 2 3.0 7.9	0.89 ± 0.08 0.8 0.7	5.1 ± 0.4 3.5 2.4	0.61 0.574-0.585	1.017 0.718-0.731	0.962 0.702	this work

6.2 Hydrated LiSCN $\cdot$ x H$_2$O

6.2.1 Phase Diagram LiSCN − H$_2$O

The content of this subsection is published in Joos et al. ref. [103]. Hydration in LiSCN occurs very facile, and can be done reversibly without decomposition or hydrolysis even above room temperature. With XRPD and IR spectroscopy (Figure B.19), it was determined that for $0 < x < 1$ a two-phase regime between LiSCN and H$_2$O occurs, until at $x = 1$ the monohydrate LiSCN $\cdot$1 H$_2$O forms (Figure 6.22). At room temperature, the monohydrate adopts a monoclinic crystal structure ($C2/m$, $a = 15.0271(3)$ Å, $b = 7.59742(1)$ Å, $c = 6.70700(1)$ Å, $\beta = 96.1470(6)°$, $V = 761.32(2)$ Å^3, $Z = 8$) termed α-phase. At 49-50 °C, it transforms into the β-phase with an orthorhombic lattice ($Pnam$, $a = 13.22578(2)$ Å, $b = 7.06191(9)$ Å, $c = 8.16628(1)$ Å, $V = 762.724(2)$ Å^3, $Z = 8$) observed by temperature dependent *in situ* XRPD (Figure 6.24) as well as DSC (Figure 6.25 and Figure B.23), and confirmed by Rietveld refinement (Figure B.21). In both α- and β-LiSCN $\cdot$ 1 H$_2$O, Li$^+$ cations are coordinated in [Li(OH$_2$)$_2$(NCS)$_2$]-tetrahedral units, a rather uncommon polyhedron for thiocyanate coordination compounds.[1–4, 6, 7, 9, 14, 19] The phase transition induces an increased disorder of the Li$^+$ cations which lowers their site occupancy to only 1/3 (Figure 6.22).
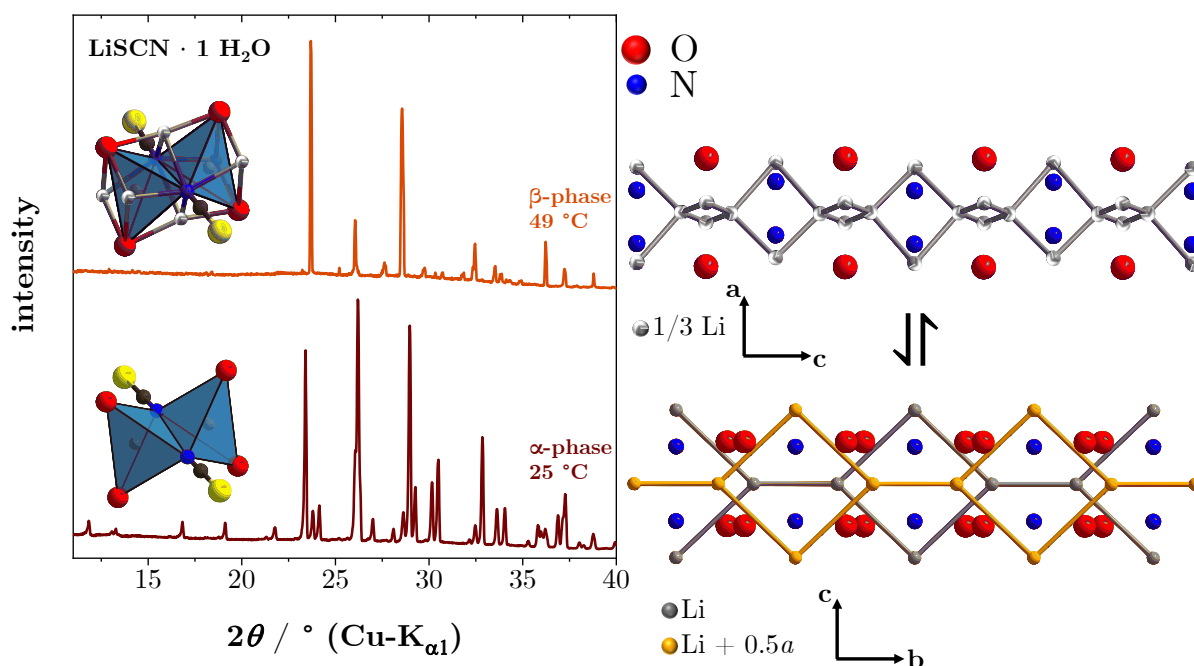
Figure 6.22: XRPD patterns of α- (bottom) and β- (top) LiSCN · 1 H$_2$O with the corresponding Li$^+$ coordination polyhedra. The right hand side shows the respective changes in the lithium sublattices, with the β-phase exhibiting a pronounced occupational disorder of the Li$^+$ sites.
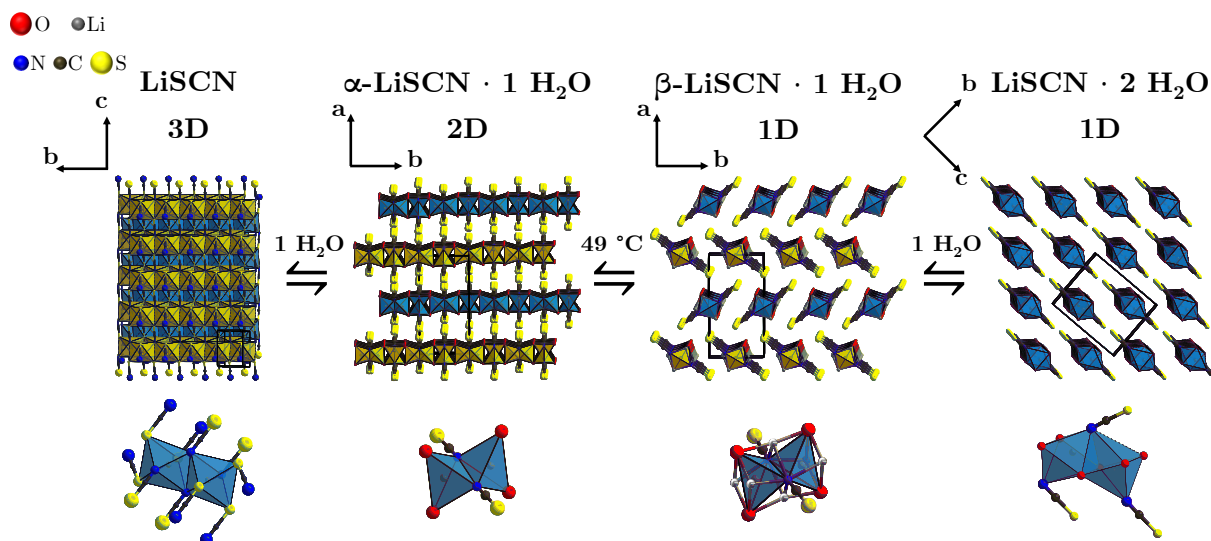
Figure 6.23: All known LiSCN · x H$_2$O phases (x = 0, 1 and 2)[22] showing the decrease in dimensionality of crystal structures with either hydration or temperature.

Figure 6.23 compares the crystal structures of all known LiSCN · x H$_2$O phases. These structures reflect the Li$^+$ bonding behaviour with the SCN$^-$ anion and H$_2$O: Li$^+$ favours Li-N and Li-O bonds while it disfavours Li-S bonds. As a result, when x is increased Li-S bonds are replaced by Li-O bonds, and since water cannot act as bridging ligand, the dimensionality of the lattice decreases from 3D for x = 0, to 2D for x = 1 and finally 1D
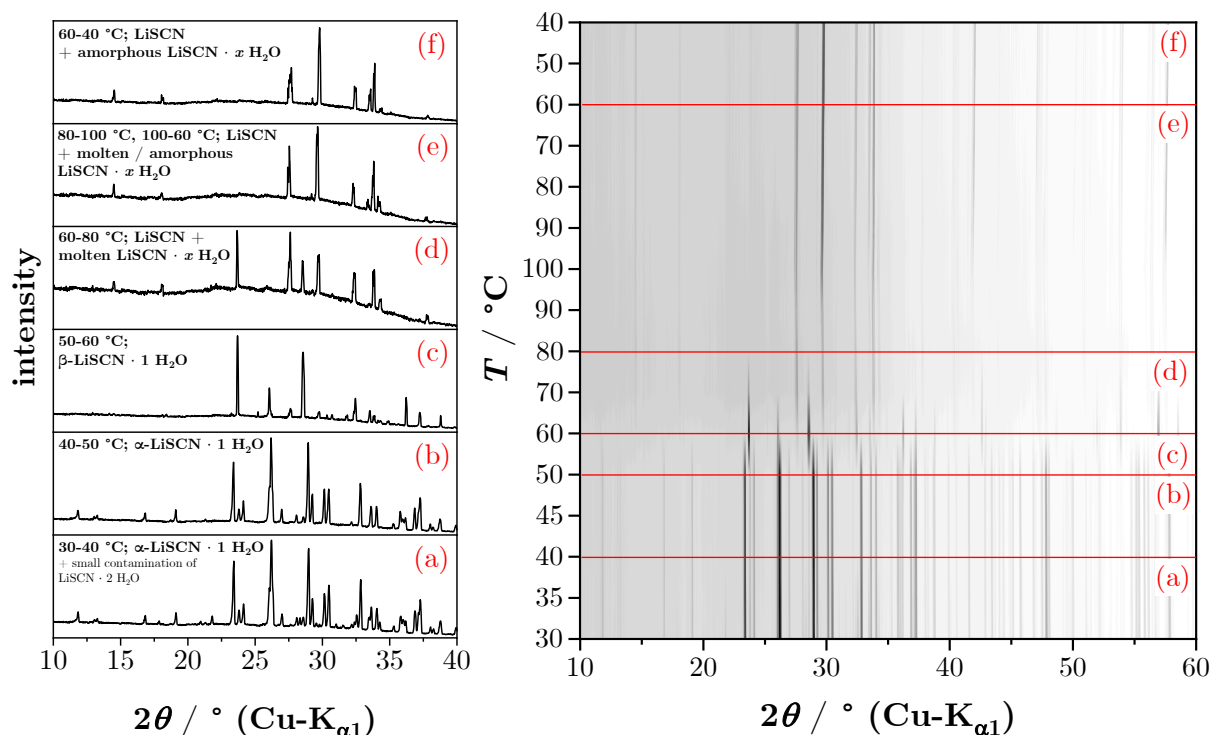
Figure 6.24: Temperature dependent *in situ* XRPD measurement of LiSCN $\cdot 1\,H_2O$ showing the α- to β-phase transition and the behaviour beyond its melting point. The left hand side displays selected XRPD patterns.

for $x = 2$. The monohydrate LiSCN $\cdot 1\,H_2O$ is a special case compared to $x = 0$ and 2, as will be discussed later with detailed thermodynamic investigations.

To investigate the stability range and temperature dependent behaviour of LiSCN $\cdot 1\,H_2O$, *in situ* XRPD measurements were performed (Figure 6.24). First, a small contamination of LiSCN $\cdot 2\,H_2O$ melted around 40 °C (Figure B.24, recrystallisation at around -30 °C). The α- to β-phase transition occurs at 49-50 °C, and finally the monohydrate melts at 60 °C (recrystallisation at ~30 °C) noticeable by the increase in amorphous background. These measurements were corroborated by *ex situ* XRPD, DSC (Figure 6.25 and B.23), p_{H_2O} measurements (Figure 6.26), visual inspection, and were in agreement with literature.[10] Due to the small dead volume in the employed capillary and inhomogeneous heating zone, water loss occurred at higher temperatures from the measured sample spot, and reflections of anhydrous LiSCN were observed. The cooling behaviour indicated that the monohydrate re-crystallises incongruently with lower crystallinity and/or as phase mixture. In contrast, when staying below 60 °C in a closed system, the monohydrate could be cycled without any discernible sign for decomposition or phase splitting, even though the β- to α-transition showed a pronounced hysteresis upon cooling (Figure B.22). The α- to β-phase transition was not clearly discernible in all DSC measurements (Figure 6.25 and B.23), which is not surprising since the energetic changes are expected to be rather small. However, an important observation from DSC measurements was
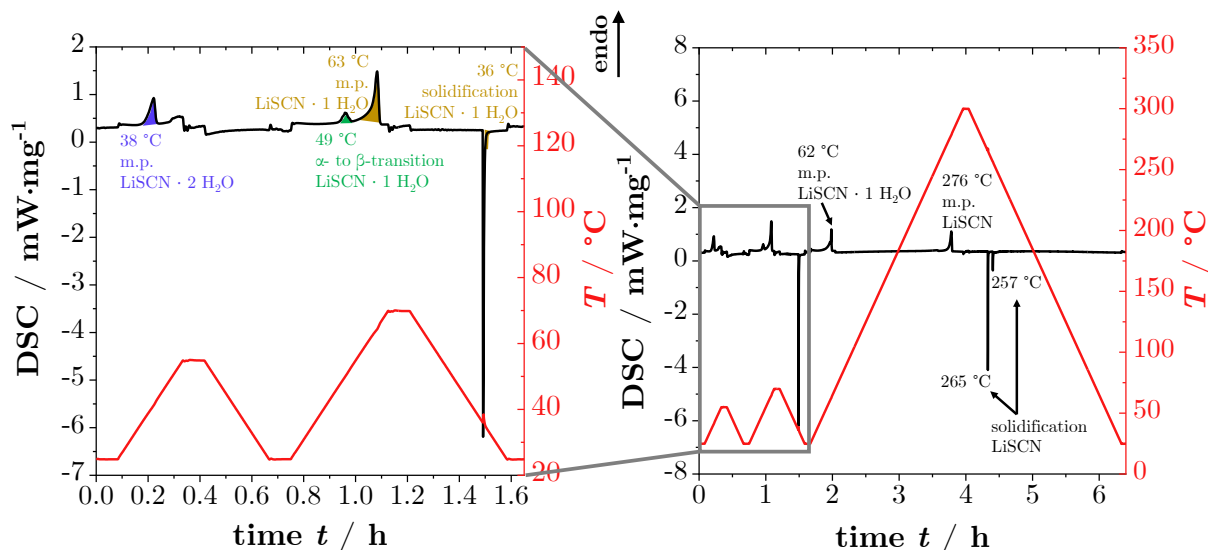
Figure 6.25: Exemplary DSC measurement of LiSCN $\cdot$ 1 H_2O with a magnification of the first two cycles on the left.

that small amounts of the dihydrate could easily form, even when the average x was below 1 (Figure B.25). This tendency can be explained with the investigated phase formation behaviour from *in situ* XRPD measurements while varying p_{H_2O} (Figure B.26). Based on Rietveld refinement (Figure B.27), at 0.5 mbar p_{H_2O} β-LiSCN $\cdot$ 1 H_2O directly formed, and surprisingly the α-phase was not observed. After ~10 h delay the dihydrate LiSCN $\cdot$ 2 H_2O starts to form as well, while the mole fraction of anhydrous LiSCN continuously decreases. The presence of a three-phase mixture indicates that even after hours of measurement time, equilibrium at the system was not fully reached. The level of hydration stays rather constant between 0.5 to 1.1 mbar, and continues at 1.5 mbar until only the hydrates remain. x increases above 1 along with the dihydrate mole fraction, and finally all reflections disappear and the sample liquefies. These measurements showed that (i) the exothermic hydration enthalpy causes local heating to at least 50 °C, by which the α-phase is "skipped" and the β-phase directly forms, and (ii), kinetic limitations can easily occur during hydration, resulting in small amounts of the dihydrate being present in a hydrated sample. These results fit perfectly to the experimental observations during synthesis of the LiSCN $\cdot x$ H_2O hydrates. When a powder sample of anhydrous LiSCN was placed together with a vial of water in a closed system for hydration via the gas phase, the powder would form hardened crystallites, and individual grains would initially become small droplets, which solidify later. This is caused by local heating in combination with the formation of small amounts of (liquid) LiSCN $\cdot$ 2 H_2O, and after longer equilibration time the sample cools down to form the final hydrate(s). The hardening effect caused the kinetic limitations, which is why small amounts of LiSCN $\cdot$ 2 H_2O were often present in the samples.

To investigate the hydration mechanism further, the equilibrium partial pressure of water

p_{H_2O} over the mono- and dihydrate was measured at various temperatures, and analysed by comparing it to that of pure water (Figure 6.26, B.28 and B.29). The measurements of the monohydrate match with the above analysis from XRPD and DSC. Below 60 °C, solid LiSCN $\cdot$ 1 H_2O can be cycled reversibly without any distinguishable changes in behaviour[18], and upon melting the water activity changes noticeably. The recrystallisation temperature at ~30 °C was the same as seen in DSC, and since it was known from XRPD that the material resolidifies incongruently, it is not surprising that the p_{H_2O} behaviour changed. Liquid LiSCN $\cdot$ 2 H_2O could be cycled reversibly above 80 °C without problem. With the polynomial term $\log(p_{H_2O}/\text{bar}) = a + b/T - c/T^2$,[153] the temperature dependence of p_{H_2O} can empirically be calculated (T in Kelvin):

- LiSCN $\cdot$ 1 H_2O (s); $a = 1.10 \pm 0.05, b = (-6.3 \pm 0.3)\,10^2$ K, $c = (1.80 \pm 0.05)\,10^5$ K^2

- LiSCN $\cdot$ 1 H_2O (l); $a = 4.88 \pm 0.03, b = (-22.8 \pm 0.2)\,10^2$ K, $c = (0.48 \pm 0.04)\,10^5$ K^2

- LiSCN $\cdot$ 2 H_2O (l); $a = 5.998 \pm 0.009, b = (-27.59 \pm 0.06)\,10^2$ K, $c = (-0.420 \pm 0.009)\,10^5$ K^2

In contrast to most literature,[153–158] the p_{H_2O} measurements shown here are within the narrow phase width of the hydrates, and no significant stoichiometric changes in x occur (changes were estimated to be $\leq 10^{-5}$). Since the system can be considered as homogeneous and closed, one can write:

$$\text{"}H_2O_{(x)}\text{"} \rightleftharpoons H_2O_{(g)} \tag{6.27}$$

as the governing reaction for the equilibrium between the water activity in the respective hydrate ($x = 1$ or 2) and the gas phase. Since the system is in equilibrium ($\mu_{H_2O,x} = \mu_{H_2O,g}$), the following set of equations based on the mass action law can be derived:[159]

$$K_h = \frac{p_{H_2O,\,x=1\,\text{or}\,2}}{a_{x=1\,\text{or}\,2}} = \exp\left(-\frac{\mu^\circ_{H_2O,\,g} - \mu^\circ_{H_2O,\,x=1\,\text{or}\,2}}{k_B T}\right) \tag{6.28}$$

$$K'_h = K_h \cdot a_{x=1\,\text{or}\,2} = p_{H_2O,\,x=1\,\text{or}\,2} \tag{6.29}$$

$$\ln(K'_h) = -\frac{\Delta_h H^\circ}{k_B T} + \frac{\Delta_h S^\circ}{k_B} \tag{6.30}$$

where $p_{H_2O,\,x=1\,\text{or}\,2}$ and $a_{x=1\,\text{or}\,2}$ are the equilibrium partial pressure (gas phase above LiSCN $\cdot x\,H_2O$) and activity (inside the phase LiSCN $\cdot x\,H_2O$) of water, $\mu^\circ_{H_2O,\,i}$ is the standard chemical potential of water in i, $\Delta_h H^\circ$ and $\Delta_h S^\circ$ are the standard enthalpy

---

[18]The α- to β-phase transition cannot be observed, since both show the same water activity.
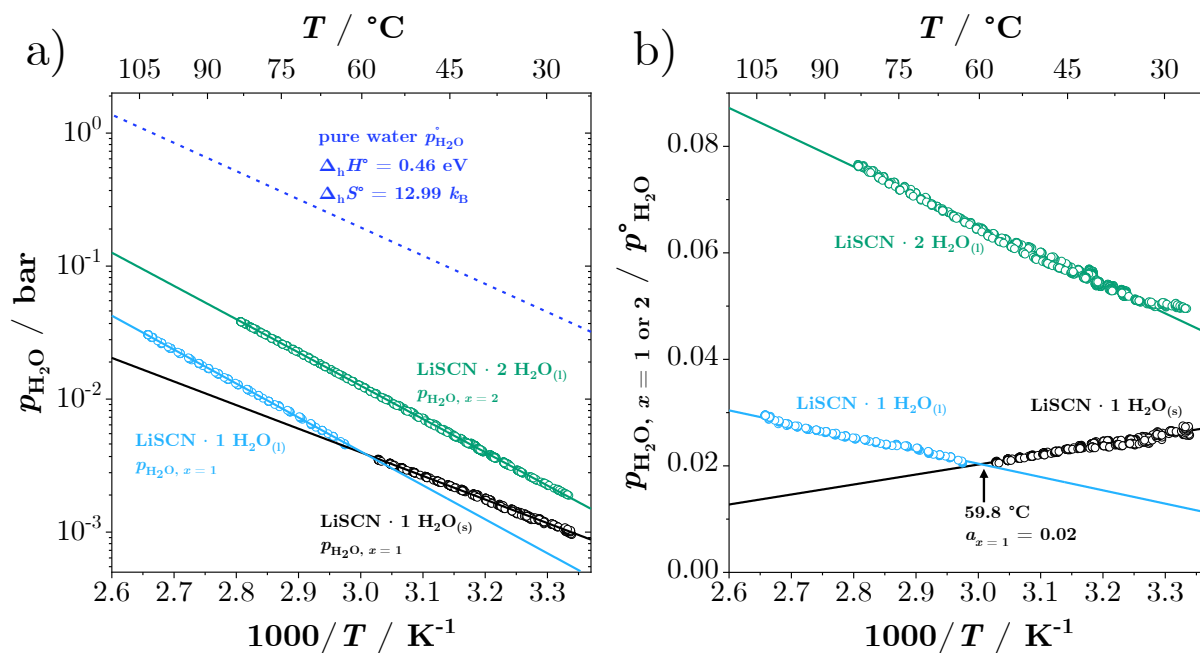
Figure 6.26: Measurement of p_{H_2O} for LiSCN $\cdot x\,H_2O$ ($x = 1$ or 2) as solid (s) and liquid (l), showing a) the measured p_{H_2O} data compared to pure water,[160] and b) the corresponding water activities.

and entropy of (de-)hydration. Since $p_{H_2O,\,x=1\,or\,2} \ll p^\circ_{H_2O}$ (equilibrium partial pressure of pure water), $a_{x=1\,or\,2}$ is much smaller than 1 and approximately constant. By plotting $\ln(p_{H_2O,\,x}\,/\,1\,\text{bar})$ vs. $1000/T$ the enthalpy and entropy of hydration can be obtained by linear fitting (Figure 6.26). By comparing the hydration enthalpy and entropy (Figure 6.26a) as well as the melting enthalpies from DSC of the monohydrate with the other LiSCN $\cdot x\,H_2O$ phases (Table 6.6), it becomes clear that the shown structural anomaly of $x = 1$ also affects its physical properties. Even though melting temperatures decrease monotonically with x, the energetic requirements for melting and dehydration of the monohydrate do not follow this trend. Evidently, the tetrahedral coordination $[\text{Li}(\text{NCS})_2(\text{OH}_2)_2]$ in the monohydrate is most unfavourable with the lowest lattice energy. It is generated out of necessity since a 6-fold octahedral coordination would require more H_2O molecules, and Li-S bonds are even less desired. A good comparison can be made with the lithium iodide hydrates, since both material systems show very similar properties. Remarkably, LiI $\cdot z\,H_2O$ ($z = 1$, 2 and 3) phases show the same trend as seen for LiSCN $\cdot x\,H_2O$, merely "shifted" by one H_2O molecule.[68, 73] While $z = 1$ and 3 behave rather similar with related structures (cubic or hexagonal, regular octahedral coordination), the dihydrate stands out with different properties and a noticeably lowered crystal symmetry (triclinic) with strongly distorted Li^+-octahedra (almost tetrahedral, $4 \times d(\text{Li} - \text{OH}_2) \approx 2\,\text{Å} + 2 \times d(\text{Li} - \text{I}) \approx 3.3\,\text{Å}$). In contrast, Li^+ in LiSCN $\cdot 1\,H_2O$ coordinates with the bidental ligand SCN^-, and instead of forming distorted $[\text{Li}(\text{NCS})_2(\text{SCN})_2(\text{OH}_2)_2]$ octahedra, it forms tetrahedra without Li-S-coordination

Table 6.6: Summary of the thermodynamic data collected with DSC and p_{H_2O} measurements of all LiSCN $\cdot x$ H$_2$O phases ($x = 0$, 1 and 2).

phase	state	melting point / °C	melting enthalpy / eV	$\Delta_h H°$ / eV	$\Delta_h S°$ / k_B
LiSCN	solid	274	0.19	—	—
LiSCN $\cdot$ 1 H$_2$O	solid	60	0.08	0.35	6.74
	liquid	—	—	0.51	12.11
LiSCN $\cdot$ 2 H$_2$O	solid	38	0.24	—	—
	liquid	—	—	0.50	12.91

and has a low symmetry 2D structure (Figure 6.23). Interestingly, liquid LiSCN $\cdot$ 1 H$_2$O behaves more similar to LiSCN $\cdot$ 2 H$_2$O regarding (de-)hydration, which indicates that in the liquid monohydrate, clusters of $[Li(H_2O)_{\lambda'}(SCN)_{\lambda''}]^{(\lambda''-1)-}$ with $\lambda' \geq 1$ and $\lambda'' \geq 0$ could form with a higher coordination number[19]. The observed trends for p_{H_2O} and water activity in Figure 6.26 fit to a highly hygroscopic ionic salt and are well in accord with Pearson's concept of hard and soft acids and bases (HSAB).[64] The following subsections 6.2.2 and 6.2.3 will show that these trends in structure and hydration thermodynamics of LiSCN $\cdot x$ H$_2$O are also reflected in their Li$^+$ ion transport behaviour. The transition from two-phase to one-phase regions in LiSCN $\cdot x$ H$_2$O is nicely mapped with the measured activity of water (p_{H_2O}) as a function of x shown in Figure 6.27a with data from this work and literature.[10] The apparent offset of XRPD-based data emphasizes the local heating effect. The slight discrepancy at $x = 2$ could be related to the high hygroscopy and narrow phase width in LiSCN $\cdot x$ H$_2$O, or could also still simply be a temperature effect.

The newly determined structural data as well as the thermodynamic investigations shown above were combined with literature work,[10, 38] and an updated phase diagram of the system LiSCN $-$ H$_2$O was constructed (Figure 6.27b). In general, most metal salt $-$ water systems ranging from alkali over alkaline earth to transition metal salts behave rather similar in their phase formation.[68, 164–169] They all show distinct peritectica with an eutecticum at low temperatures. Hydrates of LiSCN do not show congruent melting points, and after becoming liquid, they would split into several LiSCN $\cdot x$ H$_2$O phases upon recrystallisation[20]. The comparison of the LiX $-$ H$_2$O phase diagram for LiSCN and LiI yields an interesting observation. Lithium iodide is rather "special", as it is the only lithium halide which can form congruently melting phases with water or methanol.[68, 170]

---

[19]For comparison, Li$^+$ cations in aqueous systems have typically a coordination number of 4 to 5,[161, 162] and in terms of concentrated systems, molten LiI has a coordination number slightly below 6.[163]

[20]In subsection 6.2.3 it will be shown that a good method to analyse the transport mechanism of a distinct phase is to "lock" it by being close, but not exactly on the phase border; e.g. LiSCN $\cdot$ 0.9 H$_2$O allows to measure the monohydrate without being bothered by the dihydrate, and in LiSCN $\cdot$ 2.1 H$_2$O only the pure dihydrate with a small amount of water can be present, ruling out any disturbance of the monohydrate.

The fact that LiSCN hydrates do not share this property emphasizes the singularity of the bidental ligand SCN^- with respect to structure and hydration, and as discussed in the next subsection, also extends to Li^+ ion transport.
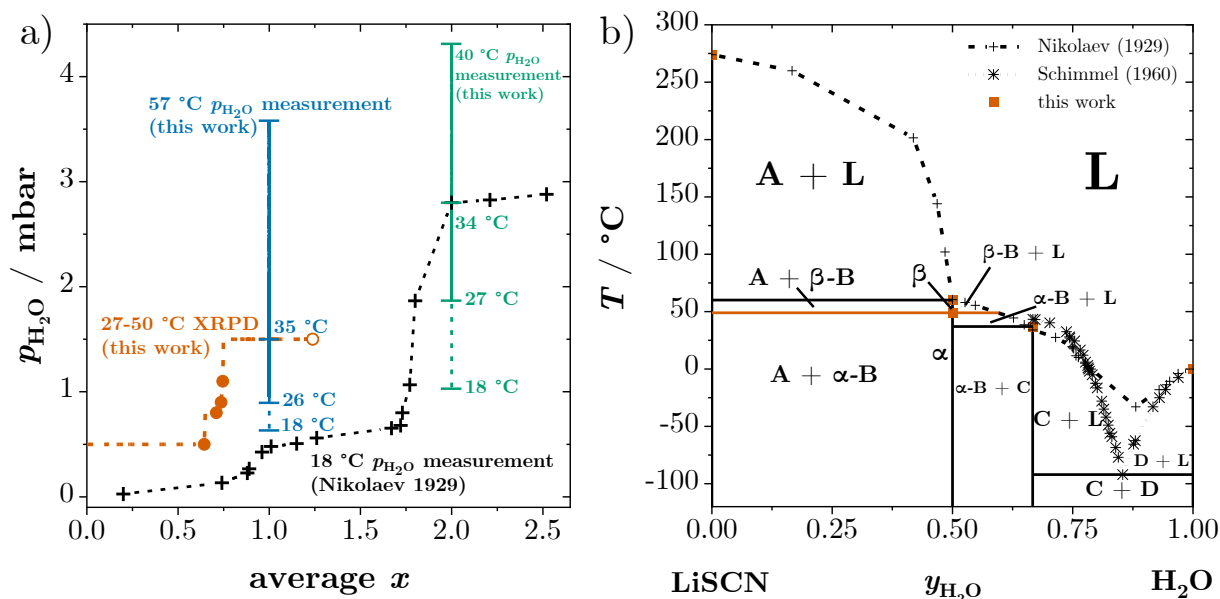
Figure 6.27: a) Variation of water activity (p_{H_2O}) with the stoichiometry x in LiSCN $\cdot$ $x\,H_2O$. The data are based on XRPD (red, T = 27-50 °C due to local heating), direct measurements of p_{H_2O} from this work (x = 1 solid in blue, x = 2 liquid in green extrapolated to 18 °C with the respective equations mentioned above) or from literature (black).[10] b) Updated phase diagram of the system $LiSCN - H_2O$ constructed with data from this thesis as well as with literature data.[10, 38] A = LiSCN, B = LiSCN $\cdot\,1\,H_2O$, C = LiSCN $\cdot\,1\,H_2O$ and D = H_2O.

6.2.2 $x \approx 0.001$: H_2O-doped LiSCN

As discussed in the previous subsection, LiSCN can reversibly be hydrated and dehydrated to form LiSCN $\cdot\,x\,H_2O$, and can thereby vary its hydration degree x within one- and two-phase regimes (Figure 6.27). The anhydrous material itself has a narrow but defined phase width in which it can incorporate H_2O molecules into its crystal structure while remaining a pure phase; i.e. anhydrous LiSCN is doped by water. In general, it is well known that molecular hydration improves ionic mobility of the dominant ionic charge carrier (cf. chapter 7), but the impact of doping by small concentrations of H_2O on ionic conductors has so far not been studied. As shown later, the concept of using H_2O as dopant is highly materials specific and can most likely only be observed in few materials. Since the mechanism discussed here is rather complex, the experimental results of TGA, EIS and ssNMR measurements are first shown, and then a defect model will be derived to explain the observed phenomena.

Figure 6.28 shows an exemplary TGA measurement of LiSCN at 140 °C while increasing
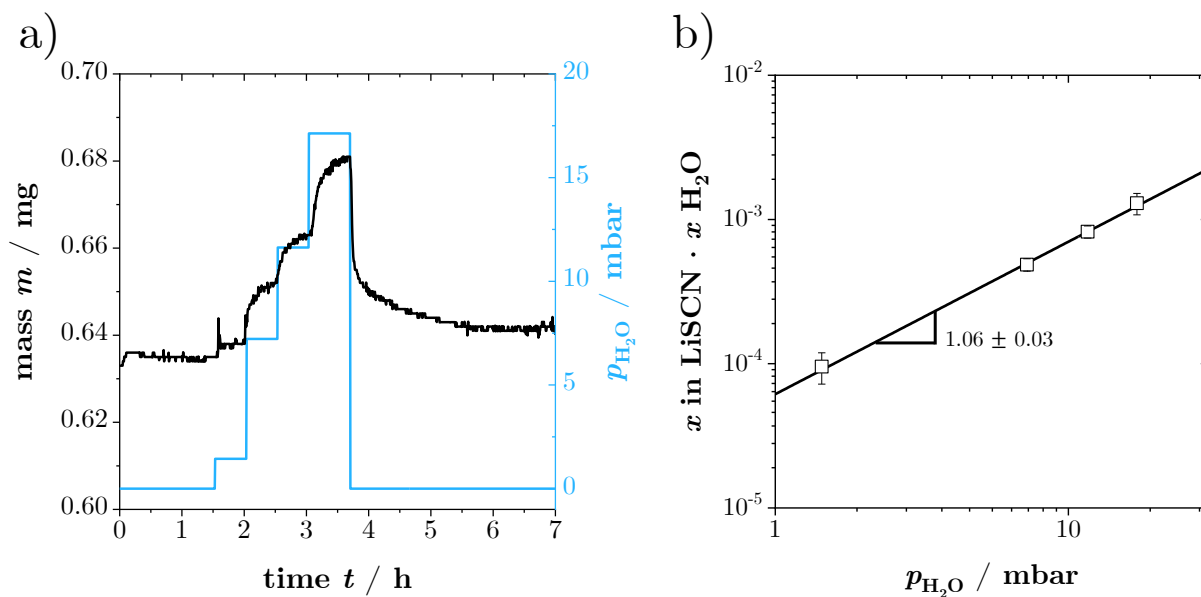
Figure 6.28: Exemplary TGA measurement of LiSCN within the single-phase regime at 140 °C for various p_{H_2O}. a) Mass change over time, and b) water uptake x in LiSCN; the line is a linear fit.

p_{H_2O}, and the respective change in water content x. These measurements were rather tedious due to several complications: (i) Since the material is highly hygroscopic, it had to be dried thoroughly to remove ppm amounts of H_2O to assess the doping regime accurately; (ii) If the relative humidity exceeded ~ 2 %, stoichiometric hydration beyond the doping range of anhydrous LiSCN began, and hydrates started to form[21]; (iii) In case very small amounts of hydrates formed, they would melt at the measurement temperatures and change the morphology of the sample from loose powder to larger, hard crystallites. This results in strong kinetic hysteresis effects, especially upon dehydration. To achieve confidence in the collected data, a number of TGA measurements at various temperatures were performed (Figure B.30). Throughout these measurements, x adopted values between $10^{-4} - 10^{-3}$, staying within the doping regime of LiSCN. The observed slope of ~ 1 for the log-log plot of x vs. p_{H_2O} in Figure 6.28b generally indicates molecular hydration, which is expected for a material that forms stable hydrates.

In addition to TGA measurements, the conductivity of LiSCN was measured with impedance spectroscopy while varying p_{H_2O} at different temperatures (Figure 6.29). The changes in slopes of the log-log plot show that at a certain relative humidity (80 °C 0.1 %, 120 °C 0.2 %, 160 °C >0.3 %) the transport mechanism changes. As shown in detail later, the left, shallow part is identified as the doping regime, while the right part represents the start of stoichiometric hydration. Figure 6.29a shows that the relevant criterion for doping or hydration with H_2O is relative humidity (RH) and not p_{H_2O}. Since EIS is more

---

[21]Almost all TGA measurements were conducted below 1 % RH, for which measurement conditions were most stable without strong hysteresis effects.
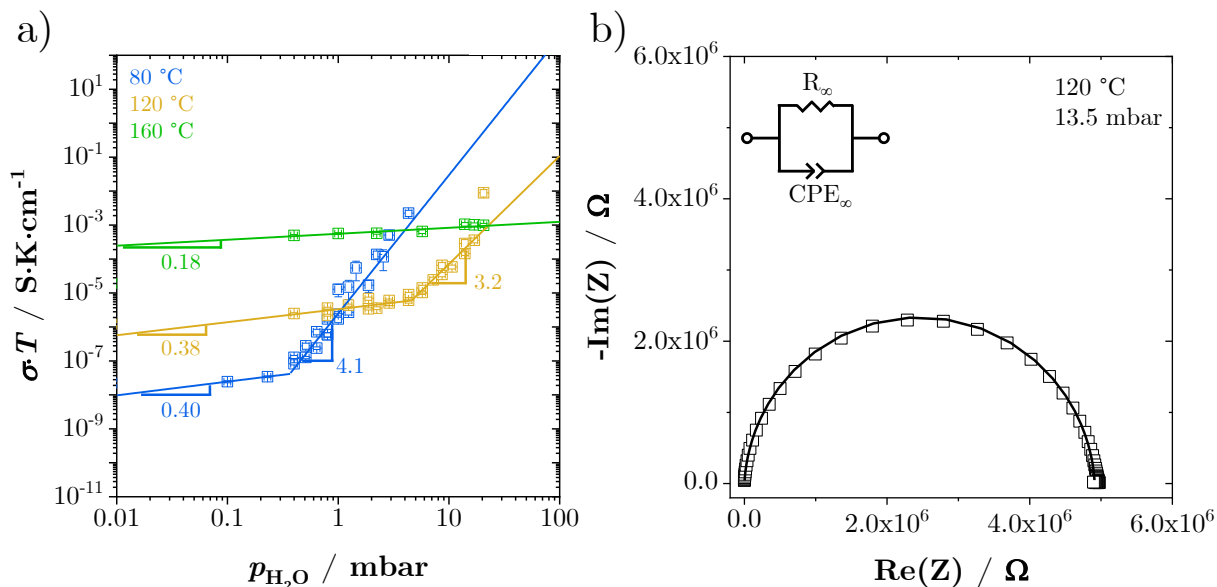
Figure 6.29: a) Conductivity of LiSCN exposed to various p_{H_2O}. Solid lines are linear fits to the data. b) Exemplary EIS spectrum, fitted with the shown equivalent circuit.

sensitive to tiny stoichiometric changes, it yields a lower bound (~ 0.3 % RH) for the start of the hydration regime than TGA (~ 1.0 % RH). The combination of TGA and EIS measurements showed that within the doping regime x has values up to 0.001.

After the range for H_2O-doping was identified, samples with $x \approx 0.001$ were prepared and their conductivities measured as a function of temperature in sealed measurement cells. The measured data of three samples are compiled in Figure 6.30, and the conductivities are compared to anhydrous LiSCN ($x = 0$) for both local (ω_1) and long-range (ω_2) V'_{Li} transport (cf. subsection 6.1.2). The measured conductivity of H_2O-doped LiSCN suggests that the incorporation of H_2O molecules into the lattice accelerates the local relaxation process of the SCN^- anion. This means that the conductivity is no longer frequency dependent, only long-range V'_{Li} transport is observed, and H_2O-doping not just increases the mobile defect concentration, but also the mobility of that charge carrier. This conclusion is supported by the following observations from impedance:

- In contrast to undoped and M^{2+}-doped anhydrous LiSCN (Figure 6.3), the impedance spectra of H_2O-doped LiSCN show only one relaxation process (Figure 6.29b and 6.30b), which suggests that only long-range ion hopping is observed.

- The dielectric constant of H_2O-doped LiSCN (Figure 6.30b and B.31b) is very similar to the value of the fast process (ω_1) in anhydrous LiSCN (Figure 6.10b), which again indicates a faster relaxation of the SCN^- anion lattice without strong polarisation effects.
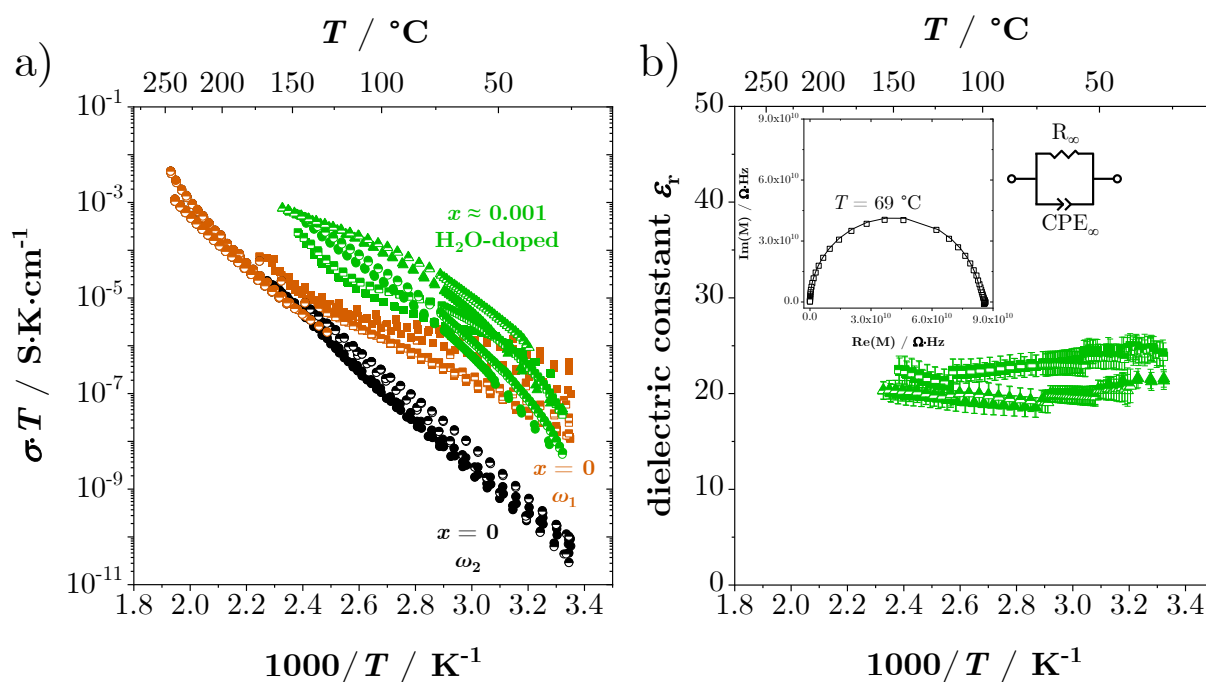
Figure 6.30: a) Conductivities of H_2O-doped LiSCN (green) compared with anhydrous LiSCN (ω_1 red and ω_2 black, subsection 6.1.2). b) Dielectric constant ε_r of H_2O-doped LiSCN of the measurements shown in (a). Heating runs are full, cooling runs are half-full symbols. Insert: exemplary impedance spectrum in modulus form, fitted with the shown equivalent circuit.

- The conductivity of H_2O-doped LiSCN is too high for only 0.1 mol% of doping (cf. Figure 6.4b), if V_{Li}' had the same long-range mobility as in anhydrous LiSCN. Since the measured data are similar to local vacancy transport at high frequencies (red squares in Figure 6.30a), V_{Li}' must have a higher mobility in H_2O-doped LiSCN.

In general, one would expect a $H_2O_{SCN}^{\cdot\cdot}$ defect to be more flexible than a regular SCN_{SCN}^x site, given that H_2O is uncharged and more spherical. It is therefore reasonable to hypothesise that the incorporation of H_2O molecules into the crystal structure of anhydrous LiSCN enables a faster anion lattice relaxation, which increases the mobility of V_{Li}'.

To support the hypothesis of increased V_{Li}' mobility, samples of both H_2O- and D_2O-doped LiSCN were prepared for ^{7}Li ssNMR measurements (Figure 6.31a). The samples showed very different NMR signals: In H_2O-doped LiSCN the central transition remains rather unchanged over the temperature range, with a small, narrow additional signal occurring at ∼50 °C. In the D_2O-doped material the narrow component becomes already visible at 35 °C and increases strongly in intensity with temperature. It is not finally clear why the [7]Li signals of H_2O- and D_2O-doped samples differ in this way, but the most likely explanation is that a small amount of secondary phase (e.g. LiSCN · 1 D_2O) is present in that sample. Regarding anhydrous LiSCN, the central transition is expected to demonstrate in ssNMR a metal-like line shape (cf. Figure 6.12).[171] Any additional contribution to
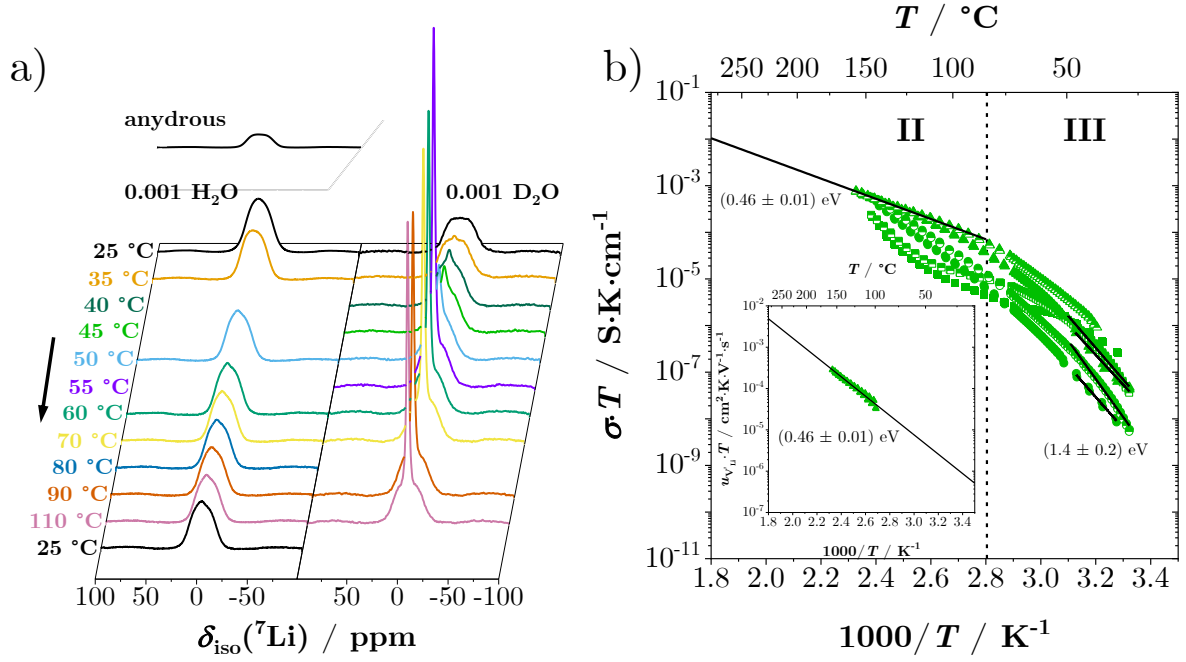
Figure 6.31: a) ^{7}Li ssNMR of H_2O- and D_2O-doped LiSCN at various temperatures. b) Conductivity of H_2O-doped LiSCN with linear fits (solid lines) of regimes II (extrinsic) and III (association). Heating runs are full, cooling runs are half-full symbols. Insert: calculated mobility data.

the mobility of Li^+ ions, e.g. dipole-dipole interactions or the presence of H_2O molecules, results in a Gaussian line shape, which is observed here for LiSCN $\cdot 0.001\,H_2O$. Therefore, the shown ssNMR data support the observations from EIS, that Li^+ ions in H_2O-doped LiSCN have a higher local mobility compared to the anhydrous case.

The defect chemical considerations as shown in subsection 6.1.1 apply also to doping with H_2O, indicating three regimes: I intrinsic, II extrinsic, and III association. Mass action laws are used to derive the thermodynamic equations to calculate relevant defect concentrations. The overall concept is that H_2O can reside on an anion position, considering both size and coordination chemistry of H_2O compared to SCN^-. Therefore, in addition to V'_{Li} and $V^{\cdot}_{SCN}$, a third charged defect $H_2O^{\cdot}_{SCN}$ is present in H_2O-doped LiSCN. Due to the strong coordination tendency of H_2O, the formation of associates $(H_2O_{SCN}V_{Li})$ at lower temperatures is expected. The mass balance for the total water concentration $[H_2O_{Total}]$ is:

$$[H_2O_{Total}] = [(H_2O_{SCN}V_{Li})] + [H_2O^{\cdot}_{SCN}] \tag{6.31}$$

Starting with the intrinsic regime at high temperatures, the Schottky equilibrium condition applies $[V'_{Li}] = [V^{\cdot}_{SCN}] = \sqrt{K_S}$. This means that if H_2O molecules are incorporated in this regime, they can directly reside in thiocyanate vacancies since many are available in the system. Associates can be neglected, as only free carriers exist at high temperatures.

This yields:

Regime I Intrinsic:

$$V^{\cdot}_{SCN} + H_2O_{(g)} \rightleftharpoons H_2O^{\cdot}_{SCN} \tag{6.32}$$

$$K_I = \frac{[H_2O^{\cdot}_{SCN}]}{[V^{\cdot}_{SCN}]p_{H_2O}} \tag{6.33}$$

$$[V^{'}_{Li}] = [V^{\cdot}_{SCN}] \quad > [H_2O^{\cdot}_{SCN}] \tag{6.34}$$

$$[H_2O_{Total}] = [H_2O^{\cdot}_{SCN}] \tag{6.35}$$

The water partial pressure p_{H_2O} is expressed as activity ($p_{H_2O} = p^{'}_{H_2O} / 1\,bar$) and is therefore dimensionless.

At lower temperatures the concentration of $V^{'}_{Li}$ is fixed by a dopant, here $H_2O^{\cdot}_{SCN}$, marking the extrinsic regime. Defect associates are still irrelevant for the mass balance and equation 6.35 still applies. In case 1 the electroneutrality condition (equation 6.38) comprises only $V^{'}_{Li}$ and $H_2O^{\cdot}_{SCN}$, while in case 2 (equation 6.41) also $V^{\cdot}_{SCN}$ are considered. This means that case 2 represents the transition from intrinsic to extrinsic case 1.

Regime II Extrinsic:
Case 1:

$$Li^x_{Li} + SCN^x_{SCN} + H_2O_{(g)} \rightleftharpoons V^{'}_{Li} + H_2O^{\cdot}_{SCN} + LiSCN_{surface} \tag{6.36}$$
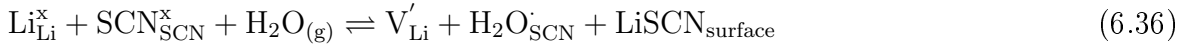
$$K_{II,1} = \frac{[H_2O^{\cdot}_{SCN}][V^{'}_{Li}]}{p_{H_2O}} = K_I K_S \tag{6.37}$$

$$[V^{'}_{Li}] = [H_2O^{\cdot}_{SCN}] \tag{6.38}$$

Case 2:

$$Li^x_{Li} + SCN^x_{SCN} + V^{\cdot}_{SCN} + 2\,H_2O_{(g)} \rightleftharpoons V^{'}_{Li} + 2\,H_2O^{\cdot}_{SCN} + LiSCN_{surface} \tag{6.39}$$
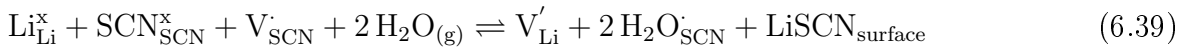
$$K_{II,2} = \frac{[H_2O^{\cdot}_{SCN}]^2[V^{'}_{Li}]}{[V^{\cdot}_{SCN}]p^2_{H_2O}} = K^2_{II,1}K^{-1}_S \tag{6.40}$$

$$[V^{'}_{Li}] = [H_2O^{\cdot}_{SCN}] + [V^{\cdot}_{SCN}] \tag{6.41}$$

The reactions 6.36 and 6.39 are not independent new reactions, but can be traced back to the water incorporation reaction 6.32 and the Schottky reaction 6.1 (6.36 = 6.32 + 6.1, 6.39 = 6.32 + 6.36). These formulations depict possible incorporation mechanisms

into the LiSCN lattice (substitution and/or addition), which are determined from the respective electroneutrality condition.

At low temperatures defect association is relevant and has to be considered in the analysis. The total concentration of incorporated water is then equivalent to the concentration of associates $[\text{H}_2\text{O}_{\text{Total}}] = [(\text{H}_2\text{O}_{\text{SCN}}\text{V}_{\text{Li}})]$. The electroneutrality conditions for cases 1 and 2 are consequently the same as in regime II (equations 6.38 and 6.41).

Regime III Association:
Case 1:

$$\text{Li}_{\text{Li}}^{\text{x}} + \text{SCN}_{\text{SCN}}^{\text{x}} + \text{H}_2\text{O}_{(g)} \rightleftharpoons (\text{H}_2\text{O}_{\text{SCN}}\text{V}_{\text{Li}}) + \text{LiSCN}_{\text{surface}} \tag{6.42}$$
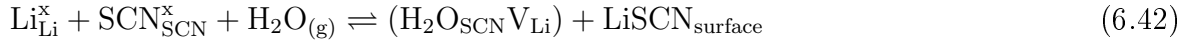
$$K_{\text{III},1} = \frac{[(\text{H}_2\text{O}_{\text{SCN}}\text{V}_{\text{Li}})]}{p_{\text{H}_2\text{O}}} = K_{\text{II},1} K_{\text{A}}^{\text{H}_2\text{O}} \tag{6.43}$$

Case 2:

$$\text{Li}_{\text{Li}}^{\text{x}} + \text{SCN}_{\text{SCN}}^{\text{x}} + \text{V}_{\text{SCN}}^{\cdot} + 2\,\text{H}_2\text{O}_{(g)} \rightleftharpoons (\text{H}_2\text{O}_{\text{SCN}}\text{V}_{\text{Li}}) + \text{H}_2\text{O}_{\text{SCN}}^{\cdot} + \text{LiSCN}_{\text{surface}} \tag{6.44}$$

$$K_{\text{III},2} = \frac{[(\text{H}_2\text{O}_{\text{SCN}}\text{V}_{\text{Li}})][\text{H}_2\text{O}_{\text{SCN}}^{\cdot}]}{[\text{V}_{\text{SCN}}^{\cdot}]p_{\text{H}_2\text{O}}^2} = K_{\text{II},1}^2 K_{\text{S}}^{-1} K_{\text{A}}^{\text{H}_2\text{O}} \tag{6.45}$$

This regime applies at very low temperatures, when the concentration of free $\text{H}_2\text{O}_{\text{SCN}}^{\cdot}$ drops so low that $[\text{V}_{\text{SCN}}^{\cdot}]$ becomes relevant again (regime III,2 in Figure 6.32). The defect association reaction is analogous to the one in dry LiSCN (cf. equation 6.3):

$$\text{H}_2\text{O}_{\text{SCN}}^{\cdot} + \text{V}_{\text{Li}}^{'} \rightleftharpoons (\text{H}_2\text{O}_{\text{SCN}}\text{V}_{\text{Li}}) \tag{6.46}$$

$$K_{\text{A}}^{\text{H}_2\text{O}} = \frac{[(\text{H}_2\text{O}_{\text{SCN}}\text{V}_{\text{Li}})]}{[\text{H}_2\text{O}_{\text{SCN}}^{\cdot}][\text{V}_{\text{Li}}^{'}]} = \frac{N_{\text{A}}^{\text{H}_2\text{O}}}{N_{\text{SCN}}N_{\text{Li}}} \cdot \exp\left(\frac{\Delta_{\text{A}}S_{\text{H}_2\text{O}}^{\circ}}{k_{\text{B}}}\right) \exp\left(-\frac{\Delta_{\text{A}}H_{\text{H}_2\text{O}}^{\circ}}{k_{\text{B}}T}\right) \tag{6.47}$$

where $N_{\text{SCN}} = N_{\text{Li}} = 4/V_{\text{UC}}$ and $N_{\text{A}}^{\text{H}_2\text{O}} = 6\,N_{\text{Li}}$ since every Li atom is coordinated by 6 SCN^{-} anions. The mass action constant for the formation of a Schottky defect pair K_{S} is the same as in dry LiSCN (cf. equation 6.4).

Finally, the respective Brouwer approximations for both cases were derived and are listed in Table 6.7. These approximations were used to calculate relevant defect concentrations and $p_{\text{H}_2\text{O}}$ dependences of the total amount of incorporated water (related to Figure 6.28 and B.30) as well as lithium vacancies (related to Figure 6.29).

Table 6.7: Overview of the Brouwer approximations and p_{H_2O} dependences used to derive the defect chemical model of H_2O-doped LiSCN.

	Case 1	Case 2
regime I **intrinsic**		$[V'_{Li}] = [V^{\cdot}_{SCN}]$
		$[V'_{Li}] = \sqrt{K_S} \; > [H_2O^{\cdot}_{SCN}]$
		$[V^{\cdot}_{SCN}] = \sqrt{K_S} \; > [H_2O^{\cdot}_{SCN}]$
		$[H_2O^{\cdot}_{SCN}] = [H_2O_{Total}]$
		$[(H_2O_{SCN}V_{Li})] = K_A^{H_2O}\sqrt{K_S}[H_2O_{Total}]$
		$[H_2O_{Total}] = K_I\sqrt{K_S}p_{H_2O}$
		$[V'_{Li}] = [H_2O_{Total}]/(K_I p_{H_2O})$
regime II **extrinsic**	$[V'_{Li}] = [H_2O^{\cdot}_{SCN}]$	$[V'_{Li}] = [H_2O^{\cdot}_{SCN}] + [V^{\cdot}_{SCN}]$
	$[V'_{Li}] = [H_2O_{Total}]$	$[V'_{Li}] = [H_2O_{Total}]/2 + \sqrt{[H_2O_{Total}]^2/4 + K_S}$
	$[V^{\cdot}_{SCN}] = K_S/[H_2O_{Total}]$	$[V^{\cdot}_{SCN}] = K_S/([H_2O_{Total}]/2 + \sqrt{[H_2O_{Total}]^2/4 + K_S})$
	$[H_2O^{\cdot}_{SCN}] = [H_2O_{Total}]$	$[H_2O^{\cdot}_{SCN}] = [H_2O_{Total}]$
	$[(H_2O_{SCN}V_{Li})] = K_A^{H_2O}[H_2O_{Total}]^2$	$[(H_2O_{SCN}V_{Li})] = \left(K_A^{H_2O}[H_2O_{Total}]^2\right)/2 + \sqrt{[H_2O_{Total}]^4/4 + K_S[H_2O_{Total}]}$
	$[H_2O_{Total}] = \sqrt{K_{II,1}p_{H_2O}}$	$[H_2O_{Total}] = p_{H_2O}\sqrt{(K_{II,2}K_S)/(p_{H_2O}\sqrt{K_{II,2}K_S} + K_S)}$
	$[V'_{Li}] = \sqrt{K_{II,1}p_{H_2O}}$	$[V'_{Li}] = \sqrt{p_{H_2O}\sqrt{K_{II,2}K_S} + K_S}$
regime III **association**	$[V'_{Li}] = [H_2O^{\cdot}_{SCN}]$	$[V'_{Li}] = [H_2O^{\cdot}_{SCN}] + [V^{\cdot}_{SCN}]$
	$[V'_{Li}] = \sqrt{[H_2O_{Total}]/K_A^{H_2O}}$	$[V'_{Li}] = \sqrt{\left([H_2O_{Total}] + K_A^{H_2O}K_S\right)/K_A^{H_2O}}$
	$[V^{\cdot}_{SCN}] = K_S\sqrt{K_A^{H_2O}/[H_2O_{Total}]}$	$[V^{\cdot}_{SCN}] = K_S/\sqrt{\left([H_2O_{Total}] + K_A^{H_2O}K_S\right)/K_A^{H_2O}}$
	$[H_2O^{\cdot}_{SCN}] = \sqrt{[H_2O_{Total}]/K_A^{H_2O}}$	$[H_2O^{\cdot}_{SCN}] = \sqrt{\left([H_2O_{Total}] + K_A^{H_2O}K_S\right)/K_A^{H_2O}} - K_S/\sqrt{\left([H_2O_{Total}] + K_A^{H_2O}K_S\right)/K_A^{H_2O}}$
	$[(H_2O_{SCN}V_{Li})] = [H_2O_{Total}]$	$[(H_2O_{SCN}V_{Li})] = [H_2O_{Total}]$
	$[H_2O_{Total}] = K_{III,1}p_{H_2O}$	$[H_2O_{Total}] = p_{H_2O}\sqrt{K_{III,2}K_A^{H_2O}K_S}$
	$[V'_{Li}] = \sqrt{(K_{III,1}p_{H_2O})/K_A^{H_2O}}$	$[V'_{Li}] = \sqrt{(K_{III,2}K_S p_{H_2O}^2 + [H_2O_{Total}]K_S)/[H_2O_{Total}]}$

The initial hypothesis is that water acts as a dopant to form $H_2O^{\cdot}_{SCN}$ defects, which associate at low temperatures. Based on the experimental findings discussed above, the data suggest that water affects also free V'_{Li} defects after they dissociated by increasing their mobility. This means that incorporated water influences its environment, i.e. SCN$^-$ relaxation, farther than its immediate surrounding. If lithium vacancies have a higher mobility in H_2O-doped LiSCN, the mobility can be calculated from the conductivity data in the extrinsic regime. The transition from association to extrinsic is reflected by a more shallow slope in conductivity, emphasized in Figure 6.31b. The doping concentration $[H_2O^{\cdot}_{SCN}]$ is equal to $[H_2O_{Total}] = 0.001 \cdot (4/V_{UC})$ and the mobilities can then be calculated

with equation 6.11 (inset Figure 6.31b)[22]:

$$(u_{V'_{Li}} T)^{H_2O} = 10^{(1.9 \pm 0.1)} \exp\left(-\frac{(0.46 \pm 0.01)\,\text{eV}}{k_B T}\right) \frac{\text{cm}^2\text{K}}{\text{Vs}} \tag{6.48}$$

To be precise, according to case 2 the concentration $[V'_{Li}]$ is not fixed in the extrinsic regime, which means the mobility term in equation 6.48 would strictly not be appropriate. However, for regime II the condition $[V'_{Li}] \gtrsim [H_2O^{\cdot}_{SCN}] \gg [V^{\cdot}_{SCN}]$ still applies, meaning the mobility term can still be used as a good approximation in case 2 as well. The equilibrium association constant $K_A^{H_2O}$ is calculated by inserting the Brouwer approximation of case 1 for $[V'_{Li}]$ in regime III into equation 6.11 as well as the resulting term for σT from linearly
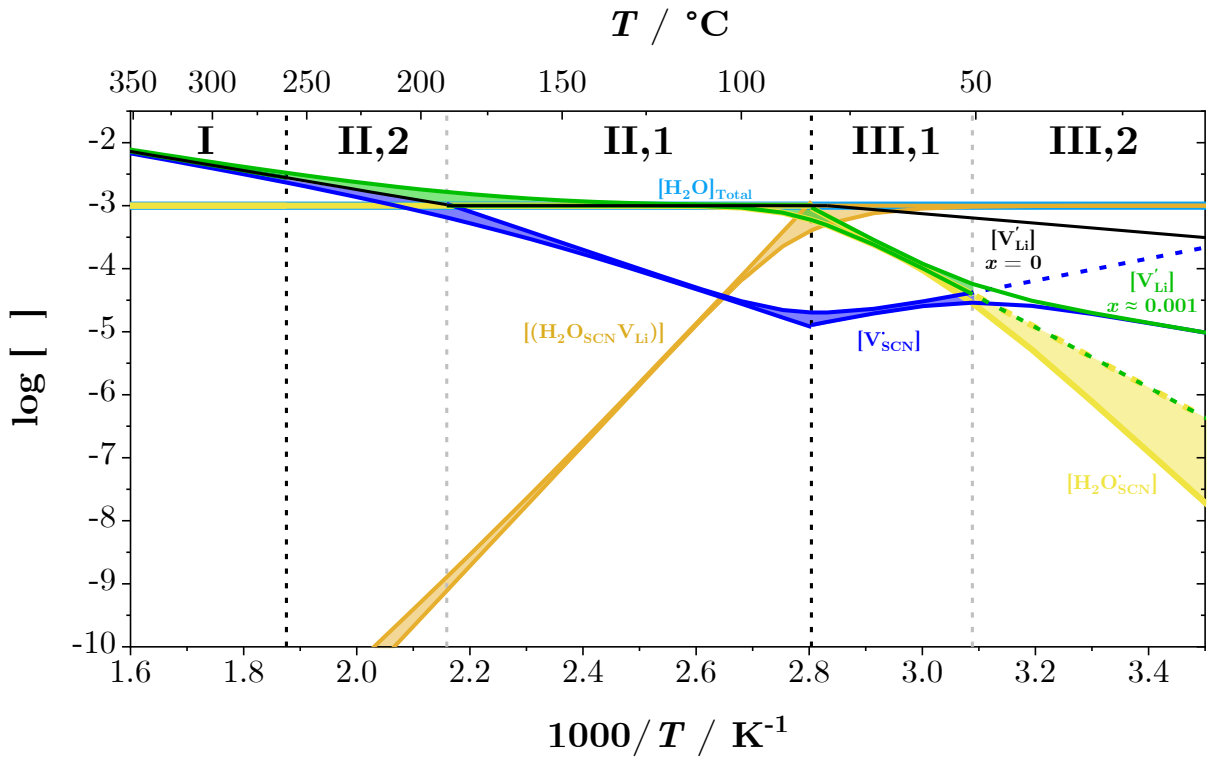
Figure 6.32: Defect model of H_2O-doped LiSCN for $x \approx 0.001$ showing various defect concentrations as a function of inverse temperature. Calculated concentrations of cases 1 and 2 are shown as solid coloured lines, except in regime III,2, where case 1 is shown as dashed lines[23]. The concentrations in H_2O-doped LiSCN are compared to $[V'_{Li}]$ of the anhydrous material. Vertical dashed lines mark the transition temperatures between regimes.

---

[22]Losses in x at elevated temperatures, especially around 100 °C or higher, can easily occur even in a sealed measurement cell due to a small yet finite dead volume. Therefore, the observed scatter in conductivity data is not surprising, and only one sample, which was judged to be eligible, was used for the calculation of the mobilities (cf. linear fit of conductivity data in regime II shown in Figure 6.31b).

[23]The defect concentrations of regimes III and II from case 1 are calculated by inserting equation 6.31 and 6.38 into 6.47, which can be solved analytically yielding: $[V'_{Li}] = -\frac{1}{2\,K_A^{H_2O}} + \sqrt{\frac{1}{4\left(K_A^{H_2O}\right)^2} + \frac{[H_2O_{Total}]}{K_A^{H_2O}}}$.

fitting the conductivity data (cf. Figure 6.31b) and equation 6.48:

$$K_A^{H_2O} = 10^{(-46\pm7)} \exp\left(-\frac{(-1.9 \pm 0.4)\,\text{eV}}{k_B T}\right)\text{cm}^3 \tag{6.49}$$

The calculation with case 2 is more complicated, since the respective Brouwer approximation for $[V_{Li}']$ in regime III (Table 6.7) is more complex, but the final result is identical to the one in equation 6.49. With the equilibrium constants $K_A^{H_2O}$ and K_S at hand, the defect concentrations of all species from Table 6.7 can be calculated and their behaviour with temperature is shown in Figure 6.32 (the dependence on p_{H_2O} is shown later in Figure 6.34). In Figure 6.32, regimes II and III are sectioned to indicate which case is appropriate. Regime II,2 reflects the transition region between extrinsic and intrinsic behaviour, where the electroneutrality condition $[V_{Li}'] = [H_2O_{SCN}^{\cdot}] + [V_{SCN}^{\cdot}]$ applies. In regimes II,1 and III,1 both cases yield almost identical results. However, in regime III,2 case 1 (shown as dashed lines) seemingly overestimates $[V_{SCN}^{\cdot}]$, and case 2 is the correct ansatz. The slopes of $[V_{Li}']$ and $[H_2O_{SCN}^{\cdot}]$ in regime III as well as $[(H_2O_{SCN}V_{Li})]$ in regime II visualize the strong tendency of H_2O to form associates, especially compared to the association in dry LiSCN. An interesting observation is the minimum in $[V_{SCN}^{\cdot}]$ at the transition temperature from association to extrinsic. The calculated concentrations $[V_{Li}']$ for both cases were used together with equations 6.48 and 6.11 to simulate the conductivity data of H_2O-doped LiSCN, and are compared with local (ω_1) and long-range (ω_2) ion conduction in anhydrous LiSCN (Figure 6.33).
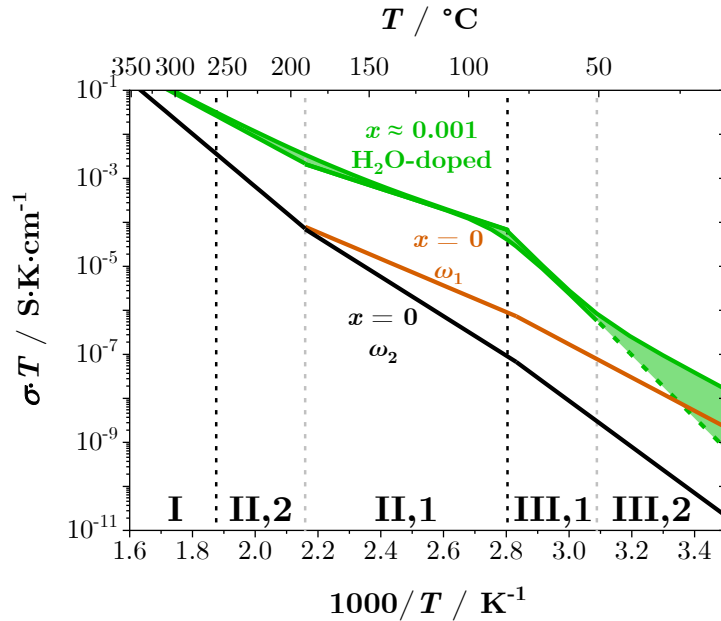
Figure 6.33: Calculated conductivity of H_2O-doped LiSCN for $x \approx 0.001$ using both case 1 and 2 (green solid line, except for case 1 in III,2 as dashed line)[24] compared to the anhydrous material at high (ω_1 solid red line) and low (ω_2 solid black line) frequencies.

The calculated conductivities in dry and H_2O-doped LiSCN nicely reflect the overall observed trends from experimental measurements (cf. Figure 6.30a). In anhydrous LiSCN, lithium vacancies can have two modes of transport, one on a local scale being fast and one on a global scale being slow. The concentration $[V'_{Li}]$ is determined by a native dopant or impurity and changes with temperature. If H_2O is used as dopant, the transport mechanism changes and long-range moving V'_{Li} become as mobile as locally hopping vacancies in dry LiSCN. The association of H_2O with V'_{Li} is much stronger than seen for a bivalent donor dopant, but the overall conductivity is still much higher due to the increase in mobility. The green shaded area in regime III,2 of Figure 6.33 indicates the region between case 1 (dashed line) and case 2 (solid line). Even though case 2 is considered more appropriate in this regime, the experimental data shown in Figure 6.30a suggests a steeper slope than predicted with the model, indicating some ambiguity between case 1 and 2.

To compare the derived model with the data from TGA and EIS (Figure 6.28b and 6.29a), a Kröger-Vink diagram was constructed showing the trends in slopes as a function of p_{H_2O} in log-log representation (Figure 6.34). The concentrations $[H_2O_{Total}]$ and $[V'_{Li}]$ were calculated by deriving the p_{H_2O} dependent mass action constants for all three regimes. In the intrinsic regime, K_I is given with equation 6.33, which can be rearranged by inserting equation 6.37 and equation 6.4:

Regime I Intrinsic:

$$K_I = \frac{K_{II,1}}{K_S} \tag{6.50}$$

The dependence of $[H_2O_{Total}]$ on p_{H_2O} is expressed as $[H_2O_{Total}] = K_I\sqrt{K_S}p_{H_2O}$ (cf. Table 6.7). The stoichiometric factor $x = n(H_2O)/n(LiSCN)$ is obtained from TGA (cf. Figure B.30), and by plotting $[H_2O_{Total}] = x \cdot (4/V_{UC})$ vs. p_{H_2O}, K_I results from the slope (K_S is known from equation 6.15). Since the intrinsic regime starts at $\sim$190 °C, only the TGA measurement at 180 °C is appropriate for this method (Figure B.32a). The TGA measurements at lower temperatures are in the extrinsic regime, in which $[H_2O_{Total}] = \sqrt{K_{II,1}p_{H_2O}}$ applies, and K_I is consequently calculated with equation 6.50. The obtained values of K_I were used to construct a van 't Hoff plot (Figure B.32b) and K_I is expressed as (analogous to equation 6.30):

$$K_I = \exp\left(-20 \pm 1\right)\exp\left(-\frac{(-0.94 \pm 0.05)\,\text{eV}}{k_B T}\right) \tag{6.51}$$

with $\Delta_h S^\circ = (-20 \pm 1)\,k_B$ and $\Delta_h H^\circ = (-0.94 \pm 0.05)$ eV for the hydration entropy and enthalpy. With equations 6.33, 6.37, 6.40, 6.43, and 6.45, the p_{H_2O} dependent equilibrium

---

[24]The conductivity of case 1 is calculated with $[V'_{Li}]$ from the equation in footnote 23.

mass action constants in regimes II and III can be expressed accordingly:

Regime II Extrinsic:

$$K_{\mathrm{II},1} = K_{\mathrm{I}}K_{\mathrm{S}} \qquad\qquad (6.52)$$

$$K_{\mathrm{II},2} = K_{\mathrm{I}}^2 K_{\mathrm{S}} \qquad\qquad (6.53)$$

Regime III Association:

$$K_{\mathrm{III},1} = K_{\mathrm{I}}K_{\mathrm{S}}K_{\mathrm{A}}^{\mathrm{H_2O}} \qquad\qquad (6.54)$$

$$K_{\mathrm{III},2} = K_{\mathrm{I}}^2 K_{\mathrm{S}}K_{\mathrm{A}}^{\mathrm{H_2O}} \qquad\qquad (6.55)$$

With the mass action constants at hand, both $[\mathrm{H_2O_{Total}}]$ and $[\mathrm{V}_{\mathrm{Li}}']$ were calculated as a function of $p_{\mathrm{H_2O}}$ at 60 °C (regime III), 120 °C (regime II) and 260 °C (regime I) (Figure 6.34). The predicted behaviour matches indeed nicely with the experimental results from TGA (Figure 6.28 and B.30) and impedance (Figure 6.29). At high temperatures within or close to the intrinsic regime the slope of $[\mathrm{H_2O_{Total}}]$ is +1, while the conductivity or rather $[\mathrm{V}_{\mathrm{Li}}']$ is (nearly) independent of $p_{\mathrm{H_2O}}$ with a slope of 0. Measurements in the extrinsic regime were possibly affected by kinetic effects, leading to slopes higher than the predicted slope of +1/2. This behaviour in the extrinsic regime is very unexpected, since a $p_{\mathrm{H_2O}}$ dependence of +1/2 is commonly associated with dissociative water incorporation in oxides,[98] and is unprecedented for molecular incorporation mechanisms. As a
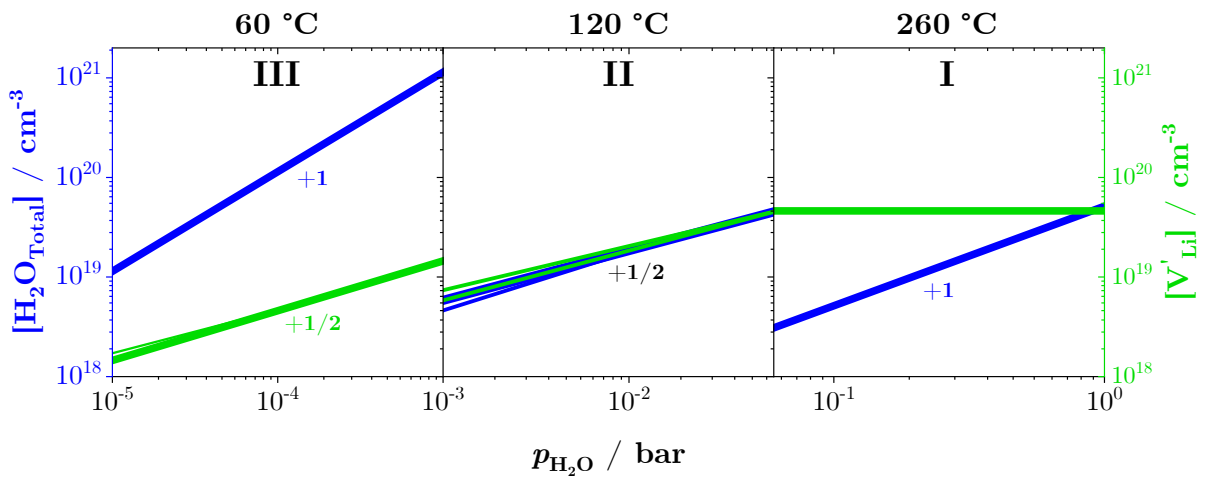
Figure 6.34: Kröger-Vink diagram showing the uptake of $\mathrm{H_2O}$ (blue) and $\mathrm{V}_{\mathrm{Li}}'$ concentration (green) as a function of water activity expressed as $p_{\mathrm{H_2O}}$ for three temperatures (60 °C, 120 °C and 260 °C). In the depicted conditions the differences between case 1 and 2 are negligible, and separate colour assignment was therefore neglected.

final remark, the defect model does not consider interstitial vacancies V_i as possible sites for water. Although the formation of H_2O_i could influence the overall mass balance for $[H_2O_{Total}]$, its impact was judged to be minor, and since it is not a charged species, it is not significant for the ion transport behaviour and was therefore neglected.

Table 6.8 gives an overview of the enthalpies and entropies collected at high frequencies (ω_1) and low frequencies (ω_2) for undoped and M^{2+}-doped LiSCN, as well as for H_2O-doped LiSCN. This summary depicts nicely the manifold conduction mechanisms in the relatively simple compound LiSCN. Not only can the Li^+ ion transport be frequency dependent, the choice of dopant can influence the defect-defect interaction behaviour as well as the mobility of the dominant charge carrier.

Table 6.8: Comparison of thermodynamic and kinetic data of anhydrous LiSCN for local (ω_1) and global (ω_2) V'_{Li} transport with H_2O-doped LiSCN.

	$\Delta_S H°$ / eV	$\Delta_S S°$ / k_B	$\Delta_m H_{V'_{Li}}$ / eV	$\Delta_m S_{V'_{Li}}$ / k_B	$\Delta_A H°$ / eV	$\Delta_A S°$ / k_B	subsection
LiSCN ω_2	0.6 ± 0.3	5 ± 2	0.89 ± 0.08	7.7 ± 0.9	-0.3 ± 0.2 ($Mg_{Li}V_{Li}$)	-8 ± 6 ($Mg_{Li}V_{Li}$)	6.1.1
LiSCN ω_1			0.6 ± 0.1	-0.7 ± 3			6.1.2
LiSCN $\cdot\, 0.001\,H_2O$			0.46 ± 0.01	0.3 ± 0.2	-1.9 ± 0.4 ($H_2O_{SCN}V_{Li}$)	-56 ± 16 ($H_2O_{SCN}V_{Li}$)	6.2.2

6.2.3 $x \geq 0.01$: Hydrated LiSCN

Going beyond the H_2O-doping regime of LiSCN causes structural changes in the material, i.e. a stoichiometric hydration reaction occurs (cf. subsection 6.2.1). Regarding the phase diagram in Figure 6.27, samples for the entire range in y_{H_2O}[25] within two-phase ($0.01 \leq y_{H_2O} < 0.5$, $0.5 < y_{H_2O} < 0.67$, $0.67 < y_{H_2O}$) and one-phase ($y_{H_2O} = 0.5$ and 0.67) regimes were investigated for ion transport properties, and the results will now be presented. Figure 6.35 shows the impedance results of samples with $x \approx 1.0$ to asses the transport properties of the monohydrate as a solid. In accordance with the results from XRPD and DSC measurements (cf. subsection 6.2.1), the α- to β-phase transition was observed by sudden behavioural changes in the impedance signals at ∼48 °C. Only a small difference in ion transport and dielectric behaviour was observed between the α- and β-phase. However, the measurements were very sensitive when $x \approx 1.0$ was exceeded by only a few mol%, as even adsorbed water would increase ion transport (Figure 6.35a, $x \gtrsim 1.0$). All LiSCN $\cdot\, x\,H_2O$ samples with $x \approx 1.0$ showed a temperature independent

---

[25]For reference, $x = (y_{H_2O}^{-1} - 1)^{-1}$.
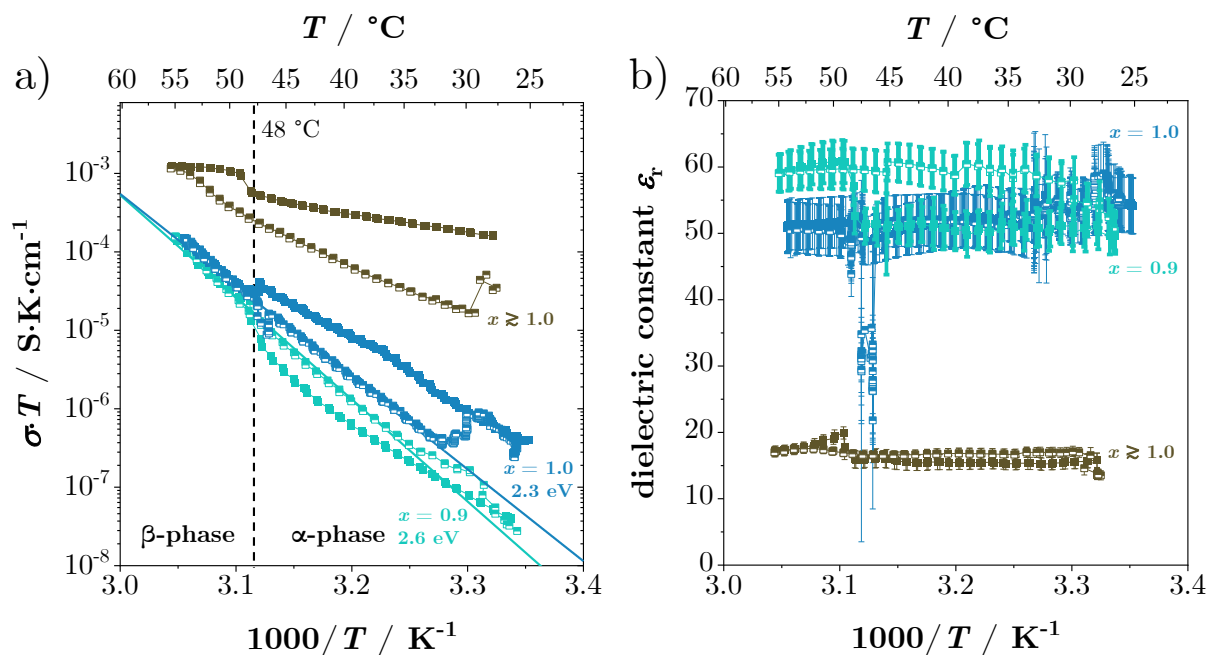
Figure 6.35: a) Measured conductivity and b) dielectric constant ε_r of the monohydrate with $x \approx 1.0$ (heating: full, cooling: half-full symbols)[26]. The dashed vertical line marks the α- to β-phase transition (cf. subsection 6.2.1).

dielectric constant of ∼20-60, a bit higher compared to LiI and H_2O-doped LiSCN (cf. subsections 6.1.2 and 6.2.2), and impedance spectra revealed only one relaxation time (comparable to ω_1 in anhydrous LiSCN, Figure B.33b). The slightly higher ε_r values relate to the stoichiometric quantities of structural water, which increase the permittivity of the system (for comparison, liquid water has a dielectric constant of ∼80 at 20 °C). The calculated activation energies for these samples are comparatively high, exceeding by far the values in anhydrous LiSCN (cf. Figure 6.4a). A possible explanation regarding the ion transport mechanism will be discussed later in detail after reviewing the combined results. An interesting yet ambiguous observation is the behaviour of LiSCN $\cdot$ 1 D_2O (Figure B.33), which shows similar ion transport but much higher polarisation properties. Since the dielectric constants of H_2O and D_2O are quite similar,[172, 173] further investigations would be necessary for a physical explanation, which are not subject of this thesis. The presented results of LiSCN $\cdot$ 1 D_2O will therefore not be further discussed.

Samples within the two-phase regime $0.01 \leq y_{H_2O} < 0.5$, i.e. $0.01 \leq x < 1.0$, have been measured by EIS shown in Figure 6.36 (also cf. Figure B.33 and B.34). The general behaviour is clear; below the melting point of LiSCN $\cdot$ 1 H_2O (∼60 °C), samples behave similar as shown in Figure 6.35. Yet above the melting point, a solid-liquid composite

---

[26]The phase purity of these samples was always checked by XRPD and DSC. Small amounts of the dihydrate were sometimes present in the samples, which were below the XRPD detection limit yet visible with DSC (as discussed in subsection 6.2.1). Trace amounts of the dihydrate or even just adsorbed H_2O could influence the conductivity behaviour strongly. An effective method to obtain reliable results, as shown in Figure 6.35, was to cycle each sample multiple times until the behaviour was stable, and compare the results of each sample.
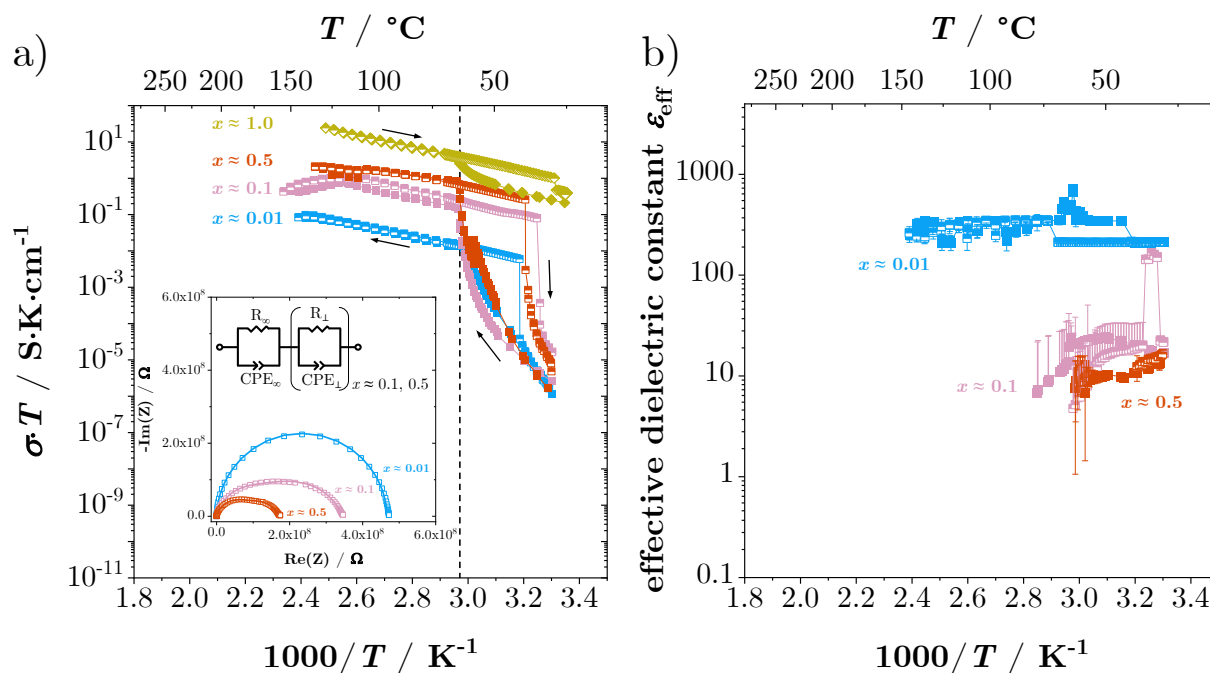
Figure 6.36: Temperature dependent a) conductivity and b) effective dielectric constant ε_{eff} data of various LiSCN $\cdot\, x\, \text{H}_2\text{O}$ samples (heating: full, cooling: half-full symbols). The dashed vertical line at $\sim$65 °C in (a) marks the melting point of the monohydrate, and the inset shows exemplary impedance spectra recorded at 30-31 °C. The impedance data were fit with the shown circuit[28]. All samples were measured with cell 2, except for $x \approx 1.0$, in which the whole sample liquefied and the measurement was conducted with cell 5 (cf. section 5.6).

consisting of solid anhydride and liquid monohydrate forms, in which ion transport is determined by percolating pathways of the liquid.[174–177] The conductivity naturally scales with the volume fraction of the liquid equal to the present amount of the monohydrate, i.e. x [27]. In accordance with DSC (cf. Figure 6.25 and B.23), a supercooling effect is observed until at $\sim$30 °C the liquid recrystallises and the solid-solid composite is reformed. This explanation is supported by PFG NMR[29] measurements (Figure B.36), which showed for all investigated x values in the two-phase regime virtually identical diffusivities of Li^+ and H_2O to liquid monohydrate. This confirms that the mobile component is molten LiSCN $\cdot\, 1\, \text{H}_2\text{O}$ in a solid matrix of anhydrous LiSCN. However, the observation that LiSCN $\cdot\, 0.1\, \text{H}_2\text{O}$ below 60 °C shows almost identical conductivities as LiSCN $\cdot\, x\, \text{H}_2\text{O}$ with $x \approx 1.0$ (Figure B.33) requires additional clarifications, which will be discussed later.

The investigations in LiSCN $\cdot\, x\, \text{H}_2\text{O}$ were continued by going beyond $x \approx 1.0$ into the

---

[27] Variations in the dielectric constant relate most likely to experimental uncertainties from the electrode contacting with the wet-bonding method. Geometric variations due to partial liquefaction of the sample were accounted for by remeasuring the geometry after EIS.

[28] The second R-CPE unit marked with $\perp$ symbols in the circuit corresponds to the contact impedance between the LiSCN $\cdot\, x\, \text{H}_2\text{O}$ ($x \approx 0.1$ or 0.5) sample and stainless steel bolts, which was sometimes observed from the wet-bonding technique for contacting (cf. section 5.6).

[29] Details about this technique are discussed in chapter 7, section 7.2.
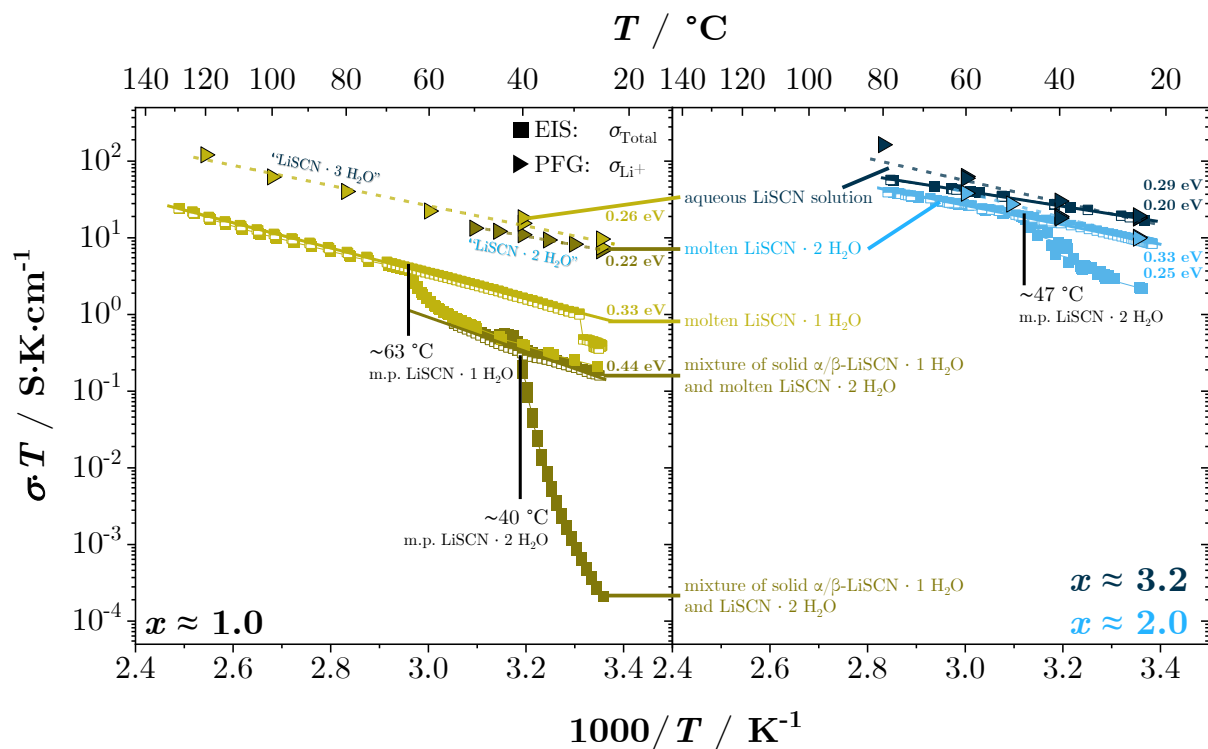
Figure 6.37: Conductivity obtained either by direct measurement (EIS; σ_{Total} as squares) or converted from measured diffusivities (^{7}Li PFG NMR; σ_{Li^+} as triangles) using the Nernst-Einstein relation (equation 6.56; heating: full, cooling: half-full symbols). Samples of LiSCN $\cdot\, x$ H$_2$O include: $x \approx 1.0$ as solid pellet (dark brown, left side), $x \approx 1.0$ solid to liquid transition (light brown, left side), $x \approx 2.0$ as liquid (blue, right side) and $x \approx 3.2$ as liquid (dark blue, right side). Coloured solid lines are linear fits to EIS data, and coloured dashed lines to PFG NMR data.

two-phase regime $0.5 < y_{H_2O} < 0.67$, i.e. $1.0 < x < 2.0$, and were extended to $x \geq 2.0$. The combined results from EIS and PFG NMR are presented in Figure 6.37. Since the explanation to the data is rather complex, the measurements are first discussed qualitatively to understand each process. Starting with the EIS data of $x \approx 1.0$ as solid pellet (dark brown, left side), the conductivity increases with temperature steeply, and reaches a plateau at ∼40 °C, after which the conductivity shows a much shallower slope. Within temperature cycles up to 45 °C this process is reversible, yet after heating to 55 °C the conductivity at the plateau is retained even after cooling to room temperature (Figure B.38 and B.39). The observed behaviour can be attributed to a small contamination of LiSCN $\cdot\,$2H$_2$O present in the sample. The dihydrate starts to melt at ∼38 °C (cf. Figure B.24) and forms percolating liquid pathways which are more conducting than the surrounding solid grains of the monohydrate. Due to supercooling the dihydrate stays liquid even after cooling back to room temperature[30]. This interpretation is supported from thoroughly analysing the DSC curve (Figure 6.25) and XRPD pattern (Figure 6.24),

---

[30]As shown with the cycle to 45 °C in Figure B.38, if the temperature is not sufficiently high, some seed crystals can remain which cause resolidification of the liquid and the conductivity drops.

which showed small traces of the dihydrate in the sample, and was confirmed with PFG NMR measurements. The measured NMR spectrum (Figure B.35) revealed, after applying a prolonged D_1 dwell time, two components in the sample: one major component with slow dynamics, i.e. solid monohydrate, and one minor component with fast dynamics, i.e. molten dihydrate. Virtually identical behaviour was observed in literature for the solid-liquid composite system of $\alpha-Al_2O_3$ and $CaCl_2 \cdot 6\,H_2O$.[174–177] The investigation was then extended by measuring a $x \approx 1.0$ sample beyond its melting point at ~60 °C (light brown, left side), after which molten monohydrate was directly measured. Since $LiSCN \cdot x\,H_2O$ hydrates tend to phase split upon recrystallisation, the resolidified monohydrate contained small traces of the dihydrate (and naturally of dry LiSCN as well), showing the same conductivity as the afore described sample. The transition temperatures matched well with the ones from DSC and XRPD.

The behaviour for $x \approx 2.0$ (blue, right side) was analogous. The sample first consisted of a slurry containing some solid chunks of $LiSCN \cdot 2\,H_2O$, which quickly melted at elevated temperatures and remained liquid after cooling. Samples with $x > 2.0$ have a melting point close to or below room temperature (Figure 6.27), and can therefore be regarded as aqueous electrolyte solutions.

Having clarified the respective sample compositions and mobile components, one can now analyse the transport mechanisms in more detail. The diffusivities measured by ^{7}Li PFG NMR were converted into conductivity data using the Nernst-Einstein equation:

$$\sigma_{Li^+}T = \frac{D^*_{eff}(Li^+) \cdot [Li^+] \cdot e^2}{k_B} \tag{6.56}$$

where $D^*_{eff}(Li^+)$ is the effective tracer diffusion coefficient of Li^+ ions, e is the charge of an electron and k_B is Boltzmann's constant. The concentration $[Li^+]$ was calculated according to:

$$[Li^+] = \frac{\rho_x}{M_x} \cdot N_A \tag{6.57}$$

in which ρ_x and M_x are the density and molar mass for $LiSCN \cdot x\,H_2O$, and N_A is the Avogadro constant (the concentration was multiplied by a factor of 0.9 to account for 10 % porosity). The calculated concentrations therefore consider all Li^+ ions present in the respective sample, which is adequate for liquid systems, but has to be used with caution for solids. As discussed above, the mobile component for the solid $x \approx 1.0$ sample was a small amount of liquid dihydrate, which means $\rho_2 = 1.24$ g/ml (cf. Figure B.43a) and $M_2 = 101.05$ g/mol. In a composite where the components are above the percolation threshold, the total conductivity is an effective term which is defined as:[178]

$$\sigma_{eff} = \Sigma_\alpha \varphi_\alpha \sigma_\alpha \tag{6.58}$$

in which α corresponds to the individual conducting phase, φ_α is the respective volume fraction[31] and σ_α the real conductivity. When comparing the conductivity of LiSCN $\cdot$ $1\,H_2O$ in Figure 6.35 with the data from molten LiSCN $\cdot\,2\,H_2O$ in Figure 6.37, one can see that the monohydrate contribution is negligible and equation 6.58 simplifies to:

$$\sigma_{\text{eff}} \approx \varphi_{x=2}\sigma_{x=2} \tag{6.59}$$

Since the conductivity converted from PFG NMR only relates to the mobile component, it follows that $\sigma_{\text{Li}+}(\text{PFG}) = \sigma_{x=2}$ and $\sigma_{\text{Total}}(\text{EIS}) = \sigma_{\text{eff}}$, yielding a dihydrate volume fraction of 2-3 %, matching with estimates from XRPD and DSC.

For $x \approx 2.0$ and 3.2, the converted values of $\sigma_{\text{Li}+}(\text{PFG})$ match nicely with $\sigma_{\text{Total}}(\text{EIS})$. This suggests a Li^+ transference number close to 1, as expected for highly concentrated liquids due to the difference in cation and anion size. However, in case of molten LiSCN $\cdot\,1\,H_2O$, there is an evident discrepancy between the measured data of EIS and PFG NMR[32]. Since the whole system is liquid and homogeneous, equation 6.57 should apply if all available Li^+ ions are mobile. Therefore, the data suggests that only $\sim1/3$ of all available lithium ions are mobile, meaning only every third Li^+ ion has a hydration shell of 3 H_2O molecules. This conclusion fits to the observations from p_{H_2O} measurements of solid and liquid LiSCN $\cdot\,1\,H_2O$ in subsection 6.2.1, and is actually not surprising considering that the first hydration shell of Li^+ ions in water consists of about 4-5 H_2O molecules.[161, 162]

Figure 6.38 shows ssNMR spectra collected at various temperatures representative of the monohydrate (aquamarine)[33], mono- and dihydrate composite (dark brown)[34] and a sample of LiSCN $\cdot\,1\,D_2O$ for comparison. The overall trend with temperature is similar to the observations from EIS above. All samples show a sudden change in the shape of the NMR signal starting at ~50 °C, indicative of the α- to β-phase transition. The cooling data shows some hysteresis. The sharp signal in LiSCN $\cdot\,0.9\,H_2O$ at 50 °C is surprising, since the conductivity of the β-phase is comparable to the α-phase, which shows a much broader signal. This might reflect higher local Li^+ dynamics in β-LiSCN $\cdot\,1\,H_2O$, which would fit to the increased disorder seen in the crystal structure, but the DC conductivity is still comparatively low. The signal difference between $x \approx 0.9$ and ~1.0 again reflects the severe impact even nominal trace amounts of LiSCN $\cdot\,2\,H_2O$ have on the overall system response. The rather peculiar line shape of the central transition observed for these

---

[31]In this system, the volume fraction φ_α is equivalent to the mole fraction y_α, since $\varphi = \frac{V_1}{V_1+V_2} = \frac{n_1/c}{n_1/c+n_2/c}$ and $c = \frac{n_{\text{LiSCN}}}{V_{\text{Total}}} = \frac{n_{H_2O}}{x \cdot V_{\text{Total}}}$.

[32]The density of molten monohydrate is unknown, but it is expected to be similar to the dihydrate, i.e. $\rho_1 \approx 1.24$ g/ml.

[33]Since the dihydrate is easy to form at $x \approx 1.0$, x was chosen slightly below the phase boundary to ensure that no traces of LiSCN $\cdot\,2\,H_2O$ are present in the sample.

[34]The spectra in Figure 6.38 look different from the spectrum in Figure B.35 since the respectively used measurement conditions varied and a different spectrometer was employed.
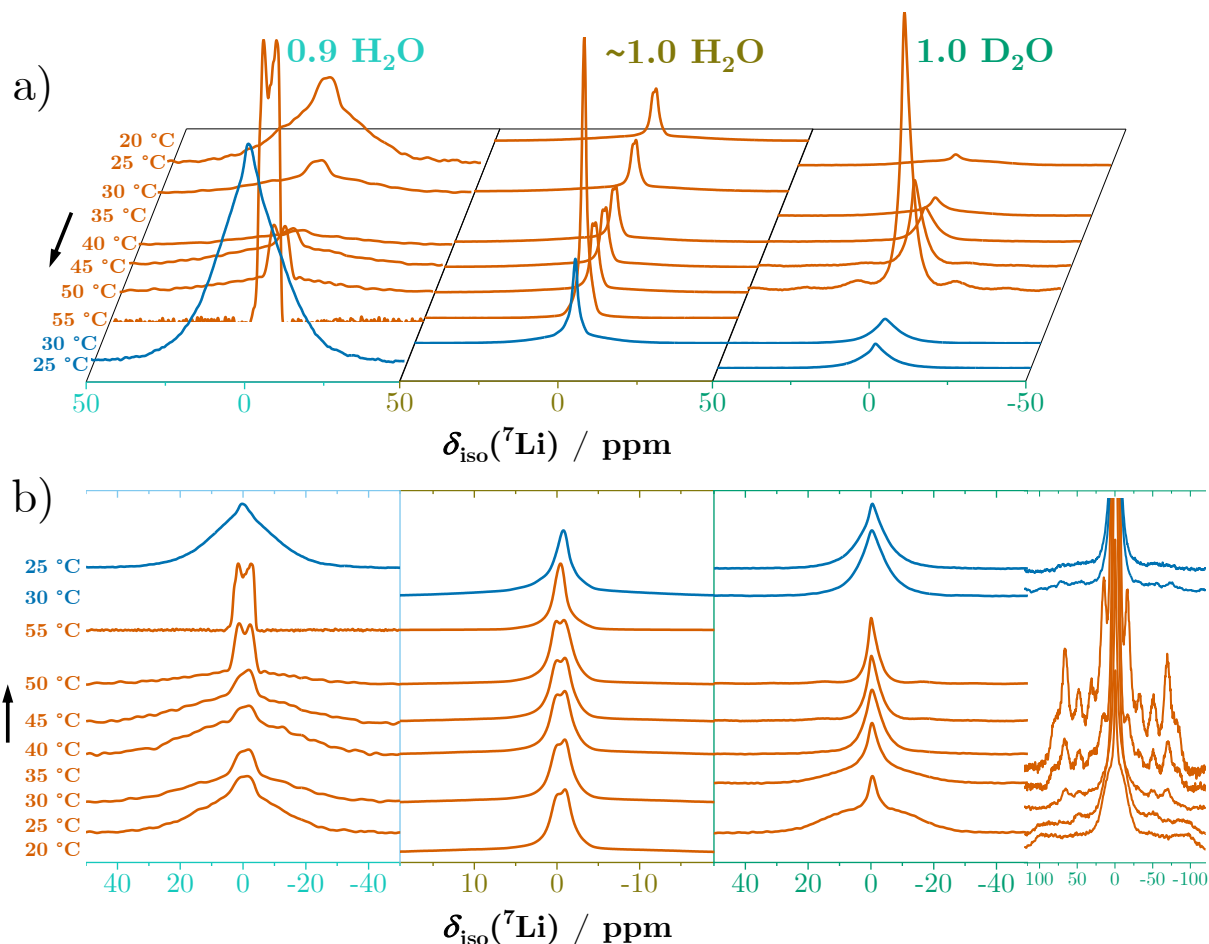
Figure 6.38: ^{7}Li ssNMR spectra of two LiSCN $\cdot x$ H$_2$O samples as well as LiSCN $\cdot 1.0$ D$_2$O (same colour coding as in Figure 6.35 and 6.37) measured at various temperatures, showing a) relative intensities and b) signal shapes. Red spectra indicate heating, blue spectra cooling.

two samples is most likely due to indirect spin-spin coupling of ^{7}Li and ^{14}N, mediated by molecular H$_2$O. For example, ssNMR spectra of hydrated LiBH$_4$ show a very similar behaviour with temperature, but the central transition does not show any sign of spin-spin coupling.[75] Since the magnetic moment of D$_2$O is weaker than H$_2$O, the coupling is not observed for LiSCN $\cdot 1$ D$_2$O. The satellite signals for the H$_2$O-containing samples are as expected for the ^{7}Li nucleus ($I = 3/2$), but are evidently more complex in case of D$_2$O. However, further analysis of the NMR data is rather complicated given the complexity of the respective signals, and will therefore not be further discussed here.

Figure 6.39 summarizes the collected impedance data of samples with $0 \leq x \lesssim 2.0$. This plot nicely emphasizes the anomaly that is seen for the two-phase regime and pure monohydrate $0.1 \lesssim x \lesssim 1.0$, i.e. an unusually high activation energy even exceeding that of dry LiSCN. Considering the crystal structure and hydration properties of the monohydrate discussed in subsection 6.2.1, this material represents a misfit compared to the other LiSCN $\cdot x$ H$_2$O phases.
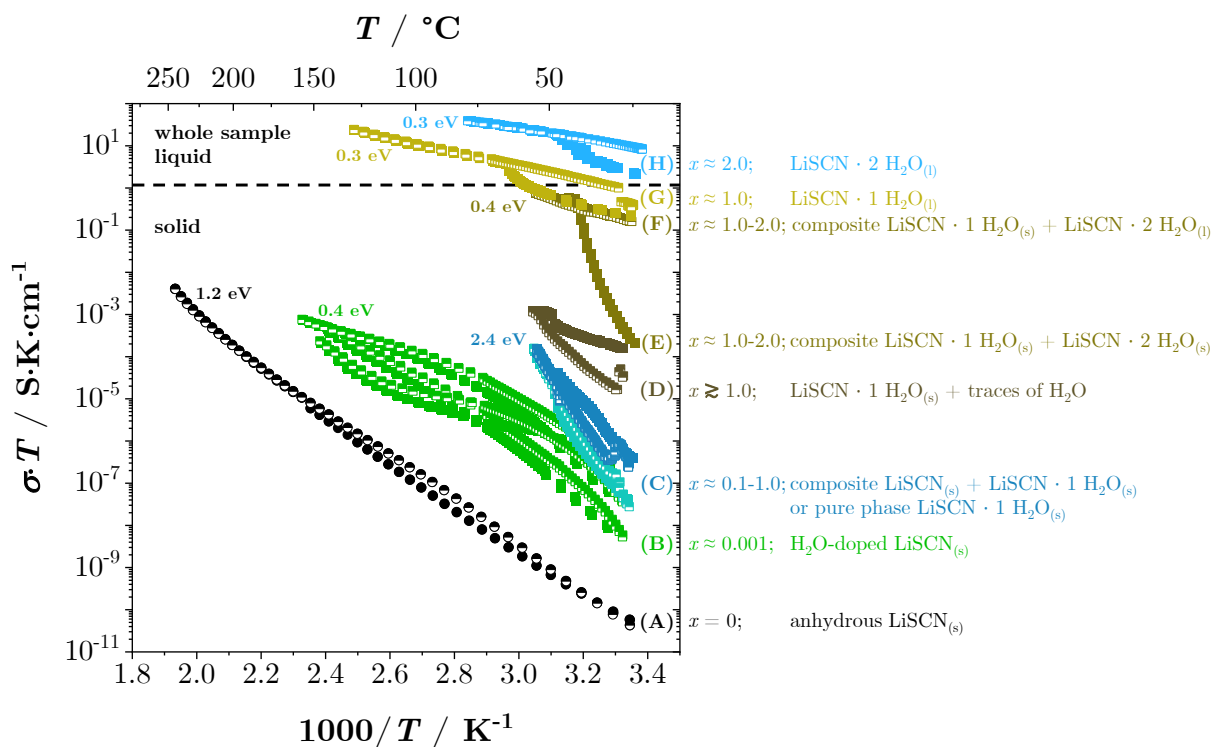
Figure 6.39: Summary of the collected impedance data on LiSCN $\cdot\, x\, H_2O$ as a function of temperature (heating: full, cooling: half-full symbols).

There are still two open questions about the ion transport mechanisms in Figure 6.39: (i) Why samples within $0.1 \lesssim x \lesssim 1.0$ (C) have virtually the same conductivities, and (ii) the reason for the higher conductivity in the composite LiSCN $\cdot\, 1\, H_2O_{(s)}$ + LiSCN $\cdot\, 2\, H_2O_{(s)}$ (E). Regarding (i), one has to realize that these phase mixtures actually consist of H_2O-doped dry LiSCN (B) and the monohydrate. As the conductivity is independent of the volume fractions of both components, explanations considering different bulk conductivities or a dominating space-charge zone can be excluded.[178, 179]. By comparing the low temperature conductivities of (B) with the data of (C) in Figure 6.39, a possible explanation for the high activation energy in (C) is that ion transport is inhibited by the formation of associates $(H_2O_{SCN}V_{Li})$ in the monohydrate phase[35]. Since the total concentration of H_2O, and consequently $[H_2O_{SCN}^{\cdot}]$[36], is orders of magnitude higher compared to H_2O-doped LiSCN, the association regime is extended and the generation of free carriers requires the breaking of $(H_2O_{SCN}V_{Li})$ associates up to the melting point. Structural water $H_2O_{H_2O}^{x}$ most likely also has an association effect, and the conductivity is therefore effectively independent of the volume fractions. If the temperature range for the solid

---

[35]Assuming that $V_{Li}^{'}$ are still the dominant mobile charge carrier species in hydrated LiSCN $\cdot\, x\, H_2O$.

[36]Every thiocyanate vacancy can potentially be occupied by H_2O, and the electroneutrality condition reads $[V_{Li}^{'}] = [H_2O_{SCN}^{\cdot}]$. This corresponds to case 1 used for H_2O-doped LiSCN in subsection 6.2.2 .

monohydrate is considered as intrinsic[37], it follows (cf. Table 6.7):

$$[V'_{Li}] = \sqrt{K_S^{H_2O}} = \sqrt{\frac{[(H_2O_{SCN}V_{Li})]}{K_A^{H_2O}}} \tag{6.60}$$

with $K_S^{H_2O}$ being the equilibrium mass action constant for the formation of a Schottky pair in the monohydrate LiSCN $\cdot$ 1 H$_2$O.

Regarding the situation for (E) in Figure 6.39, the estimated volume fraction of 2-3 % for LiSCN $\cdot$ 2 H$_2$O is too low for a bulk dominated process, which makes an interfacial ion transport mechanism more likely. The Li$^+$ coordination polyhedra of the mono- and di-hydrate (Figure 6.23) show that the coordination with SCN$^-$ and H$_2$O is consistently via the N-atom [Li-NCS] and via the O-atom [Li-OH$_2$], while S- and H-atoms are terminal. Both the SCN$^-$ anion and H$_2$O molecule have an asymmetric charge distribution in their structure, with the positive charge polarisation being on the sulphur atom in SCN$^-$,[106] and on the hydrogen atoms in H$_2$O. Since these atoms are terminal, they are expected to point towards the grain-boundary core and constitute a local positive charge. The consequently positively charged space-charge zone accumulates negatively charged defects such as V$'_{Li}$. Therefore, it is proposed that ion transport in the composite LiSCN $\cdot$ 1 H$_2$O$_{(s)}$
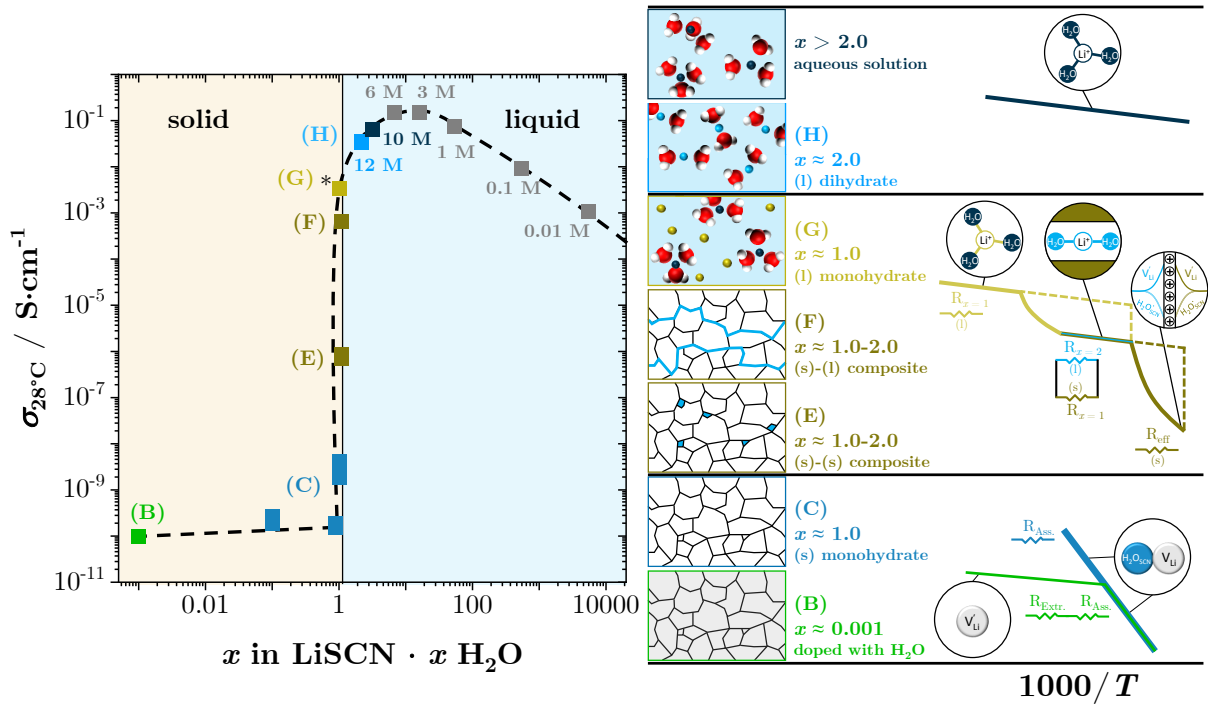
Figure 6.40: Measured conductivity at 27-28 °C (the data point with an asterisk was extrapolated) as a function of x. The right hand side shows a representative depiction of the sample morphology as well as the temperature dependences (more details are given in the text).

---

[37] The α- to β-phase transition can be ignored here, since their transport properties are almost identical.

$+ \text{LiSCN} \cdot 2\,\text{H}_2\text{O}_{(s)}$ is dominated by an accumulation of free V'_{Li} in the grain-boundary space-charge zone[38].

Figure 6.40 summarizes the described mechanisms with depictions of the individual sample morphologies on the right hand side (cf. also Figure 6.39). Starting from the extremely low conducting anhydrous material (A: $x = 0$), when the system is doped with H_2O (B: $x \approx 0.001$), both the mobility and concentration of mobile charge carriers increase, but the conductivity is still comparably low. The low temperature behaviour is dominated by associates (association regime), which decouple to free carriers with increasing temperature (extrinsic regime). When the hydration degree is increased to stoichiometric amounts (C: $x \approx 0.1 - 1.0$), the conductivity stays rather constant as nearly all charge carriers are trapped from the association with water. Small traces of additional H_2O increase the conductivity (D: $x \gtrsim 1.0$), until a composite of the mono- and dihydrate forms (E: $x \approx 1.0 - 2.0$). Upon heating the dihydrate melts first while the monohydrate remains solid, and the conductivity increases strongly (F: $x \approx 1.0 - 2.0$). After reaching the percolation threshold, the material's ion transport is determined by the liquid phase in the intergranular network. This highly conducting solid-liquid composite is also obtained from resolidification of molten monohydrate (G: $x \approx 1.0$), in which only $1/3$ of Li^+ ions are mobile with a hydration shell. Further hydration leads to the pure dihydrate, which is (typically) liquid at room temperature (H: $x \approx 2.0$). Further increases in x produce aqueous electrolyte solutions. The conductivity increases to a maximum at $\sim$6 mol/L. For higher water contents the dilution effect decreases the absolute conductivity, and below
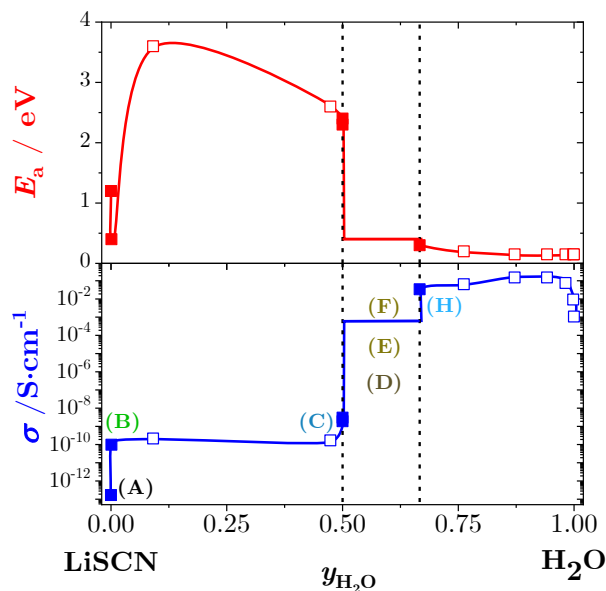
Figure 6.41: Phase diagram of the $\text{LiSCN} - \text{H}_2\text{O}$ system (cf. Figure 6.27) showing room temperature conductivities and activation energies for one- (full squares) and two- (empty squares) phase regimes.

---

[38]This hypothesis implies that association in the dihydrate is much weaker than in the monohydrate.

~1 mol/L the specific conductivity is approximately constant (approaching ideally dilute behaviour).

In analogy to the phase diagram in Figure 6.27, Figure 6.41 gives an overview of the long-range conductivities and activation energies E_a[39] for the system LiSCN − H_2O. The general trend is as expected, the conductivity increases with decreasing E_a. However, as discussed above, both two-phase regimes $0.01 \leq y_{H_2O} < 0.5$ and $0.5 < y_{H_2O} < 0.67$ possess specific ion transport features, which either prevent (association) or promote (space-charge zone and liquid pathways) fast ion transport.

Finally, the collected results of LiSCN $\cdot x\,H_2O$ are compared to selected other hydrated ion conductors (Figure 6.42). The previously reported transport data of the dihydrate[43] match nicely with the one from this work. Overall, most reported hydrates are distinguishable by a rather flat activation energy, which is not surprising given that water is well-known for its Coulombic shielding properties which naturally lowers the migration enthalpy. In an ideal case, this shielding effect is realized with a complete hydration shell and is usually observed in layered materials.[77, 80, 180] This implies a transport mechanism of the ion together with its hydration shell, which requires a sufficiently open and flexi-
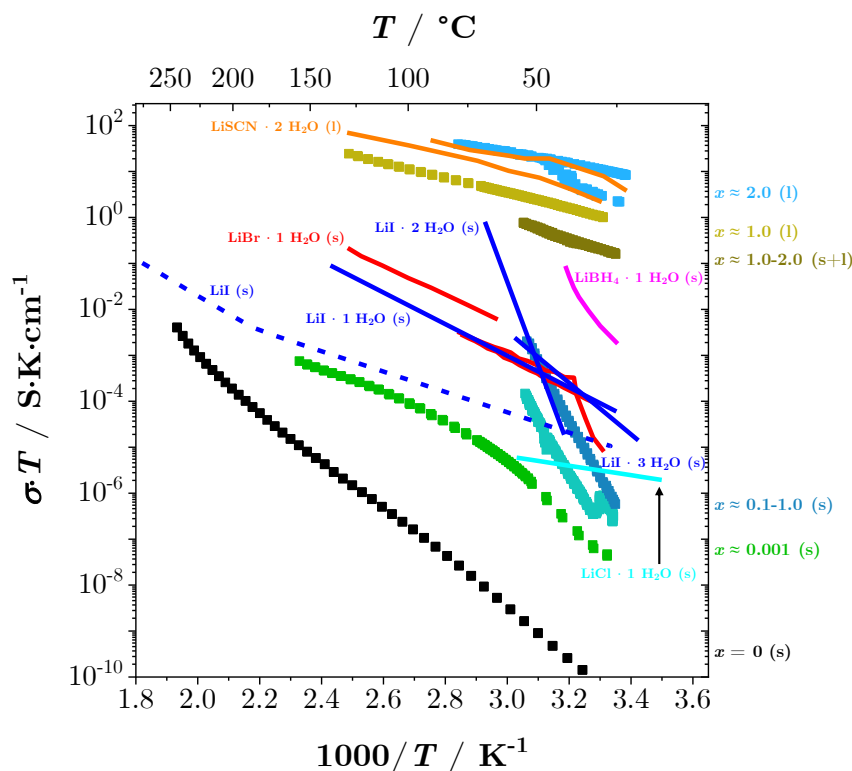
Figure 6.42: Comparison of LiSCN $\cdot x\,H_2O$ $(x = 0 − 2.0)$ conductivities from this work (cf. Figure 6.39 for colour assignment) with selected hydrated ion conductors from literature; LiSCN $\cdot 2\,H_2O$,[43] LiI $\cdot z\,H_2O$ $(z = 0, 1, 2, 3)$,[73, 74] LiBr $\cdot 1\,H_2O$,[69, 70] LiCl $\cdot 1\,H_2O$,[69] and LiBH$_4$ $\cdot 1\,H_2O$.[75]

---

[39]Activation energies for $x \gtrsim 2.0$ were collected from the data shown in Figure B.43b.

ble lattice (liquid-like ion transport between layers). However, immobile structural water units, which are more common in hydrated materials, can also have a (partial) Coulombic shielding effect, although less effective. It is therefore even more astonishing to see that $LiSCN \cdot 1\,H_2O$ as well as $LiI \cdot 2\,H_2O$ have a much higher activation energy, very untypical compared to most hydrates. The discovery of similar activation energies for both these compounds is even more intriguing, considering that they had already been compared on their crystal structures and phase formation thermodynamics in subsection 6.2.1. This suggests broader connections between crystal structure, hydration behaviour and ion transport mechanism for hydrated materials. If a structural compromise is present in a material, hydration might have an adverse effect on ion transport by forming strongly bonded associates with the dominant mobile charge carrier.

7 | Lithium Tin Sulphide Li₂Sn₂S₅

The content of the first 3 sections is published in Joos et al. ref. [180]. The compound $Li_2Sn_2S_5$ is a layered material consisting of partially Li-substituted tin sulphide sheets (25 % of Li^+ ions, termed $Li^+_\perp$) and Li-ions in the interlayer galleries between the sheets (75 % of Li^+ ions, termed $Li^+_\parallel$).[52, 53] Following up on work of anhydrous[53] and exfoliated $Li_2Sn_2S_5$,[52, 56, 181] here the structure and transport properties of the hydrated material $Li_2Sn_2S_5 \cdot x\,H_2O$ are investigated. Upon exposure to humidity water intercalates between the layers and increases the interlayer distance, while keeping the layered arrangement intact. The water content in $Li_2Sn_2S_5 \cdot x\,H_2O$ can be reversibly varied from $x = 0$ to 10 by adjusting the humidity. The material $Li_2Sn_2S_5 \cdot x\,H_2O$ thus bridges the gap between a hydrated solid electrolyte and a confined liquid electrolyte, which is scientifically interesting and potentially useful in battery applications.

Here, the hydration process, Li^+ and H^+ diffusion, and conductivity of differently hydrated samples are investigated in detail, and the potential application as electrolyte material is explored.

7.1 Hydration Mechanism

The hydration of $Li_2Sn_2S_5$ was analysed by conducting a series of hydration experiments (either by TGA or with p_{H_2O} over salt solutions) to resolve the mechanism of water uptake and monitor possible phase transitions. Figure 7.1a shows an exemplary TGA measurement at 39 °C in which the average uptake of water x (i.e. x in $Li_2Sn_2S_5 \cdot x\,H_2O$) was recorded. After an increase of p_{H_2O} water uptake occurred spontaneously, and typically stabilized on a time scale of hours (cf. Figure B.44-B.47a). At short hydration times, the mass change during hydration was proportional to time (Figure B.47b). However, it is unclear if the hydration behaviour is bulk diffusion- or surface-limited, since the incorporation of water further accelerates the hydration as will be shown later. Under the assumption of surface-limited kinetics, the surface exchange constant $\bar{k}$ can be estimated from $\bar{k} = 0.5 \cdot (L_{1/2}/t_{1/2})$, where $L_{1/2}$ is the particle radius ($\sim$25 μm, cf. Figure B.57) and $t_{1/2}$ is the time at which the uptake is half finished.[98] From the data in Figure 7.1a,
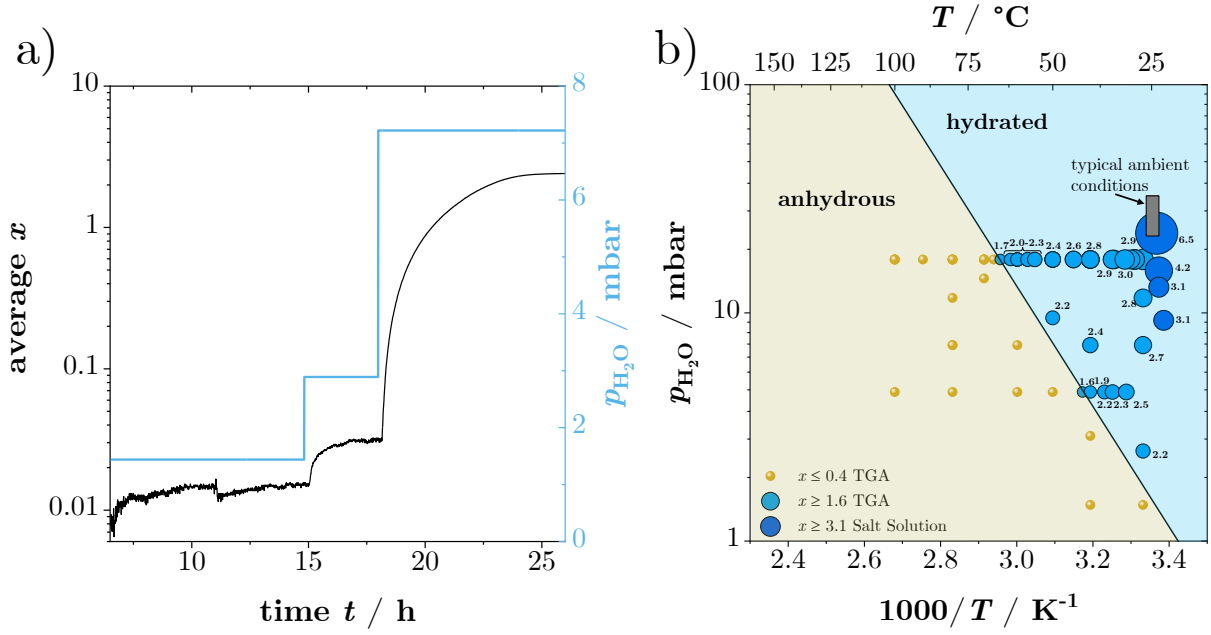
Figure 7.1: Degree of hydration x in Li$_2$Sn$_2$S$_5$ $\cdot x$ H$_2$O; a) Isothermal TGA measurement (39 °C) at various partial pressures of water p_{H_2O}. b) Collected data of hydration experiments, showing the dependence of x on p_{H_2O} and temperature, from isothermal and isobaric TGA measurements (brown and light blue circles) and weighing of hydrated material using p_{H_2O} over salt solutions (dark blue circles). The black line shows the estimated phase boundary.

$\overline{k}$ is estimated to be 1.3×10^{-7} cm/s at 39 °C. However, overall it is more likely that the hydration mechanism is bulk diffusion-limited, especially considering the long equilibration times. The results from hydration experiments are summarized in Figure 7.1b. Repetition measurements at similar or even identical conditions showed that x could vary quite substantially, which indicates a rather pronounced phase width for Li$_2$Sn$_2$S$_5$ $\cdot x$ H$_2$O hydrates. Between the anhydrous phase ($x \leqslant 0.4$) and the first hydrated phase ($x \geq 1.6$) no gradual water uptake was observed (i.e. miscibility gap), which suggests a first-order phase transition. The black line in Figure 7.1b indicates the phase boundary for this phase transition. When all observed x values near the phase boundary are considered, the formed hydrate phase is Li$_2$Sn$_2$S$_5$ $\cdot x$ H$_2$O with $x \approx 2$. One can therefore formulate the mass action law for the phase transition[40]:

$$K_{h} = \left(\frac{p_{H_2O}}{1 \, \text{bar}} \right)^{-x} = \exp \left(-\frac{(\Delta_{h}H° - T\Delta_{h}S°)}{k_{B}T} \right) \tag{7.1}$$

In equation 7.1 K_{h} is the hydration equilibrium constant, $\Delta_{h}H°$ and $\Delta_{h}S°$ are the standard enthalpy and entropy of hydration, and k_{B} and T are the Boltzmann con-

---

[40]Equivalent to equation 6.30 in subsection 6.2.1 for LiSCN $\cdot x$ H$_2$O, only that here p_{H_2O} corresponds to the hydration reaction to form the hydrate Li$_2$Sn$_2$S$_5$ $\cdot 2$ H$_2$O, and stoichiometric changes in x occur. $\Delta_{h}H°$ and $\Delta_{h}S°$ in Table 6.6 refer to the dehydration process, and are therefore the negative equivalents to the hydration data shown here.

stant and temperature. The slope and intercept of the black line in Figure 7.1b yields $\Delta_h H° = (-0.52 \pm 0.03)$ eV and $\Delta_h S° = (-14 \pm 1) k_B$ per mole of water. For all measurements the hydration was observed to be much faster than dehydration, and the removal of H$_2$O usually occurred at temperatures 20-30 °C higher compared to the uptake. This asymmetry between hydration and dehydration resulted in a pronounced but reproducible hysteresis shown in Figure B.44-B.46. Hydrolysis of Li$_2$Sn$_2$S$_5$ was ruled out since uptake and removal of H$_2$O were found to be reversible confirmed by XRPD and by its electron micrograph images. Figure B.57 shows that the particle morphologies barely change by hydrating or dehydrating the material, except for some lamellar cracking. The formation of cracks is linked to the degree of hydration (higher x results in more cracking, Figure B.58), culminating in complete exfoliation when immersed in liquid water (Figure 3 in ref. [52]). After exfoliation some degree of hydrolysis is observed, yet the SnS$_2$-layers remain largely intact, which is expected given that SnS$_2$ itself is unaffected by H$_2$O.[61, 182] In general, lithium tin sulphides have been shown to be rather resilient against hydrolysis[54, 55, 183–186] and can also form stable hydrates.[187] Nonetheless, a faint smell of H$_2$S was indeed noticeable when exposing Li$_2$Sn$_2$S$_5$ to humid atmosphere. Given the high sensitivity of the human nose to H$_2$S (ppb range),[188] any occurring hydrolysis is judged to be minor. Oxidation in dry atmosphere could also be ruled out based on a TGA measurement under dry O$_2$ flow.

The TGA investigations to study the hydration mechanism were corroborated by XRPD shown in Figure 7.2. The pattern obtained for $x = 0$ (green) is virtually identical to the published data,[53] although small differences due to stacking faults[189, 190] or dislocations (twinning, mosaicism, Figure B.57) were generally observed. Upon increasing x to 1.0 a new reflection appears at 4.9°(orange) while the reflection at 6.5°for $x = 0$ starts to disappear. Between $x = 1.9$ and 3.4 only the reflection at 4.9° is present, until at $x = 5.9$ a new reflection occurs at 3.7°(red). These low 2θ reflections corresponding to the lattice plane (001) are indicative of the interlayer distances which were calculated using Bragg's law. They increase from 6.24 Å for $x = 0$ to 11.0 Å for $x = 10.5$ (Figure 7.2b). The appearance of new reflections indicates first-order phase transitions to different hydrate phases. The first hydrate corresponds to $x = 1.9$-3.4 and the second to $x = 10.5$, which is termed 'swollen' phase. Since between $x = 1.9$-3.4 no additional reflections were observed, the increase from 1.9 to 3.4 does not cause structural changes but rather suggests a reorientation of H$_2$O molecules to accommodate higher packing densities. The simultaneous presence of two low 2θ reflections represent two-phase regimes for x. Compared to the anhydrous material at $x = 0$, the distance between the (Li,Sn)S$_2$-sheets increases by 2.0 Å for the first hydrate and another 2.6 Å for the swollen phase. The latter is rather close to the size of a water molecule.[191] An interesting difference between these hydrates is their mechanical properties. The anhydrous ($x = 0$) and hydrated ($x = 1.9$-3.4) phase remained hard, ceramic powders (Figure B.57). Starting already at $x = 4.0$, the material
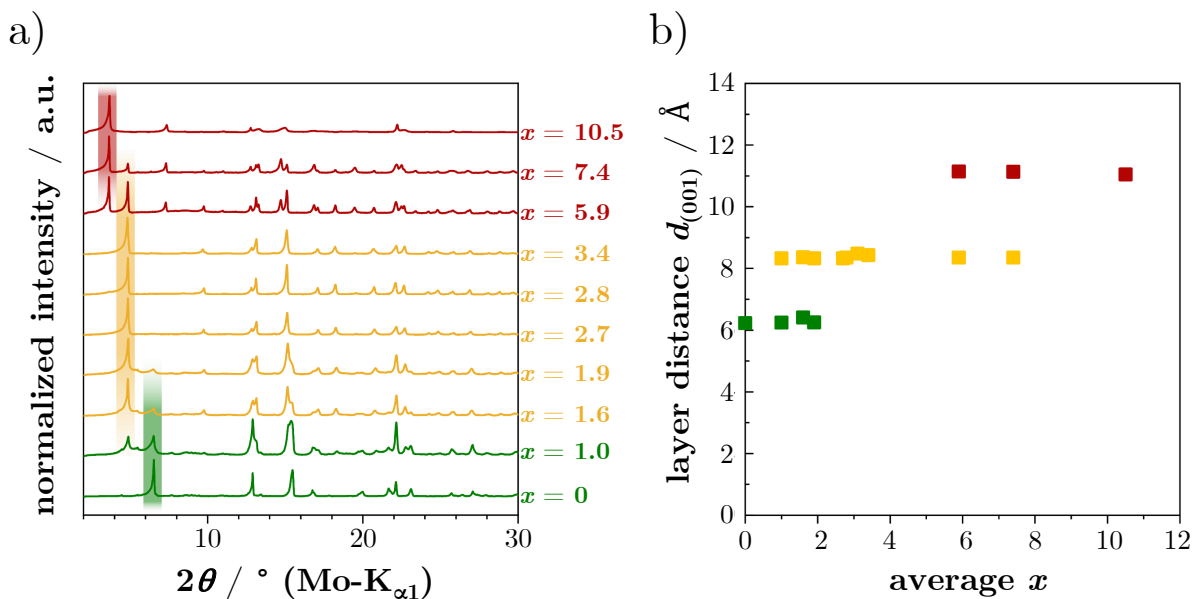
Figure 7.2: a) XRPD patterns for $Li_2Sn_2S_5 \cdot x\,H_2O$ with increasing x. b) Estimated layer distances using Bragg's law corresponding to the (001) reflections in (a).

became noticeably softer and stickier, which intensified for the fully hydrated material, i.e. the swollen phase ($x = 8.0$-10.5, cf. Figure B.58), for which water could even be squeezed out. At $x > 10$ the powder could no longer contain the hydration water which resulted in a solid-liquid mixture.

7.2 Li^+ and H^+ Diffusion

The results from the hydration mechanism investigation as well as the previous exfoliation study[52] suggest that water molecules are primarily accommodated in the interlayer galleries and coordinate with $Li_\parallel^+$. As long as the degree of hydration is $x \lesssim 10$, the layered arrangement is kept intact. The anisotropy of the crystal structure suggests that in-plane diffusion (only $Li_\parallel^+$) is faster than out-of-plane diffusion (both $Li_\parallel^+$ and $Li_\perp^+$), which was predicted by electron density calculations.[53] A good technique to probe the dimensionality of ion transport is PFG NMR, in which the shape of the normalized echo signal attenuation is related to the anisotropy of diffusion in solids.[96] Isotropic and unconfined 3D diffusion (typically in liquids or highly disordered solids) is described by the Stejskal and Tanner equation:[96]

$$M(G) = M(0) \cdot \exp\left(-\gamma_i^2 G^2 D_{iso}^*(i)\delta^2 \left(\Delta - \frac{\delta}{3}\right)\right) \tag{7.2}$$

where $M(G)$ and $M(0)$ are the area of the Fourier transformed attenuating spin-echo signal of the measured and maximum value, γ_i is the gyromagnetic ratio of nucleus i, G and δ are the gradient strength and length of the magnetic field pulse, Δ is the diffusion time

and $D^*_{iso}(i)$ is the isotropic tracer diffusion coefficient of species i. In contrast, anisotropic 2D diffusion is described by accounting for in-plane ($D^*_{xy}(i)$) and out-of-plane ($D^*_z(i)$) diffusion as well as integrating over all possible orientations, which results in the following expressions:[97]

$$M(G) = M(0) \cdot \exp\left(-\gamma_i^2 D^*_{xy}(i) I(G)\right) \int_0^1 \exp(\xi\chi^2)\,\mathrm{d}\chi \tag{7.3}$$

$$I(G) = G^2\delta^2 \left(\Delta - \frac{\delta}{3}\right) \tag{7.4}$$

$$\xi = (D^*_{xy}(i) - D^*_z(i))\gamma_i^2 \cdot I(G) \tag{7.5}$$

$$D^*_{eff}(i) = \frac{2}{3}D^*_{xy}(i) + \frac{1}{3}D^*_z(i) \tag{7.6}$$

in which χ is an integration variable and $D^*_{eff}(i)$ is the overall effective diffusivity. In equation 7.4 $I(G)$ is the so-called double integral, which describes the pulse shape. In this work a rectangular pulse shape is used to approximate the real shape, which yielded satisfactory results with negligible error. If the ion transport in the sample occurs predominantly in-plane, $D^*_z(i)$ is set to zero, as done for $Li_2Sn_2S_5 \cdot x\,H_2O$. Figure 7.3 shows the normalized echo signal attenuation for three different x, which were all fitted by equation 7.3. The 2D diffusion model used here to fit the PFG data yielded satisfactory fits for all $Li_2Sn_2S_5 \cdot x\,H_2O$ hydrates, and acceptable goodness of fits (Figure B.49). For comparison, other models were also attempted and compared (cf. Figure B.50):

- isotropic (3D) diffusion according to equation 7.2, yielded visually unsatisfactory fits and worse goodness of fits.

- anisotropic (2D) diffusion with $D^*_z(i) \neq 0$: the fits were similar in quality as for setting $D^*_z(i) = 0$, with a slight improvement given that an extra fitting parameter was added. However, values of $D^*_z(i)$ were typically close to or below zero, confirming that out-of-plane diffusivity in $Li_2Sn_2S_5 \cdot x\,H_2O$ is negligible (at least one order of magnitude smaller than $D^*_{xy}(i)$). Considering the physical meaning of the model, $D^*_z(i)$ could be reasonably set to zero.
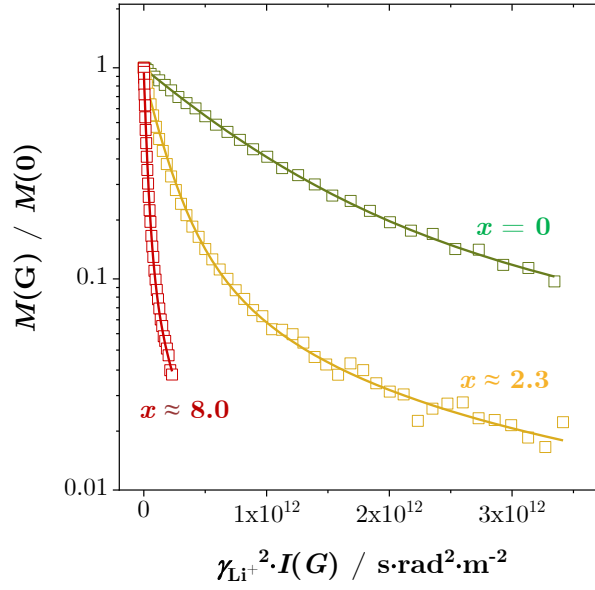
Figure 7.3: ^{7}Li PFG NMR normalized attenuated echo signal versus the squared gyromagnetic ratio times the double integral $I(G)$ of different Li$_2$Sn$_2$S$_5$ $\cdot$ x H$_2$O samples collected at 180 °C (green), 140 °C (orange) and 60 °C (red). Points are raw data, lines are fits by the 2D model.

- isotropic (3D) diffusion with two mobile species (i and j):

$$
\begin{aligned}
M(G) = M(0)_\mathrm{i} \cdot \exp\left(-\gamma_\mathrm{i}^2 G^2 D_\mathrm{iso}^*(\mathrm{i})\delta^2\left(\Delta - \frac{\delta}{3}\right)\right) \\
+ M(0)_\mathrm{j} \cdot \exp\left(-\gamma_\mathrm{j}^2 G^2 D_\mathrm{iso}^*(\mathrm{j})\delta^2\left(\Delta - \frac{\delta}{3}\right)\right)
\end{aligned}
\tag{7.7}
$$

This model was also able to describe the normalized echo signal satisfactorily, yet lacked physical meaning, considering that only one carrier is expected to be mobile, and the model was consequently discarded.

The non-linear fitting was performed with Matlab (*Mathworks*, Version R2017a) using the built-in *nlinfit*-function. It should be noted that bending of the normalized echo signal attenuation can in principle also be caused by geometric confinement (grain-boundaries, dislocations, ...), typically encountered in nanomaterials.[96] Measurements at different diffusion times Δ can indicate the impact from geometric confinement, since longer Δ values would cause lower diffusivities. Figure B.48 shows PFG NMR measurements for different Li$_2$Sn$_2$S$_5$ $\cdot x$ H$_2$O hydrates as a function of Δ. The impact is minor (factor of 1.5-3 between 10 and 100 ms, also at different temperatures, Figure B.48b). Given the layered crystal structure and high quality fits of the 2D diffusion model, geometric confinement effects were judged to be negligible. To be precise, the 'true' in-plane diffusivity without any geometric constrictions is probably higher than what is observed here, and the 'true'
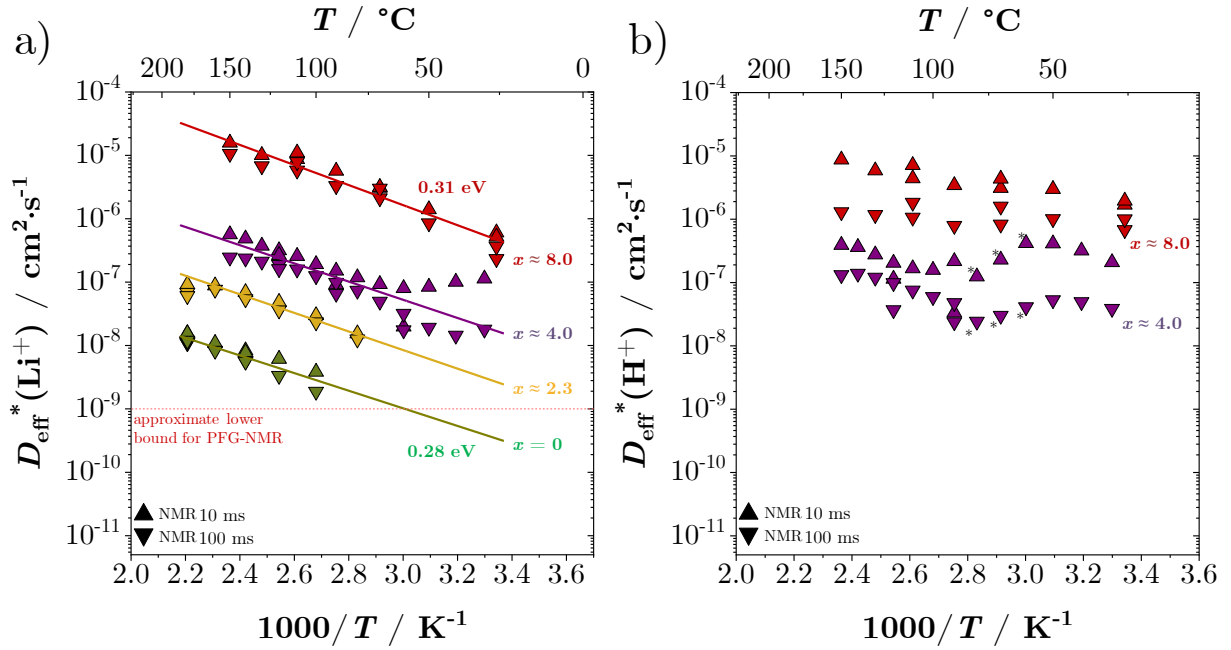
Figure 7.4: Effective tracer diffusion coefficients of a) Li^+ and b) H^+ in $Li_2Sn_2S_5 \cdot x\,H_2O$ samples measured with ^7Li and ^1H PFG NMR at 10 or 100 ms diffusion time (solid lines are linear fits of selected data point regions). Data of $x \approx 4.0$ below 80 °C in (a) showed significant scatter and were excluded for the linear fit. Data points with a comparably low goodness of fit from the 2D fitting in (b) are marked with an asterisk.

long-range diffusivity (i.e. DC value) would even be slightly lower than the one seen at 100 ms. However, for practical reasons neither are experimentally obtainable.

^7Li PFG NMR was used to measure the effective tracer diffusivities of Li^+ ions at different temperatures shown in Figure 7.4a (both heating and cooling cycles). For all diffusion times Li^+ diffusivities $D^*_{eff}(Li^+)$ systematically increase with x, reaching high values up to 5×10^{-7} cm^2/s at room temperature for $x \approx 8.0$. The linear fits in Figure 7.4a were used to calculate the activation energies: 0.28 eV ($x = 0$), 0.29 eV ($x \approx 2.3$), 0.28 eV ($x \approx 4.0$) and 0.31 eV ($x \approx 8.0$). Possible reasons for these rather unchanged migration barriers will be discussed later in section 7.3. Based on these results, Li^+ diffusivities shown for anhydrous $Li_2Sn_2S_5$ in reference [53] were actually collected on a highly hydrated material with $x \geq 6$.

Proton diffusivity $D^*_{eff}(H^+)$ was measured from the same samples and the values extracted using the 2D diffusion model as discussed above (Figure 7.4b). The behaviour is the same as observed for Li^+, the diffusivities increase with x up to 2×10^{-6} cm^2/s for $x \approx 8.0$, and the overall observed values are similar to the ones for Li^+. In $Li_2Sn_2S_5$ there is no significant chemical reason for the H_2O molecule to dissociate and produce protonic defects (acid-base reaction). Therefore, the proton diffusivity observed here refers to the mobility of molecular H_2O, and the dominant mobile charged species are lithium ions. Measurements with lower x values were attempted, yet turned out to be unfeasible, given the short T_2 relaxation times. The datasets for Li^+ and H^+ displayed in Figure 7.4 show
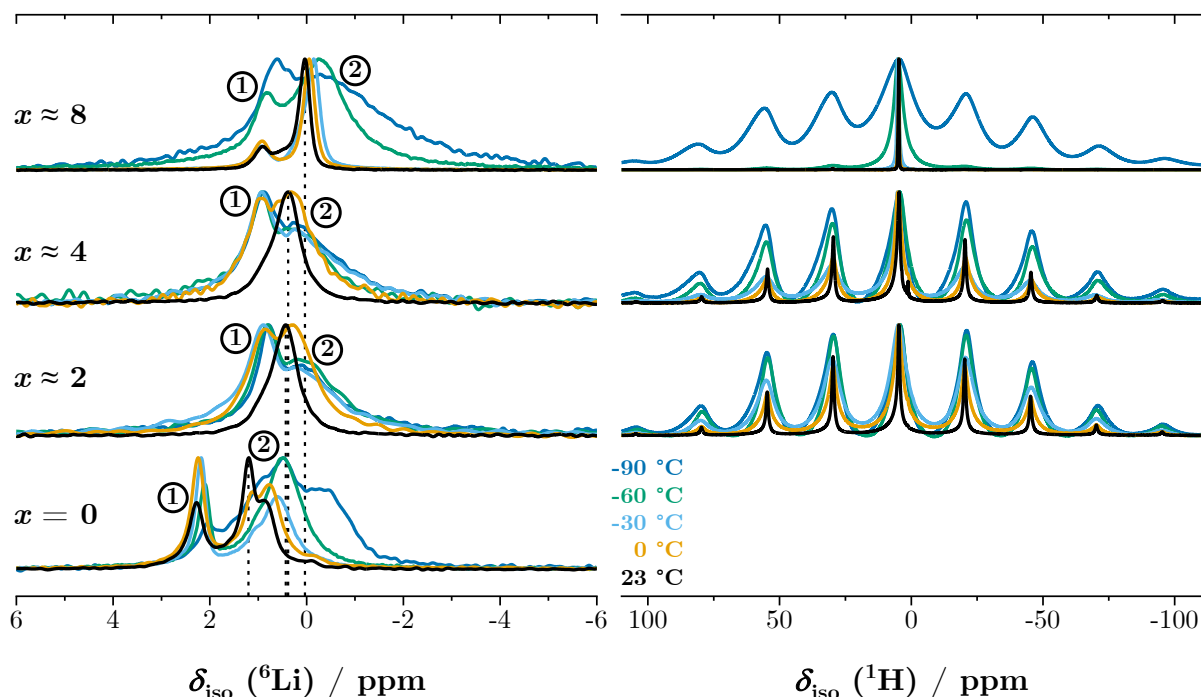
Figure 7.5: ^{6}Li and ^{1}H ssNMR measurements of $Li_2Sn_2S_5 \cdot x\,H_2O$ for various water contents and temperatures. For better comparison, all spectra were normalized to the maximum peak intensity.

some scatter, both at high and low temperatures, which is probably due to small losses of water during heating (cf. the condensation as discussed in section 5.5), especially since the scatter is more severe for H^+.

The similarity of Li^+ and H_2O diffusivities indicates that the transport of both species is probably coupled. To probe this hypothesis, the local dynamics were investigated by temperature dependent magic angle spinning (MAS) NMR experiments of selected $Li_2Sn_2S_5 \cdot x\,H_2O$ hydrates (Figure 7.5). For all x the ^{6}Li NMR spectra show (at least) two signals, marked as signals 1 and 2. For $x = 0$ at 23 °C, these signals are located at 2.3 and 1.2 ppm, and represent $Li_\perp^+$ and $Li_\parallel^+$ ions, as determined previously.[53]

The overall trend of signals 1 and 2 in Figure 7.5 is clear: with increasing temperature, the shape and position of signal 1 remains approximately constant, while signal 2 shows strong narrowing and shifts to low field (chemical shifts and full width at half maximum FWHM shown in Figure B.52). The sharpening of peak 2 with temperature is a sign of motional narrowing,[171] which again demonstrates that the dominant mobile carriers are $Li_\parallel^+$ ions, while $Li_\perp^+$ is rather immobile. At constant temperature, with increasing x signal 2 shifts more and more high field towards 0 ppm (indiacted by the dashed lines). The most significant changes in both shape and position occur when switching from $x = 0$ to 2, and from $x \approx 4$ to 8, matching with the XRPD results for first-order phase transitions. From $x \approx 2$ to 4 only minimal changes are observed, since the increase in x is within the phase width of the first hydrate and no structural changes occur. The shift of signal 2 to $\sim$0 ppm

in the swollen phase with $x \approx 8$ reflects the solvation of $Li_{\parallel}^+$ ions by forming a hydration shell with H_2O, since a similar signal is reported for aqueous Li^+ electrolytes.[192, 193]

The results from ^{1}H NMR shown in Figure 7.5 support the conclusions from ^{6}Li NMR. Motional narrowing is observed for all x when increasing the temperature, which suggests a coupled short-range motion for both Li^+ and H_2O. While the spectra for $x \approx 2\text{-}4$ are virtually identical and show rather broad signals typical for solids (spinning side bands), the swollen phase with $x \approx 8$ displays a sharp, narrow signal as usually observed for liquid electrolytes.

The following conclusions from MAS NMR can be summarized: (i) $Li_{\perp}^+$ and $Li_{\parallel}^+$ are present at all temperatures, yet only the latter species is mobile; (ii) the first-order phase transitions seen by TGA and XRPD are supported by NMR; (iii) motional narrowing is observed for both Li^+ and H_2O, suggesting a coupled diffusion mechanism, in line with the results from PFG NMR; (iv) the first hydrate $x \approx 2\text{-}4$ behaves like a solid, while the swollen phase $x \approx 8$ rather represents a liquid electrolyte.

7.3   Ion Transport Mechanism

$Li_2Sn_2S_5 \cdot x\,H_2O$ was investigated by electrochemical impedance spectroscopy to corroborate the above findings and further elucidate the transport mechanism of the Li^+ ions. Representative spectra of selected hydrates are shown in Figure 7.6. The arcs show a certain degree of depression, and despite some small deviations, they are well described with the indicated circuit. At lower frequencies a blocking feature (Warburg diffusion) is observed, which can be attributed to the electrode process of Li^+-irreversible electrodes (here; ruthenium). Starting at $x \approx 4$, the resistance becomes too small and the full arc can only be resolved at lower temperatures (Figure 7.6b). The high frequency arc scales linearly with sample thickness (Figure B.53), and can consequently be ascribed to the bulk conductivity. The capacitances were used to calculate the dielectric constants ε_r (Figure B.56). The obtained values of all $Li_2Sn_2S_5 \cdot x\,H_2O$ are unusually high for a bulk response. A similar observation was made for $Li_3InCl_6 \cdot 1.5\ H_2O$,[194] which could indicate that layered hydrates generally have an increased dielectric constant. It would even be expected that the incorporation of mobile H_2O molecules (rotation, translation) in the structure of $Li_2Sn_2S_5 \cdot x\,H_2O$ induces polarisation effects given the dipole moment of H_2O^{41}. It is yet unclear why the anhydrous material also shows an increased dielectric constant. Blocking grain-boundaries can be ruled out since no low-frequency semicircle was observed. Perhaps the anisotropic ion conduction and the layered crystal structure induce a yet unknown polarisation effect.

The conductivities are shown as a function of temperature in Figure 7.7. The respective

---

[41]Liquid water has an ε_r value of 80 at 20 °C,[195] and $LiSCN \cdot x\,H_2O$ hydrates also showed increased dielectric constants.
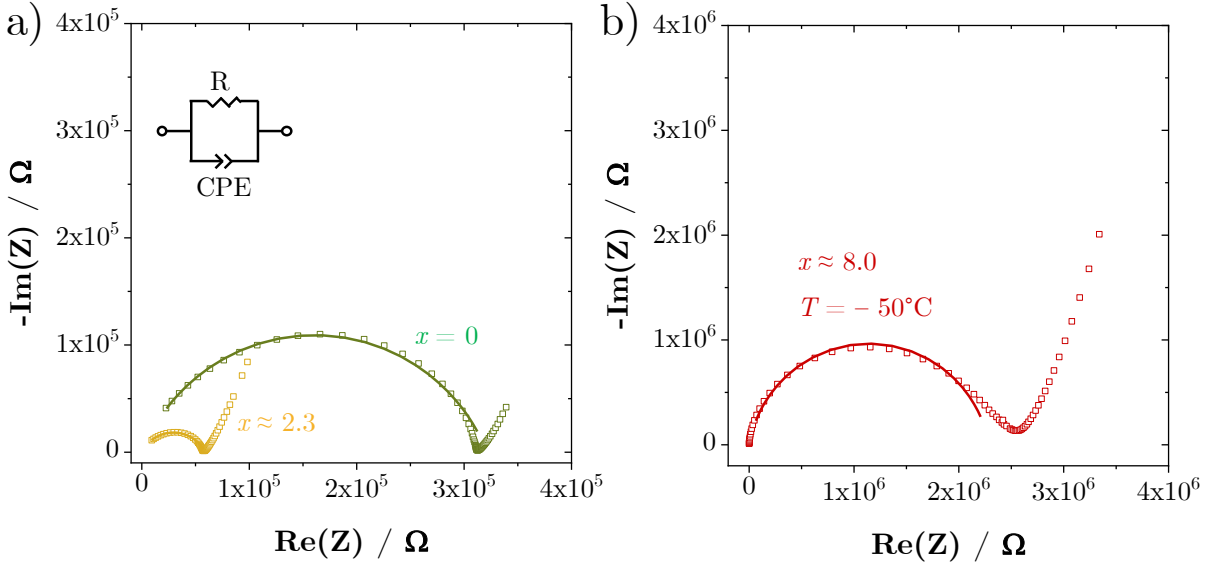
Figure 7.6: Exemplary impedance spectra of Li$_2$Sn$_2$S$_5$ $\cdot\, x$ H$_2$O samples: a) at 30 °C ($x = 0$ and $x \approx 2.3$), and b) at -50 °C ($x \approx 8.0$).

activation enthalpies are 0.42 eV ($x = 0$), 0.59 eV ($x \approx 2.3$), 0.39 eV ($x \approx 4.0$), 0.34 eV ($x \approx 8.0$) and 0.24 eV ($x \approx 10.0$). Heating and cooling runs as well as different sample batches and set-ups confirmed the results (Figure B.54). The conductivities systematically increase with x by more than three orders of magnitude, and for $x \approx 10.0$ a value of 2×10^{-2} S/cm was measured at 27 °C. The conductivities are compared to the results from PFG NMR by converting the diffusivities using the Nernst-Einstein equation (equation 6.56). The concentration of lithium ions [Li$^+$] was estimated based on the crystal structure:

$$[\text{Li}^+] = \frac{d_0}{d_\text{x}} \cdot \frac{Z_\text{Li}}{V_\text{UC}} \tag{7.8}$$

in which d_0 and d_x are the interlayer spacing for $x = 0$ and $x > 0$ (Figure 7.2), Z_Li and V_UC are the number of Li$_\parallel$ atoms (3.78) and volume (438.8 Å^3) per unit cell for $x = 0$. Note that the concentration estimated here is an upper bound, since, at least for $x = 0$, it is unclear how variations of crystallinity affect the ionic transport (referring to the less crystalline content in Figure 7.5, cf. Figure B.51). To account for porosity, [Li$^+$] from equation 7.8 was multiplied by a factor of 0.9 (pressed pellets of Li$_2$Sn$_2$S$_5$ $\cdot\, x$ H$_2$O were estimated to have a relative density of 90 % on average). Figure 7.7 compares the two datasets from EIS and PFG NMR, and good agreement is found between the two techniques. It can therefore be concluded that the dominant charge carriers in Li$_2$Sn$_2$S$_5$ $\cdot x$ H$_2$O are indeed Li$_\parallel^+$ ions, and ion transport increases with hydration. In addition, it appears that the previously reported high conductivity values of anhydrous Li$_2$Sn$_2$S$_5$ in reference [53] measured by impedance may have been misinterpreted, and are most likely based on a rather high circuitry resistance from the employed set-up.
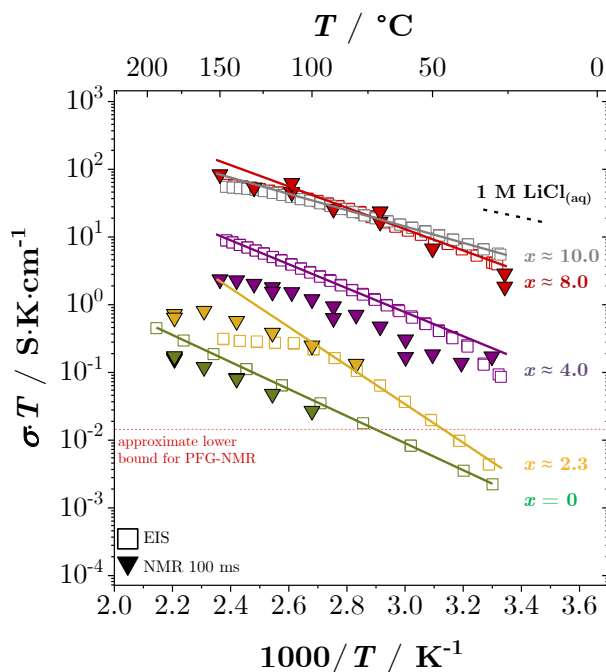
Figure 7.7: Transport data of $Li_2Sn_2S_5 \cdot x\,H_2O$ measured by EIS (squares) and PFG NMR (triangles, $D_{eff}^*(Li^+)$ values converted with the Nernst-Einstein equation). Solid lines are linear fits to the EIS data. The dashed line shows the conductivity of a concentrated aqueous LiCl solution.[196]

The good quantitative agreement between impedance and PFG NMR suggests that the increase in conductivity can predominantly be attributed to an increase in mobility, while the charge carrier concentration stays relatively constant (only a small decrease due to volume expansion). Since the activation energies from PFG NMR barely change with x, it can be concluded that the significant increase in mobility is related to the pre-exponential factor, and specifically an increased attempt frequency, since the entropy of migration is expected to be small. The dependence of the coupled diffusivity of Li^+ and H_2O on x explains the observed hydration and dehydration kinetics from TGA in section 7.1. As the material is dehydrated, the mobility of H_2O decreases which results in slower kinetics, and it suggests a diffusion-limited process.

The results found here about the ion transport mechanism are depicted in Figure 7.8 and can be summarized as follows: In anhydrous $Li_2Sn_2S_5$ with $x = 0$ the conductivity is low since $Li_{\parallel}^+$ ions are hindered (or trapped) by the electrostatic interaction with the negatively charged tin sulphide layers (A). This interaction is screened by introducing a moderate amount of water, i.e. $x \approx$ 2-4 (B). Interestingly, for $x \approx 2.0$ the conductivity is still comparatively low, while it increases by $\sim$1.5 orders of magnitude within the phase width up to $x \approx 4.0$. In case of full hydration (swollen phase, $x \approx$ 8-10) $Li_{\parallel}^+$ ions can move with a complete hydration shell of 4-5 H_2O molecules (C).[161, 162] The switch from merely screening the electrostatic interaction to fully decoupling it by forming a hydration shell explains why the conductivity increases by almost 2 orders of magnitude from $x \approx 4$ to
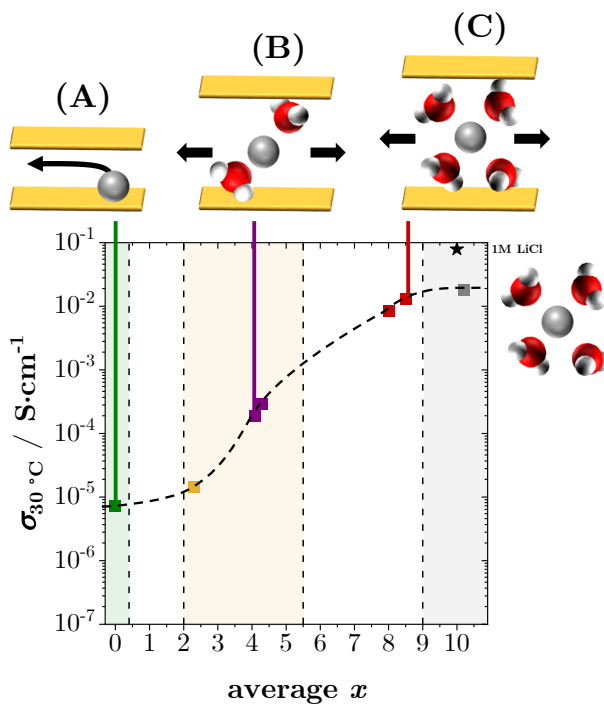
Figure 7.8: Depiction of the transport mechanisms as x in Li$_2$Sn$_2$S$_5$ $\cdot$ x H$_2$O increases. The dashed curved line is a guide for the eye. Vertical dashed lines mark borders between crystallographically different phases with shaded areas indicating one-phase regimes, as deduced from Figure 7.2.

8, while from $x \approx 8$ to 10 the impact is minor. This mechanism however promotes the mobility of Li$^+$ ions only if the incorporation of water does not disturb ion transport via the Li-sublattice (lithium interstitials in the interlayer gallery), which has been found for Li$_3$InCl$_6$ hydrates.[194]

With this simple picture broader connections between hydrated solids and liquid electrolytes can be drawn. A 1 M aqueous LiCl solution has a conductivity of 7.2×10^{-2} S/cm at 25 °C (black, dashed line in Figure 7.7).[196] Considering that cation transference numbers in liquid solutions are typically around 1/3, the Li$^+$ conductivity amounts to 2×10^{-2} S/cm, almost identical to the swollen phase ($x \approx 8$-10) with $0.5 - 2 \times 10^{-3}$ S/cm. Thus, Li$_2$Sn$_2$S$_5$ $\cdot$8-10 H$_2$O shows a liquid-like, fast conductivity with a solid-like Li$^+$ transference number close to one (immobile tin sulphide sheets), approaching state-of-the-art electrolyte materials such as Li$_{9.54}$Si$_{1.74}$P$_{1.44}$S$_{11.7}$Cl$_{0.3}$ (2.5×10^{-2} S/cm).[197]

The model described here which is based on changes in mobility is well suited to describe the major trends above room temperature. However, below 25 °C further discussion is necessary. Figure B.55 shows that the conductivity of Li$_2$Sn$_2$S$_5$ $\cdot$8 H$_2$O decreases strongly upon cooling and even crosses with anhydrous Li$_2$Sn$_2$S$_5$ at -60 °C. The activation energy continuously increases up to $\sim$1.2 eV. This behaviour differs from an aqueous solution, which would spontaneously undergo a first-order phase transition below 0 °C (freezing), with a sharp conductivity drop.[198] Even though Li$_2$Sn$_2$S$_5$ $\cdot$8 H$_2$O behaves essentially like

a liquid regarding ion transport, the geometric confinement of H$_2$O prevents the formation of a complete ice lattice. However, the reason for this strong decrease in conductivity cannot be clearly determined, since "ice-like" clusters may form and associate with Li$^+$ ions (decrease in carrier concentration), and/or changes in the potential landscape may occur (decease in mobility).

7.4   Possible Application as Electrolyte

In terms of practical applications, a usage of Li$_2$Sn$_2$S$_5$ as a potential solid electrolyte material in battery systems appears interesting. The material Li$_4$SnS$_4$ from the solid solution system Li$_{4z}$Sn$_{1-z}$S$_2$ has already been tested as such.[183–186] Figure 7.9 shows conductivity measurements of anhydrous Li$_2$Sn$_2$S$_5$ with Li metal electrodes. In contrast to EIS measurements with Li$^+$ ion-blocking Ru electrodes (Figure 7.6), no Warburg diffusion at low frequencies is observed as expected. Over time, the shape of the impedance arc changes noticeably, and the conductivity increases by $\sim$2 orders of magnitude. The larger characteristic time of this process for thicker samples confirms that the observed change is indeed connected with the sample, and not a measurement artefact.

To better understand the change in impedance, electromotive force (EMF) measurements were conducted employing Li metal and LiAl as electrodes (Nernst voltage at 30 °C is 0.38 V).[199] Figure 7.10a shows that the measured open-circuit voltage (OCV) decreases
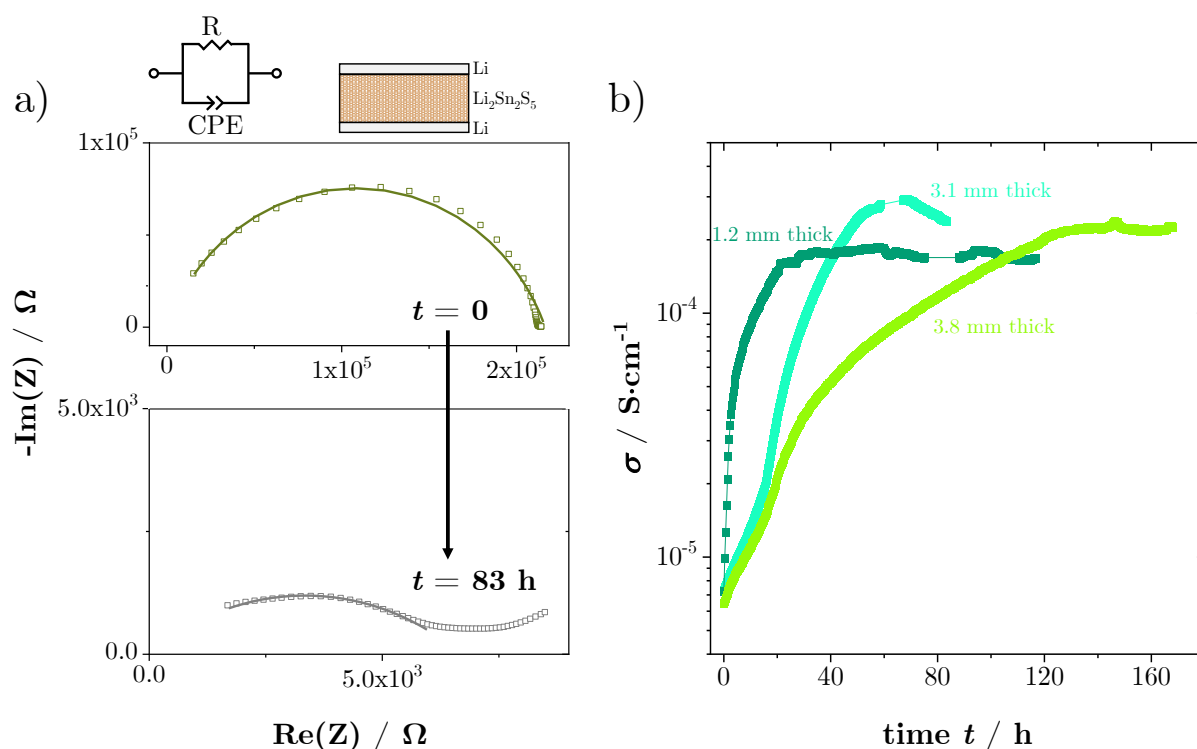
Figure 7.9: a) Impedance spectra and b) conductivity of anhydrous Li$_2$Sn$_2$S$_5$ (3 samples of different thicknesses) at 25 °C after being contacted by Li metal electrodes.
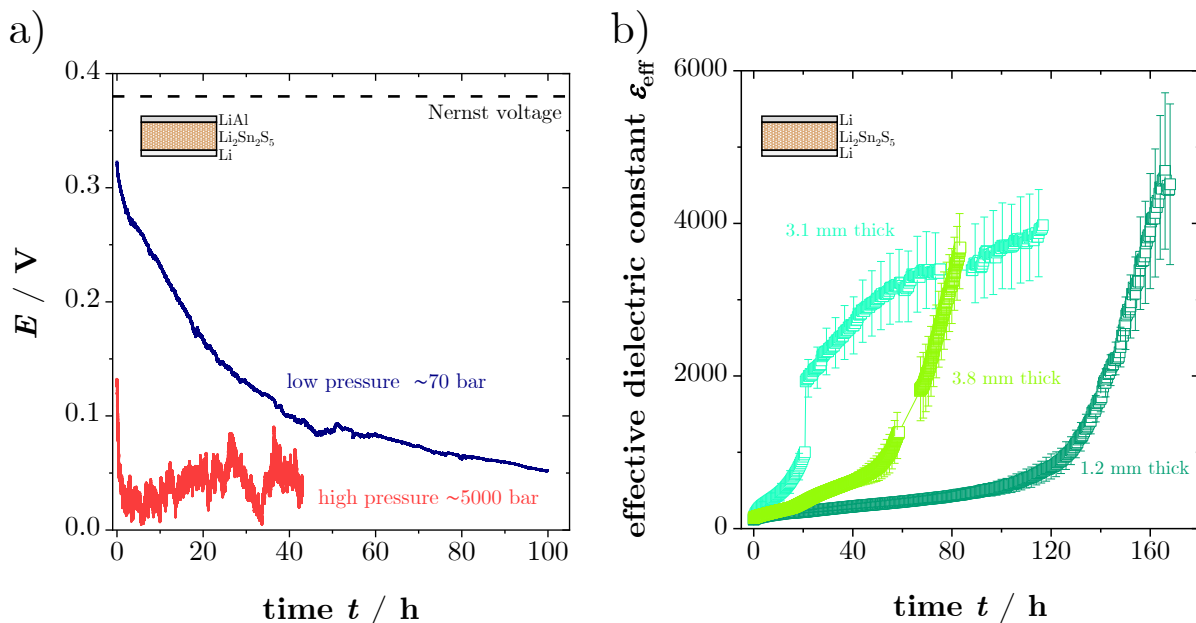
Figure 7.10: a) EMF measurement of $Li_2Sn_2S_5$ at 30 °C with Li and LiAl as electrodes under high and low pressure. The Nernst voltage for this cell is 0.38 V shown as dashed line.[199] b) Effective dielectric constant ε_{eff} of anhydrous $Li_2Sn_2S_5$ at 25 °C after being contacted by Li metal electrodes (corresponding conductivities are shown in Figure 7.9b).

gradually over time, while the conductivity increases (Figure 7.9b). These results indicate that $Li_2Sn_2S_5$ is unstable versus Li metal or Li-alloys, and the transport changes from ionic to predominately electronic. Indeed, a previously performed DC measurement with LiAl electrodes (cf. Figure 4b in ref. [53]) does not show any signs of polarisation, which is typically observed for electronic conductors. The reported conductivity of 1.2×10^{-4} S/cm also matches to the conductivities shown in Figure 7.9b after the decomposition reaction (after tens of hours, depending on sample thickness). It can therefore be concluded that anhydrous $Li_2Sn_2S_5$ is unstable against a high Li activity.

Interestingly, along with the conductivity, the measured dielectric constant ε_r also increases by a factor of ~ 50, reaching unreasonably high values of ~ 5000 for bulk response (Figure 7.10b). This apparent increase in ε_r suggests that the decomposition reaction occurs along interfaces, creating percolating pathways for electronic conduction within the grain-boundary network. XRPD and SEM (Figure B.59a) indeed do not show any discernable signs of bulk decomposition, merely the optical appearance of the sample changes from a brown-beige colour to black. Even though the electrochemical stability window of lithium tin sulphides is generally expected to be small,[60, 200] the formation of electronic pathways is nonetheless surprising, given that such a behaviour has not been reported for Li_4SnS_4 or Li_2SnS_3.[183-186, 201] One can think of two mechanisms how the decomposition reaction in contact with Li could proceed: $Li_2Sn_2S_5$ becomes lithiated, i.e. Li^+ ions and electrons enter the lattice by reducing Sn^{4+} and form an electronically conducting Li-Sn-(S)-compound along the grain-boundaries, or Li metal directly enters the sample

by forming dendrites. The former mechanism is considered the more likely scenario, since a similar process has already been observed for Ti^{4+} reduction in $LiLaTiO_3$.[202] However, XPS measurements of $Li_2Sn_2S_5$ sample powder after contact with Li (Figure B.59b) do not show any changes in the oxidation state of Sn^{4+}, and rather support a dendrite formation mechanism, given that the amount of Li increases[42]. Besides the increased Li content, the sulphur signal S 2p shows evident changes, suggesting that the interfacial decomposition reaction only involves Li^+ and S^{2-}, while leaving Sn^{4+} unaffected. These observations match with the behaviour predicted by DFT calculations for the lithiation of SnS_2.[60] Accordingly, a topotactic intercalation reaction of Li (cf. $LiCoO_2$) in a layered tin sulphide is unfavourable, since the reduction to Sn^{3+} would result in a disproportionation (Sn^{4+} and Sn^{2+}) involving a severe lattice rearrangement (Sn^{2+} prefers tetrahedral coordination due to its $5s^2$ lone-pair). This might explain why electronic conduction via Sn^{4+} reduction (effectively short-circuiting of a battery cell) has not been observed for other lithium tin sulphides, and does possibly also not occur in $Li_2Sn_2S_5$. Why $Li_2Sn_2S_5$ is the only $Li_{4z}Sn_{1-z}S_2$ phase which nonetheless becomes electronically conducting could be related to the crystal structures: Li dendrites could grow in the interlayer gallery along the interface of the $(Li,Sn)S_2$ sheets, coating themselves with a thermodynamically stable surface layer of Li_xS_y, which would explain the results presented here. However, further studies are necessary to determine the reaction mechanism which go beyond the scope of this thesis.

Moving on to the potential application of $Li_2Sn_2S_5 \cdot x\,H_2O$, a recent work on a hydrated Na^+ ion conductor has shown that it is possible to form an artificial, kinetically stable SEI of hydrolysis products.[203] Since the hydrolysis products of Li are electronically blocking (e.g. $LiOH$, LiH, Li_2O), hydrated $Li_2Sn_2S_5 \cdot x\,H_2O$ might prevent the formation of electronic pathways. However, to prevent a successive dehydration of $Li_2Sn_2S_5 \cdot x\,H_2O$, which could potentially destroy the electrodes, the passivation layer would also have to be blocking for H_2O molecules, which is usually not the case.[204, 205] Figure 7.11 and 7.12a show the results from impedance measurements with $Li_2Sn_2S_5 \cdot x\,H_2O$ in contact with Li-reversible electrodes. The impedance signal (Figure 7.11a) shows two distinguishable semicircles, which correspond to the bulk sample (high frequency) and a formed SEI layer (low frequency). The impedance of the SEI grows continuously over time while its capacitance (or effective dielectric constant ε_{eff}) decreases (Figure 7.11b). This means that the passivation layer grows in thickness, and the growth rate increases with x. The ε_{r} values of the bulk signal for $x \approx 2.0$ and 3.0 seem to increase slightly. However, this might just be an artefact from fitting the impedance spectra, and compared with the values from blocking electrodes, the increase is negligible. For $x \gtrsim 4.0$ only the SEI signal can be distinguished.

---

[42]The absolute values for the Li 1s signal are inaccurate due to the large error bar for Li in XPS, yet the increase is nonetheless discernable.

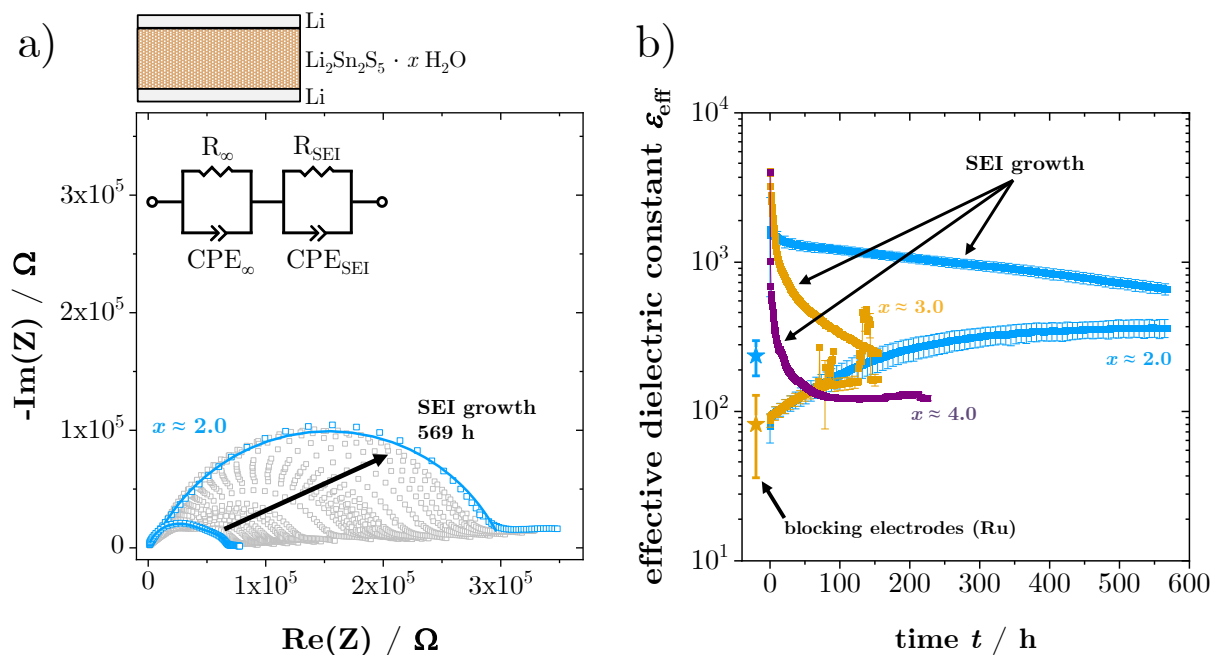Figure 7.11: a) Impedance spectra and b) effective dielectric constant ε_{eff} of $Li_2Sn_2S_5 \cdot x\,H_2O$ at 25 °C after being contacted by Li metal electrodes. Stars correspond to blocking Ru electrodes.

Figure 7.12a shows the total conductivity $(R_\infty + R_{SEI})$ of different $Li_2Sn_2S_5 \cdot x\,H_2O$ phases contacted with various Li-reversible electrodes. The general trend is clear: an SEI layer forms initially by hydrolysis of the electrode, which (mostly) decreases the total conductivity until the growth of the SEI slows down and a plateau is reached. The EMF measurement in Figure 7.12b confirms that even for low x values the formed SEI severely hinders short-circuiting of the cell[43], and at higher hydration levels seems to be able to prevent it completely. Obviously, the growth and chemical composition of the SEI can be altered depending on the choice of Li-reversible electrode. By choosing electrodes with a lower Li activity, i.e. LiAl and $Li_7Ti_5O_{12}$ (LTO7), the drop in conductivity can significantly be alleviated, and in case of LTO7, even be prevented. As expected, XRPD analysis (Figure B.60) shows that in contact with Li metal the main hydrolysis product is LiOH. Its amount increases with x, and further hydrolysis products form (LiH). The images shown there fit to the results from electrochemical measurements; at low $x \approx 2.0$ the SEI layer can mostly prevent the reduction process (only slight black colouration on the surface of the pellet), and the formation of hydrolysis products is low. With increasing x the protective effect of the SEI increases, until no reduction occurs and a thick SEI layer forms for $x \approx 4.0$. Since the formation of hydrolysis products effectively means a dehydration of $Li_2Sn_2S_5 \cdot x\,H_2O$, the accompanied volume changes can lead to cracking

---

[43]The observation of an initially higher voltage than the Nernst voltage is either an artefact due to sluggish kinetics (non-equilibrium value), or related to the formation of hydrolysis products; e.g. a mixed conducting Li-Al-H compound.
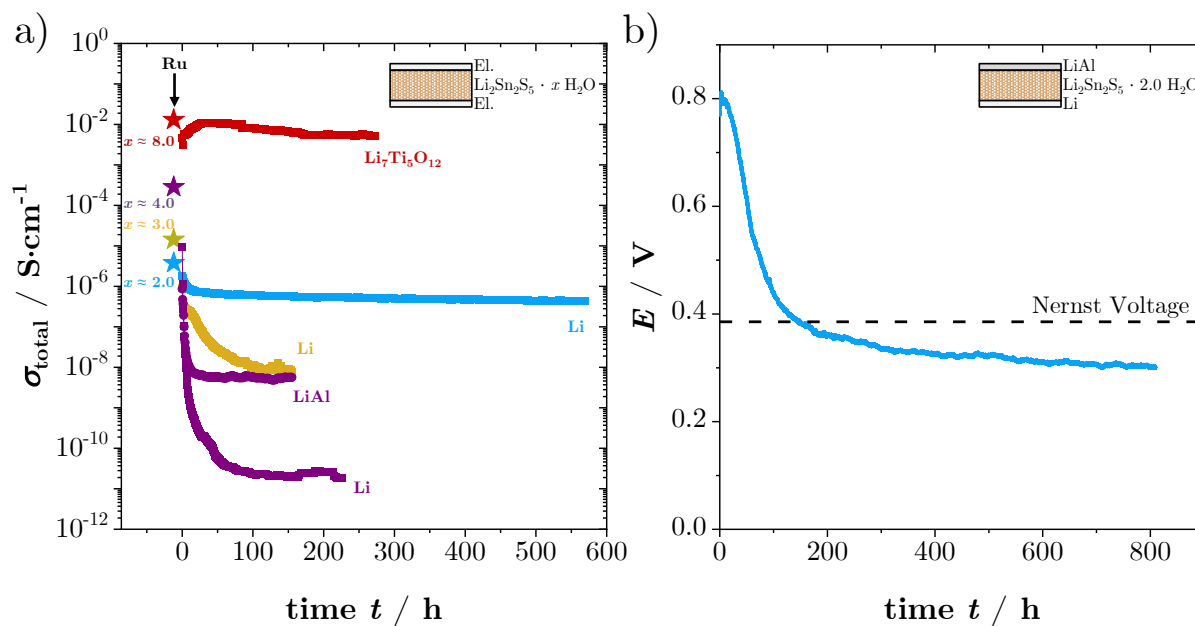
Figure 7.12: a) Total conductivity of $Li_2Sn_2S_5 \cdot x\,H_2O$ at 25 °C after being contacted with different Li-electrodes. Stars correspond to blocking Ru electrodes. b) EMF measurement of $Li_2Sn_2S_5 \cdot 2.0\,H_2O$ at 25 °C with Li and LiAl as electrodes.

of the electrolyte pellet, as seen for $x \approx 4.0$. In contrast, with a LiAl electrode no LiOH formation was observed (only LiH), and the electrolyte becomes significantly less dehydrated. Especially the suppression of LiOH with the choice of electrode is an interesting discovery for the design of an appropriate cell.

Based on these results, it should be possible to design a functioning battery cell with fully hydrated $Li_2Sn_2S_5 \cdot x\,H_2O$ ($x \gtrsim 8.0$) as solid electrolyte. Conductivity and contact with the electrodes should not be an issue, since the material's ion transport performance is similar to a liquid electrolyte, and it is sufficiently soft that simple pressing creates good interfacial contact. In contrast to liquid systems, the Li^+ transference number is close to unity, and the geometric confinement of H_2O helps to widen the voltage window of water splitting.[206]

Even though the presence of H_2O prevents short-circuiting of the cell, finding suitable materials as cathode and anode with $Li_2Sn_2S_5 \cdot 8\,H_2O$ as electrolyte will be challenging,[204, 205] and a few concerns are worth mentioning here. The thickness of the passivation layer has to be controlled by suppressing the reactivity with the electrodes. Stoichiometric dehydration has to be avoided, since the material's conductivity will decrease and the accompanied volumetric changes cause cracking of the electrolyte pellet. Since the stability window of lithium tin sulphides is narrow,[200] and despite geometric confinement water splitting will most likely still be an issue, such a battery cell will have a notably lower power output than state-of-the-art high voltage cells. However, regarding the potential advantages such as cost, safety and environmental friendliness, research of this topic is still attractive and scientifically important. The here presented results deepen the knowledge in hydration

and ion transport of lithium ion conductors, and provide potential avenues to employ solvated solid electrolyte systems in battery applications (e.g. by replacing water with organic solvents).

7.5 Literature Comparison

In the light of these findings two important points from previous work[53] on $Li_2Sn_2S_5$ have to be clarified:

1. Anhydrous $Li_2Sn_2S_5$ is not a fast conductor. Numerous samples of $Li_2Sn_2S_5$ consistently showed a room temperature conductivity of 10^{-6} S/cm (cold pressed) or 10^{-5} S/cm (sintered), and a diffusivity below 10^{-9} cm^2/s. After carefully studying the results from the previous work, it is concluded that the impedance data was not correctly interpreted, i.e. the low resistances at high frequencies were measurement artefacts, and that the previously measured high diffusivities of 10^{-7} cm^2/s were collected on an inadvertently hydrated sample with $x \geq 6$.

2. Anhydrous $Li_2Sn_2S_5$ is unstable against a high Li activity, such as from contact with Li metal or Li alloys, e.g. LiAl. The previously reported high conductivity of 10^{-4} S/cm from a galvanostatic DC measurement corresponds to the electronic conductivity of a reduced decomposition product or percolating Li dendrites within the grain-boundary network of $Li_2Sn_2S_5$.

8 | Discussion

8.1 Transport Mechanism in Anhydrous LiSCN and Li$_2$Sn$_2$S$_5$

The two investigated compounds in this thesis, LiSCN and Li$_2$Sn$_2$S$_5$, are fascinating materials to elucidate the link between defect chemistry, crystal structure and cation-anion lattice coordination chemistry. Both materials are solid Li$^+$ ion conductors, undergo molecular hydration and can form stable hydrates, but their transport properties as anhydrous samples are distinctly different (Figure 8.1). Anhydrous LiSCN forms Schottky defect pairs, with V$'_{Li}$ being the dominant mobile defect (subsection 6.1.1). Their formation enthalpy is relatively low (0.6 eV), but these defects are very slow due to the peculiar bidental ligand coordination between Li$^+$ and SCN$^-$ (subsection 6.1.2). The densely ordered crystal structure prevents fast relaxation of the anion lattice, causing a frequency dependent conductivity. High defect concentration and fast jump relaxation occur only at high temperatures (subsection 6.1.3). In contrast, anhydrous Li$_2$Sn$_2$S$_5$ is already a highly disordered material at room temperature with a low-dimensional (2D) crystal structure (section 3.2 and 7.1). Mobile Li$^+$ ions are situated between negatively charged tin sulphide sheets, to which they are bound by moderate Coulombic interaction, meaning Li$^+$ ion transport is free of strong cation-anion coordination as seen for LiSCN. The defect formation enthalpy is not relevant, and the present Li$^+$ ions between the tin sulphide sheets are all considered to be mobile[44]. The measured conductivity directly relates to the mobility of the Li$^+$ ions in anhydrous Li$_2$Sn$_2$S$_5$.

---

[44]The material can be characterized as superionic, since the lattice is highly disordered. This superionic state can be realized either by structural configuration as seen for Li$_2$Sn$_2$S$_5$, or by Coulombic defect-defect stabilisation as seen in the premelting regime of LiSCN (cf. subsection 6.1.3).
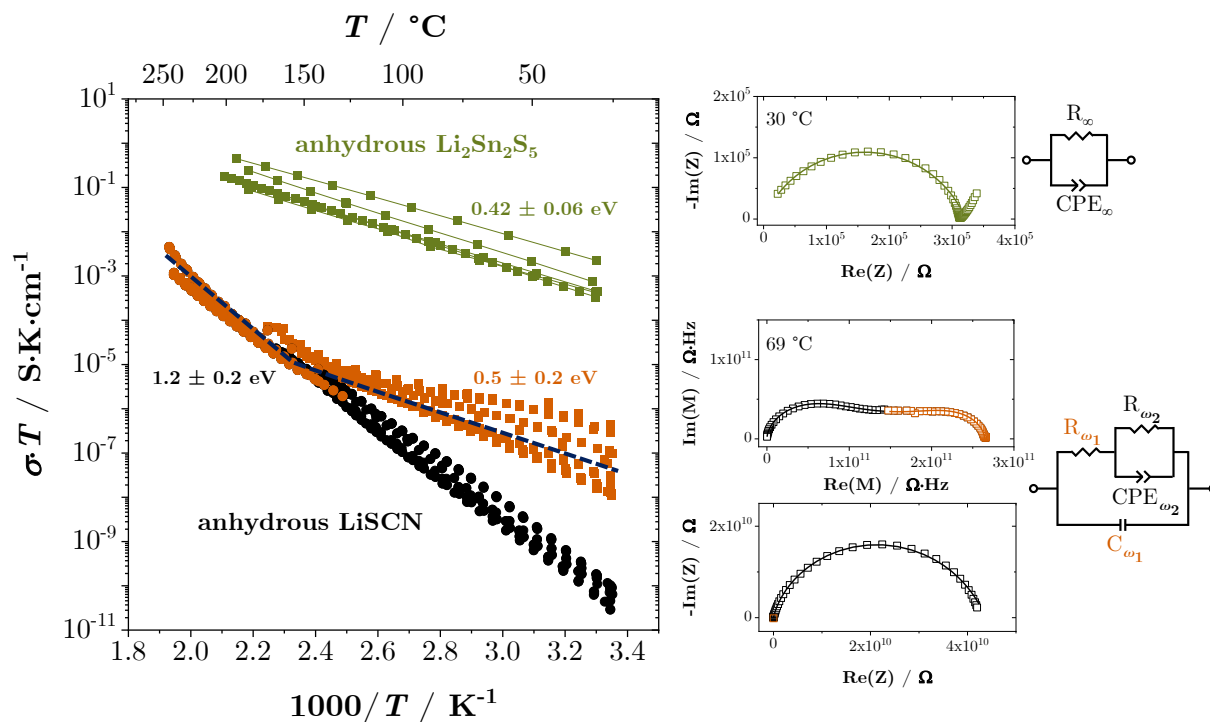
Figure 8.1: Comparison of the conductivity of anhydrous LiSCN and $Li_2Sn_2S_5$ at various temperatures, showing short-range (LiSCN, red squares) and long-range (LiSCN black, $Li_2Sn_2S_5$ green squares) Li^+ ion transport. The right hand side depicts representative EIS spectra, fitted with the shown circuits.

8.2 Hydration Behaviour of LiSCN and $Li_2Sn_2S_5$

The two materials are well suited for hydration studies, as molecular hydration occurs facile without hydrolysis (subsection 6.2.1 and section 7.1). Figure 8.2 compares the equilibrium water partial pressure p_{H_2O} data of the hydration for LiSCN and $Li_2Sn_2S_5$, measured either directly above the respective hydrates, via mass changes from TGA, or equilibration over salt solutions. In case of H_2O-doping, the measured $p_{H_2O} - 1000/T$-range is shown together with calculated values based on the defect model (case 1) in subsection 6.2.2. The model nicely reflects the experimentally observed boundaries of the H_2O-doping regime. The table compares the corresponding hydration enthalpies and entropies.

Liquid hydrates of LiSCN $\cdot x\,H_2O$ are quite comparable in their hydration behaviour to the first solid hydrate of $Li_2Sn_2S_5 \cdot 2$-$4\,H_2O$. However, solid LiSCN $\cdot x\,H_2O$ is noticeably different. Solid LiSCN that contains water only exists at p_{H_2O} values lower compared to $Li_2Sn_2S_5$. This reflects their chemical behaviour, as LiSCN is much more hygroscopic than $Li_2Sn_2S_5$. The reason for the willing hydration in LiSCN is related to the crystal structures of LiSCN $\cdot x\,H_2O$ with $x = 0$, 1 and 2 (Figure 6.23), since both Li-S bonds and tetrahedral coordination are disfavoured. The Gibbs free enthalpy of hydration emphasizes this nicely when comparing LiSCN $\cdot 0.001\,H_2O$ with $Li_2Sn_2S_5 \cdot 2$-$4\,H_2O$. While

LiSCN $\cdot\, x\,$H$_2$O hydrates are line compounds with negligible phase widths (Figure 6.27), the layered crystal structure in Li$_2$Sn$_2$S$_5 \cdot x\,$H$_2$O allows for larger homogeneity ranges for the hydrates (Figure 7.2). Since the anion lattice (tin sulphide sheets) are effectively unaffected by the incorporation of H$_2$O (for $x \lesssim 10$)[45], hydration merely increases the interlayer distance and structural units are retained, which enables much higher x values compared to LiSCN $\cdot\, x\,$H$_2$O. It is therefore concluded that solid Li$_2$Sn$_2$S$_5 \cdot x\,$H$_2$O behaves similar to the liquid hydrates of LiSCN $\cdot\, x\,$H$_2$O, meaning a highly concentrated liquid electrolyte system, which matches with the ion transport behaviour, shown in the subsequent section.

	$\Delta_h H^\circ$ / eV	$\Delta_h S^\circ$ / k_B	$\Delta_h G^\circ$ (300 K) / eV
LiSCN $\cdot$ 0.001 H$_2$O$_{(s)}$	-0.94	-20	-0.42
LiSCN $\cdot$ 1 H$_2$O$_{(s)}$	-0.35	-7	-0.17
LiSCN $\cdot$ 1 H$_2$O$_{(l)}$	-0.51	-12	-0.20
LiSCN $\cdot$ 2 H$_2$O$_{(l)}$	-0.50	-13	-0.16
Li$_2$Sn$_2$S$_5 \cdot$ (2-4) H$_2$O$_{(s)}$	-0.52	-14	-0.16
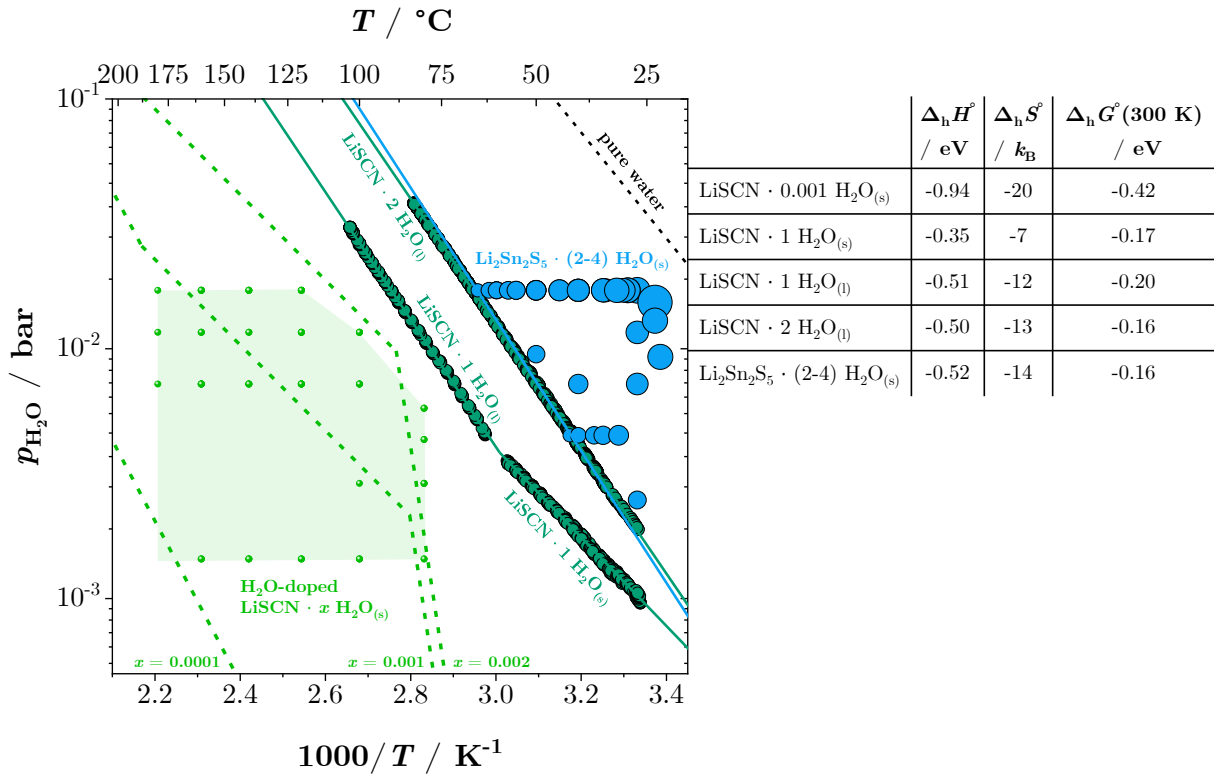
Figure 8.2: Comparison of the equilibrium partial pressures of water p_{H_2O} for solid (s) and liquid (l) hydrates of LiSCN $\cdot\, x\,$H$_2$O and Li$_2$Sn$_2$S$_5 \cdot x\,$H$_2$O within their phase widths (for more information cf. Figure B.32, 6.26 and 7.1). Solid lines are linear fits to measured p_{H_2O} data shown as spheres or circles, and dashed lines are calculated p_{H_2O} from a defect model (green, subsection 6.2.2) or pure water (black, ref. [160]). The table lists the respective enthalpies and entropies of hydration.

---

[45]As shown in references [52] and [181], the exfoliation of Li$_2$Sn$_2$S$_5$ in liquid water yields (defective) nanolayers of tin sulphide, and SnS$_2$ is anyway stable in liquid water.[61, 182]

8.3 Transport Mechanism in Hydrated LiSCN $\cdot\,x\,$H$_2$O and Li$_2$Sn$_2$S$_5$ $\cdot\,x\,$H$_2$O

Figure 8.3 shows that the conductivity of LiSCN $\cdot\,x\,$H$_2$O can vary between more than 10 orders of magnitude from insulating to well conducting, while Li$_2$Sn$_2$S$_5$ $\cdot\,x\,$H$_2$O phases are all comparatively good ion conductors and span a smaller range of 4 orders of magnitude. The fundamental differences between these materials deduced in this thesis are emphasized with the horizontal dashed line and can be summarized accordingly:

● Below the horizontal dashed line, Li$^+$ ionic conductivity is determined by both defect formation ($\Delta_{\mathrm{K}}H°$) and migration ($\Delta_{\mathrm{m}}H_{\mathrm{j}}$) enthalpies. At these temperatures defect concentrations are rather low (ppm range, Figure 6.7 and 6.32), and even though the incorporation of water increases the mobility of mobile defects (Figure 6.6 and 6.31b), the formation of associates prevents high conductivities.

● Above the dashed line, the temperature dependence of Li$^+$ ionic conductivity is determined only by defect migration ($\Delta_{\mathrm{m}}H_{\mathrm{j}}$), while the concentration of mobile ions is (almost) constant. For anhydrous LiSCN, this state is only accessible at high temperatures in the premelting regime (Figure 6.20), while anhydrous Li$_2$Sn$_2$S$_5$ is highly disordered already
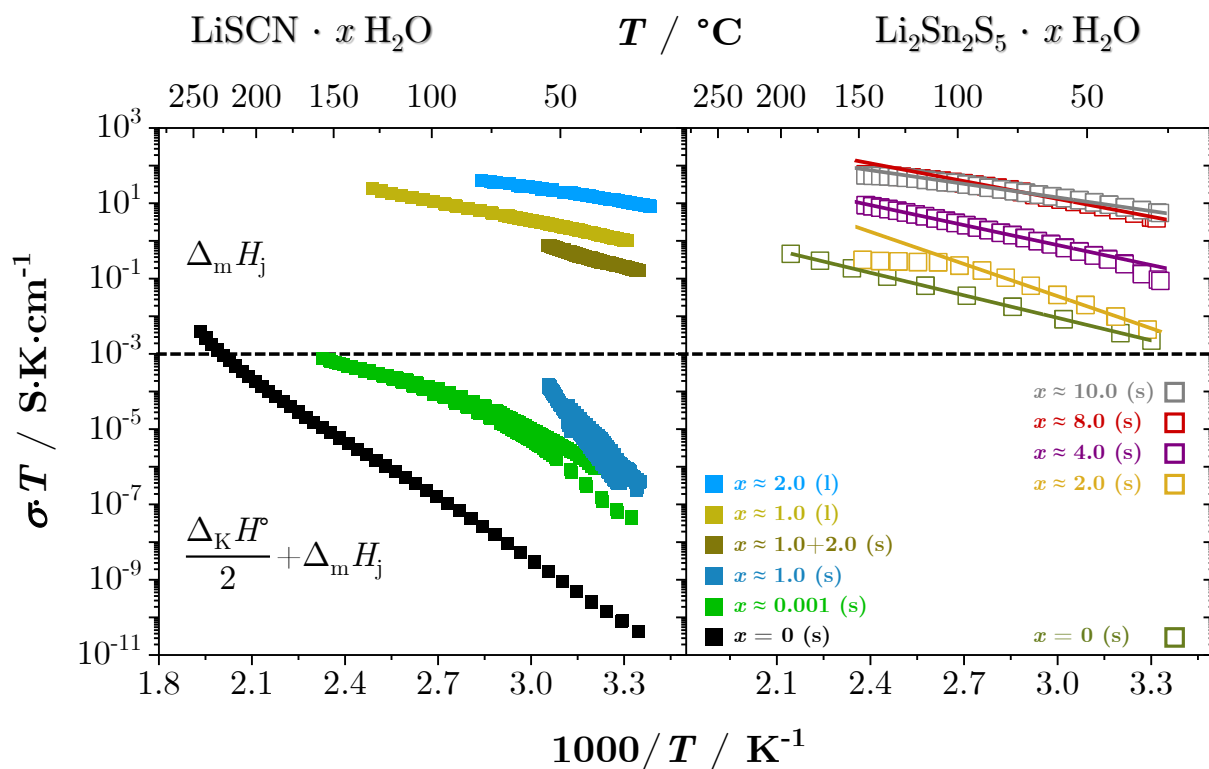
Figure 8.3: Conductivity data of hydrated (including H$_2$O-doped) LiSCN $\cdot\,x\,$H$_2$O and Li$_2$Sn$_2$S$_5$ $\cdot\,x\,$H$_2$O at various temperatures (more details in Figure 6.39 and 7.7). The dashed horizontal line roughly indicates the transition into a "superionic" state, where the concentration of mobile ions is high and (nearly) constant.

at room temperature. Within the $LiSCN \cdot x\,H_2O$ two-phase regime $1 < x < 2$, the material stays solid but conduction is determined by the liquid dihydrate in the intergranular network (Figure 6.37), and defect formation is irrelevant. This mechanism is analogous to $Li_2Sn_2S_5 \cdot x\,H_2O$ with $4 \leq x \leq 10$, only that the layered structure and chemical composition of the sheets allows for liquid-like conductivity without liquefaction (Figure 7.8). An interesting, yet not fully understood observation is the dielectric behaviour, which shows unusually high ε_r values for both $LiSCN \cdot x\,H_2O$ and $Li_2Sn_2S_5 \cdot x\,H_2O$ (Figure B.38b and B.56), when the conductivity is determined by a confined liquid(-like) part with Li^+ ions that have hydration shells.

The above described mechanisms for Li^+ ion transport of $LiSCN \cdot x\,H_2O$ and $Li_2Sn_2S_5 \cdot x\,H_2O$ are depicted in Figure 8.4, emphasizing similarities and differences between the transport mechanisms of both materials. The highest room temperature conductivities of the hydrated solids are 6.5×10^{-4} and 1.8×10^{-2} S/cm, respectively.

In summary, the study of the impact of hydration on structure, defect chemistry and Li^+ ion transport of these two materials proved to be a fascinating and manifold research topic, which deepens the knowledge in solid state ionics of hydrated (solvated) systems, and might inspire new avenues in the research of renewable energy technologies.
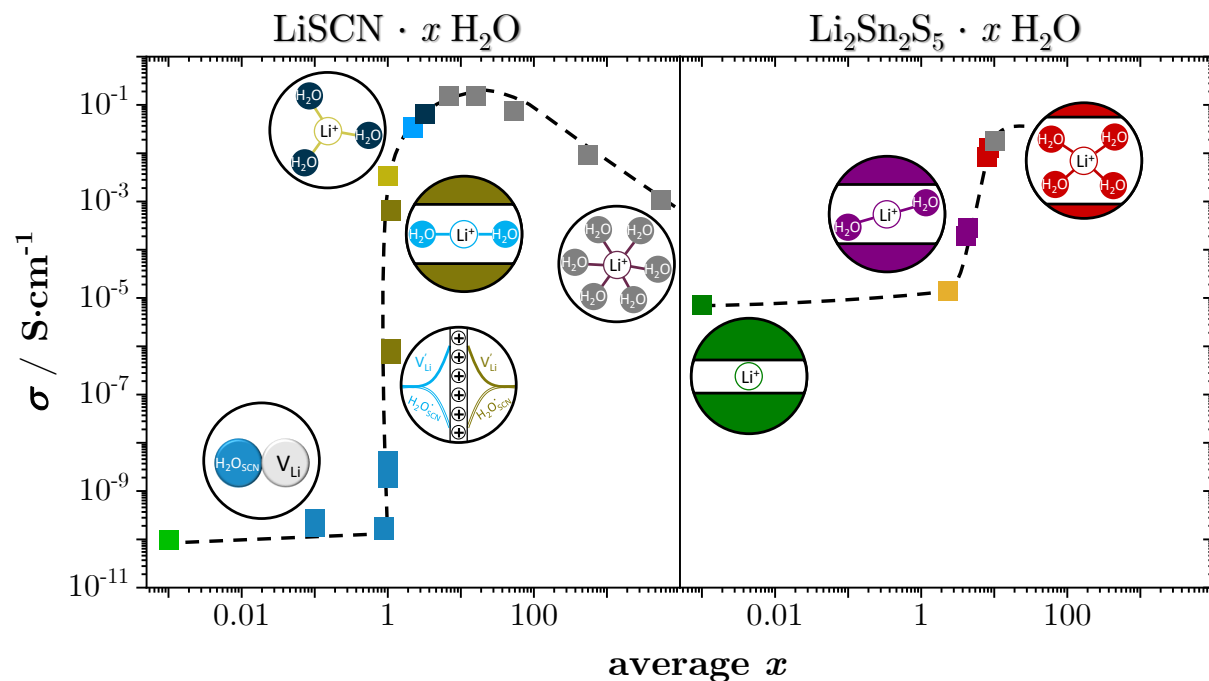
Figure 8.4: Conductivity data of all investigated materials of $LiSCN \cdot x\,H_2O$ (except $x = 0$) and $Li_2Sn_2S_5 \cdot x\,H_2O$ as a function of water content x at room temperature (for more information cf. Figure 6.40 and 7.8). Inserts: cartoons of the respective transport mechanisms.

9 | Conclusion

This thesis explores the defect chemistry and ion transport mechanisms in the Li^+ ion conducting materials LiSCN and $Li_2Sn_2S_5$, especially in regard to the impact of molecular hydration. Both materials are well-suited for hydration studies, and they exemplify the striking differences of molecular water incorporation effects in solid state ionics.

LiSCN is intrinsically Schottky defective (Li^+ and SCN^- vacancies). The immense impact of water as a dopant (H_2O substituting on SCN^- sites as positive defect) results from a combination of two effects; an increase of Li vacancy V'_{Li} concentration, and an increase of their mobility induced by accelerated rotational disorder in the anion lattice. A quantitative defect chemical model comprising defect formation, association, and migration enthalpies was developed on the basis of undoped, M^{2+}-doped and H_2O-doped LiSCN.

Stoichiometric hydration leads to the formation of the mono- and dihydrate, with the common driving force to replace Li-S with Li-O bonds. The monohydrate is identified as a special case, since both its structure and conductivity differ from the expected $LiSCN \cdot x\,H_2O$ behaviour, and deviate also compared to most other hydrated salt systems. Fast ion transport can only be achieved for solid-liquid composites of the mono- and dihydrate, reaching values up to 7×10^{-4} S/cm at room temperature. Nonetheless, LiSCN cannot be regarded as a promising candidate for typical energy applications, since it is difficult to handle and has only low to moderate ion transport properties. However, it is a great material to study complex defect chemical phenomena in combination with molecular hydration studies, and is a fascinating and complex material despite its nominal (stoichiometric) simplicity.

The second material $Li_2Sn_2S_5$ is a perfect candidate to emphasize the contrasting effects of molecular hydration compared to LiSCN in the research of ionic materials. Here, Li^+ cations bond to a polyatomic tin sulfide sheet. The incorporation of H_2O predominantly affects Li^+ cations, and most structural features such as the layered arrangement are retained. The crystal structure is flexible enough to incorporate up to 10 molecules of H_2O per $Li_2Sn_2S_5$, and the interlayer distance increases sufficiently to form a full hydration shell around the Li^+ cations. The Li^+ ion transport mechanism consequently resembles that of a liquid electrolyte confined within the solid tin sulfide layers. A conductivity

of up to 2×10^{-2} S/cm can be reached, which makes hydrated $Li_2Sn_2S_5$ a competitive and adventurous candidate as electrolyte for solid state batteries, and first investigations indicate that a successful cell design can be achieved.

The comparison of LiSCN and $Li_2Sn_2S_5$ regarding their hydration properties depicts the wide range of molecular hydration effects: a pure ionic salt with high lattice energy and high symmetry possesses a low structural flexibility, thus the incorporation of water leads to the formation of new hydrate phases with negligible phase widths. Ion transport in solid hydrates occurs via hopping of the mobile defect, typically with an increased mobility and possibly increased defect concentration. On the other hand, a more complex low-dimensional structure with alternating layers of polyanionic sheets and loosely bound cations is more flexible in its lattice arrangement. The incorporation of H_2O is thereby buffered and anhydrides as well as hydrates have far greater phase widths. As a limiting case, the mobile ion can form a full hydration shell enabling liquid-like ion transport in a solid matrix.

In summary, this thesis provides new insights into the properties of hydrated materials in the field of solid state ionics. The concept of H_2O-doping of an ionic conductor has been observed for the first time, and complete defect models for LiSCN doped with various bivalent metal cations as well as H_2O have been derived. Furthermore, a detailed transport mechanism is provided for hydrated $Li_2Sn_2S_5$, explaining the high conductivity and suggesting potential avenues in the field of solid state batteries.

A | Symbols and Abbreviations

Table A.1: List of symbols used in this thesis.

Symbol		
K_S	Schottky reaction equilibrium constant	[cm^{-6}]
$\Delta_\text{S} G^\circ$	standard free enthalpy of Schottky defect formation	[eV]
$\Delta_\text{S} H^\circ$	standard enthalpy of Schottky defect formation	[eV]
$\Delta_\text{S} S^\circ$	standard entropy of Schottky defect formation	[k_B]
K_A	association equilibrium constant	[cm^3]
$\Delta_\text{A} H^\circ$	standard enthalpy of defect association	[eV]
$\Delta_\text{A} S^\circ$	standard entropy of defect association	[eV]
K_e	electronic disorder equilibrium constant	[cm^{-3}]
K_h	hydration equilibrium constant	[ ]
$\Delta_\text{h} H^\circ$	standard enthalpy of hydration	[eV]
$\Delta_\text{h} S^\circ$	standard entropy of hydration	[k_B]
K_III	H$_2$O-doping association equilibrium constant	[cm^{-3}]
K_II	H$_2$O-doping extrinsic equilibrium constant	[cm^{-6}]
K_I	H$_2$O-doping intrinsic equilibrium constant	[ ]
U_M	Madelung energy	[eV]
J	Coulombic interaction parameter	[eV]
$G(T, p, n)$	Gibbs free energy (free enthalpy)	[eV]
μ_j	chemical potential of j	[eV]

Symbol

a_j	activity of j	[ ]
c	concentration	[ ]
p_{H_2O}	equilibrium water partial pressure	[bar]
n_j	stoichiometric coefficient / number of moles of j	[/ mol]
y_j	mole fraction of j	[ ]
φ_j	volume fraction of j	[ ]
x	degree of hydration	[ ]
E_A	activation energy (enthalpy)	[eV]
$\Delta_m H_j$	migration enthalpy of j	[eV]
$\Delta_m S_j$	migration entropy of j	[k_B]
Δ_{JRM}	high frequency activation energy (enthalpy)	[eV]
δ_{JRM}	energetic mismatch parameter between neighbouring sites	[eV]
δ'_{JRM}	high frequency relaxation parameter between neighbouring sites	[eV]
ΔH_{SCN}	relaxation enthalpy of SCN$^-$	[eV]
u_j	mobility of j	[cm$^2 \cdot$ (Vs)$^{-1}$]
ν_0	jump attempt frequency	[Hz]
$\overline{k}$	surface exchange constant	[cm/s]
$D^*(j)$	tracer diffusion coefficient of j	[cm^2/s]
T_1	spin-lattice relaxation time	[s]
T_2	spin-spin relaxation time	[s]
D_1	NMR remagnetization dwell time	[s]
Δ	diffusion time	[s]
δ	length of the magnetic field pulse	[s]
G	gradient strength of the magnetic field pulse	[T/m]
$M(G)/M(0)$	area of the Fourier transformed attenuating spin-echo signal of the measured / maximum value	[ ]

Symbol

δ_{iso}	NMR chemical shift	[ppm]
I	nuclear spin quantum number	[ ]
γ_j	gyromagnetic ratio of nucleus j	$[\mathrm{rad} \cdot \mathrm{s}^{-1} \mathrm{T}^{-1}]$
T_{c}	onset temperature of motional narrowing	[K]
σ	conductivity	[S/cm]
$\omega_n \ / \ \tau_n$	characteristic frequency / relaxation time n	[Hz / s]
R	resistance	[Ω]
E	voltage	[V]
$\langle t_j \rangle$	transference number of j	[ ]
z_j	charge (number) of j	[ ]
ε_{r}	dielectric constant	[ ]
C_{eff}	effective capacitance	[F]
Q	magnitude of CPE	[ ]
n	exponent of CPE	[ ]
Z	cell formula units	[ ]
N	number of neighbouring sites	[ ]
N_j	number of available lattice sites for j	$[\mathrm{cm}^{-3}]$
g_j	degeneracy of the lattice site of j	[ ]
α_j	number of occupiable sites of j	[ ]
γ	parameter to quantify order of phase transition	[ ]
f	Madelung constant	[ ]
f_{d}	effective Madelung constant of the defect superlattice	[ ]
b	distance between nearest neighbours	[cm]
r_j	distance to a neighbouring available site of j	[cm]
d	interlayer spacing	[Å]
L	sample thickness	[cm]
A	electrode area	$[\mathrm{cm}^2]$

Symbol		
V_j	volume of j	[cm^3]
$\Delta V(T)$	volume expansion	[cm^3]
ρ	density	[g/cm^3]
M	molar mass	[g/mol]
T	temperature	[K]
t	time	[s]
ε_0	electrical permittivity of free space	[ ]
e	charge of an electron	[C]
k_{B}	Boltzmann's constant	[eV/K]
N_{A}	Avogadro constant	[1/mol]

Table A.2: List of abbreviations used in this thesis.

Abbreviation	
CPE	constant phase element
DC	direct current
DFT	density functional theory
DSC	differential scanning calorimetry
EDX	energy dispersive X-ray
EMF	electromotive force
EIS	electrochemical impedance spectroscopy
FWHM	full width at half maximum
GB	grain-boundary
ICP-OES	inductively coupled plasma optical emission spectroscopy
IR	infrared
MAS	magic angle spinning
OCV	open-circuit voltage
PFG	pulsed field gradient
RF	radio frequency
SEI	solid electrolyte interface
SEM	scanning electron microscopy
ssNMR	solid state nuclear magnetic resonance
SXRD	single crystal X-ray diffraction
TGA	thermogravimetric Analysis
XPS	X-ray photoelectron spectroscopy
XRPD	X-ray powder diffraction

B | Supplemental

B.1 Anhydrous Lithium Thiocyanate LiSCN
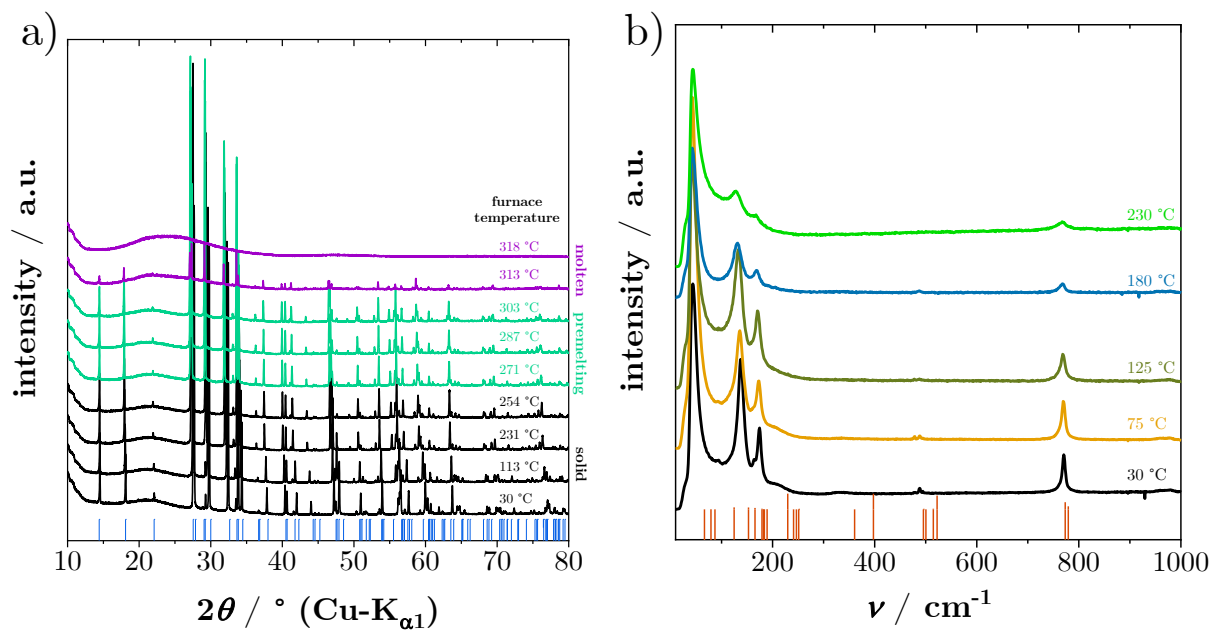
Figure B.1: Temperature dependent *in situ* measurements of anhydrous LiSCN by a) XRPD and b) Raman spectroscopy. Blue bars in (a) correspond to the crystal structure of LiSCN in literature,[22] and red bars in (b) to calculated bands of LiSCN (calculated by Florian Pielnhofer).
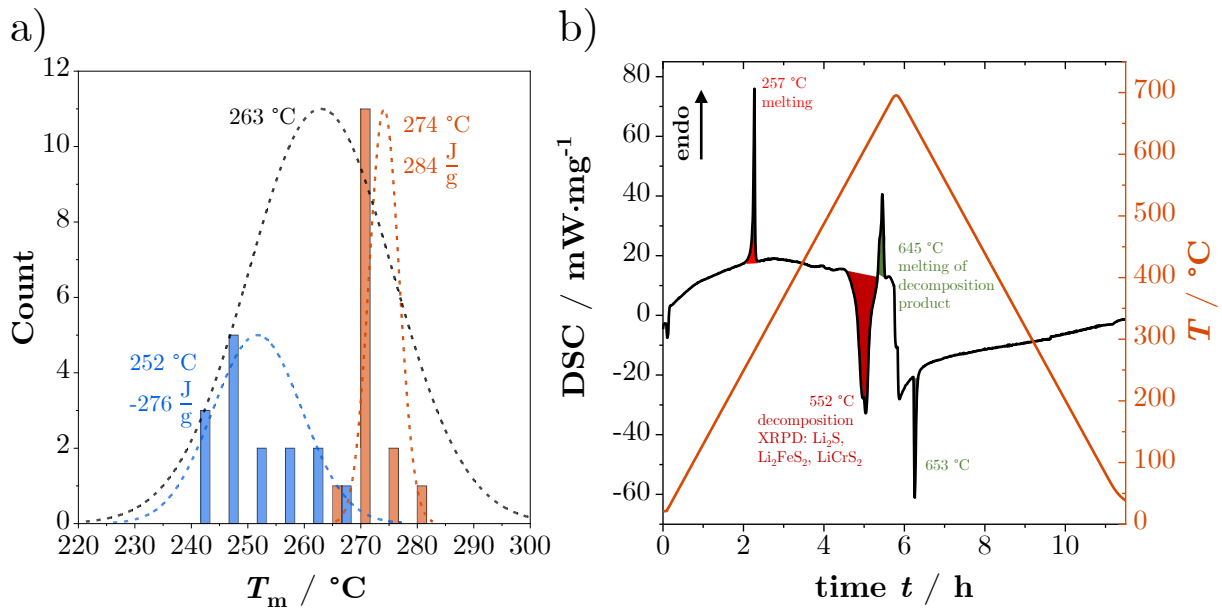
Figure B.2: Collection of DSC measurements for anhydrous LiSCN; a) Statistical result for melting (red) and recrystallisation (blue) temperatures within the stability range of LiSCN. b) DSC measurement beyond the stability range of LiSCN in a steel crucible.
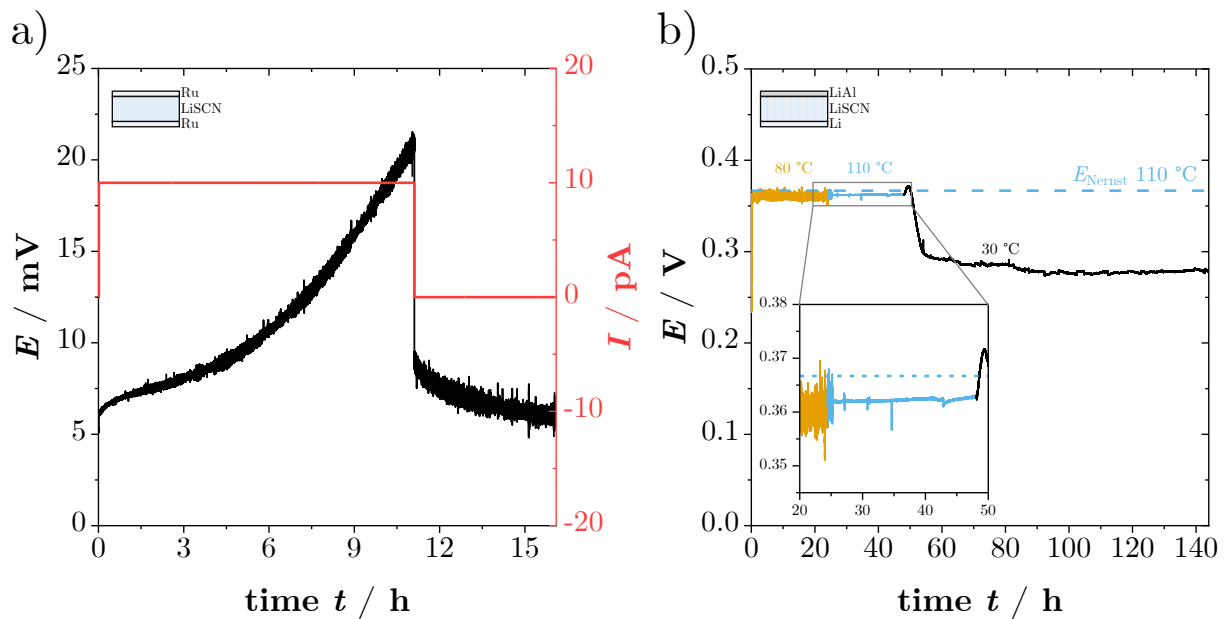
Figure B.3: DC measurements of anhydrous LiSCN with a) Li$^+$ ion blocking (30 °C in 100 ml/min N$_2$ flow) and b) Li$^+$ ion reversible electrodes (100 ml/min Ar flow). The dashed blue line in (b) corresponds to the Nernst voltage of Li-LiAl electrodes at 110 °C.[199]
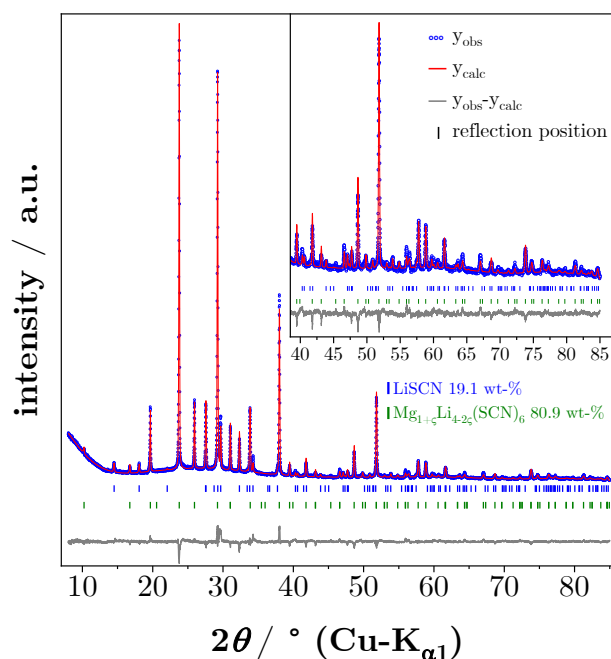
Figure B.4: Rietveld plot to determine the structure of $Mg_{1+\varsigma}Li_{4-2\varsigma}(SCN)_6$. The mixed occupancy of Li and Mg was estimated as $\varsigma = 0.02$ according to Rietveld refinement.
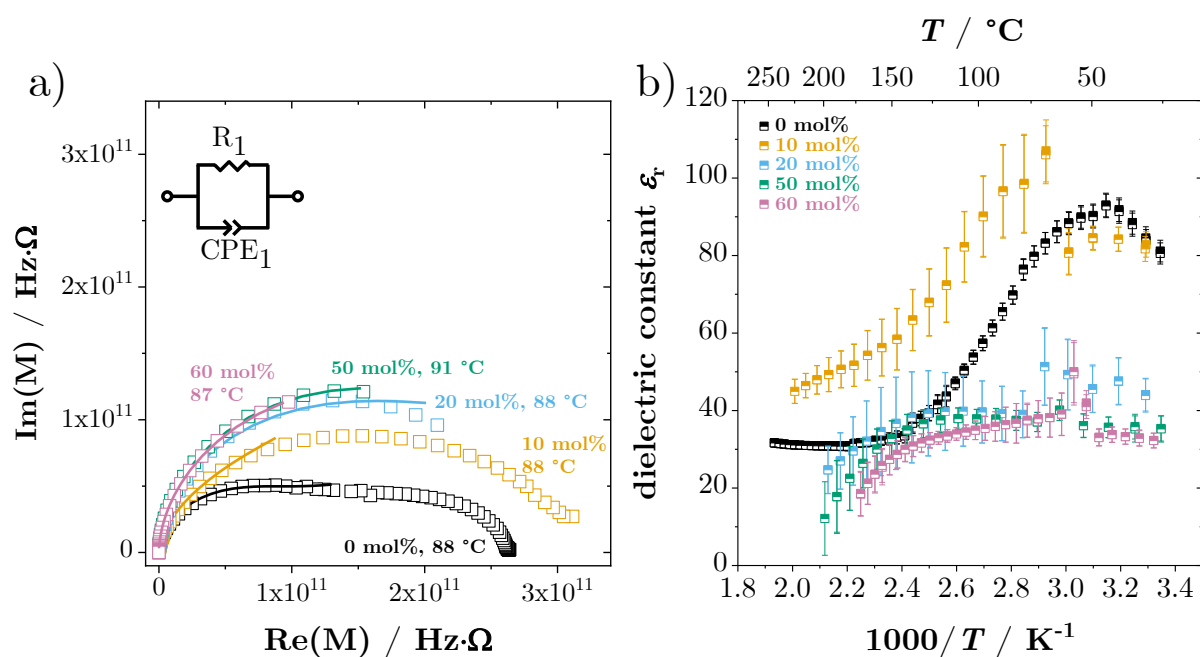
Figure B.5: a) Complex modulus spectra and b) dielectric constants ε_r of various LiSCN + $Mg_{1+\varsigma}Li_{4-2\varsigma}(SCN)_6$ ($\varsigma = 0.02$) sample mixtures. The molar percentages refer to the synthesis conditions, i.e. LiSCN + Υ mol% $Mg(SCN)_2$ ($\Upsilon = 0$, 10, 20, 50, 60 mol%). Spectra in (a) were fit with the shown equivalent circuit within the respective frequency range.
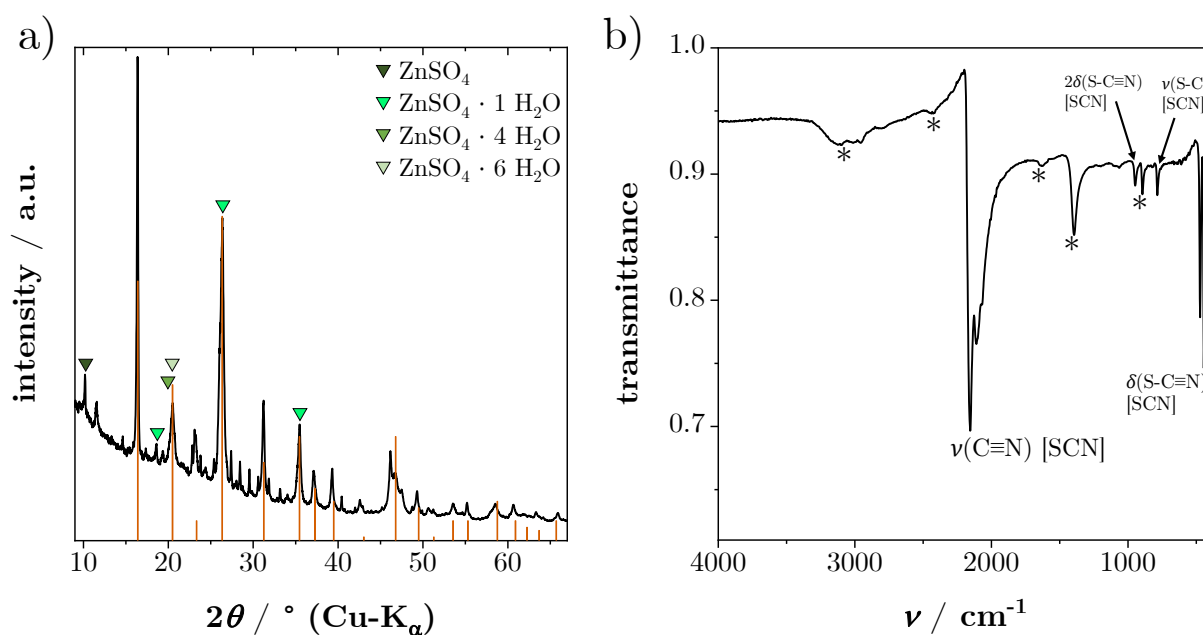
Figure B.6: a) XRPD pattern and b) IR spectrum of synthesized $Zn(SCN)_2$ (cf. section 5.2). The red bars in (a) correspond to a reference pattern from literature.[207] The IR peaks in (b) marked with asterisks belong to contaminants, most likely $ZnSO_4$ hydrates.[208]

element	at.-%				
Zn	11.30	12.55	13.25	11.84	12.14
S	37.09	27.85	28.52	23.35	22.37
C	48.75	34.81	53.02	36.66	37.40
N	-	23.50	-	25.89	24.69
O	2.83	1.30	5.15	2.24	3.32
Al	0.03	0.00	0.06	0.02	0.08

element	wt.-%	at.-%	ratio
Zn	35.1 ± 0.4	0.534 ± 0.006	1
S	36.1 ± 0.4	1.17 ± 0.01	2.2
C	13.0 ± 0.2	1.08 ± 0.02	2.0
N	13.7 ± 0.2	0.98 ± 0.01	1.8
Ba	1.97 ± 0.06	0.0143 ± 0.0004	0.03
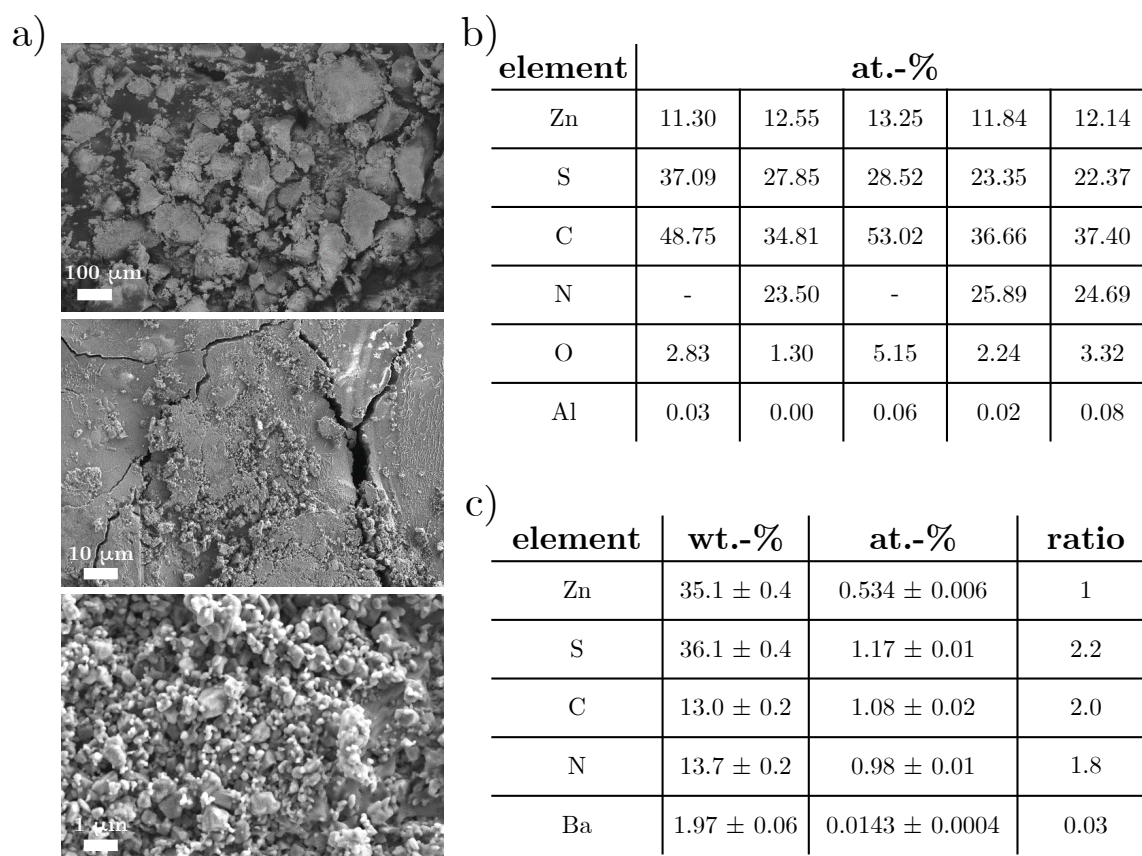
Figure B.7: a) SEM micrographs, b) EDX analysis and c) ICP-OES analysis of synthesized $Zn(SCN)_2$.
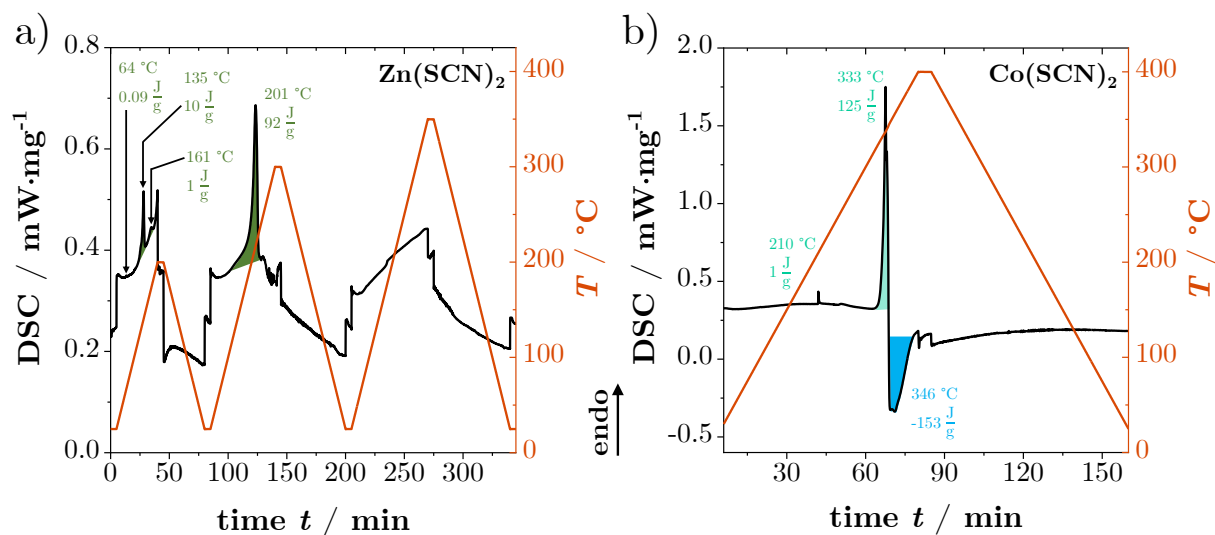
Figure B.8: DSC measurements of the donor dopants; a) $Zn(SCN)_2$ and b) $Co(SCN)_2$, with a heating and cooling rate of 5 K/min.

atom	Spectrum 43		Spectrum 44		Spectrum 45	
	at.-%	at.-% sigma	at.-%	at.-% sigma	at.-%	at.-% sigma
N	41.8	0.4	63.0	0.4	50.9	0.4
O	3.6	0.1	4.0	0.1	12.3	0.2
Mg	0.18	0.06	0.24	0.05	2.20	0.08
Si	0.21	0.06	0.14	0.06	0.37	0.07
S	54.2	0.2	32.6	0.2	34.2	0.2

atom	Map	
	at.-%	at.-% sigma
N	25.6	0.1
O	33.68	0.08
Na	0.71	0.02
Mg	2.62	0.03
Si	0.81	0.02
S	36.57	0.06
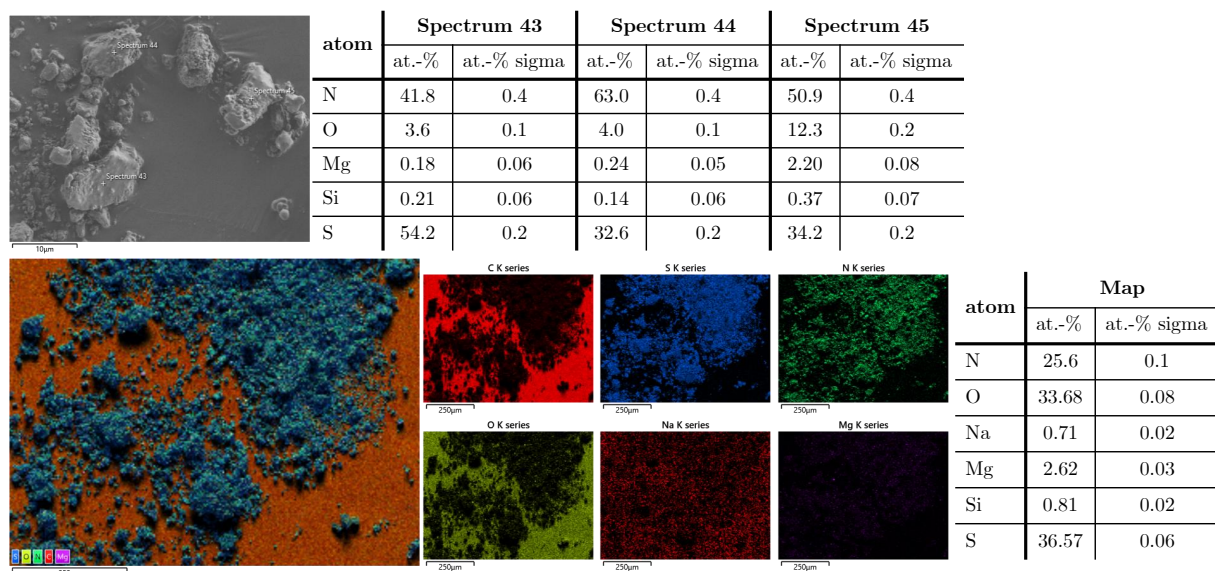
Figure B.9: EDX analysis of a 5.0 mol% Mg^{2+}-doped LiSCN sample by measuring either individual grains (top) or by performing a map analysis (bottom).
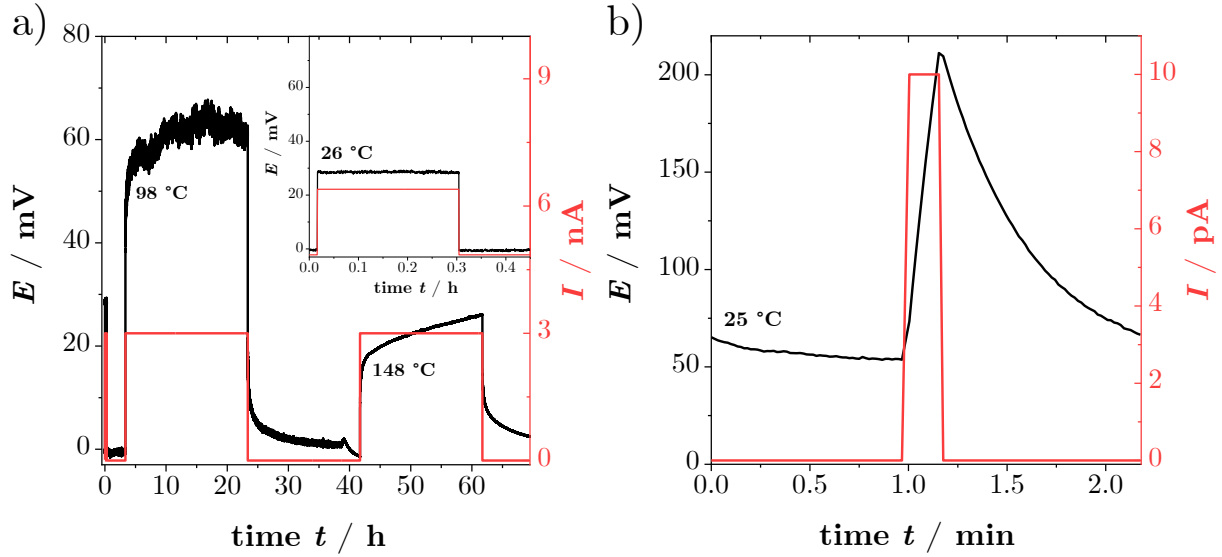
Figure B.10: Li$^+$ ion blocking DC polarisation measurements of a) 1.5 mol% Co^{2+}-doped and b) 1.5 mol% Zn^{2+}-doped LiSCN.
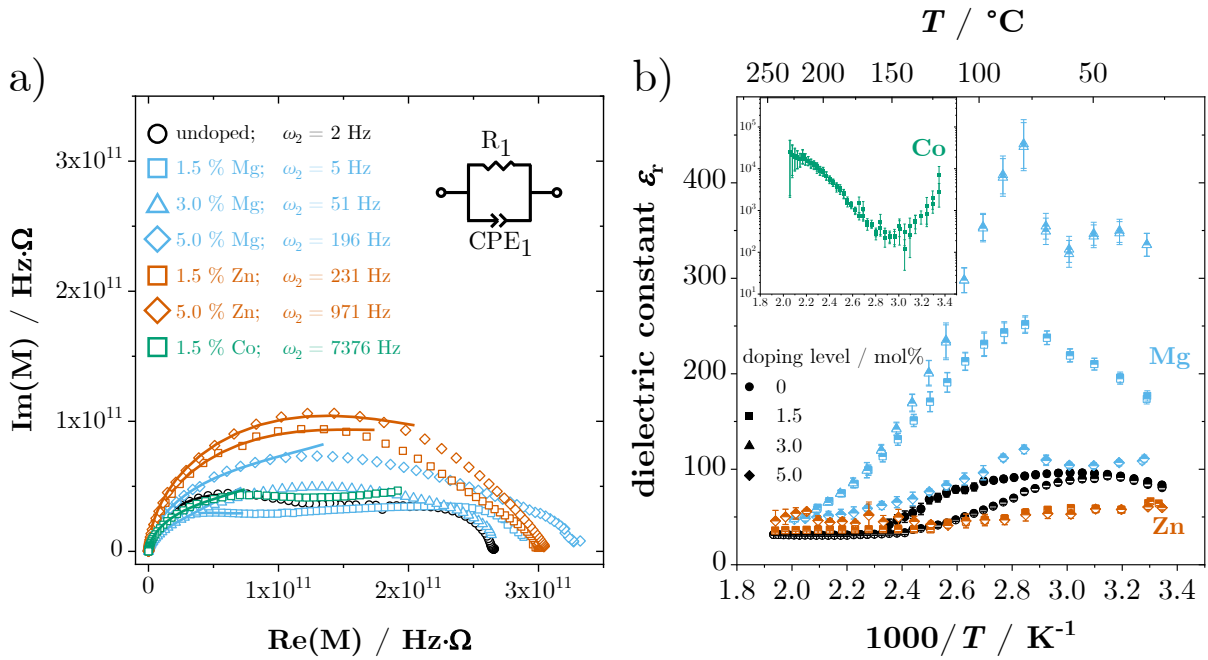
Figure B.11: a) Complex modulus spectra (68-69 °C) and b) dielectric constants ε_r of donor doped LiSCN, employing Mg(SCN)$_2$, Zn(SCN)$_2$ and Co(SCN)$_2$ as dopants. Spectra in (a) were fitted with the shown equivalent circuit.
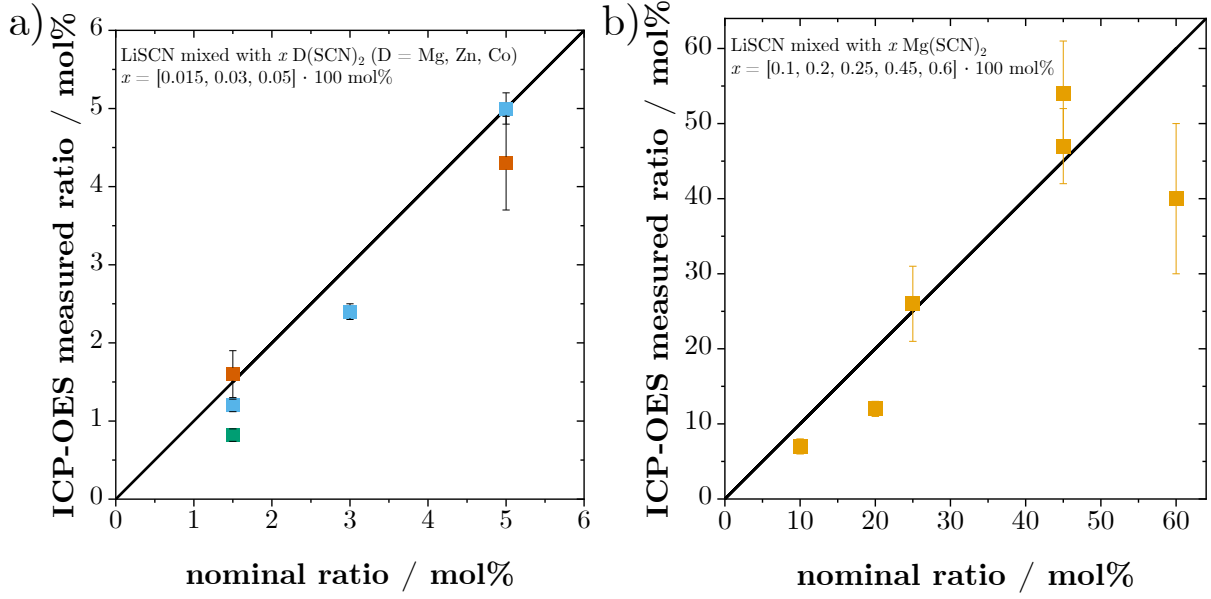
Figure B.12: ICP-OES measured molar ratios of Li, Mg, Zn and Co in a) doped LiSCN samples, and b) mixtures of LiSCN + $Mg_{1+\varsigma}Li_{4-2\varsigma}(SCN)_6$ ($\varsigma = 0.02$). Solid lines are linear fits.
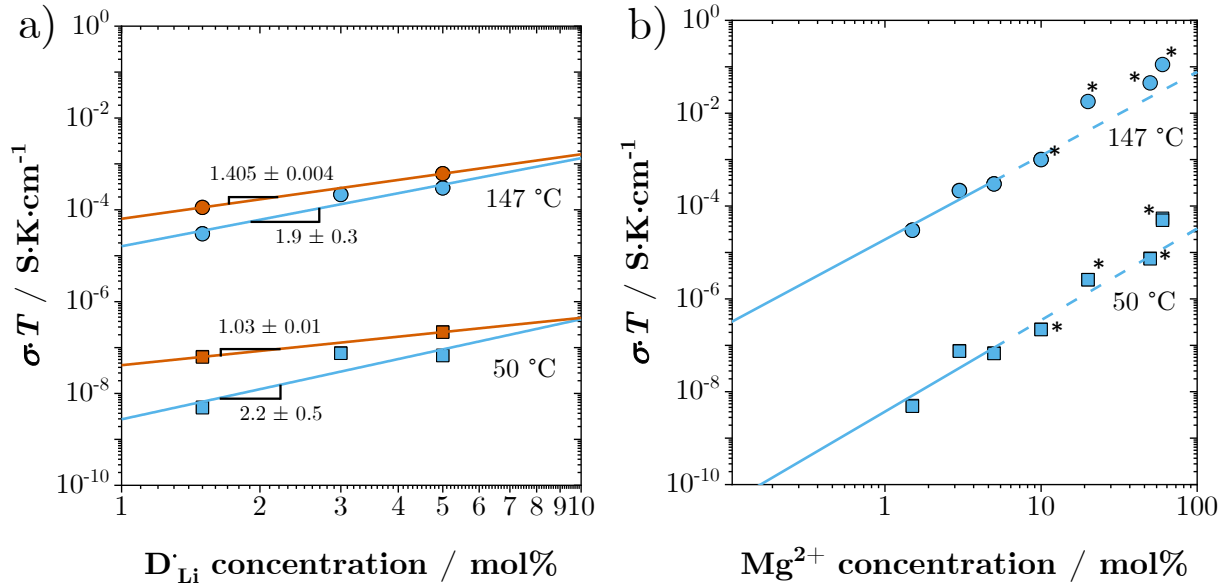
Figure B.13: Measured conductivities at 50 and 147 °C: a) Mg^{2+}- (blue) and Zn^{2+}- (red) doped LiSCN; b) Mg^{2+}-doped LiSCN and mixtures of LiSCN and $Mg_{1+\varsigma}Li_{4-2\varsigma}(SCN)_6$ ($\varsigma = 0.02$) as a function of dopant $D_{Li}^{\cdot}$ or Mg^{2+} concentration. Solid lines are linear fits to the data, and the slopes of the blue lines in (a) and (b) are the same.
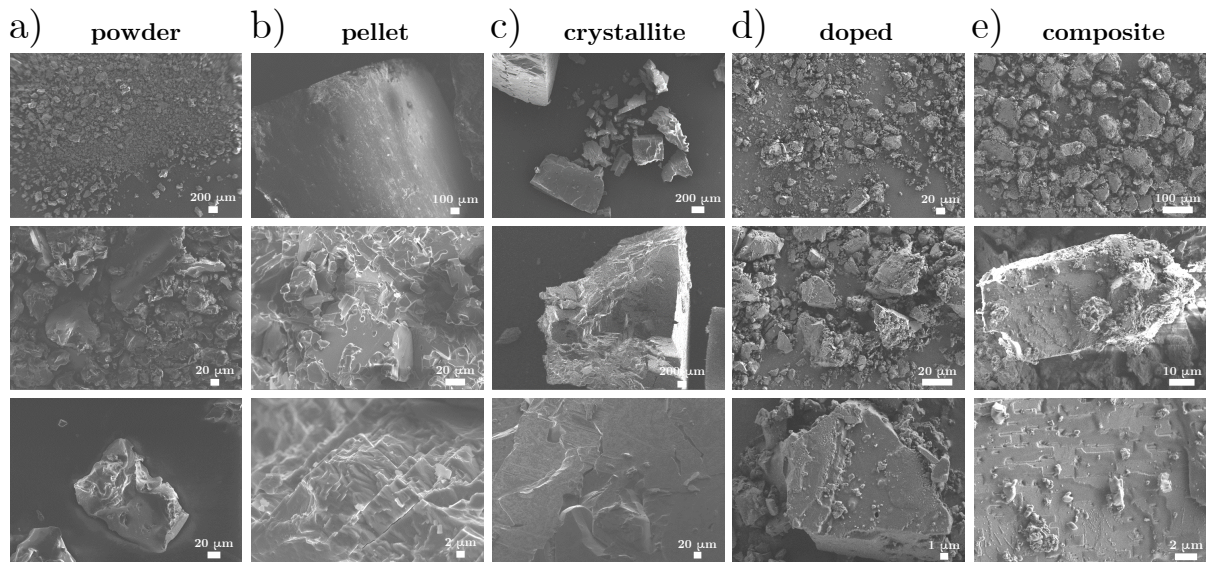
Figure B.14: SEM images of various LiSCN samples: a) loose powder, b) compacted pellet, c) melt-grown crystallites, d) 1.5 mol% Mg^{2+}-doped LiSCN, and e) mixture of LiSCN and $Mg_{1+\varsigma}Li_{4-2\varsigma}(SCN)_6$ ($\varsigma = 0.02$).
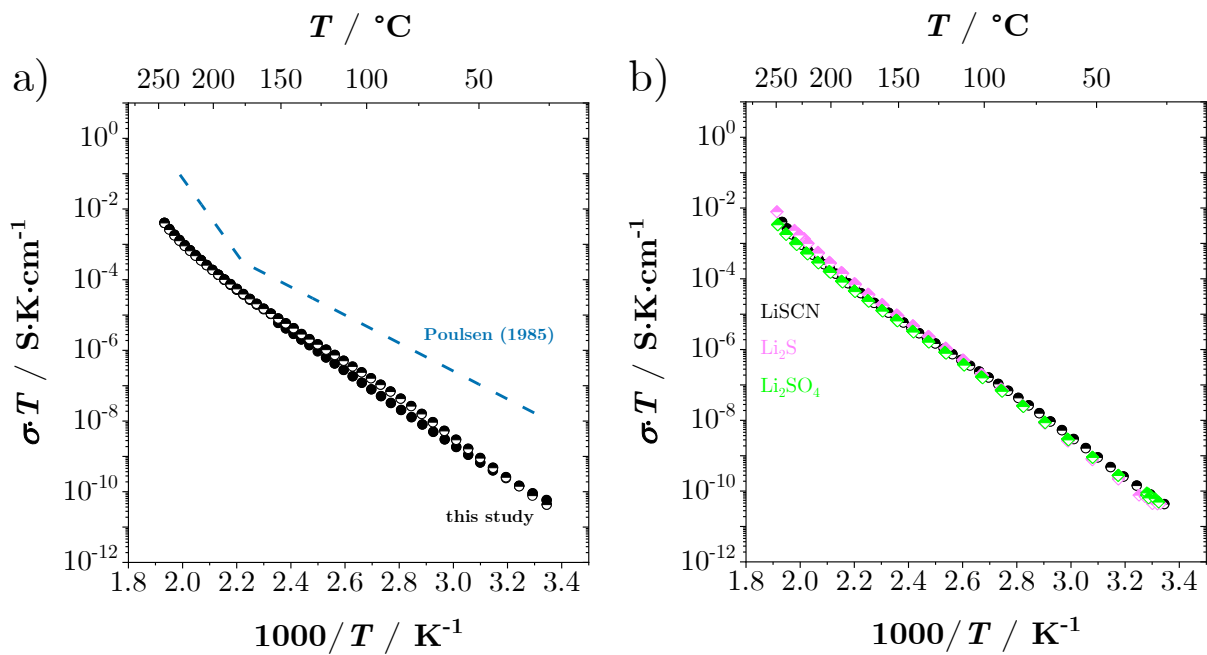
Figure B.15: a) Comparison of the low frequency (DC) conductivity of undoped, anhydrous LiSCN to previously reported values by Poulsen in 1985.[43] b) Measured conductivity of attempted LiSCN acceptor doping with Li_2S (magenta) and Li_2SO_4 (green) compared to nominally undoped LiSCN (black).
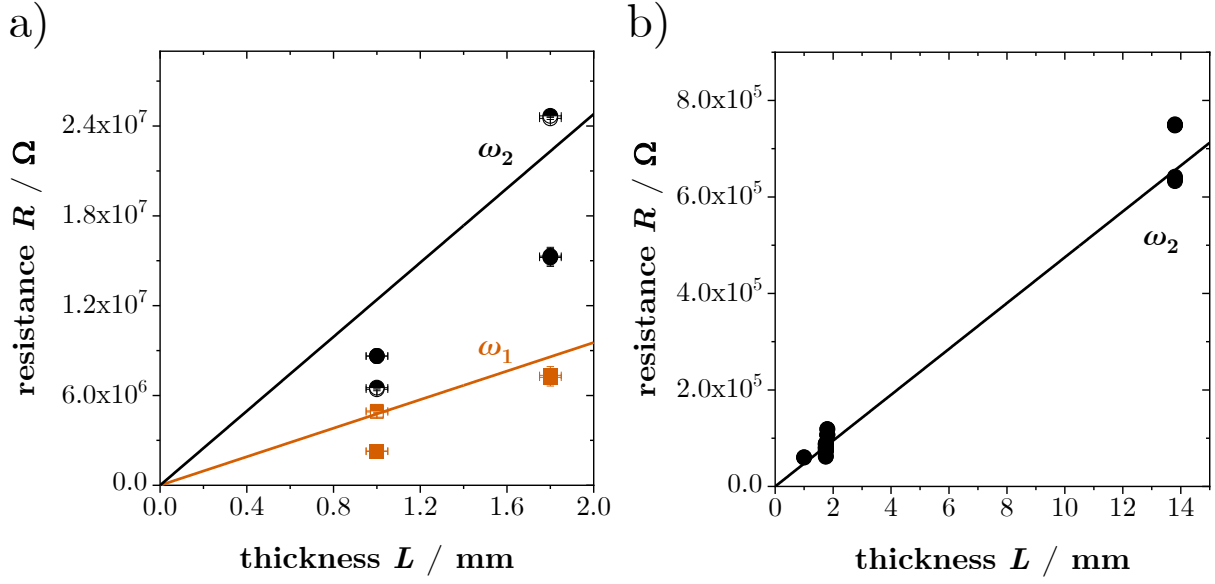
Figure B.16: Measured resistance R as a function of pellet thickness L for anhydrous LiSCN samples: a) both high (ω_1) and low (ω_2) frequency signals extracted with the circuit shown in Figure 6.9a at 157-162 °C; b) only the low frequency resistance corresponding to ω_2.
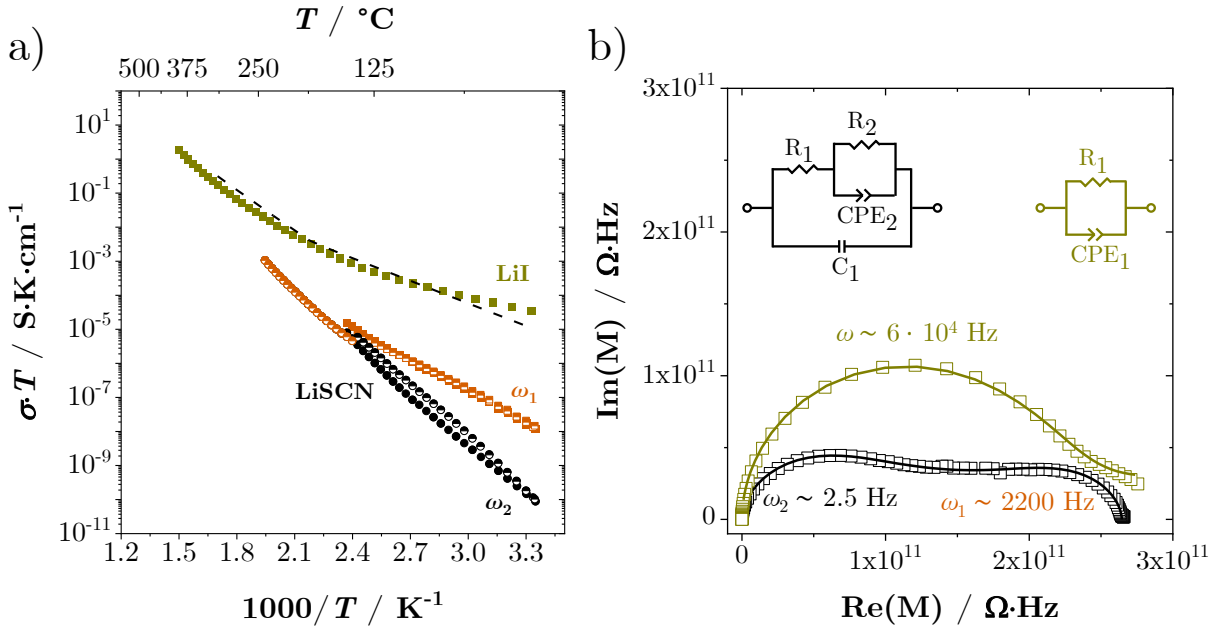
Figure B.17: Comparison of a) the conductivities and b) the complex moduli of anhydrous LiSCN and LiI. The dashed line in (a) corresponds to literature values of LiI.[74] Spectra in (b) were fitted with the shown equivalent circuits, respectively.

The LiI was purchased from *Sigma Aldrich* and dried at 300 °C under dynamic vacuum ($p \leq 10^{-2}$ mbar) at a Schlenk line. The pellet was cold pressed and sputtered as described in section 5.3 (relative density 94 %) and section 5.6 for anhydrous LiSCN, and measured under high dynamic vacuum (cell 1, $p \leq 3 \cdot 10^{-3}$ mbar). Around 400 °C, the sample started

to sublimate and a cooling run could not be measured.
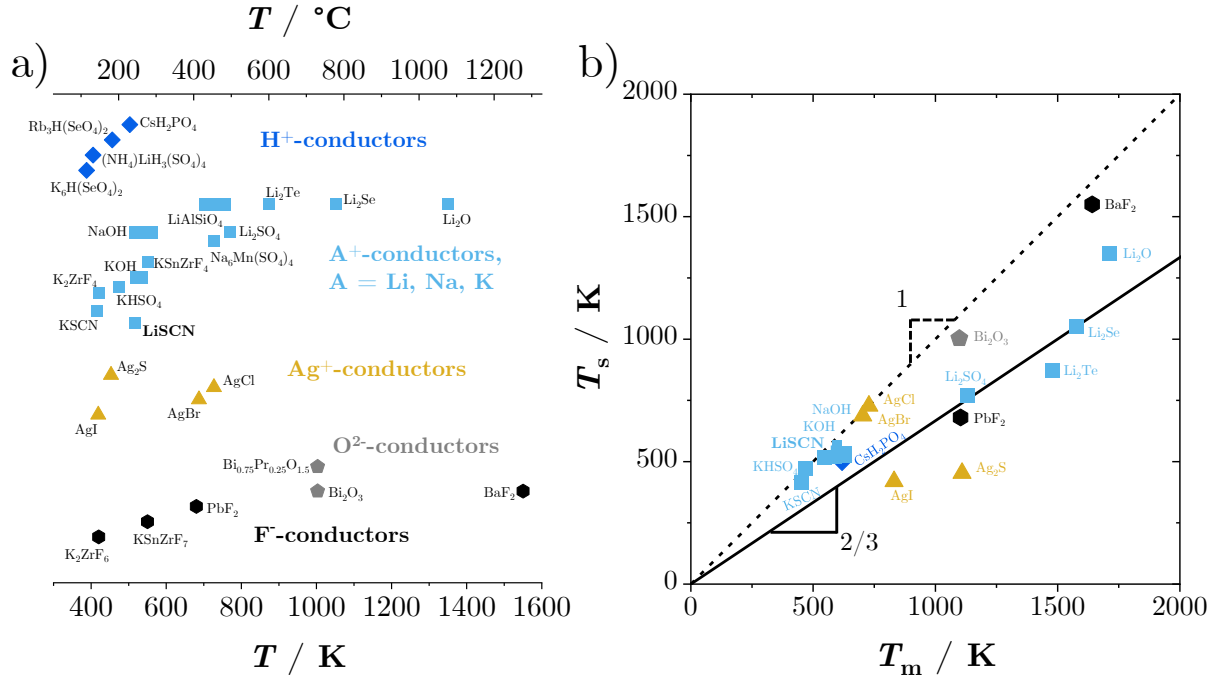
Figure B.18: a) Overview of superionic transition temperatures for various material systems, including; F$^-$-conductors,[148, 209] O^{2-}-conductors,[149, 210] Ag$^+$-conductors,[148, 211] A$^+$-conductors (A = Li,[138, 212, 213] Na,[214, 215] K[119, 209, 215, 216]) and H$^+$-conductors.[217–220] b) Graphical depiction of the Tammann rule with selected materials shown in (a). T_s and T_m are the superionic transition temperature and melting point, respectively.

B.2 Hydrated Lithium Thiocyanate LiSCN $\cdot\,x\,$H$_2$O
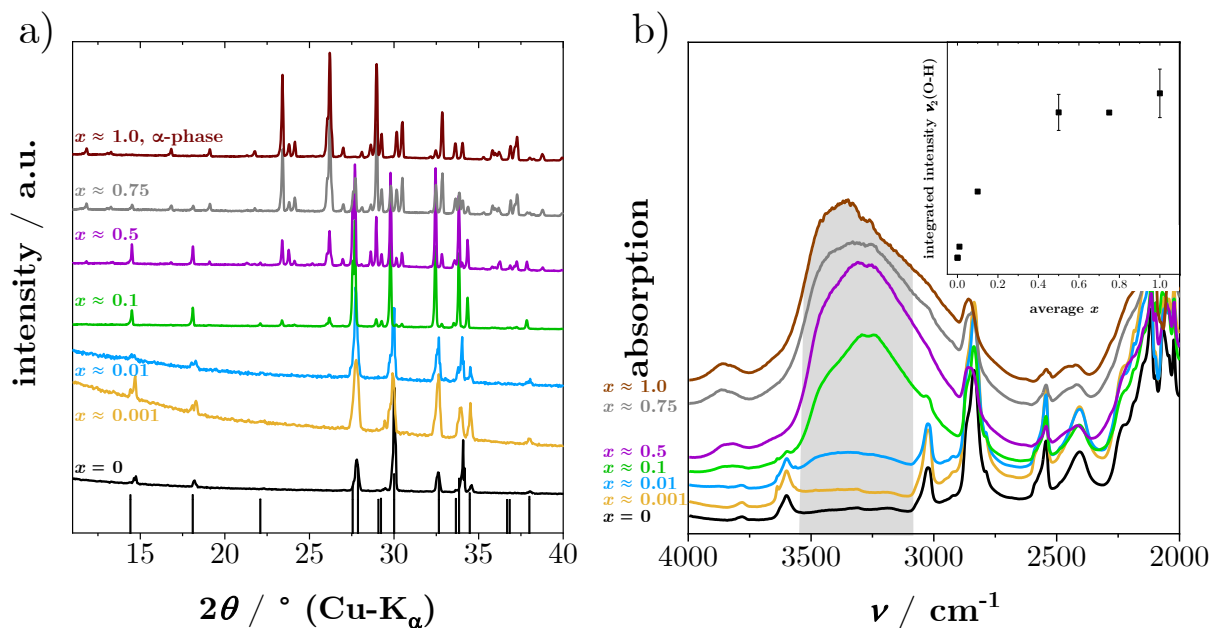
Figure B.19: a) XRPD patterns and b) IR spectra of synthesized LiSCN $\cdot x\,$H$_2$O samples. The inserted black bars in (a) correspond to $x = 0$,[22] and the insert in (b) shows the comparison of x from integrating the shaded area (ν_2(O $-$ H)) with the nominal value.

At higher x values the data points flatten and strongly deviate from the nominal value. This is because the integration of the ν_2(O $-$ H) band underestimates x, considering that the peak at 2845 cm^{-1} (combination band ν_1(C $\equiv$ N) $+\,\nu_3$(C $-$ S))[221] apparently decreases. The values can therefore be regarded as a lower bound.
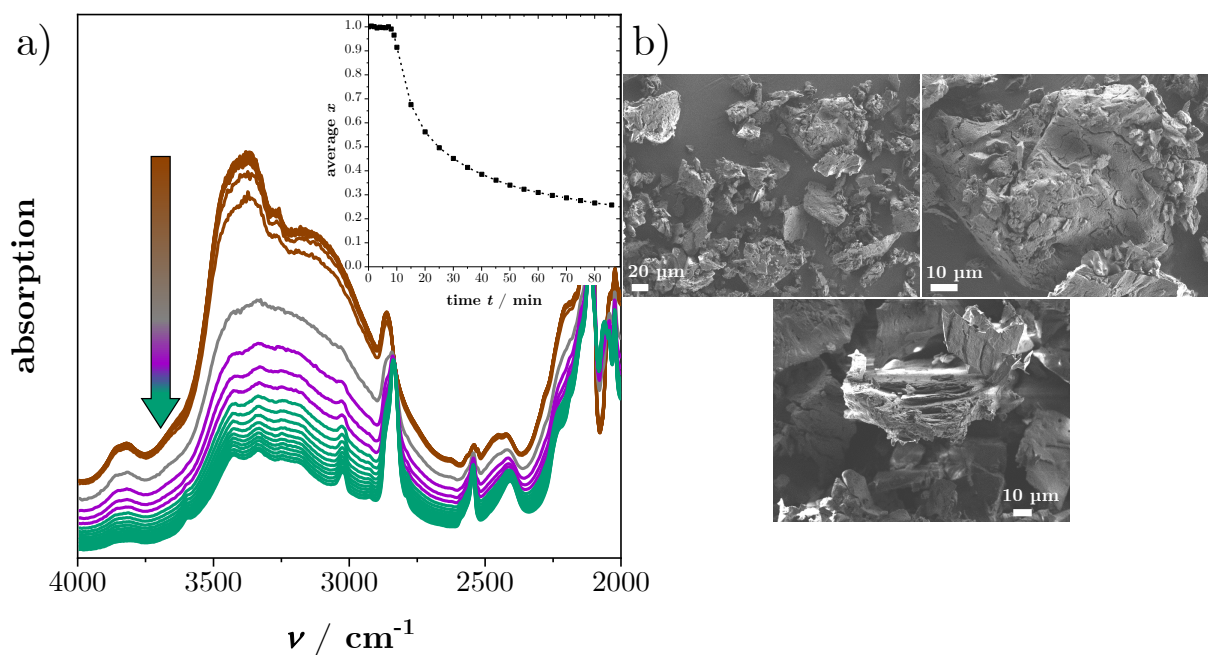
Figure B.20: a) Continuous recording of LiSCN $\cdot 1\,H_2O$ IR spectra inside a glove box to assess the velocity and magnitude of losses in x. The decrease in x over time shown in the inset corresponds to the $\nu_2(O-H)$ band of water. The velocity of the decrease in x varied between different samples. Many showed an even faster loss of water as presented here. b) SEM images recorded of a LiSCN $\cdot 1\,H_2O$ sample which had beforehand been pressed (5.1 kbar) and heated to 55 °C.
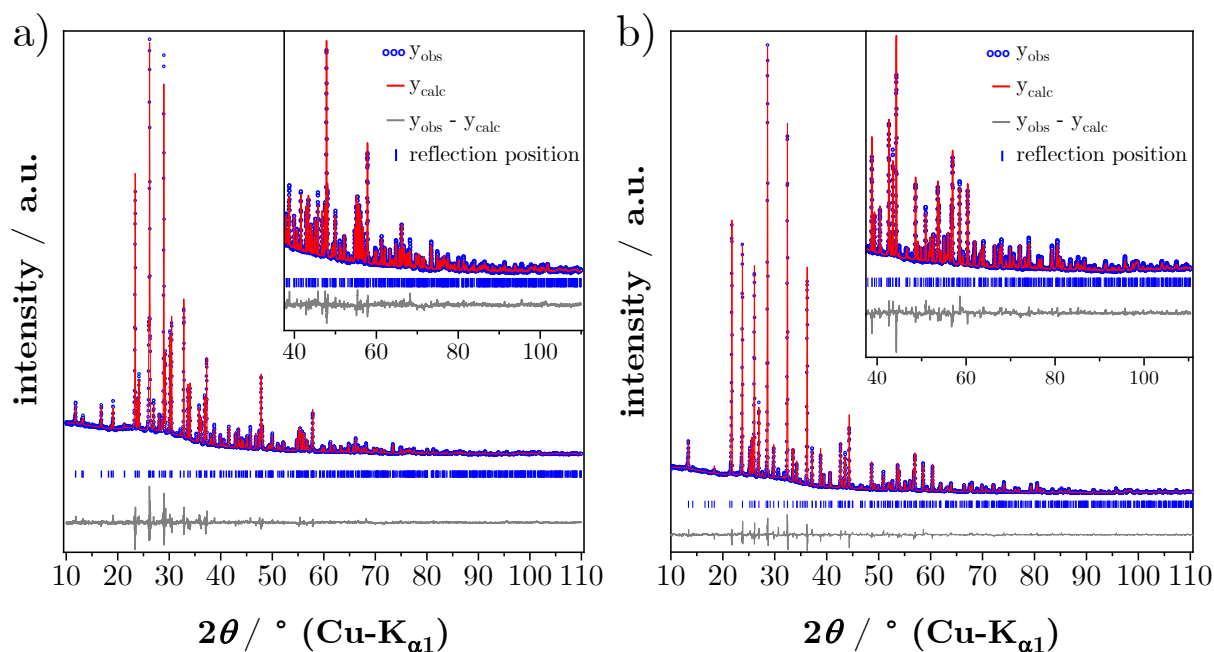
Figure B.21: Final Rietveld refinement of a) α- and b) β-LiSCN $\cdot 1\,H_2O$ with a respective magnification of the high diffraction angle region (inset).
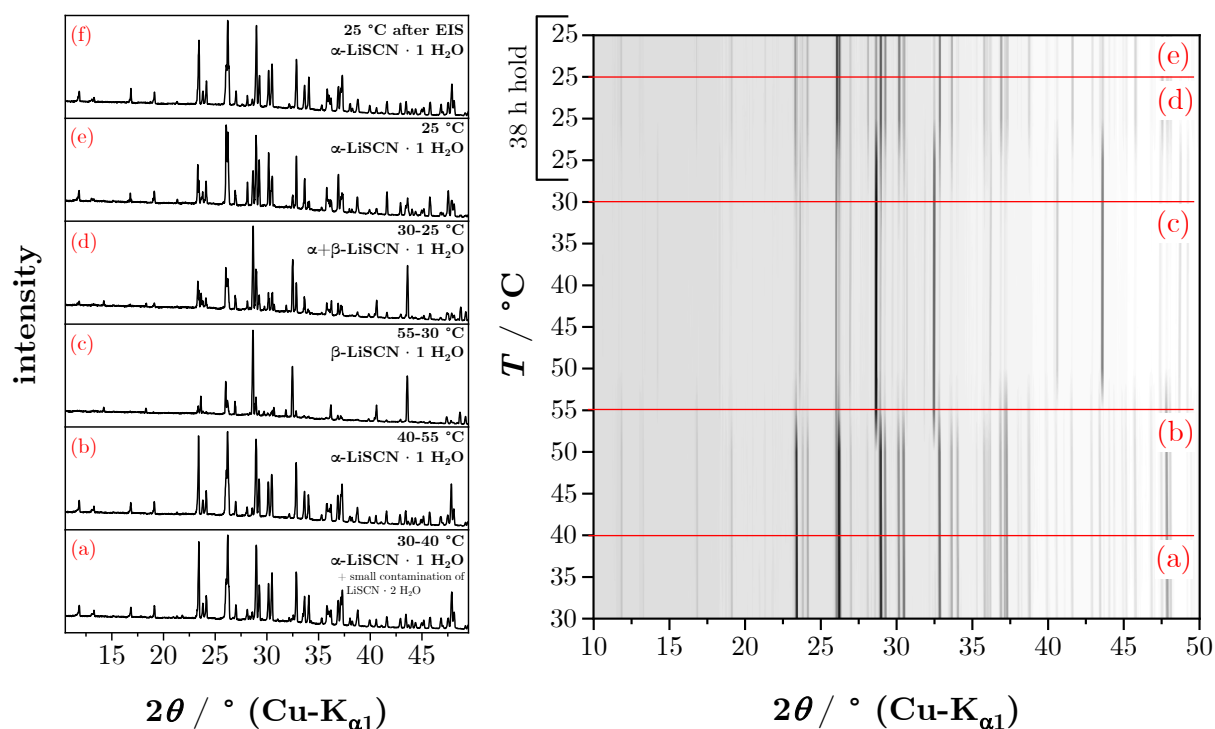
Figure B.22: Temperature dependent *in situ* XRPD measurement of LiSCN $\cdot\,1\,H_2O$ up to 55 °C, showing the α- to β-phase transition. The left hand side displays selected XRPD patterns.
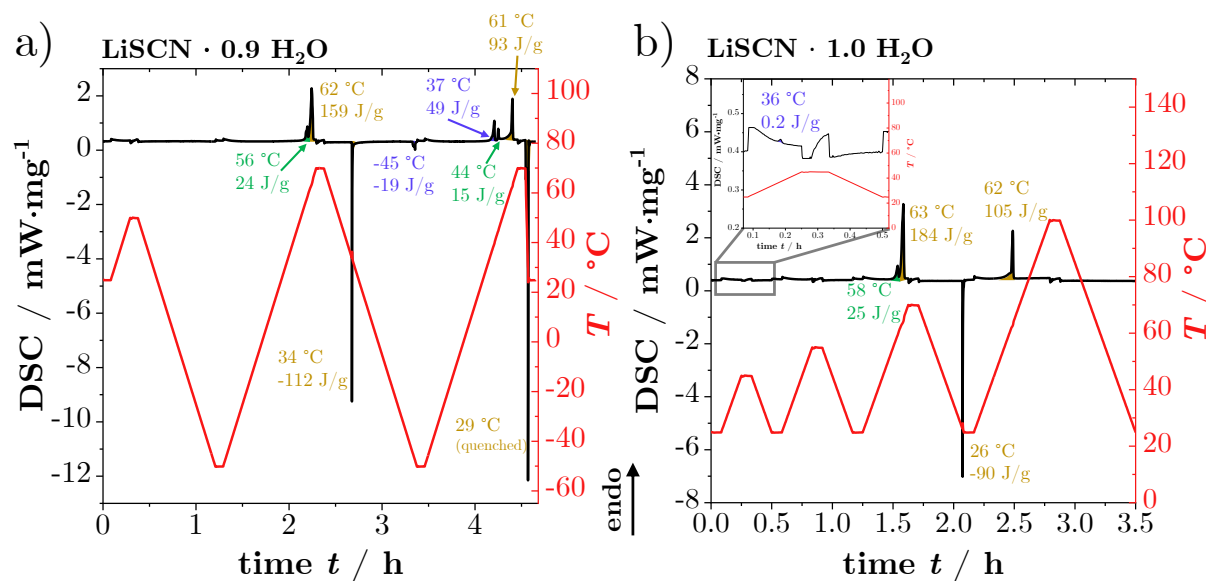
Figure B.23: Exemplary DSC measurements with multiple heating and cooling cycles of a) LiSCN $\cdot$ 0.9 H_2O and b) LiSCN $\cdot\,1\,H_2O$.
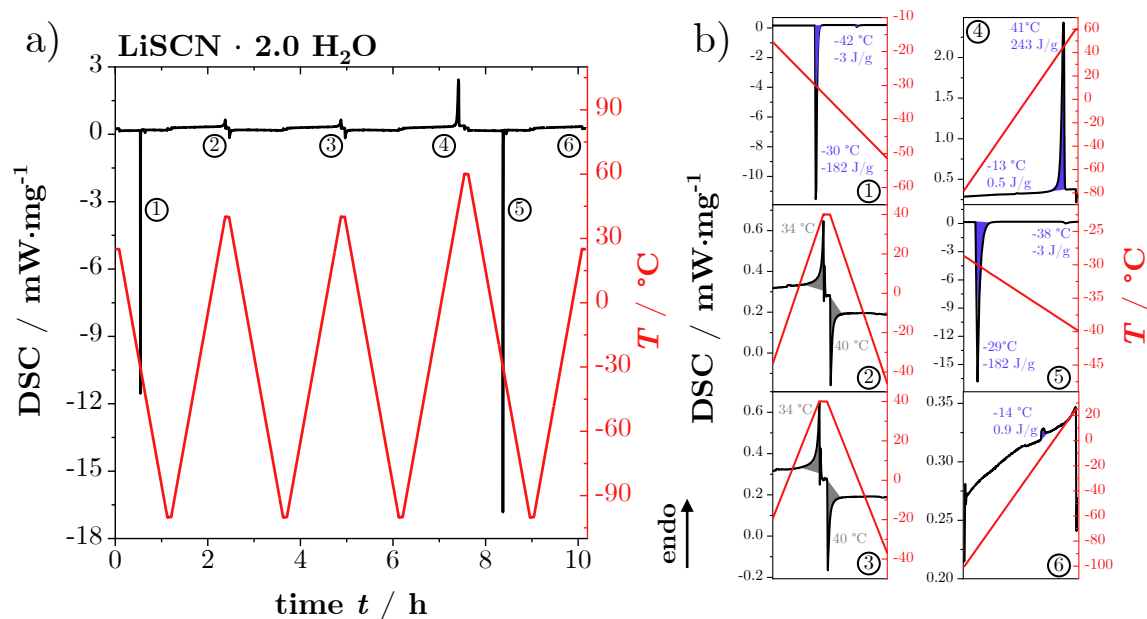
Figure B.24: DSC measurement of LiSCN $\cdot$ 2 H$_2$O with various heating and cooling cycles above and below room temperature (heating and cooling rate 2 K/min): a) full measurement, b) selected magnifications of occurring peaks. The gray coloured peaks in (2) and (3) are incomplete, as the temperature cycle was ended to early. Negligible signals are omitted for clarity.
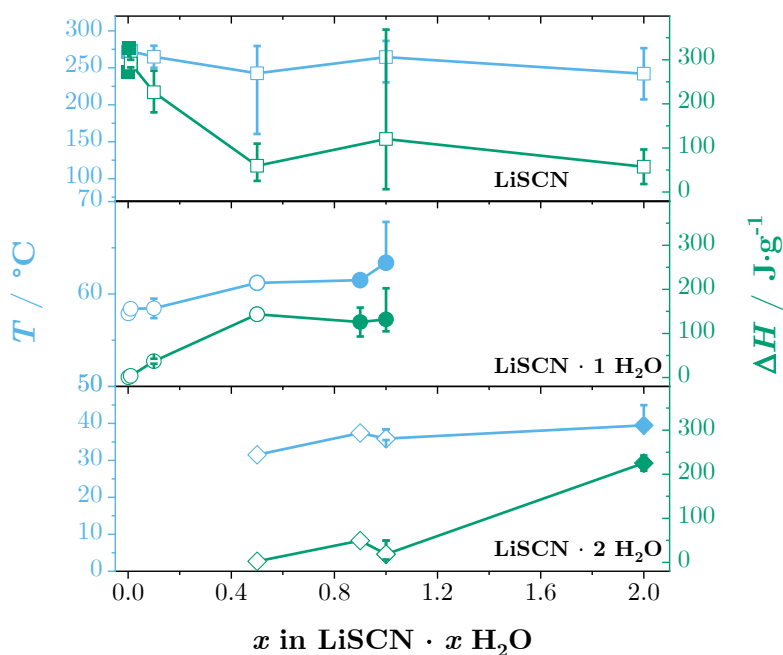
Figure B.25: Summary of melting temperatures (blue, left hand ordinate) and enthalpies (green, right hand ordinate) of various LiSCN $\cdot$ x H$_2$O samples obtained from DSC measurements. When x was a non-integer, a sample consisted of at least two phases (e.g. LiSCN $\cdot$ 1.1 H$_2$O = 0.9 LiSCN $\cdot$ 1 H$_2$O + 0.1 LiSCN $\cdot$ 2 H$_2$O), and the occurring peaks were assigned to the respective phases based on the melting points (open symbols). Above 100 °C water loss during measurements was unavoidable, and the thereafter occurring peaks corresponded to (partially) dried LiSCN.
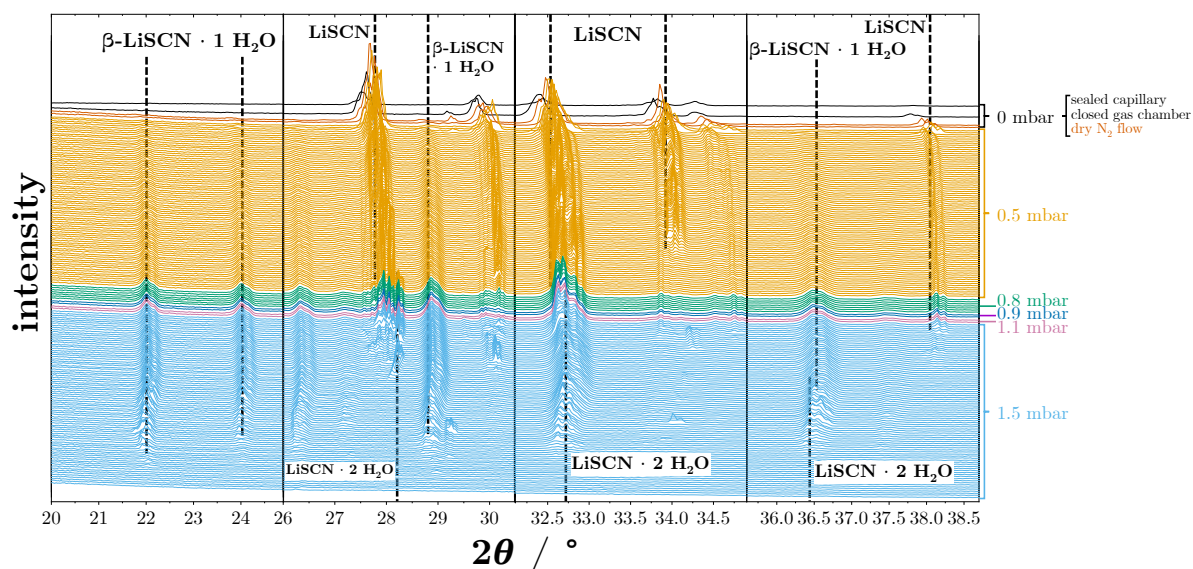
Figure B.26: Isothermal *in situ* XRPD measurements at 27 °C while varying the p_{H_2O} of the atmosphere near the LiSCN sample. Characteristic diffraction peaks of LiSCN $\cdot x\,H_2O$ phases are marked with dashed lines.
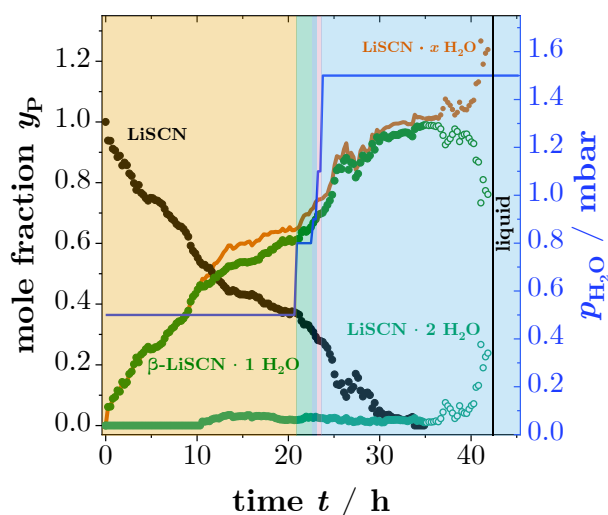
Figure B.27: Phase analysis results from Rietveld refinement of the XRPD patterns shown in Figure B.26. Full circles are mole fractions y_P of LiSCN (black), β-LiSCN $\cdot 1\,H_2O$ (olive) and LiSCN $\cdot 2\,H_2O$ (jade) compared to the average water uptake x (red line, left vertical scale). Open circles and the dotted red line are based on the scaling factor from the refinement.
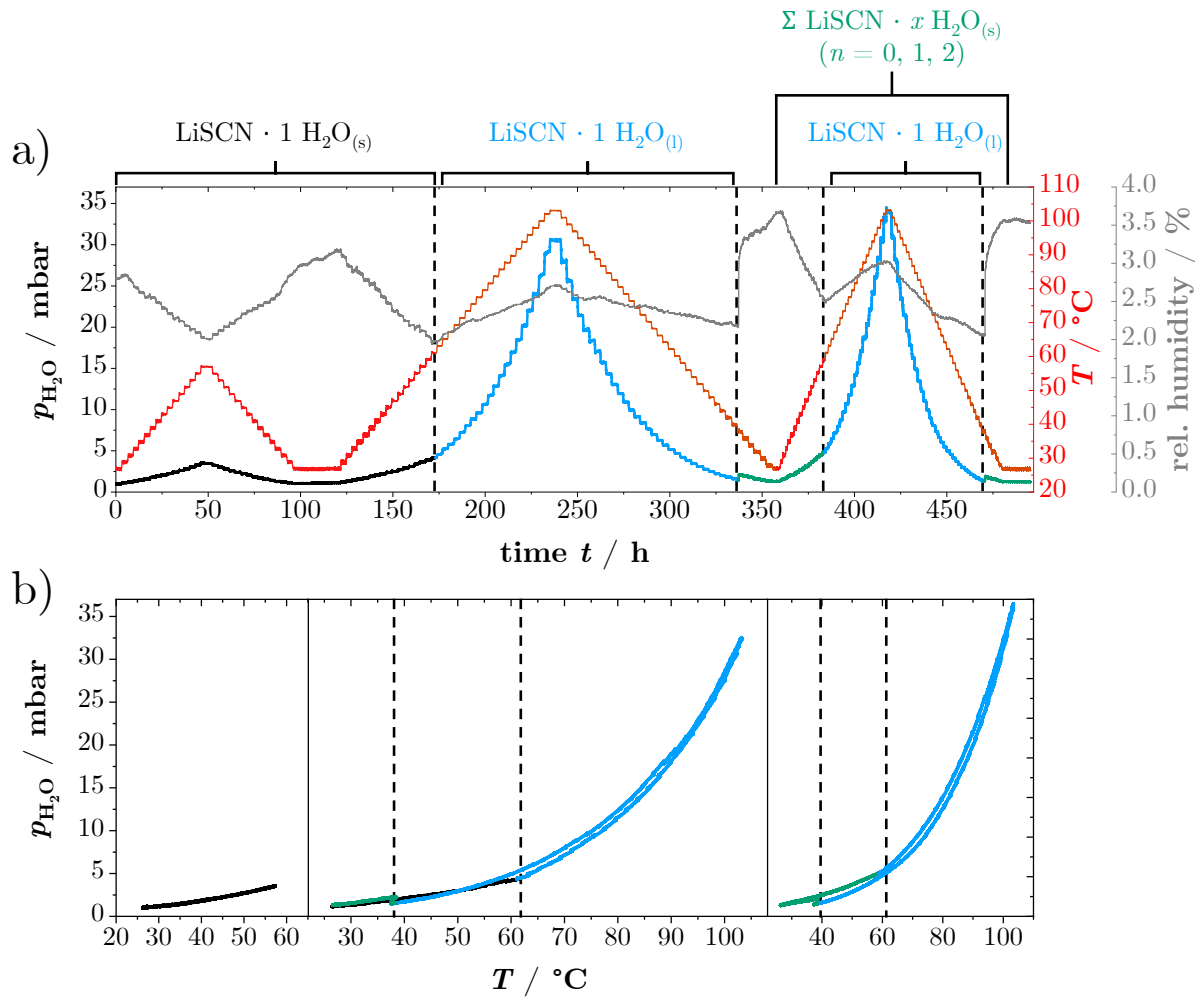
Figure B.28: Measurement of p_{H_2O} (and relative humidity) in solid and liquid LiSCN · $1\,H_2O$, showing the temperature dependent behaviour as a function of a) time and b) temperature.
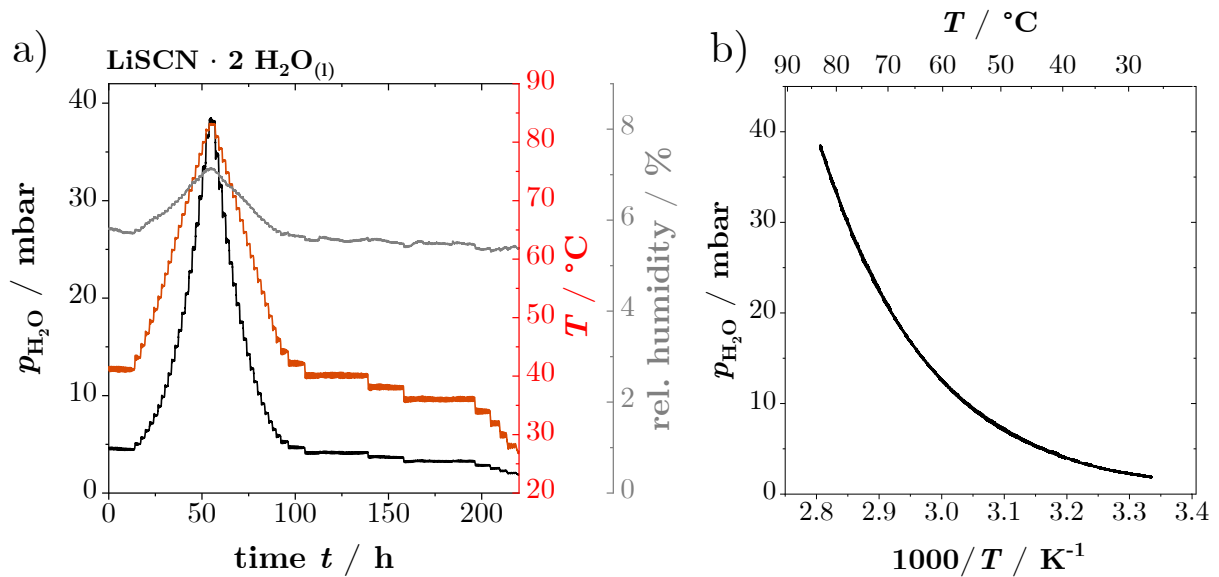
Figure B.29: Measurement of p_{H_2O} (and relative humidity) in liquid LiSCN $\cdot$ 2 H$_2$O, showing the temperature dependent behaviour as a function of a) time and b) inverse temperature.
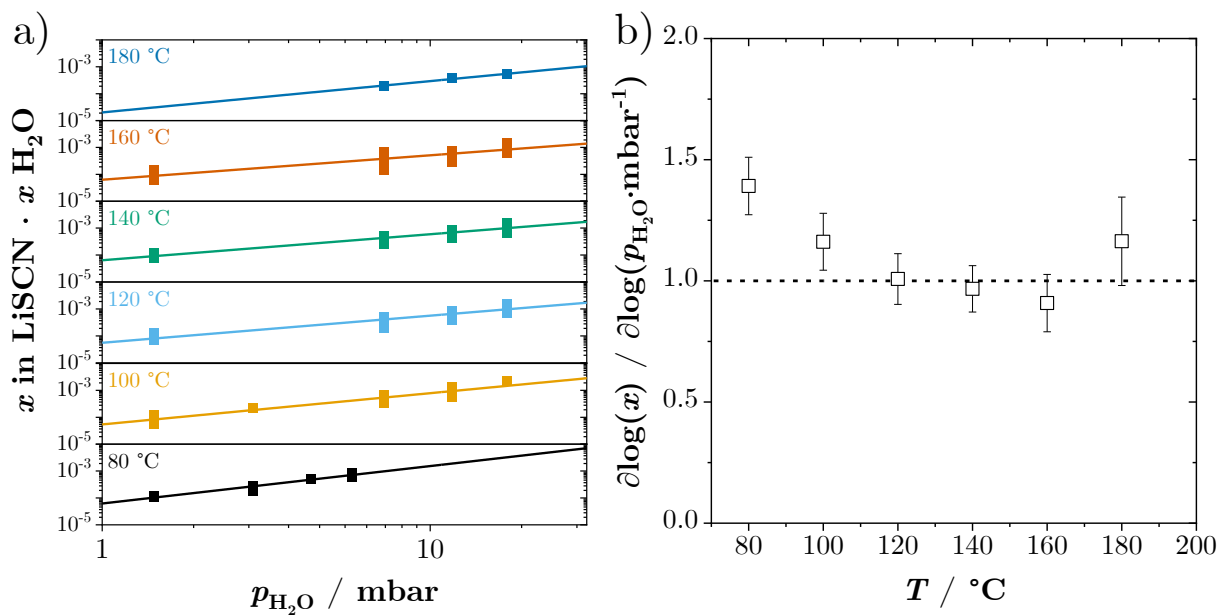
Figure B.30: TGA measurements of LiSCN at various p_{H_2O} and temperatures within the H$_2$O-doping regime, showing a) linear fits to the data and b) progression of the respective slopes with increasing temperature.
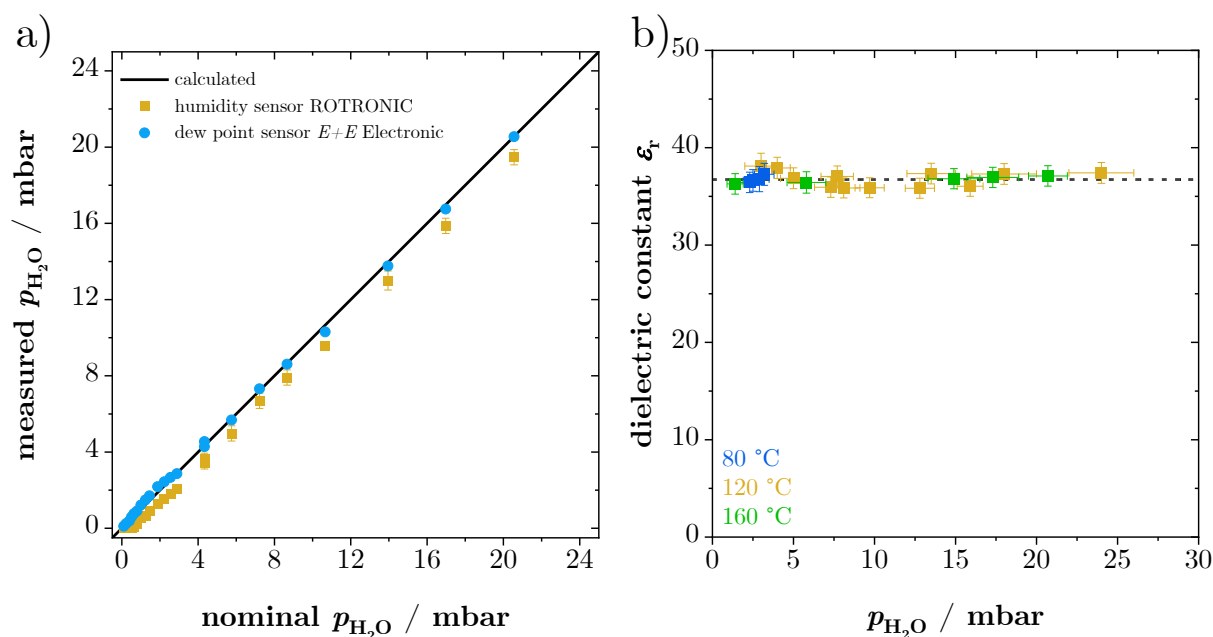
Figure B.31: a) Comparison of p_{H_2O} values calculated according to the Antoine equation and measured with a humidity or dew point sensor. b) Dielectric constants ε_r from impedance measurements of anhydrous LiSCN while exposed to various p_{H_2O} at different temperatures (cf. Figure 6.29).
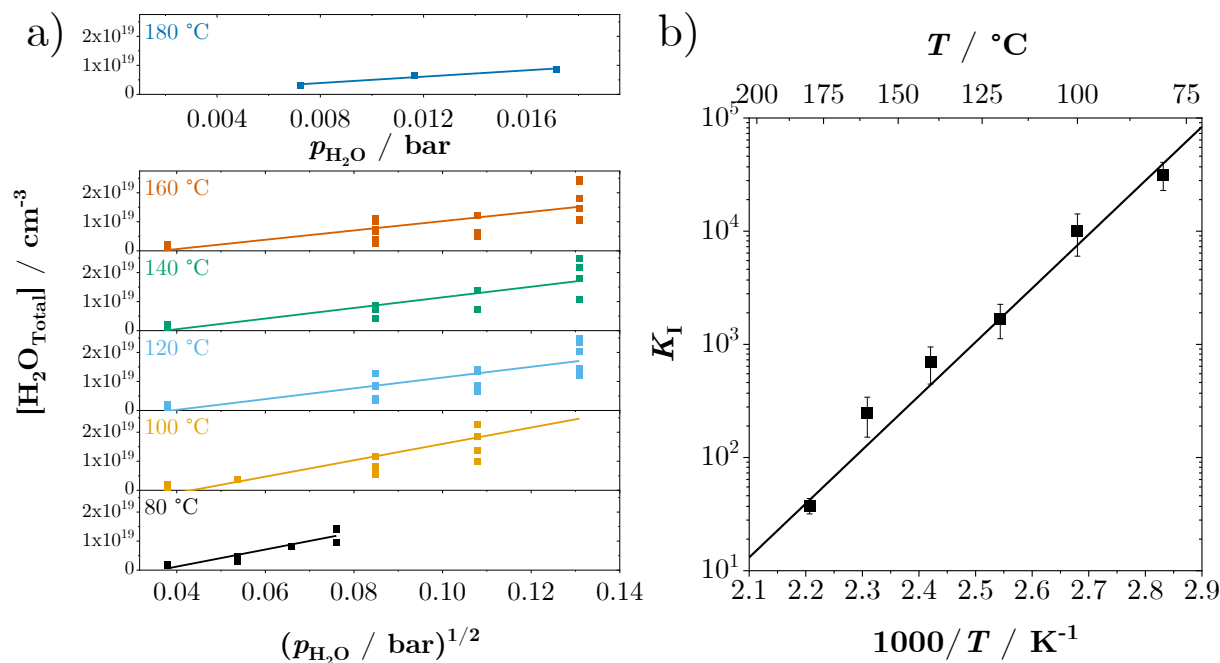
Figure B.32: a) Total H_2O concentration in H_2O-doped LiSCN as a function of $\sqrt{p_{H_2O}}$ (extrinsic) and p_{H_2O} (intrinsic) at various temperatures. b) Van 't Hoff plot of the equilibrium mass action constant K_I for H_2O-doped LiSCN. Solid lines are linear fits.
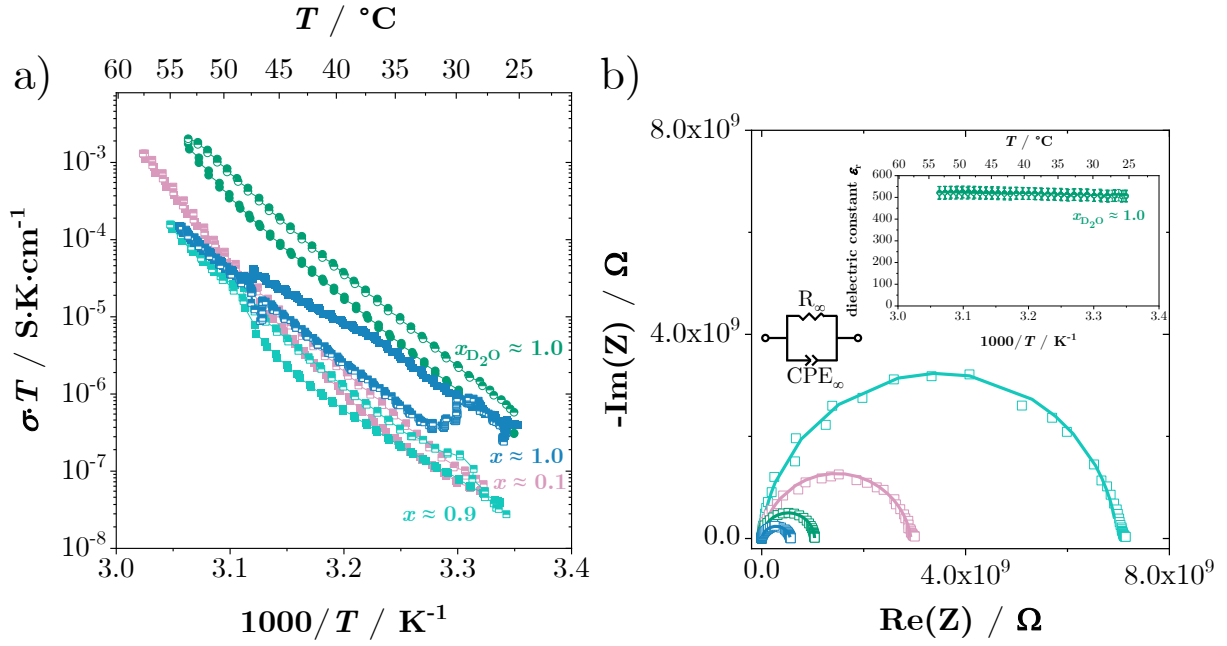
Figure B.33: a) Conductivities (heating: full, cooling: half-full symbols) and b) impedance spectra (30 °C) of three LiSCN $\cdot\, x\,$H$_2$O samples ($x \approx 0.1$, 0.9 and 1.0) compared to LiSCN $\cdot\,1.0\,$D$_2$O. The impedance spectra were fit with the shown circuit. Inset in b: measured dielectric constant ε_r of LiSCN $\cdot\,1.0\,$D$_2$O.
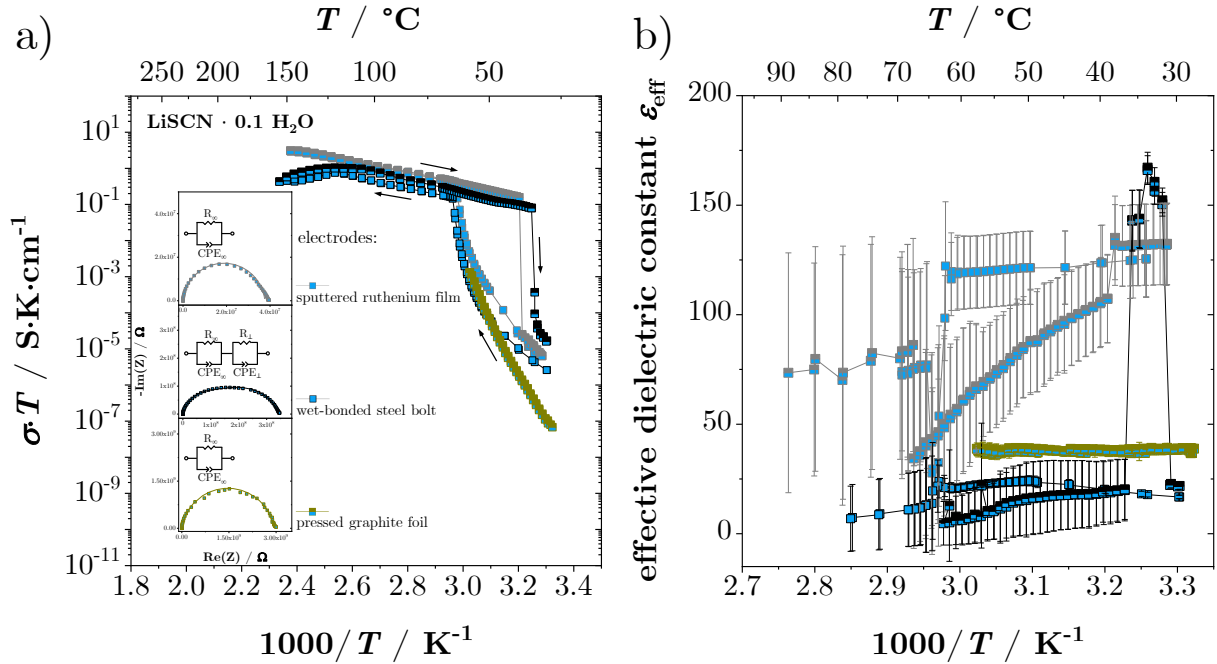
Figure B.34: Temperature dependent a) conductivity and b) effective dielectric constant ε_r data of various LiSCN $\cdot 0.1\,$H$_2$O samples contacted with different electrodes (for comparison, cf. Figure 6.36). The inserted impedance spectra (30-31 °C) indicate the influence of different contacting methods (spectra were fitted with shown equivalent circuits, respectively).
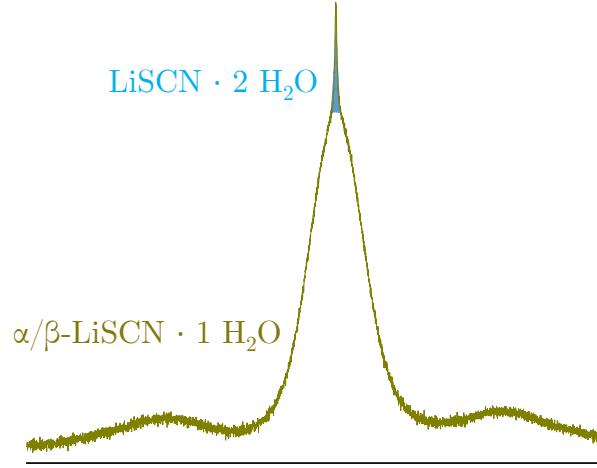
Figure B.35: NMR spectrum at 25 °C of a LiSCN $\cdot\, x\, H_2O$ sample as solid pellet with $x \approx 1.0$, collected with a D_1 dwell time of 1000 s. The sample contains a small amount of liquid dihydrate LiSCN $\cdot\, 2\, H_2O$, indicated with the blue shading.
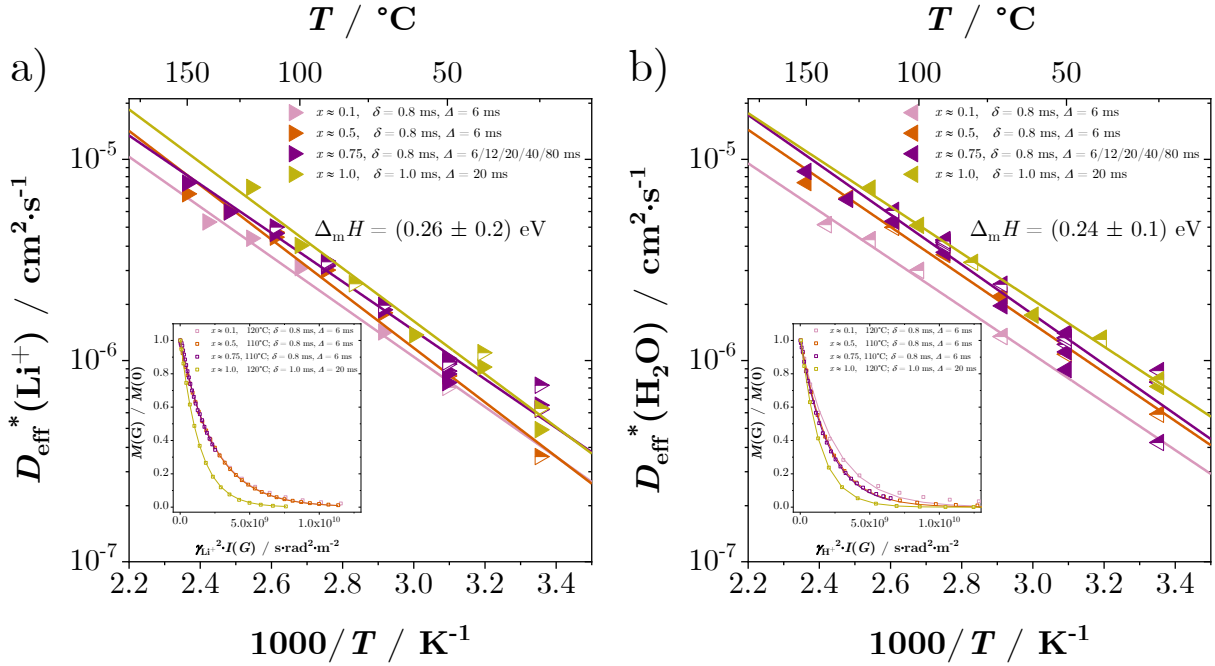
Figure B.36: Temperature dependent diffusivities of a) Li^+ and b) H_2O from PFG NMR measurements of various LiSCN $\cdot\, x\, H_2O$ samples (heating: full, cooling: half-full symbols). Solid straight lines are linear fits to the data. The insets show the respective normalized intensity as a function of the squared gyromagnetic ratio times the double integral $I(G)$. The attenuation data was fit with the standard model for 3D diffusion (cf. Equation 7.2, software TOPSPIN).
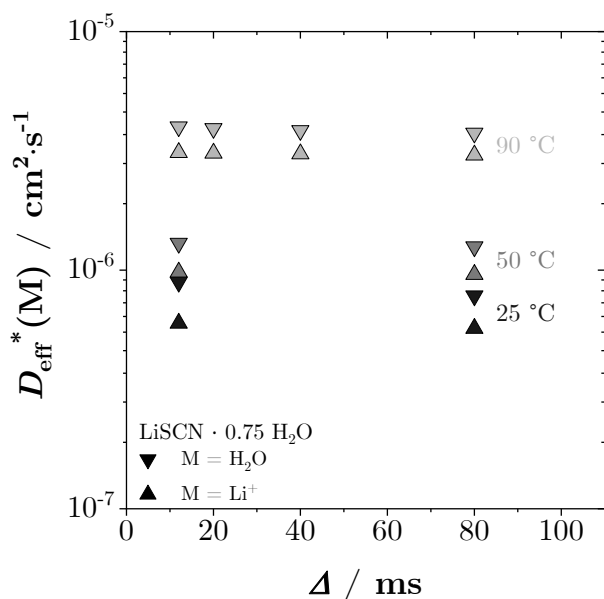
Figure B.37: ^{7}Li and ^{1}H PFG NMR tracer diffusion coefficients of LiSCN · 0.75 H$_2$O as a function of the applied diffusion time Δ recorded at different temperatures.
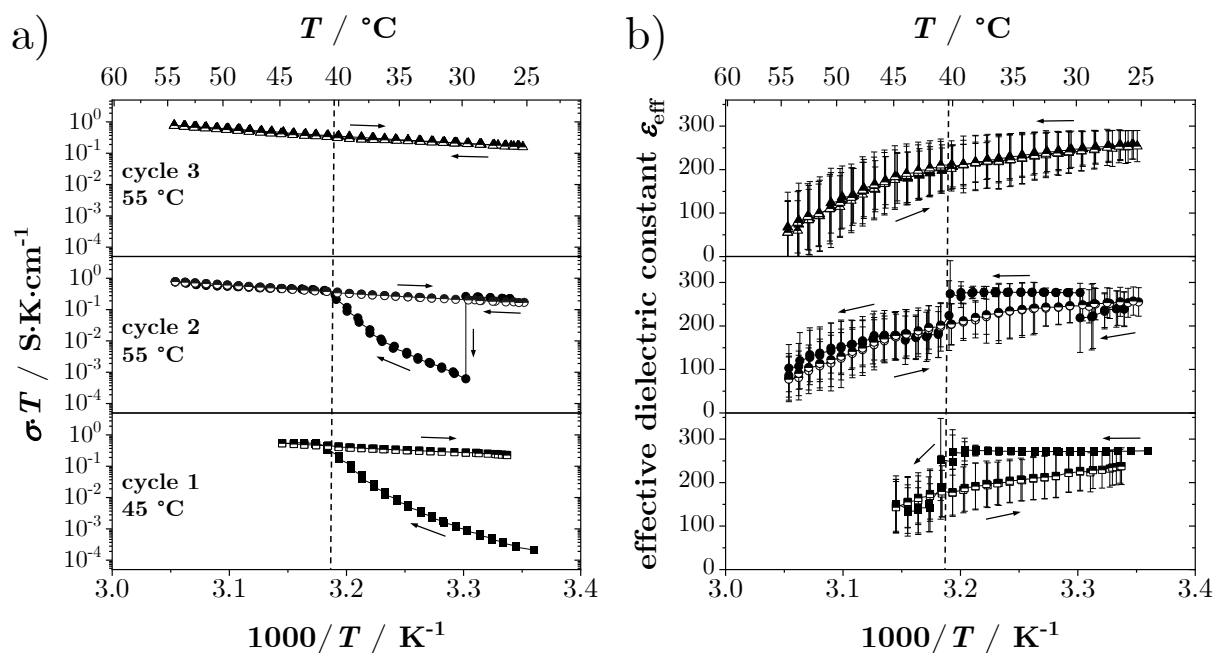
Figure B.38: a) Conductivities and b) effective dielectric constants ε_r of LiSCN · 1.0 H$_2$O which contained a small amount ($\sim$2-3 %) of the dihydrate (cf. Figure 6.37). The vertical dashed line at $\sim$40 °C marks the melting of the dihydrate. Heating runs are full, cooling runs are half-full symbols.

The origin of the high values for ε_{eff} between 100-300 is unclear. If the two components were only connected in parallel, the conduction length for each would be equal to the sample thickness and measured capacitances should be similar to bulk values ($\sim$10-50). The sample might therefore posses serial connections which would indeed show an elevated

effective dielectric constant.[222] Other effects concerning the solid to liquid transition of the dihydrate, which entail a higher rotational degree of freedom for H_2O, could be superimposed.
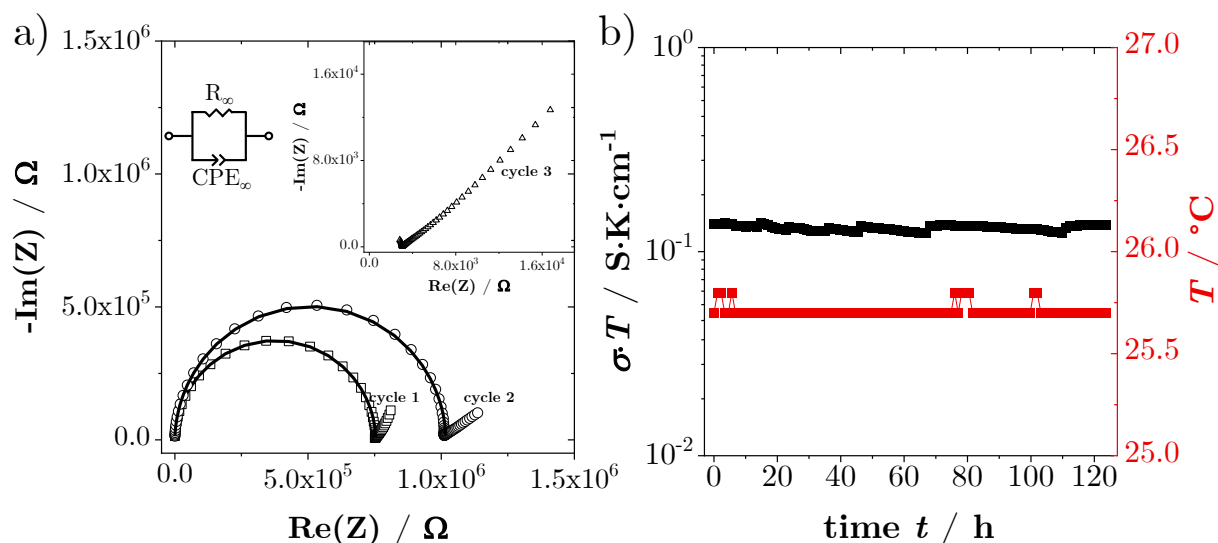

Figure B.39: a) Impedance spectra of LiSCN · 1.0 H_2O (30 °C) shown in Figure B.38 with the respective equivalent circuit used to fit the data. b) Recorded conductivity data of the sample shown in (a) and Figure B.38 over tens of hours at constant temperature after cycle 3.
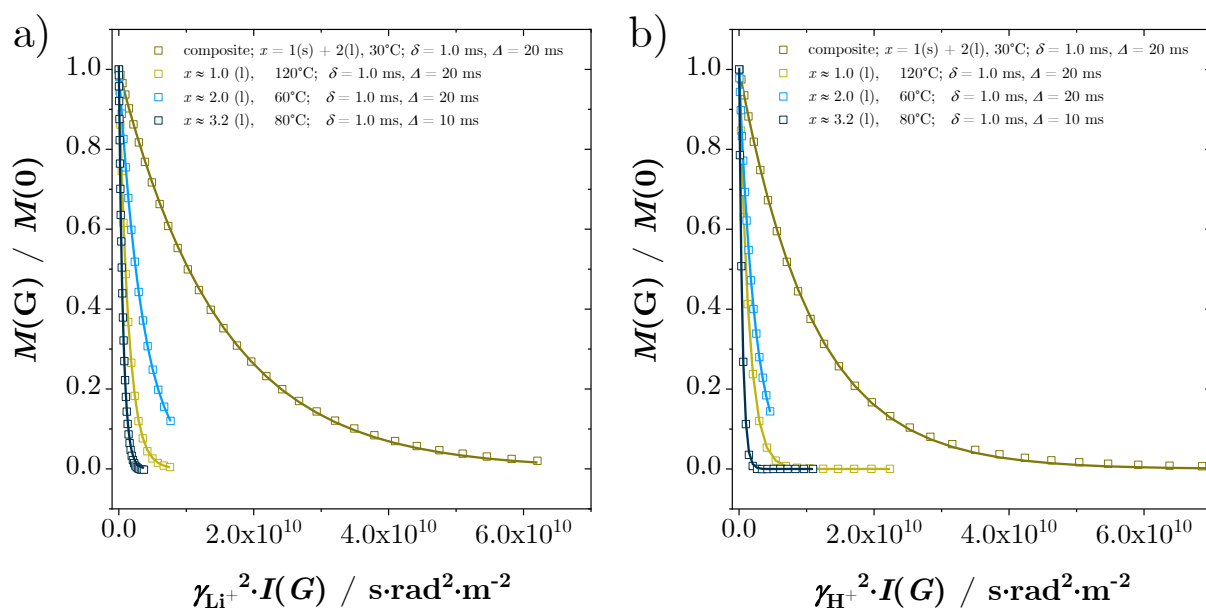

Figure B.40: a) ^{7}Li and b) ^{1}H PFG NMR normalized attenuation signal versus the squared gyromagnetic ratio times the double integral $I(G)$ from different LiSCN · x H_2O samples. All data were fit with the standard 3D diffusion model (cf. Equation 7.2, software TOP-SPIN).
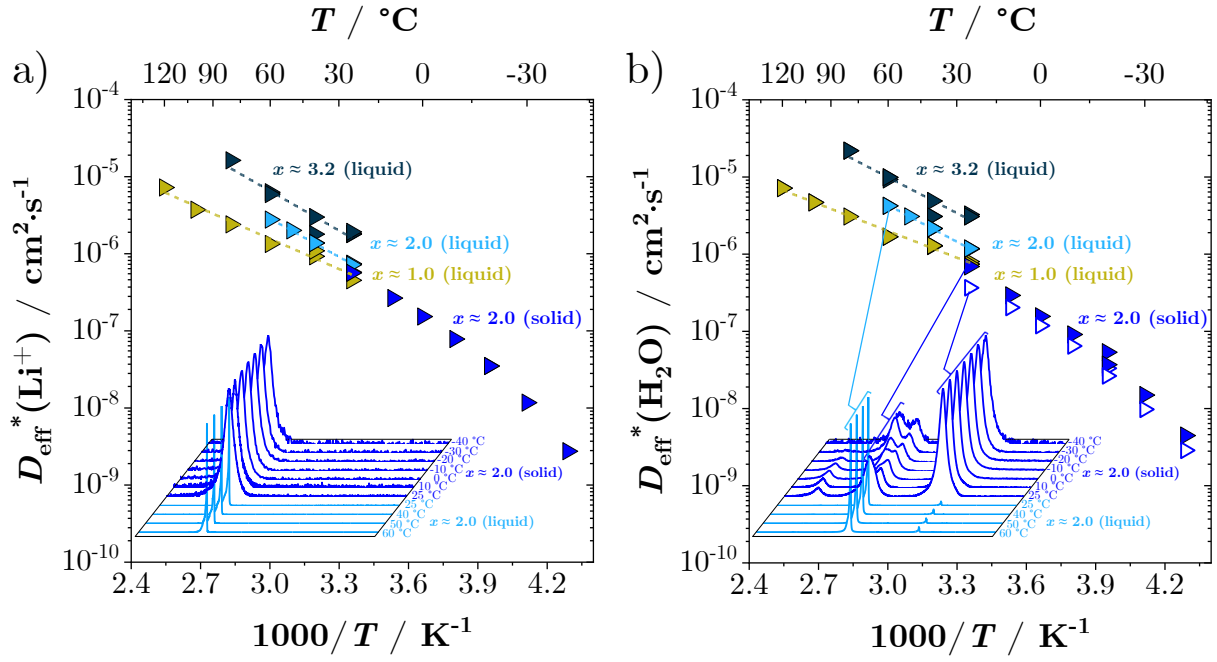
Figure B.41: Measured diffusivities of a) Li^+ and b) H_2O of solid and liquid LiSCN $\cdot x\, H_2O$ samples collected at various temperatures. The insets show respective ^{7}Li and ^{1}H NMR spectra of LiSCN $\cdot$ 2.0 H_2O, which emphasize the difference between structural water (solid) and H_2O as hydration shell (liquid).
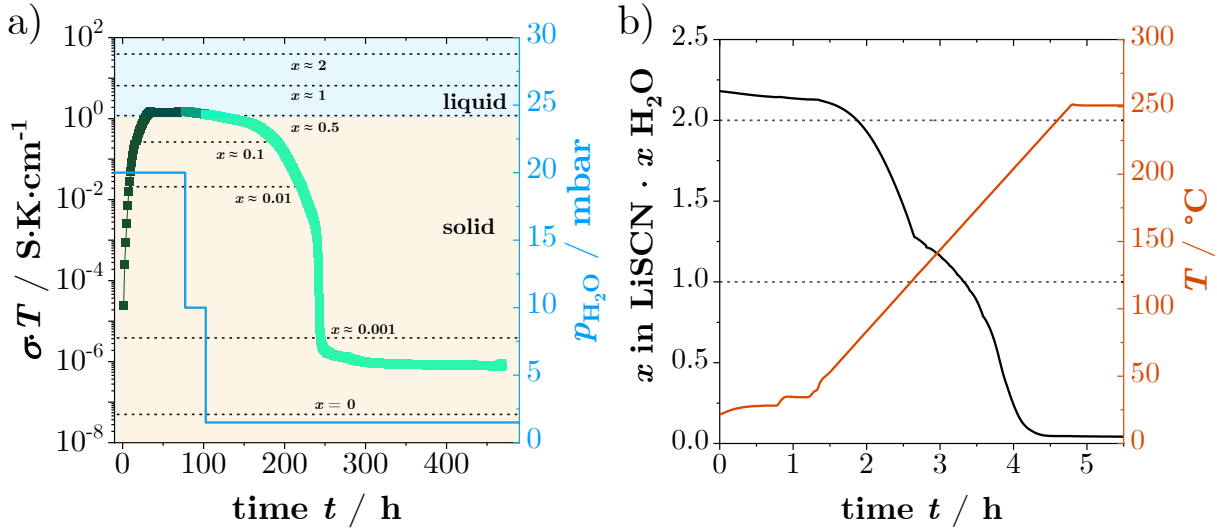

Figure B.42: a) Measured conductivities of LiSCN $\cdot x\, H_2O$ at 80 °C in cell 4 (cf. section 5.6) while varying the p_{H_2O}, depicting the solid to liquid transition. The experimental set-up to vary the p_{H_2O} is the same as described for doping with H_2O, cf. section 5.3. b) TGA measurement of commercially available LiSCN $\cdot x\, H_2O$ to assess x.
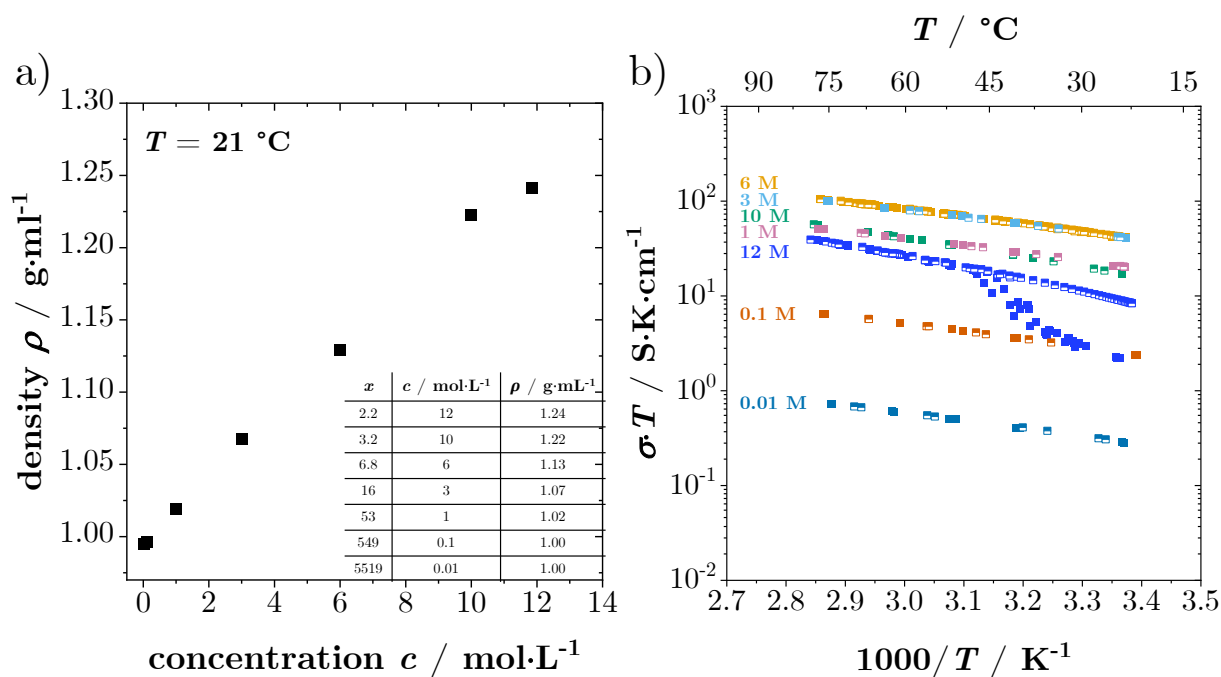
Figure B.43: a) Measured densities at 21 °C and b) temperature dependent conductivities of aqueous LiSCN solutions of different concentrations (heating: full, cooling: half-full symbols); $12\,M \equiv x \approx 2.2$, $10\,M \equiv x \approx 3.2$, $6\,M \equiv x \approx 6.8$, $3\,M \equiv x \approx 16$, $1\,M \equiv x \approx 53$, $0.1\,M \equiv x \approx 549$ and $0.01\,M \equiv x \approx 5519$.

B.3   Hydrated Lithium Tin Sulphide $Li_2Sn_2S_5 \cdot x\,H_2O$

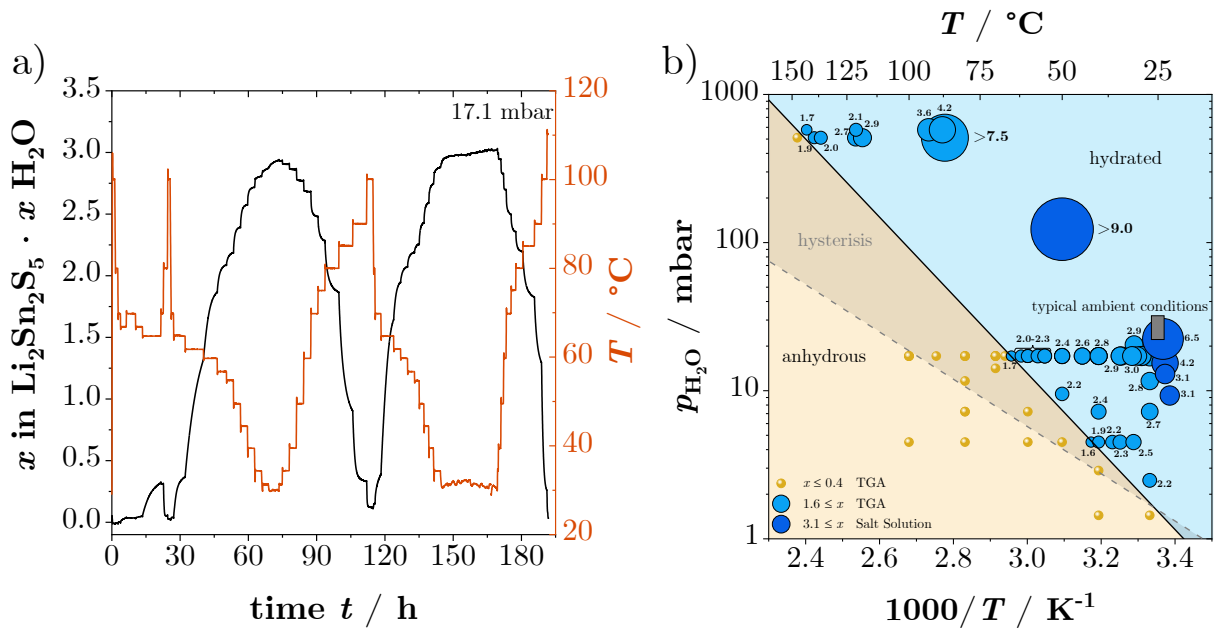Figure B.44: a) Exemplary isobaric TGA measurement of $Li_2Sn_2S_5 \cdot x\,H_2O$ at 17.1 mbar for various temperatures. b) Equilibrated water content x as a function of p_{H_2O} and temperature. The data of the light brown and blue circles were collected by TGA, while the data from the dark blue circles were collected with salt solutions.
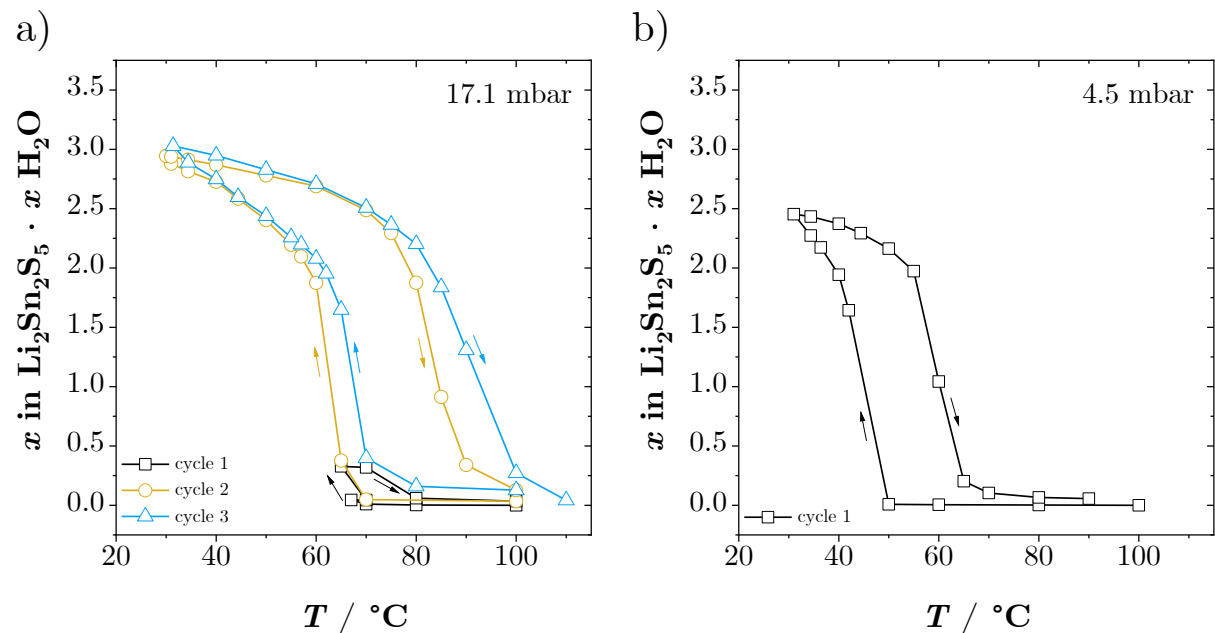

Figure B.45: Isobaric TGA data of x depicting the observed hysteresis in $Li_2Sn_2S_5 \cdot x\,H_2O$: a) 17.1 mbar; b) 4.5 mbar. The measurements were always started with freshly prepared anhydrous $Li_2Sn_2S_5$ powder.
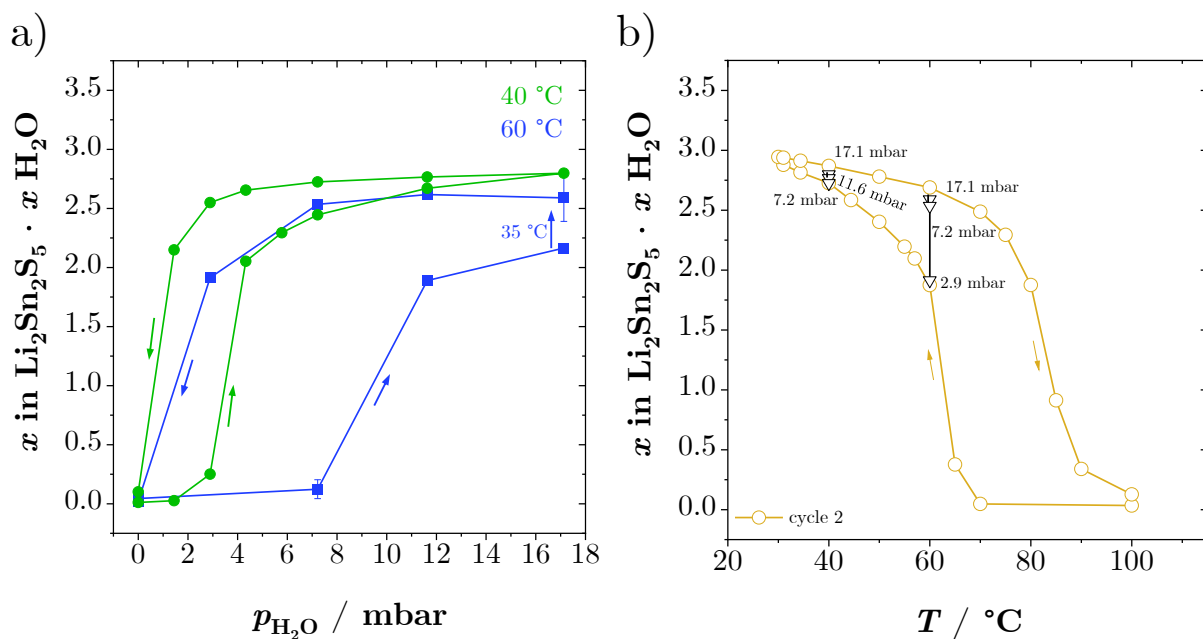
a)

b)

Figure B.46: a) Isothermal TGA data of x at 40 °C and 60 °C complementary to Figure B.45. The starting material was always freshly prepared anhydrous $Li_2Sn_2S_5$. b) Isobaric measurement cycle shown in Figure B.45a with inserted isothermal data points.

a)

b)

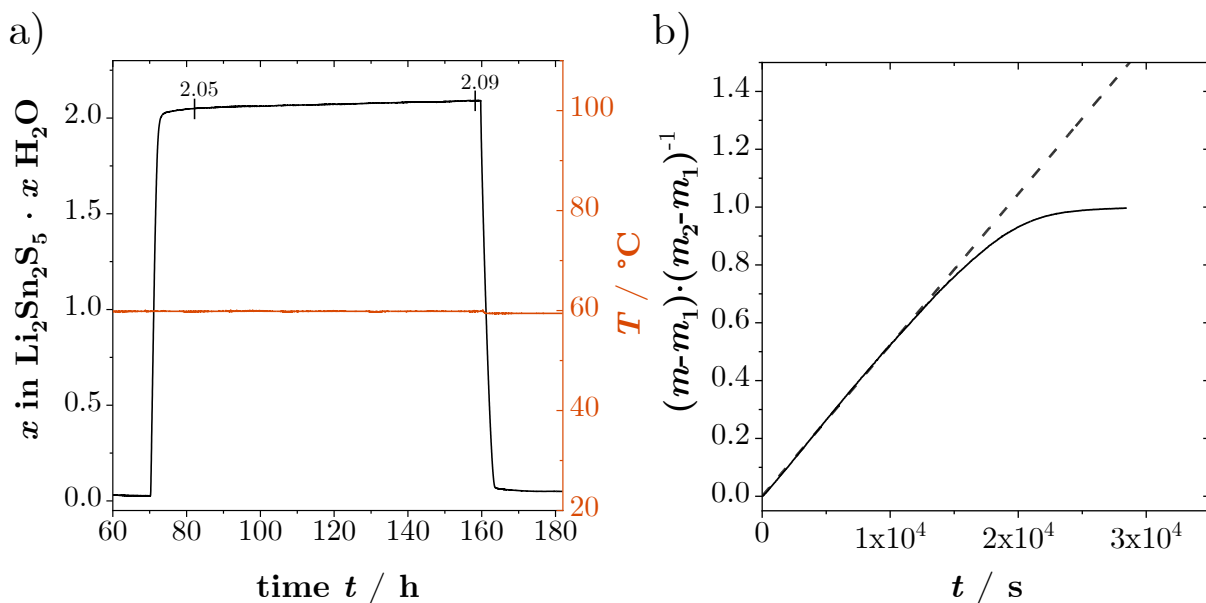Figure B.47: a) Isobaric TGA measurement (17.1 mbar) of $Li_2Sn_2S_5 \cdot x\,H_2O$ to show the long-time equilibration behaviour of x to assess its error. The resolution of the TGA is about 0.01 in x with an error of ~0.1. b) Short-time diffusion behaviour for water incorporation in $Li_2Sn_2S_5 \cdot x\,H_2O$; normalized mass change from the TGA data in Figure 7.1a (m is the mass at time t, m_1 is the initial mass, and m_2 the mass at equilibration).
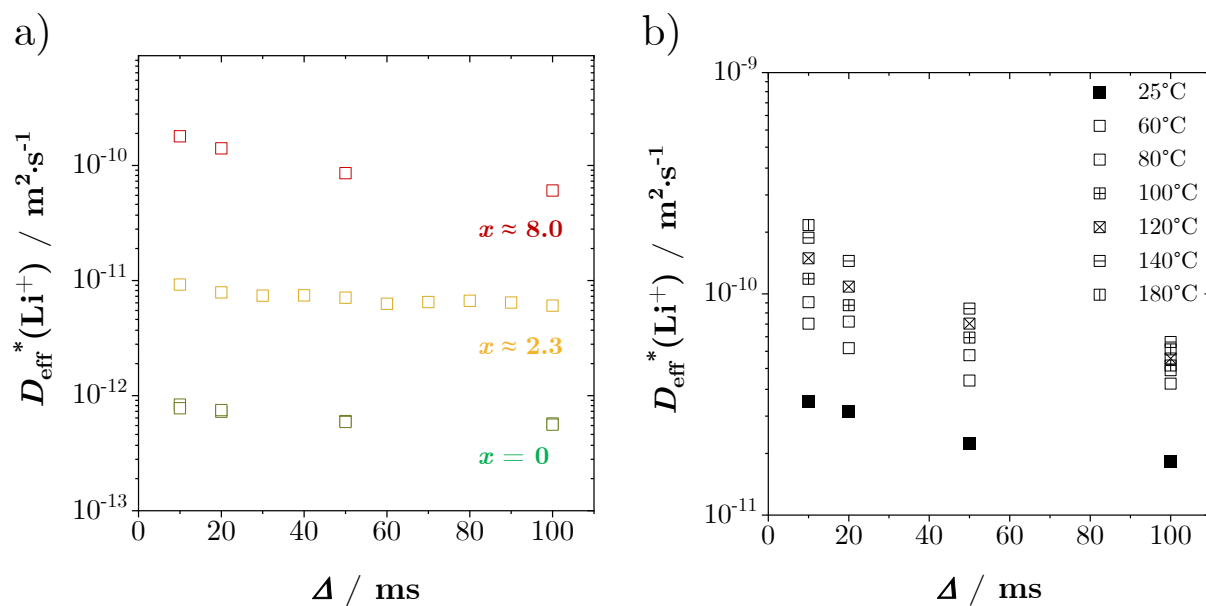
Figure B.48: ^{7}Li PFG NMR measurements showing the extracted effective Li$^+$ tracer diffusion coefficients as a function of diffusion times: a) $x = 0$ (140 °C), $x \approx 2.3$ (180 °C) and $x \approx 8.0$ (140 °C); b) $x \approx 8.0$ at various temperatures. The 2D model was used for data fitting (cf. Equation 7.3).
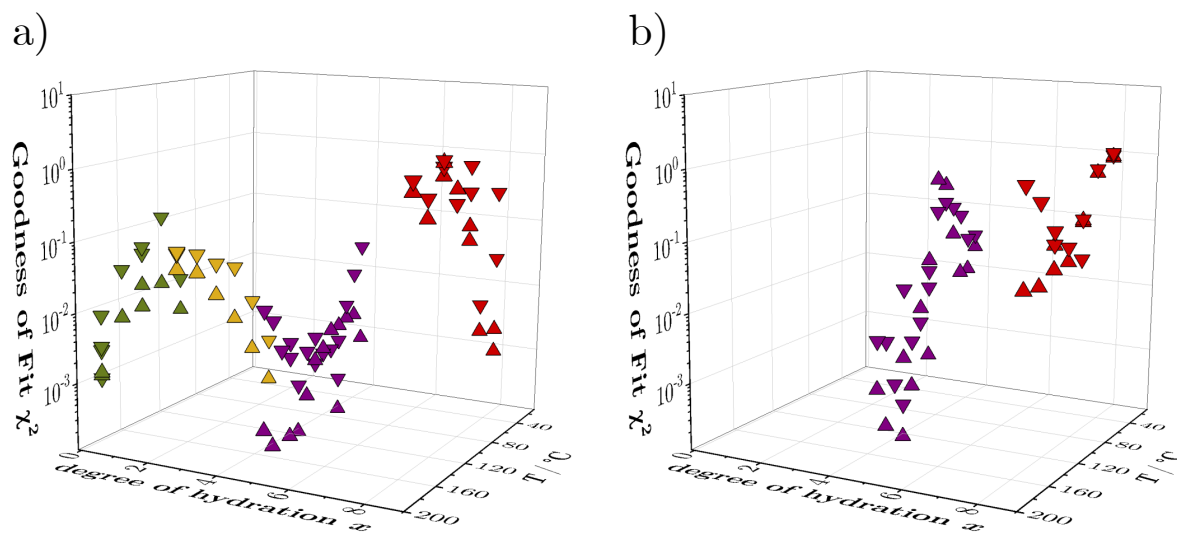

Figure B.49: Goodness of fit χ^2 values for all fits performed with the 2D diffusion model at various temperatures and values of x; a) Li$^+$ diffusion, b) H$^+$ diffusion.
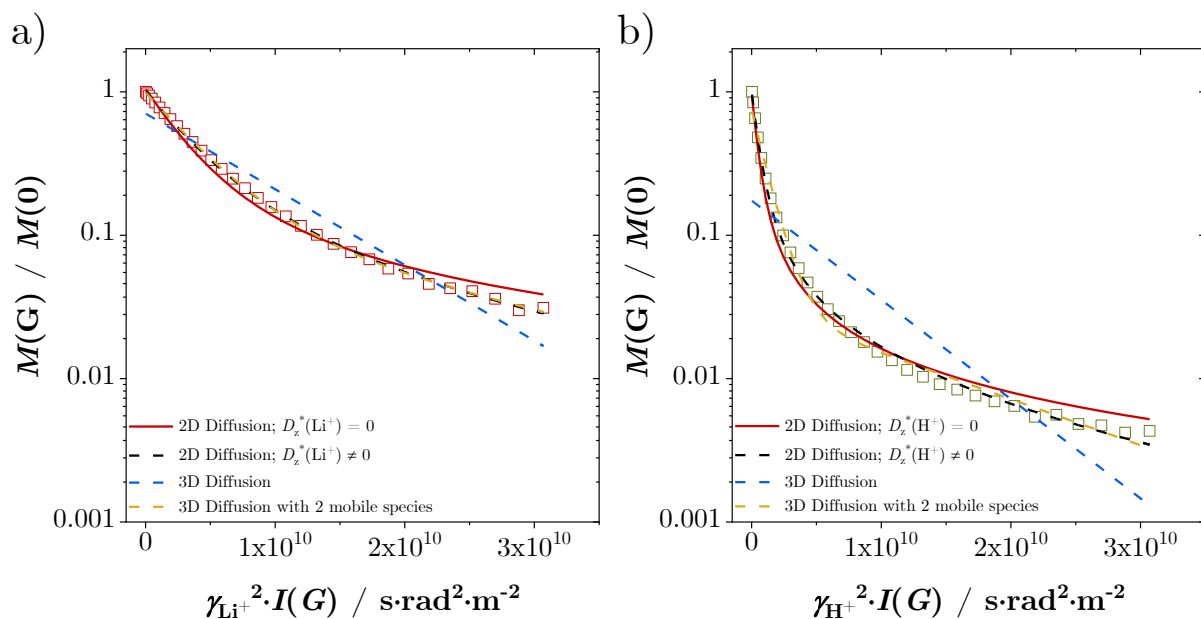
Figure B.50: Comparison of the employed diffusion models to fit PFG NMR data of $Li_2Sn_2S_5 \cdot x\,H_2O$. Shown here are exemplary measurements of a) ^7Li and b) ^1H with $x \approx$ 8.0 at 70 °C.
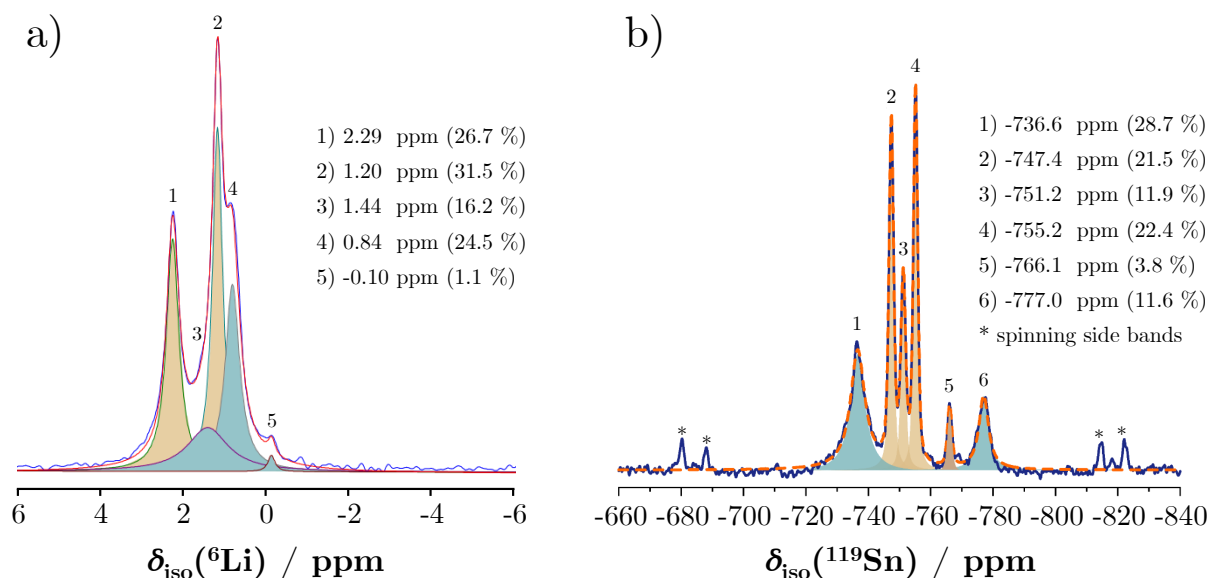
Figure B.51: a) ^6Li and b) ^{119}Sn MAS NMR spectra of anhydrous $Li_2Sn_2S_5$. Brown coloured signals correspond to highly crystalline material, while turquoise coloured signals show a lower degree of crystallinity (most likely a higher concentration of stacking faults). Signal 5 in the ^{119}Sn spectrum belongs possibly to Li_2SnS_3 as a small contaminant side phase.

In Figure B.51 additional signals were observed at 1.4, 0.8 and -0.1 ppm which had not been previously reported. These additional signals account for approximately 40 % of the overall integrated intensity. Based on the peak shapes, they most likely arise

due to differences in crystallinity in the sample powder, meaning that some grains have higher concentrations of stacking faults and/or dislocations, causing slight changes in the chemical environment. This explanations follows the general trend in $Li_2Sn_2S_5$ observed from XRPD to produce stacking fault reflections (section 7.1) as well as its tendency for higher dimensional defects (Figure B.57). The ^{119}Sn NMR spectrum (Figure B.51b) shows a similar picture, with the signals 2, 3, 4 corresponding to highly crystalline $Li_2Sn_2S_5$, and signals 1 and 6 showing broader shapes due to lower crystallinity. The signals labeled 5 in Figure B.51 possibly belong to Li_2SnS_3 as a small contaminant (probably as low as 1 %, since neither XRPD or SEM showed any signs of a contaminant).
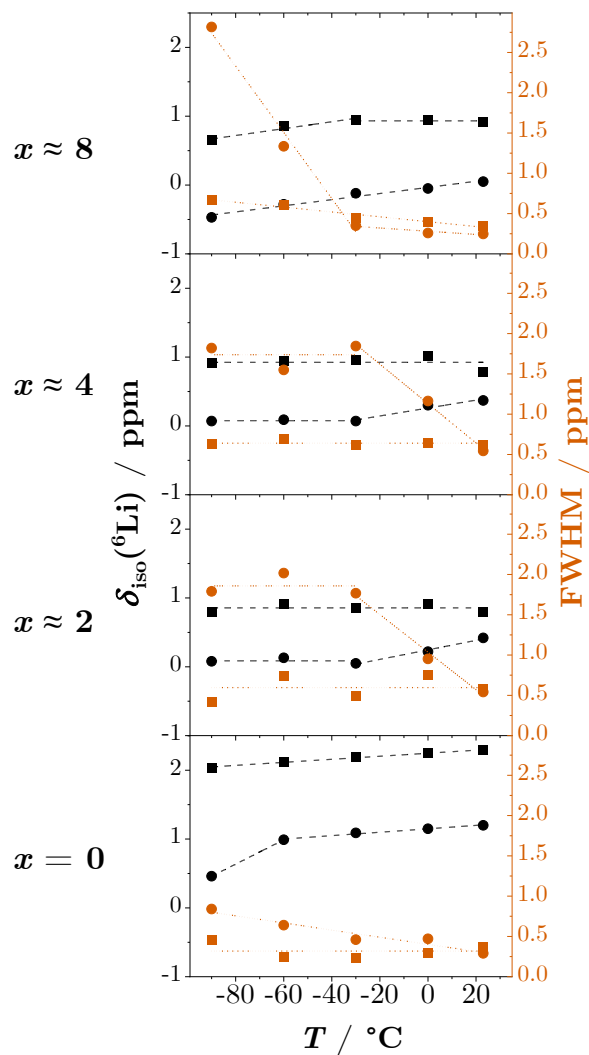
Figure B.52: From the ^{6}Li NMR spectra in Figure 7.5: temperature dependence of chemical shifts δ_{iso} (black) and full widths at half-maximum FWHM (orange) corresponding to signal 1 (squares) and signal 2 (circles). A Lorentzian line shape was used in all fits for the NMR data. Dashed and dotted lines are guides for the eye.
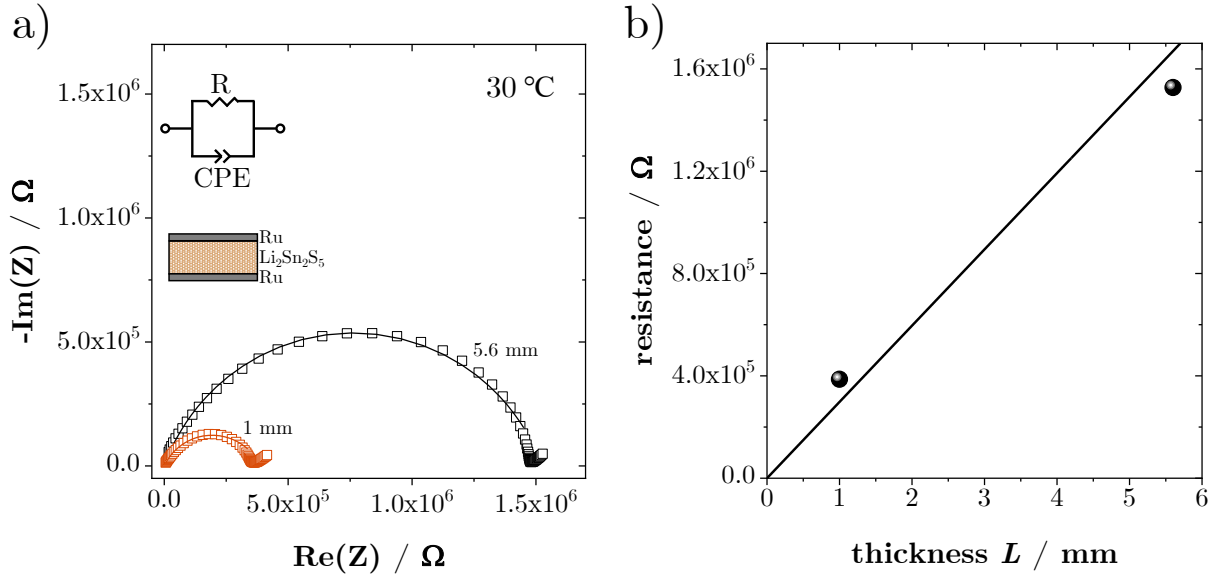
Figure B.53: Thickness scaling of an anhydrous $Li_2Sn_2S_5$ pellet at 30 °C showing a) the impedance spectra and b) the linear scaling of the resistance with thickness. The solid line in (b) is a linear fit through the origin.
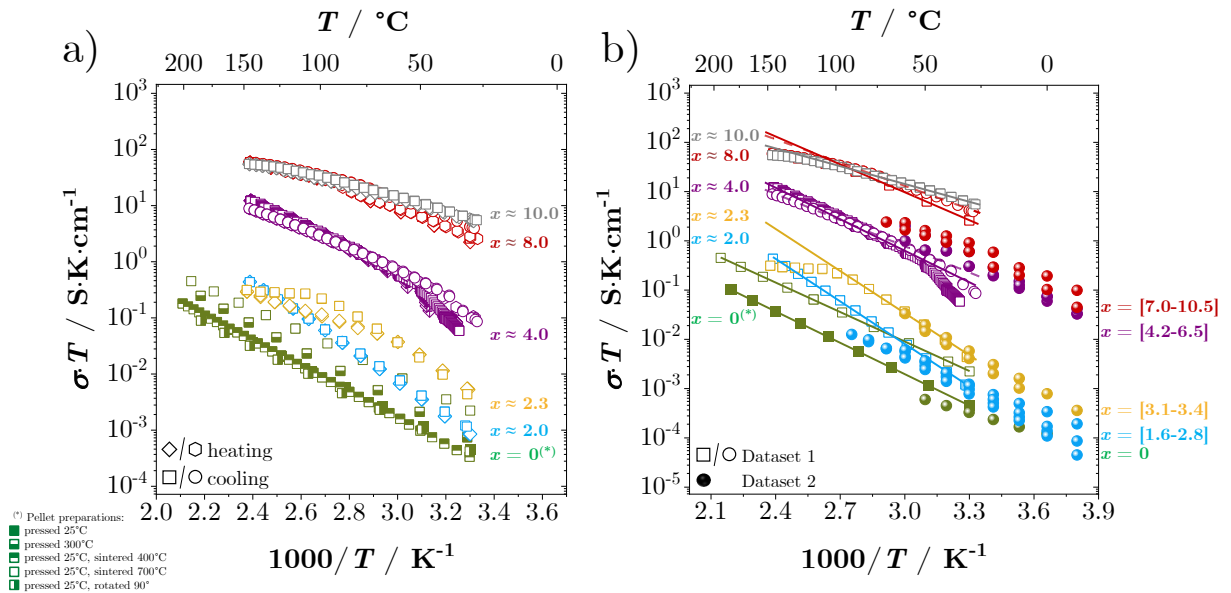
Figure B.54: Overview of the recorded impedance data for $Li_2Sn_2S_5 \cdot x\,H_2O$; a) Extension of the EIS data set shown in Figure 7.7 including additional samples, preparation methods for $x = 0$, as well as heating and cooling runs for $x > 0$. b) Comparison of the conductivity data in (a) with measurements collected by Christian Schneider (Dataset 2) using a different experimental set-up (cf. section 5.6).
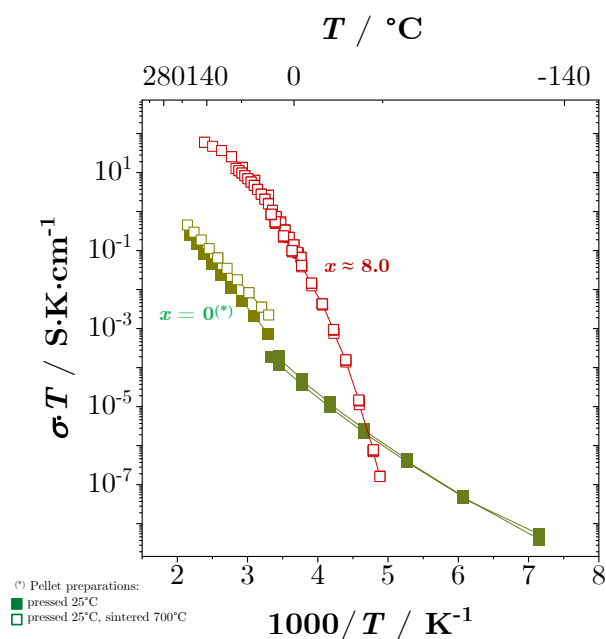
Figure B.55: EIS measurement of $Li_2Sn_2S_5 \cdot x\,H_2O$ going to very low temperatures, comparing anhydrous ($x = 0$) and fully hydrated ($x \approx 8.0$) samples.
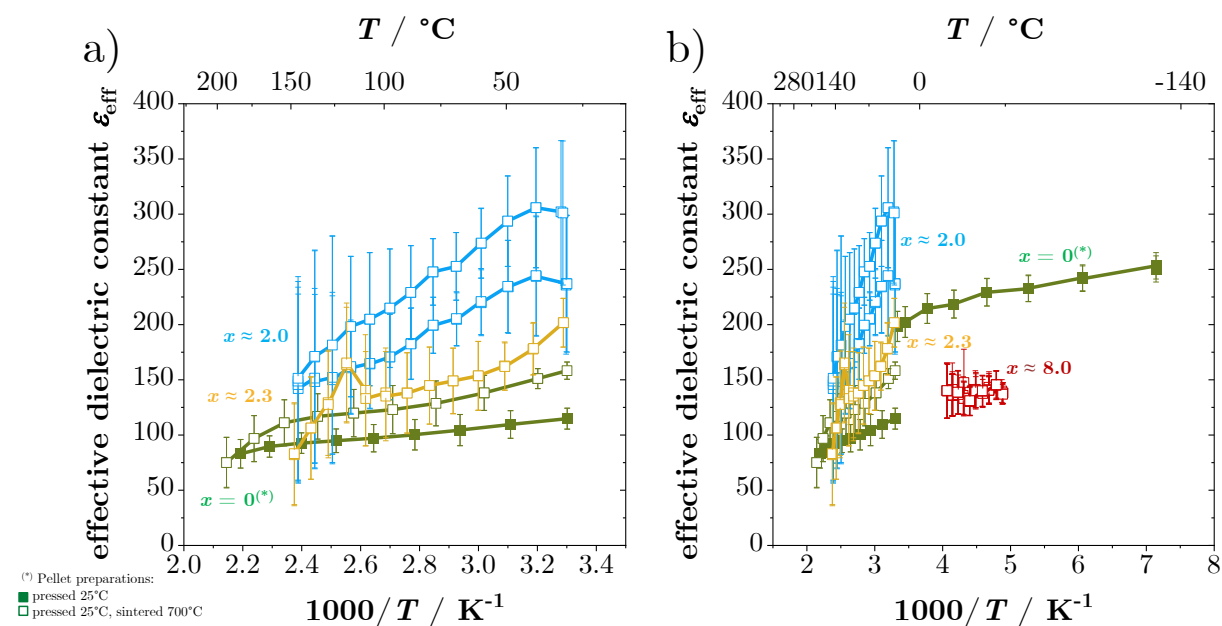
Figure B.56: Effective dielectric constant ε_{eff} of various $Li_2Sn_2S_5 \cdot x\,H_2O$ samples measured a) above and b) below room temperature.
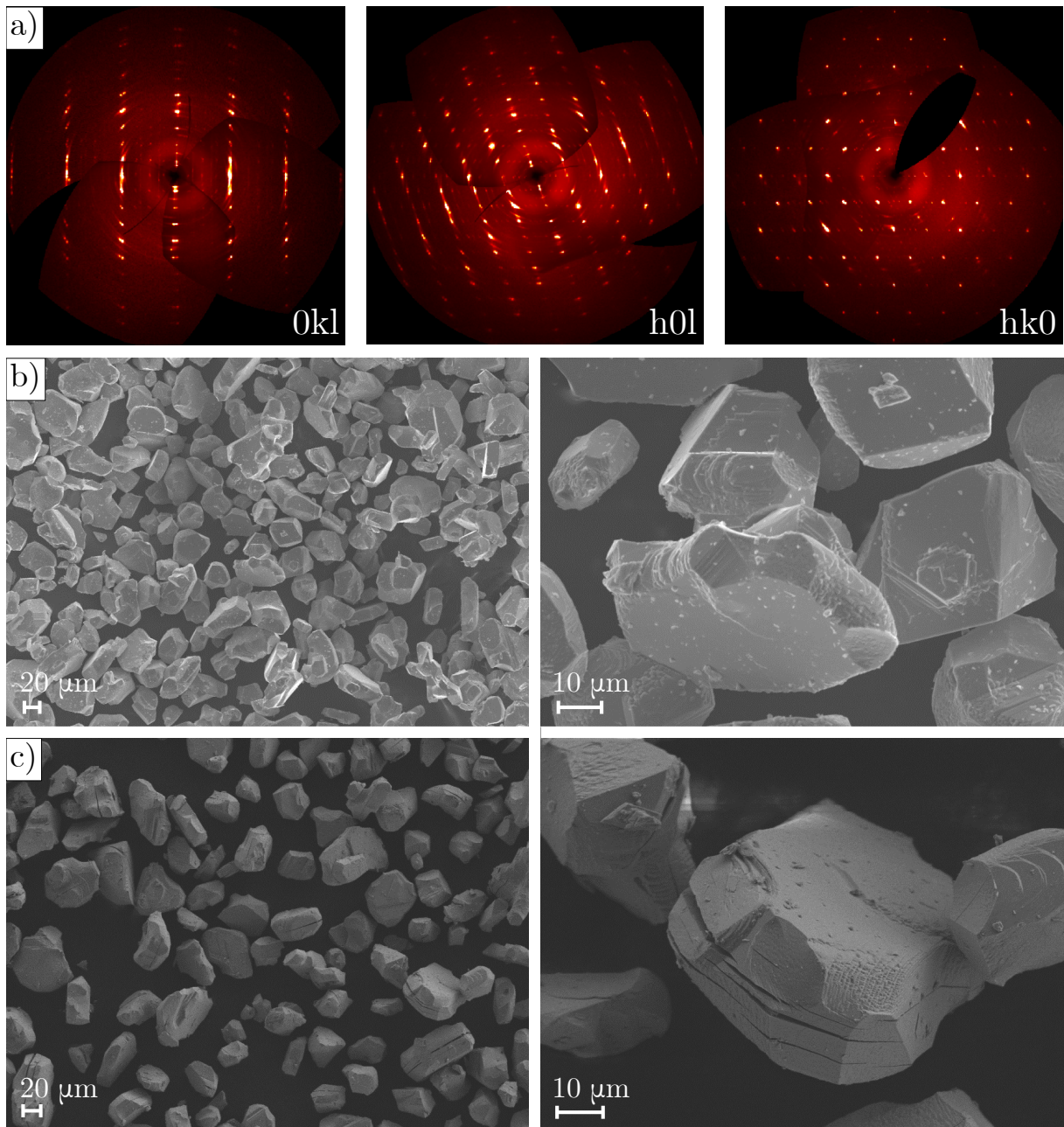
Figure B.57: a) Reciprocal space diffraction images of an anhydrous $Li_2Sn_2S_5$ grain recorded by single crystal diffraction. b) and c): SEM images of $Li_2Sn_2S_5 \cdot x\,H_2O$ with $x = 0$ and $x \approx 2.7$, respectively. Due to the high vacuum in the SEM chamber, the images in (c) show (partially) dehydrated sample powder.
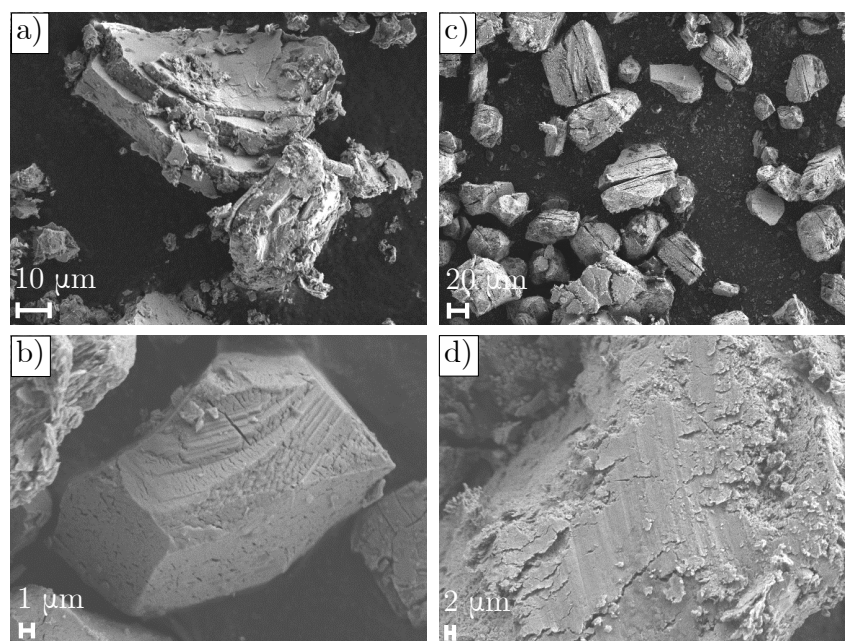
Figure B.58: Scanning electron micrographs of $Li_2Sn_2S_5 \cdot x\,H_2O$; a) $x \approx 4.1$; b) $x \approx 8.5$; c) $x \approx 9.0$; d) $x \approx 10.2$ (partially dehydrated material as mentioned in Figure B.57).

	after synthesis / at.-%	after contact with Li / at.-%
O 1s	6.86	35.33
Sn 3d	17.34	1.00
C 1s	17.21	18.49
S 2p	33.69	2.74
Li 1s	24.91	42.44
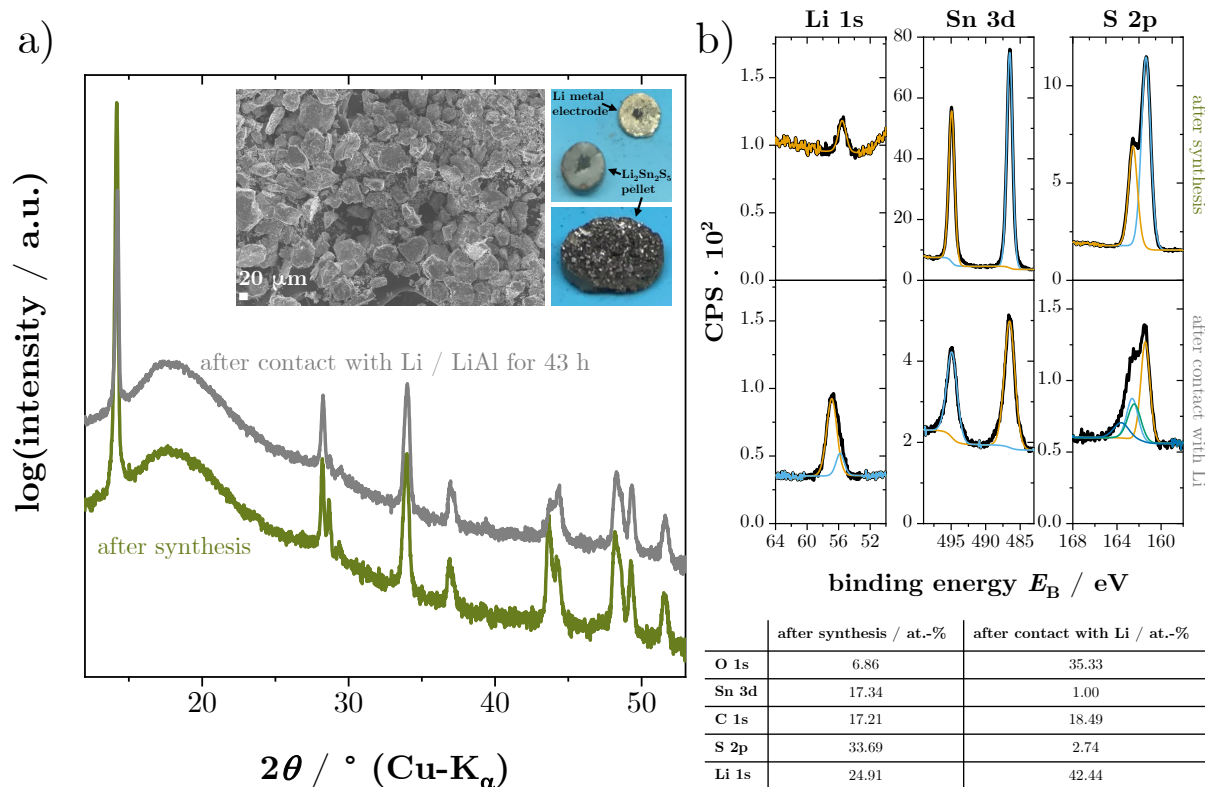
Figure B.59: a) XRPD patterns of anhydrous $Li_2Sn_2S_5$ before and after being contacted with Li or LiAl electrodes for 43 h (or longer). Inserted are a SEM image of $Li_2Sn_2S_5$ powder after contact with Li as well as images of the Li metal electrode and the $Li_2Sn_2S_5$ pellet from the EMF measurement shown in Figure 7.10. b) XPS measurements of the samples shown in (a), displaying the signals for Li 1s, Sn 3d and S 2p.
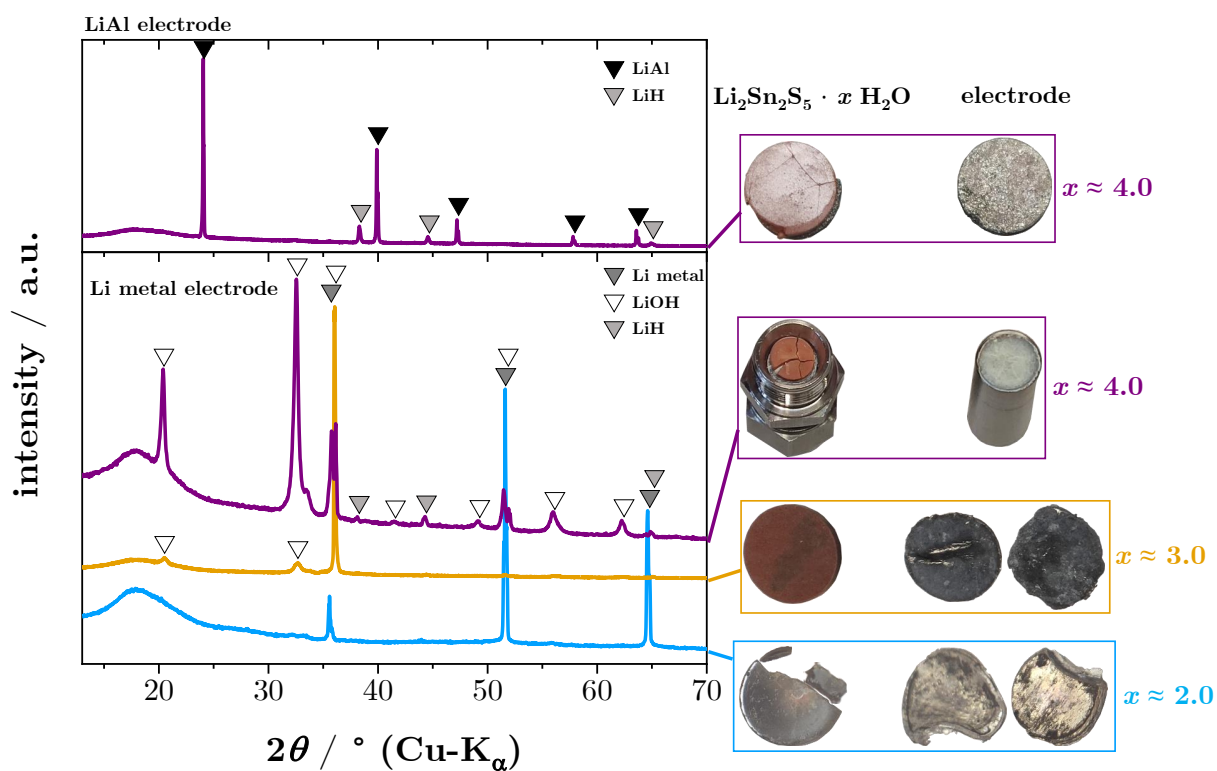
Figure B.60: XRPD patterns of Li metal and LiAl electrodes after having been contacted with various $Li_2Sn_2S_5 \cdot x\,H_2O$ hydrates. The right hand side shows respective images of $Li_2Sn_2S_5 \cdot x\,H_2O$ pellets and the corresponding electrodes after opening the measurement cells.

C | References

[1] J. M. Bakker, G. B. Deacon, C. M. Forsyth, P. C. Junk, and M. Wiecko, "A structural investigation of trivalent and divalent rare earth thiocyanate complexes synthesised by redox transmetallation," *European Journal of Inorganic Chemistry*, vol. 6, 2813–2825, 2010.

[2] E. Shurdha, S. H. Lapidus, P. W. Stephens, C. E. Moore, A. L. Rheingold, and J. S. Miller, "Extended network thiocyanate- and tetracyanoethanide-based first-row transition metal complexes," *Inorganic Chemistry*, vol. 51, 9655–9665, 2012.

[3] E. Shurdha, C. E. Moore, A. L. Rheingold, S. H. Lapidus, P. W. Stephens, A. M. Arif, and J. S. Miller, "First Row Transition Metal(II) Thiocyanate Complexes, and Formation of 1-, 2-, and 3-Dimensional Extended Network Structures of $M(NCS)_2(Solvent)_2$ (M = Cr, Mn, Co) Composition," *Inorganic Chemistry*, vol. 52, 10583–10594, 2013.

[4] A. Jochim, M. Ceglarska, M. Rams, and C. Näther, "Synthesis, Crystal Structures, and Properties of $Ni(NCS)_2$-4-methoxypyridine Coordination Compounds," *Zeitschrift für Anorganische und Allgemeine Chemie*, vol. 644, 1760–1770, 2018.

[5] A. Jochim, M. Rams, T. Neumann, C. Wellm, H. Reinsch, G. M. Wójtowicz, and C. Näther, "Structural Diversity in Ni Chain Coordination Polymers: Synthesis, Structures, Isomerism and Magnetism," *European Journal of Inorganic Chemistry*, vol. 2018, 4779–4789, 2018.

[6] C. Wellm and C. Näther, "Crystal structure, synthesis and thermal properties of bis(acetonitrile-κN)bis(4-benzoylpyridine-κN)bis(isothiocyanato-κN)nickel(II)," *Acta Crystallographica*, vol. E75, 1685–1688, 2019.

[7] C. Wellm, T. Neumann, M. Ceglarska, G. Gallo, M. Rams, R. E. Dinnebier, and C. Näther, "New isomeric $Ni(NCS)_2$ coordination compounds: crystal structures, magnetic properties as well as ex situ and in situ investigations on their synthesis and transition behaviour," *CrystEngComm*, vol. 22, 2350–2360, 2020.

[8] T. Neumann, G. Gallo, R. E. Dinnebier, and C. Näther, "Synthesis, Crystal Structures, and Properties of $Mn(NCS)_2$ Coordination Compounds with 4-Picoline as Coligand and Crystal Structure of $Mn(NCS)_2$," *Zeitschrift für Anorganische und Allgemeine Chemie*, vol. 2, 88–94, 2020.

[9] M. Joos, M. Conrad, R. Merkle, Th. Schleid, J. Maier, R. E. Dinnebier, and S. Bette, "Synthesis, characterization and thermal behaviour of solid phases in the quasi-ternary system $Mg(SCN)_2$–H_2O–THF," *Dalton Transactions*, vol. 50, 6949–6991, 2021.

[10] V. I. Nikolaev, "Hydrates of LiSCN," *Journal of Russian Physical Chemistry Society*, vol. 61, 939, 1929.

[11] F. H. Cano, S. García-Blanco, and A. G. Laverat, "The crystal structure of cobalt(II) thiocyanate trihydrate," *Acta Crystallographica*, vol. B32, 1526–1529, 1976.

[12] K. Mereiter and A. Preisinger, "Structure of magnesium isothiocyanate tetrahydrate," *Acta Crystallographica*, vol. B38, 1263–1265, 1982.

[13] K. Mereiter and A. Preisinger, "Barium Thiocyanate Trihydrate," *Acta Crystallographica*, vol. B38, 382–385, 1982.

[14] K. Mereiter and A. Preisinger, "Crystal structure and Raman spectra of alpha- and beta-NaSCN · 2 H_2O," *Zeitschrift für Kristallographie*, vol. 169, 95–107, 1984.

[15] K. Mereiter and A. Preisinger, "Structure of strontium thiocyanate trihydrate, $Sr(SCN)_2$ · 3 H_2O, at 295 and 125 K," *Acta Crystallographica*, vol. C48, 1367–1370, 1992.

[16] B. Beagley, C. A. McAuliffe, A. G. Mackie, and R. G. Pritchard, "Preparation and crystal structure of manganese(II) isothiocyanate tetrahydrate," *Inorganica Chimica Acta*, vol. 89, 163–166, 1984.

[17] L.-X. Li, W.-T. Yu, X.-T. Tao, and J.-Y. Wang, "Study on crystal structure and Raman spectra of $Zn(SCN)_2$ · 2 H_2O crystal," *Zhongguo Jiguang*, vol. 17, 278–281, 1990.

[18] P. Held and L. Bohatý, "Crystal structure of calcium dithiocyanate tetrahydrate, $Ca(NCS)_2$ · 4 H_2O," *Zeitschrift für Kristallographie*, vol. 216, 359, 2001.

[19] C. Wickleder and P. Larsen, "$Ca(SCN)_2$ and $Ca(SCN)_2$ · 2 H_2O: Crystal Structure, Thermal Behavior and Vibrational Spectroscopy," *Zeitschrift für Naturforschung*, vol. 57b, 1419–1426, 2002.

[20] C. Wickleder and P. Larsen, "Crystal structure, second harmonic generation, and vibrational spectroscopy of $K_2Mg_2(SCN)_6$ · 3 H_2O," *Chemistry of Materials*, vol. 16, 4016–4021, 2004.

[21] T. Wu, M. Z. Ma, R. Zhou, D. Li, and S. W. Ng, "Diaquadithiocyanatocopper (II)," *Acta Crystallographica*, vol. E61, m1404–m1402, 2005.

[22] O. Reckeweg, A. Schulz, B. Blaschkowski, Th. Schleid, and F. J. DiSalvo, "Single-crystal structures and vibrational spectra of Li[SCN] and Li[SCN] · 2 H_2O," *Zeitschrift für Naturforschung*, vol. 69b, 17–24, 2014.

[23] P. H. van Rooyen and J. C. A. Boeyens, "Sodium thiocyanate," *Acta Crystallographica*, vol. B31, 2933–2934, 1975.

[24] S. Manolatos, M. Tillinger, and B. Post, "Polymorphism in Cesium Thiocyanate," *Journal of Solid State Chemistry*, vol. 7, 31–35, 1973.

[25] C. Wickleder, "$M(SCN)_2$ (M = Eu, Sr, Ba): Kristallstruktur, thermisches Verhalten, Schwingungsspektroskopie," *Zeitschrift für Anorganische und Allgemeine Chemie*, vol. 627, 1693, 2001.

[26] Z. Zvonkova and G. Zhdanov, "The crystal structure of rhodonides. 3. The x-ray analysis of the crystals $Ba(SCN)_2 (H_2O)_2$," *Zhurnal Fizicheskoi Khimii*, vol. 24, 1345–1349, 1950.

[27] E. Dubler, A. Reller, and H. R. Oswald, "Intermediates in thermal decomposition of nickel(II) complexes: The crystal structures of $Ni(SCN)_2(NH_3)_2$ and $Ni(SCN)_2$," *Zeitschrift für Kristallographie*, vol. 161, 265–277, 1982.

[28] Chemspider, "Ni(SCN)$_2$ · 6 H$_2$O", *http://www.chemspider.com*

[29] M. Kabešová, M. Dunaj-jurčo, M. Serator, J. Gažo, and J. Garaj, "The crystal structure of copper(I) thiocyanate and its relation to the crystal structure of copper(II) diammine dithiocyanate complex," *Inorganica Chimica Acta*, vol. 17, 161–165, 1976.

[30] M. J. Cliffe, J. Lee, J. A. Paddison, S. Schott, P. Mukherjee, M. W. Gaultois, P. Manuel, H. Sirringhaus, S. E. Dutton, and C. P. Grey, "Low-dimensional quantum magnetism in Cu(NCS)$_2$: A molecular framework material," *Physical Review B*, vol. 97, 1–10, 2018.

[31] I. Lindqvist, "On the crystal structure of silver thiocyanate," *Acta Crystallographica*, vol. 10, 29–32, 1957.

[32] L. Aslanov, V. Ionov, and K. Kynev, "Crystal Structure of Anhydrous Zinc Rhodanide," *Kristallografiya*, vol. 21, 1198–1199, 1976.

[33] M. Cannas, G. Carta, A. Cristini, and G. Marongiu, "Three-co-ordinate Thiocyanate in Cadmium Dithiocyanate," *Journal of the Chemical Society, Dalton Transactions*, 300–301, 1976.

[34] A. L. Beauchamp and D. Goutier, "Structure cristalline et moléculaire du thiocyanate mercurique," *Canadian Journal of Chemistry*, vol. 50, 977–981, 1972.

[35] M. Strada, "Ricerche sulla struttura dei pseudo-alogeni e dei loro composti. - I. Tiocianato di tallio," *Gazzetta Chimica Italiana*, vol. 64, 400–409, 1934.

[36] A. G. Filby, R. A. Howie, and W. Moser, "The Structure of Tin(II) Thiocyanate," *Journal of the Chemical Society, Dalton Transactions*, 1797–1799, 1978.

[37] J. A. A. Mokuolu and J. C. Speakman, "The Crystal Structure of Lead(II) Thiocyanate," *Acta Crystallographica*, vol. B31, 172–176, 1975.

[38] F. A. Schimmel, "Solubilities of Lithium Chloride and Lithium Thiocyanate at Low Temperatures," *Journal of Chemical and Engineering Data*, vol. 5, 519–520, 1960.

[39] D. A. Lee, "Anhydrous Lithium Thiocyanate," *Inorganic Chemistry*, vol. 3, 289–290, 1964.

[40] C. B. Baddiel and G. J. Janz, "Molten thiocyanates: Raman spectra and structure," *Transactions of the Faraday Society*, vol. 60, 2009–2012, 1964.

[41] B. Rao, D. Eustace, and J. Shropshire, "The Li / TiS$_2$ cell with LiSCN electrolyte," *Journal of Applied Electrochemistry*, vol. 10, 757–763, 1980.

[42] B. M. L. Rao and G. E. Milliman, "Thermal Decomposition of LiSCN - Containing Lithium Battery Electrolyte," *Journal of The Electrochemical Society*, vol. 127, 2333–2335, 1980.

[43] F. W. Poulsen, "Ionic Conductivity of Solid and Molten Lithiumthiocyanate and its Hydrate," *Acta Chemica Scandinavica*, vol. A39, 290–292, 1985.

[44] B. Gorska, P. Bujewska, and K. Fic, "Thiocyanates as attractive redox-active electrolytes for high-energy and environmentally-friendly electrochemical capacitors," *Physical Chemistry Chemical Physics*, vol. 19, 7923–7935, 2017.

[45] M. Watanabe, K. Sanui, N. Ogata, F. Inoue, T. Kobayashi, and Z. Ohtaki, "Ionic conductivity and mobility of poly(propylene oxide) networks dissolving alkali metal thiocyanates," *Polymer Journal*, vol. 17, 549–555, 1985.

[46] M. Watanabe, M. Rikukawa, K. Sanui, and N. Ogata, "Effects of Polymer Structure and Incorporated Salt Species on Ionic Conductivity of Polymer Complexes Formed by Aliphatic Polyester and Alkali Metal Thiocyanate," *Macromolecules*, vol. 19, 188–192, 1986.

[47] K. Mitani and K. Adachi, "Ionic conduction in LiSCN/Dimethylformamide/Poly(propylene oxide) system II. Mobility of lithium and thiocyanate ions," *Journal of Polymer Science*, vol. B33, 947–954, 1995.

[48] P. V. Wright, "Ionic conductivity and organisation of macromolecular polyether-alkali-metal salt complexes," *Journal of Materials Chemistry*, vol. 5, 1275–1283, 1995.

[49] C. Liu and C. A. Angell, "Phase equilibria, high conductivity ambient temperature liquids, and glasses in the pseudo-halide systems $AlCl_3$-MSCN (M = Li, Na, K)," *Solid State Ionics*, vol. 86-88, 467–473, 1996.

[50] K. Hasegawa, M. Tatsumisago, and T. Minami, "Preparation of Novel Lithium-Ion Conductors Composed of LiSCN - $AlCl_3$ and Silica Particles," *Journal of The Electrochemical Society*, vol. 146, 3539–3542, 1999.

[51] A. le Blanc and J. Rouxel, "Sur les types structuraux des composes intercalaires $MSnS_2$ (M = Li, Na, K, Rb)," *Comptes Rendus Hebdomadaires des Seances de l'Academie des Sciences, Serie C, Sciences Chimiques*, 788–789, 1972.

[52] A. Kuhn, T. Holzmann, J. Nuss, and B. V. Lotsch, "A facile wet chemistry approach towards unilamellar tin sulfide nanosheets from $Li_{4x}Sn_{1-x}S_2$ solid solutions," *Journal of Materials Chemistry A*, vol. 2, 6100–6106, 2014.

[53] T. Holzmann, L. M. Schoop, M. N. Ali, I. Moudrakovski, G. Gregori, J. Maier, R. J. Cava, and B. V. Lotsch, "$Li_{0.6}[Li_{0.2}Sn_{0.8}S_2]$ – a layered lithium superionic conductor," *Energy and Environmental Science*, vol. 9, 2578–2585, 2016.

[54] J. A. Brant, D. M. Massi, N. A. W. Holzwarth, J. H. Macneil, A. P. Douvalis, T. Bakas, S. W. Martin, M. D. Gross, and J. A. Aitken, "Fast lithium ion conduction in Li_2SnS_3: Synthesis, Physicochemical characterization, and electronic structure," *Chemistry of Materials*, vol. 27, 189–196, 2015.

[55] J. H. MacNeil, D. M. Massi, J.-H. Zhang, K. A. Rosmus, C. D. Brunetta, T. A. Gentile, and J. A. Aitken, "Synthesis, structure, physicochemical characterization and electronic structure of thio-lithium super ionic conductors, Li_4GeS_4 and Li_4SnS_4," *Journal of Alloys and Compounds*, vol. 586, 736–744, 2014.

[56] K. Szendrei-Temesi, O. Sanchez-Sobrado, S. B. Betzler, K. M. Durner, T. Holzmann, and B. V. Lotsch, "Lithium Tin Sulfide—A High-Refractive-Index 2D Material for Humidity-Responsive Photonic Crystals," *Advanced Functional Materials*, vol. 28, 1–10, 2018.

[57] P. T. Cunningham, S. A. Johnson, and E. J. Cairns, "Phase Equilibria in Lithium-Chalcogen Systems," *Journal of The Electrochemical Society*, vol. 119, 1448–1450, 1972.

[58] R. C. Sharma and Y. A. Chang, "The S-Sn (Sulfur-Tin) system," *Bulletin of Alloy Phase Diagrams*, vol. 7, 269–273, 1986.

[59] J. Sangster and C. W. Bale, "The Li-Sn (Lithium-Tin) System," *Journal of Phase Equilibria*, vol. 19, 70–75, 1998.

[60] F. Kaboudvand, J. Vinckeviciute, S. Kolli, M. D. Radin, and A. Van Der Ven, "Phase Stability and Electronic Structure of Tin Sulfide Compounds for Li-ion Batteries," *Journal of Physical Chemistry C*, vol. 123, 29086–29095, 2019.

[61] A. Hollemann, E. Wiberg, and N. Wiberg, *Lehrbuch der Anorganischen Chemie.* Walter de Gruyter, 102 ed., 2007.

[62] Y. Haven, "The Ionic Conductivity of Li-Halide Crystals," *RECUEIL*, vol. 69, 1471–1489, 1950.

[63] S. Pizzini, "Ionic conductivity in lithium compounds," *Journal of Applied Electrochemistry*, vol. 1, 153–161, 1971.

[64] R. G. Pearson, "Hard and Soft Acids and Bases," *Journal of the American Chemical Society*, vol. 85, 3533–3539, 1963.

[65] G. Gregori, M. Shirpour, and J. Maier, "Proton conduction in dense and porous nanocrystalline ceria thin films," *Advanced Functional Materials*, vol. 23, 5861–5867, 2013.

[66] S. Ø. Stub, E. Vøllestad, and T. Norby, "Mechanisms of Protonic Surface Transport in Porous Oxides: Example of YSZ," *Journal of Physical Chemistry C*, vol. 121, 12817–12825, 2017.

[67] K. D. Kreuer, "Proton-Conducting Oxides," *Annual Review of Materials Research*, vol. 33, 333–359, 2003.

[68] J. Sohr, H. Schmidt, and W. Voigt, "Higher hydrates of lithium chloride, lithium bromide and lithium iodide.," *Acta Crystallographica*, vol. C74, 194–202, 2018.

[69] G. Schwering, A. Hönnerscheid, L. van Wüllen, and M. Jansen, "High lithium ionic conductivity in the lithium halide hydrates $Li_{3-n}(OH_n)Cl$ ($0.83 \leq n \leq 2$) and $Li_{3-n}(OH_n)Br$ ($1 \leq n \leq 2$) at ambient temperatures," *ChemPhysChem*, vol. 4, 343–348, 2003.

[70] O. Nakamura and J. B. Goodenough, "Conductivity enhancement of lithium bromide monohydrate by Al_2O_3 particles," *Solid State Ionics*, vol. 7, 119–123, 1982.

[71] A. C. Khandkar and J. B. Wagner, "On the thermodynamics of $LiBr \cdot xH_2O$ ($x = 0, 1/2, 1$) and electrical conductivity of $LiBr \cdot xH_2O$ (Al_2O_3) composites," *Solid State Ionics*, vol. 20, 267–275, 1986.

[72] K. Rudo, P. Hartwig, and W. Weppner, "Ionic conductivities and phase equilibria of the lithium iodide hydrates," *Revue de Chimie minérale*, vol. 17, 420, 1980.

[73] P. Hartwig and W. Weppner, "Ionic conductivities of Lithium-Halide-based quaternary compounds," *Solid State Ionics*, vol. 3/4, 249–254, 1981.

[74] F. W. Poulsen, "Ionic conductivity of solid lithium iodide and its monohydrate," *Solid State Ionics*, vol. 2, 53–57, 1981.

[75] A. Takano, I. Oikawa, A. Kamegawa, and H. Takamura, "Enhancement of the lithium-ion conductivity of $LiBH_4$ by hydration," *Solid State Ionics*, vol. 285, 47–50, 2016.

[76] J. Hougardy, W. E. E. Stone, and J. J. Fripiat, "NMR study of adsorbed water. I. Molecular orientation and protonic motions in the two-layer hydrate of a Na vermiculite," *The Journal of Chemical Physics*, vol. 64, 3840–3851, 1976.

[77] M. S. Whittingham, "Sodium ion conduction in single crystal vermiculite," *Solid State Ionics*, vol. 25, 295–300, 1987.

[78] M. Suzuki, N. Wada, D. R. Hines, and M. S. Whittingham, "Hydration states and phase transitions in vermiculite intercalation compounds," *Physical Review B*, vol. 36, 2844–2851, 1987.

[79] H. Maraqah, J. Li, and M. S. Whittingham, "The ionic conductivity of hydrogen vermiculite," *Journal of The Electrochemical Society*, vol. 138, L61–L63, 1991.

[80] M. S. Whittingham, "Hydrogen motion in oxides: From insulators to bronzes," *Solid State Ionics*, vol. 168, 255–263, 2004.

[81] S. H. Sheffield and A. T. Howe, "High proton conductivity in pressed pellets of H-montmorillonite, HAl-montmorillonite and HAlFe-montmorillonite clays," *Materials Research Bulletin*, vol. 14, 929–935, 1979.

[82] R. C. T. Slade, J. Barker, P. R. Hirst, T. K. Halstead, and P. I. Reid, "Conduction and diffusion in exchanged montmorillonite clays," *Solid State Comunications*, vol. 24, 289–295, 1987.

[83] T. Kawada, H. Yokokawa, and M. Dokiya, "Ionic conductivity of montmorillonite/alkali salt mixtures," *Solid State Ionics*, vol. 28-30, 210–213, 1988.

[84] J. Dost, "Über die Lumineszenz des mit Sn^{2+} oder mit Pb^{2+} aktivierten Zinkrhodanids," *Zeitschrift für Physikalische Chemie*, vol. 236, 145–150, 1964.

[85] C. Schneider, *in preparation*, PhD thesis, Max Planck Institute for Solid State Research, University of Stuttgart.

[86] X. Lu, L. Zhao, X. He, R. Xiao, L. Gu, Y. S. Hu, H. Li, Z. Wang, X. Duan, L. Chen, J. Maier, and Y. Ikuhara, "Lithium storage in $Li_4Ti_5O_{12}$ spinel: The full static picture from electron microscopy," *Advanced Materials*, vol. 24, 3233–3238, 2012.

[87] A. A. Coelho, "TOPAS and TOPAS-Academic: an optimization program integrating computer algebra and crystallographic objects written in C++," *Journal of Applied Crystallography*, vol. 51, 210–218, 2018.

[88] A. A. Coelho, "Indexing of powder diffraction patterns by iterative use of singular value decomposition," *Journal of Applied Crystallography*, vol. 36, 86–95, 2003.

[89] R. W. Cheary and A. Coelho, "A fundamental parameters approach to X-ray line-profile fitting," *Journal of Applied Crystallography*, vol. 25, 109–121, 1992.

[90] R. W. Cheary, A. A. Coelho, and J. P. Cline, "Fundamental parameters line profile fitting in laboratory diffractometers," *Journal of Research of the National Institute of Standards and Technology*, vol. 109, 1–25, 2004.

[91] Bruker Suite Version 2019/1, Bruker AXS Inc., Madison, WI, USA, 2019.

[92] K. MacKenzie and M. E. Smith, *Multinuclear Solid-State NMR of Inorganic Materials*. Pergamon, 1 ed., 2002.

[93] D. C. Apperley, R. K. Harris, and P. Hodgkinson, *Solid State NMR: Basic Principles and Practice*. New York: Momentum Press, 2012.

[94] A. Bielecki and D. P. Burum, "Temperature Dependence of ^{207}Pb MAS Spectra of Solid Lead Nitrate. An Accurate, Sensitive Thermometer for Variable-Temperature MAS," *Journal of Magnetic Resonance, Series A*, vol. 116, 215–220, 1995.

[95] R. K. Harris, E. D. Becker, S. M. De Menezes, R. Goodfellow, and P. Granger, "NMR nomenclature: Nuclear spin properties and conventions for chemical shifts - IUPAC recommendations 2001," *Solid State Nuclear Magnetic Resonance*, vol. 22, 458–483, 2002.

[96] W. S. Price, "Pulsed-field gradient nuclear magnetic resonance as a tool for studying translational diffusion: Part 1. Basic theory," *Concepts in Magnetic Resonance*, vol. 9, 299–336, 1997.

[97] F. Kimmerle, G. Majer, U. Kaess, A. J. Maeland, M. S. Conradi, and A. F. McDowell, "NMR Studies of hydrogen diffusion in ZrBe$_2$H$_{1.4}$," *Journal of Alloys and Compounds*, vol. 264, 63–70, 1998.

[98] J. Maier, *Physical Chemistry of Ionic Materials*, John Wiley & Sons, Ltd, 2004.

[99] M. E. Orazem and B. Tribollet, *Electrochemical Impedance Spectroscopy*, vol. 48. John Wiley & Sons, 2011, 2008.

[100] K. Funke, "Jump relaxation in solid electrolytes," *Progress in Solid State Chemistry*, vol. 22, 111–195, 1993.

[101] N. Hainovsky and J. Maier, "Simple phenomenological approach to premelting and sublattice melting in Frenkel disordered ionic crystals," *Physical Review B*, vol. 51, 15789–15797, 1995.

[102] R. D. Shannon, "Revised effective ionic radii and systematic studies of interatomic distances in halides and chalcogenides," *Acta Crystallographica*, vol. A32, 751–767, sep 1976.

[103] M. Joos, M. Conrad, S. Bette, R. Merkle, R. E. Dinnebier, Th. Schleid, and J. Maier, "On the crystal structures of lithium thiocyanate monohydrate LiSCN · 1 H$_2$O and the phase diagram LiSCN - H$_2$O," *Journal of Physics and Chemistry of Solids*, vol. 160, 110299, 2022.

[104] M. Ikeya, "Electrical Properties of Lithium Hydride," *Journal of the Physical Society of Japan*, vol. 42, 168–174, 1977.

[105] S. Lorger, R. E. Usiskin, and J. Maier, "Transport and Charge Carrier Chemistry in Lithium Sulfide," *Advanced Functional Materials*, vol. 29, 1–11, 2019.

[106] J. W. Bats, P. Coppens, and Å. . Kvick, "The experimental charge distribution in sulfür-containing molecules. Structure determination and electron density study of NaSCN at reduced temperatures," *Acta Crystallographica*, vol. B33, 1534–1542, 1977.

[107] J. S. Pap, B. Kripli, M. Giorgi, J. Kaizer, and G. Speier, "Redox properties of cobalt(II) complexes with isoindoline-based ligands," *Transition Metal Chemistry*, vol. 36, 481–487, 2011.

[108] "ligand field theory," *https://www.uni-muenster.de/imperia/md/content/anorganische_ und_ analytische_ chemie/lehre/lehramt/b2fchemie/lftheorie.pdf*, 2021.

[109] S. Lorger, R. Usiskin, and J. Maier, "Transport and Charge Carrier Chemistry in Lithium Oxide," *Journal of The Electrochemical Society*, vol. 166, A2215–A2220, 2019.

[110] A. Rabenau, *Lithiumnitrid und verwandte Stoffe*, vol. 53. Stuttgart: Westdeutscher Verlag, 1981.

[111] H. Mehrer, *Diffusion in Solids*. Springer, 2007.

[112] T. G. Stoebe and R. A. Huggins, "Measurement of ionic diffusion in lithium fluoride by nuclear magnetic resonance techniques," *Journal of Materials Science*, vol. 1, 117–126, 1966.

[113] O. S. Spencer and C. A. Plint, "Formation energy of individual cation vacancies in LiF and NaCl," *Journal of Applied Physics*, vol. 40, 168–172, 1969.

[114] J. Pan, *Understanding Electrical Conduction in Lithium Ion Batteries through Multi-Scale Modeling*. PhD thesis, University of Kentucky, 2016.

[115] B. J. Jackson and D. A. Young, "Ionic conduction in pure and doped single-crystalline lithium iodide," *Journal of Physics and Chemistry of Solids*, vol. 30, 1973–1976, 1969.

[116] J. S. Lee, S. Adams, and J. Maier, "Defect chemistry and transport characteristics of β-AgI," *Journal of Physics and Chemistry of Solids*, vol. 61, 1607–1622, 2000.

[117] D. Prutsch, B. Gadermaier, H. Brandstätter, V. Pregartner, B. Stanje, D. Wohlmuth, V. Epp, D. Rettenwander, I. Hanzu, and H. M. R. Wilkening, "Nuclear Spin Relaxation in Nanocrystalline β-Li$_3$PS$_4$ Reveals Low-Dimensional Li Diffusion in an Isotropic Matrix," *Chemistry of Materials*, vol. 30, 7575–7586, 2018.

[118] A. K. Jonscher, "The 'universal' dielectric response," *Nature*, vol. 267, 673–679, 1977.

[119] W. Schranz, "Static and dynamic properties of the order-disorder phase transition in KSCN and related crystals," in *Phase Transitions*, vol. 51, 1–66, 1994 Gordon and Breach Science Publishers, S.A., 1994.

[120] A. Kuhn, S. Narayanan, L. Spencer, G. Goward, V. Thangadurai, and M. Wilkening, "Li self-diffusion in garnet-type Li$_7$La$_3$Zr$_2$O$_{12}$ as probed directly by diffusion-induced ^{7}Li spin-lattice relaxation NMR spectroscopy," *Physical Review B*, vol. 83, 1–11, 2011.

[121] J. Waugh and E. Fedin, "Determination of Hindered-Rotation Barriers in Solids," *Soviet Physics-Solid State*, vol. 4, 1633–1636, 1963.

[122] T. Førland and J. Krogh-Moe, "Bemerkung zur Struktur von geschmolzenem Li$_2$SO$_4$," *Zeitschrift für Elektrochemie*, vol. 61, 1342, 1957.

[123] U. M. Gundusharma, C. Maclean, and E. A. Secco, "Rotating Sulfate Ion Contribution to Electrical Conductivity in Li$_2$SO$_4$ and LiNaSO$_4$," *Solid State Communications*, vol. 57, 479–481, 1986.

[124] A. Lundén, "Enhancement of Cation Mobility in Some Sulphate Phases due to a Paddle-Wheel Mechanism," *Solid State Ionics*, vol. 28-30, 163–167, 1988.

[125] A. Lundén, "Evidence for and against the Paddle-Wheel Mechanism of Ion Transport in Superionic Sulphate Phases," *Solid State Communications*, vol. 65, 1237–1240, 1988.

[126] A. Lundén and M. A. Dissanayake, "On the ionic conductivity and phase transitions in the Li$_2$SO$_4$-Li$_2$WO$_4$ system and their relation to ion transport mechanism," *Journal of Solid State Chemistry*, vol. 90, 179–184, 1991.

[127] A. Lundén, "Cation Transport Mechanisms in High-Temperature Rotor Phases of Sulfates," *Journal of Solid State Chemistry*, vol. 107, 296–298, 1993.

[128] A. Lundén, "On the Paddle-Wheel Mechanism for Cation Conduction in Lithium Sulphate," *Zeitschrift für Naturforschung*, vol. 50a, 1067–1076, 1995.

[129] A. S. Campbell, K. G. MacDonald, and E. A. Secco, "Ionic conductivity and solid-phase transitions in Li_2SO_4-Li_2WO_4 system relating to ion transport mechanism," *Journal of Solid State Chemistry*, vol. 81, 65–69, 1989.

[130] M. A. Dissanayake, M. A. Careem, P. W. Bandaranayake, and C. N. Wijayasekera, "Ionic conductivity of solid solutions of α-Li_2SO_4 with Li_2WO_4: Strong evidence for the paddle wheel mechanism of ion transport," *Solid State Ionics*, vol. 48, 277–281, 1991.

[131] E. A. Secco, "Paddle wheel mechanism in lithium sulfates: Arguments in defense and evidence against," *Journal of Solid State Chemistry*, vol. 96, 366–375, 1992.

[132] N. H. Andersen, P. W. Bandaranayake, M. A. Careem, M. A. Dissanayake, C. N. Wijayasekera, R. Kaber, A. Lundén, B. E. Mellander, L. Nilsson, and J. O. Thomas, "Paddle-wheel versus percolation mechanism for cation transport in some sulphate phases," *Solid State Ionics*, vol. 57, 203–209, 1992.

[133] R. Kaber, L. Nilsson, N. H. Andersen, A. Lunden, and J. O. Thomas, "A single-crystal neutron diffraction study of the structure of the high-temperature rotor phase of lithium sulphate," *Journal of Physics: Condensed Matter*, vol. 4, 1925–1933, 1992.

[134] H. von Benda and K. von Benda, "Zur Polymorphie des $Na_2S_2O_3$," *Zeitschrift für Naturforschung*, vol. 34b, 957–968, 1979.

[135] T. Veszprémi, T. Pasinszki, and M. Fehér, "The Structure of Pseudohalides-The Existence of a New Isomer," *Journal of the American Chemical Society*, vol. 116, 6303–6306, 1994.

[136] K. Funke, "Jump Relaxation in Solid Ionic Conductors," *Solid State Ionics*, vol. 28-30, 100–107, 1988.

[137] L. Zhou, A. Assoud, Q. Zhang, X. Wu, and L. F. Nazar, "New Family of Argyrodite Thioantimonate Lithium Superionic Conductors," *Journal of the American Chemical Society*, vol. 141, 19002–19013, 2019.

[138] L. Zhou, N. Minafra, W. G. Zeier, and L. F. Nazar, "Innovative Approaches to Li-Argyrodite Solid Electrolytes for All-Solid-State Lithium Batteries," *Accounts of Chemical Research*, 2021.

[139] S. Muy, R. Schlem, Y. Shao-Horn, and W. G. Zeier, "Phonon–Ion Interactions: Designing Ion Mobility Based on Lattice Dynamics," *Advanced Energy Materials*, vol. 11, 1–14, 2021.

[140] Z. Zhang, P. N. Roy, H. Li, M. Avdeev, and L. F. Nazar, "Coupled Cation-Anion Dynamics Enhances Cation Mobility in Room-Temperature Superionic Solid-State Electrolytes," *Journal of the American Chemical Society*, vol. 141, 19360–19372, 2019.

[141] F. Wang, H. A. Evans, K. Kim, L. Yin, Y. Li, P. C. Tsai, J. Liu, S. H. Lapidus, C. M. Brown, D. J. Siegel, and Y. M. Chiang, "Dynamics of Hydroxyl Anions Promotes Lithium Ion Conduction in Antiperovskite Li_2OHCl," *Chemistry of Materials*, vol. 32, 8481–8491, 2020.

[142] B. G. Kale, "Phase transition and transport properties of solid Li_2CO_3," *Indian Journal of Pure & Applied Physics*, vol. 29, 738–740, 1991.

[143] C. N. Wijayasekera and B. E. Mellander, "Phase transitions and ionic conductivity of the lithium sulphate-lithium phosphate system," *Solid State Ionics*, vol. 45, 293–298, 1991.

[144] B. Wang, C. Chakoumakos, B. C. Sales, B. S. Kwak, and J. B. Bates, "Synthesis, Crystal Structure, and Ionic Conductivity of Polycrystalline Lithium Phosphorus Oxynitride with the γ-Li_3PO_4 Structure," *Journal of Solid State Chemistry*, vol. 115, 313–323, 1995.

[145] M. Tachez, J. Malugani, R. Mercier, and G. Robert, "Ionic Conductivity of and Phase Transition in Lithium Thiophosphate Li_3PS_4," *Solid State Ionics*, vol. 14, 181–185, 1984.

[146] Hermann Schmalzried, "Zur Fehlordnung in Silberbromid," *Zeitschrift für Physikalische Chemie*, vol. 22, 199–208, 1959.

[147] J. Maier and W. Münch, "Thermal destiny of an ionic crystal," *Zeitschrift für Anorganische und Allgemeine Chemie*, vol. 626, 264–269, 2000.

[148] R. Merkle and J. Maier, "On the Tammann-rule," *Zeitschrift für Anorganische und Allgemeine Chemie*, vol. 631, 1163–1166, 2005.

[149] J. Jamroz, M. Malys, F. Krok, J. Maier, A. Kyriacou, S. J. Ahmed, I. Abrahams, and W. Wrobel, "The influence of defect structure changes at phase transition on electrical properties in the $Bi_{0.75}Pr_{0.25}O_{1.5}$ oxide ion conductor," *Solid State Ionics*, vol. 348, 115284, 2020.

[150] F. Zimmer, P. Ballone, M. Parrinello, and J. Maier, "Conductivity anomaly in PbF_2: A numerical investigation by classical MD and MC simulations," *Solid State Ionics*, vol. 127, 277–284, 2000.

[151] R. Merkle and J. Maier, "Defect association in acceptor-doped $SrTiO_3$: case study for $Fe'_{Ti}V_O^{\cdot\cdot}$ and $Mn''_{Ti}V_O^{\cdot\cdot}$," *Physical Chemistry Chemical Physics*, vol. 5, 2297–2303, 2003.

[152] K. F. Young and H. P. Frederikse, "Compilation of the Static Dielectric Constant of Inorganic Solids," *Journal of Physical and Chemical Reference Data*, vol. 2, 313–410, 1973.

[153] R. M. Caven and J. Ferguson, "The Dissociation Pressures of Hydrated Double Sulphates. Part I. Hydrated Cupric Alkali Sulphates," *Journal of the Chemical Society, Transactions*, vol. 121, 1406–1414, 1922.

[154] J. R. Partington, "The Determination of the Dissociation Pressures of Hydrated Salts by a Dynamical Method.," *Journal of the Chemical Society*, vol. 99, 466–478, 1911.

[155] J. R. Partington and D. B. Huntingford, "The Determination of the Dissociation Pressures of Hydrated Salts by a Dynamical Method. Part II.," *Journal of the Chemical Society*, vol. 123, 160–170, 1923.

[156] J. R. Partington and R. J. Winterton, "The Determination of the Dissociation Pressures of Hydrated Salts by a Dynamical Method. Part III:," *Journal of the Chemical Society*, 635–643, 1930.

[157] W. C. Schumb, "The dissociation pressures of certain salt hydrates by the gas-current saturation method," *Journal of the American Chemical Society*, vol. 45, 342–354, 1923.

[158] D. G. Bonnell and L. W. Burridge, "The dissociation pressures of some salt hydrates," *Transactions of the Faraday Society*, vol. 31, 473–478, 1935.

[159] G. Wedler, *Lehrbuch der Physikalischen Chemie*. Wiley-VCH Weinheim, 5 ed., 2004.

[160] I. Barin and O. Knacke, *Thermochemical properties of inorganic substances*. Springer Verlag Berlin Heidelberg New York, 1973.

[161] P. E. Mason, S. Ansell, G. W. Neilson, and S. B. Rempe, "Neutron scattering studies of the hydration structure of Li^+," *Journal of Physical Chemistry A*, vol. 119, 2003–2009, 2015.

[162] E. Glueckauf, "The influence of ionic hydration on activity coefficients in concentrated electrolyte solutions," *Transactions of the Faraday Society*, vol. 51, 1235–1244, 1955.

[163] H. A. Levy, P. A. Agron, M. A. Bredig, and M. D. Danford, "X-Ray and Neutron Diffraction Studies of Molten Alkali Halides," *Annals of the New York Academy of Sciences*, vol. 79, 762–780, 1960.

[164] P. Paricaud, "Modeling the Dissociation Conditions of Salt Hydrates and Gas Semi-clathrate Hydrates: Application to Lithium Bromide, Hydrogen Iodide, and Tetra-*n*-butylammonium Bromide + Carbon Dioxide Systems," *Journal of Physical Chemistry B*, vol. 115, 288–299, 2011.

[165] C.-H. Yim and Y. A. Abu-Lebdeh, "Connection between Phase Diagram, Structure and Ion Transport in Liquid, Aqueous Electrolyte Solutions of Lithium Chloride," *Journal of The Electrochemical Society*, vol. 165, A547–A556, 2018.

[166] M. S. Ding and K. Xu, "Phase Diagram, Conductivity, and Glass Transition of LiTFSI-H_2O Binary Electrolytes," *Journal of Physical Chemistry C*, vol. 122, 16624–16629, 2018.

[167] M. S. Ding, L. Ma, M. A. Schroeder, and K. Xu, "Phase diagram and conductivity of Zn(TfSi)$_2$-H_2O electrolytes," *Journal of Physical Chemistry C*, vol. 124, 25249–25253, 2020.

[168] A. Atbir, A. Marroitche, H. Atif, L. Boukbir, M. El Hacfek, and R. Cohen-Adad, "Calcul des diagrammes de phases des systemes binaires H_2O-MCl$_n$ (M = Mg^{2+}, Fe^{2+}, Fe^{3+})," *Journal of Thermal Analysis and Calorimetry*, vol. 61, 849–860, 2000.

[169] F. Paulik, J. Paulik, and M. Arnold, "Investigation of the phase diagram for the system Ni(NO$_3$)$_2$-H_2O and examination of the decomposition of Ni(NO$_3$)$_2 \cdot$ 6 H_2O," *Thermochimica Acta*, vol. 121, 137–149, 1987.

[170] W. Weppner, W. Welzel, R. Kniep, and A. Rabenau, "Fast Ionic Conduction in LiI·4 Methanol: [Li(CH$_3$OH)$_4$]$^+$I$^-$," *Angewandte Chemie International Edition in Eng.*, vol. 25, 1087–1089, 1986.

[171] A. Abragam, *The Principles of Nuclear Magnetism*. Oxford University Press, 1961.

[172] C. H. Collie, J. B. Hasted, and D. M. Ritson, "The dielectric properties of water and heavy water," *Proceedings of the Physical Society*, vol. 60, 145–160, 1948.

[173] C. Malmberg, "Dielectric constant of deuterium oxide," *Journal of Research of the National Bureau of Standards*, vol. 60, 609, 1958.

[174] S. Deki, S.-y. Nakamura, A. Kajinami, Y. Kanaji, and M. Mizuhata, "Properties of CaCl$_2$ Hydrate with an Inorganic Powder Part1.-Electrical Conductivity of CaCl$_2 \cdot n\,H_2O$ ($n = 6.00-7.35$) with α-Al$_2$O$_3$ Powder," *Journal of the Chemical Society, Faraday Transactions*, vol. 89, 3805–3810, 1993.

[175] S. Deki, A. Kajinami, Y. Kanaji, M. Mizuhata, and K. Nagata, "Properties of $CaCl_2$ Hydrate with an Inorganic Powder Part 2.-Melting Behaviour and Thermodynamic Properties of $CaCl_2 \cdot n\,H_2O$ ($n = 6.00 - 7.35$) with α-Al_2O_3 or α-SiC Powder," *Journal of the Chemical Society, Faraday Transactions*, vol. 89, 3811–3815, 1993.

[176] S. Deki, M. Mizuhata, S.-y. Nakamura, K. Nakamura, A. Kajinami, and Y. Kanaji, "The Electrical Conductivity of Solid/Liquid Coexisting Systems: α-Al_2O_3 Powder/$CaCl_2$ Aqueous Solution System," *Journal of the Electrochemical Society*, vol. 139, 996–1000, 1992.

[177] S. Deki, M. Mizuhata, S. Rakuno, A. Kajinami, and Y. Kanaji, "Electrical Conductivity of Solid/Liquid Coexisting Systems: Dependence of Electrical Conductivity on Surface Hydrophilicity," *Journal of Colloid and Interface Science*, vol. 168, 198–205, 1994.

[178] J. Maier, "Space Charge Regions in Solid Two-Phase Systems and their Conduction Contribution-I. Conductance Enhancement in the System Ionic Conductor-'Inert' Phase and Application on $AgCl:Al_2O_3$ and $AgCl:SiO_2$," *Journal of Physics and Chemistry of Solids*, vol. 46, 309–320, 1985.

[179] J. Maier, "Space Charge Regions in Solid Two Phase Systems and Their Conduction Contribution - II. Contact Equilibrium At the Interface of Two Ionic Conductors and the Related Conductivity Effect," *Berichte der Bunsengesellschaft für physikalische Chemie*, vol. 89, 355–362, 1985.

[180] M. Joos, C. Schneider, A. Münchinger, I. Moudrakovski, R. Usiskin, J. Maier, and B. V. Lotsch, "Impact of hydration on ion transport in $Li_2Sn_2S_5 \cdot x\,H_2O$," *Journal of Materials Chemistry A*, vol. 9, 16532–16544, 2021.

[181] A.-K. Hatz, I. Moudrakovski, S. Bette, M. Terban, M. Etter, M. Joos, N. Vargas-Barbosa, R. E. Dinnebier, and B. V. Lotsch, "Fast Water-Assisted Lithium Ion Conduction in Restacked Lithium Tin Sulfide Nanosheets," *Chemistry of Materials*, 2021.

[182] M. Binnewies, M. Jäckel, H. Willner, and G. Rayner-Canham, *Allgemeine und Anorganische Chemie*. Spektrum Akademischer Verlag, 2 ed., 2011.

[183] K. H. Park, D. Y. Oh, Y. E. Choi, Y. J. Nam, L. Han, J. Y. Kim, H. Xin, F. Lin, S. M. Oh, and Y. S. Jung, "Solution-Processable Glass LiI-Li_4SnS_4 Superionic Conductors for All-Solid-State Li-Ion Batteries," *Advanced Materials*, vol. 28, 1874–1883, 2016.

[184] H. Kwak, K. H. Park, D. Han, K. W. Nam, H. Kim, and Y. S. Jung, "Li^+ conduction in air-stable Sb-Substituted Li_4SnS_4 for all-solid-state Li-Ion batteries," *Journal of Power Sources*, vol. 446, 227338, 2020.

[185] G. Sahu, Z. Lin, J. Li, Z. Liu, N. Dudney, and C. Liang, "Air-stable, high-conduction solid electrolytes of arsenic-substituted Li_4SnS_4," *Energy and Environmental Science*, vol. 7, 1053–1058, 2014.

[186] Y. E. Choi, K. H. Park, D. H. Kim, D. Y. Oh, H. R. Kwak, Y. G. Lee, and Y. S. Jung, "Coatable Li_4SnS_4 Solid Electrolytes Prepared from Aqueous Solutions for All-Solid-State Lithium-Ion Batteries," *ChemSusChem*, vol. 10, 2605–2611, 2017.

[187] T. Kaib, S. Haddadpour, M. Kapitein, P. Bron, C. Schröder, H. Eckert, B. Roling, and S. Dehnen, "New lithium chalcogenidotetrelates, LiChT: Synthesis and characterization of the Li^+-conducting tetralithium ortho-sulfidostannate Li_4SnS_4," *Chemistry of Materials*, vol. 24, 2211–2219, 2012.

[188] G. Leonardos, D. Kendall, and N. Barnard, "Odor threshold determinations of 53 odorant chemicals," *Journal of the Air Pollution Control Association*, vol. 19, 91–95, 1969.

[189] S. Bette, R. E. Dinnebier, and D. Freyer, "Structure solution and refinement of stacking-faulted NiCl(OH)," *Journal of Applied Crystallography*, vol. 48, 1706–1718, 2015.

[190] L. Diehl, S. Bette, F. Pielnhofer, S. Betzler, I. Moudrakovski, G. A. Ozin, R. Dinnebier, and B. V. Lotsch, "Structure-Directing Lone Pairs: Synthesis and Structural Characterization of $SnTiO_3$," *Chemistry of Materials*, vol. 30, 8932–8938, 2018.

[191] Y. Zhang and Z. Xu, "Atomic radii of noble gas elements in condensed phases," *American Mineralogist*, vol. 80, 670–675, 1995.

[192] C. Hall, G. L. Haller, and R. E. Richards, "N.M.R. studies of lithium chloride and lithium bromide solutions in methanol-water mixtures," *Molecular Physics*, vol. 16, 377–394, 1969.

[193] T. Umecky, T. Takamuku, T. Matsumoto, E. Kawai, M. Takagi, and T. Funazukuri, "Effects of dissolved water on Li^+ solvation in 1-ethyl-3-methylimidazolium bis(trifluoromethanesulfonyl)amide ionic liquid studied by NMR," *Journal of Physical Chemistry B*, vol. 117, 16219–16226, 2013.

[194] R. L. Sacci, T. H. Bennett, A. R. Drews, V. Anandan, M. J. Kirkham, L. L. Daemen, and J. Nanda, "Phase evolution during lithium-indium halide superionic conductor dehydration," *Journal of Materials Chemistry A*, vol. 9, 990–996, 2021.

[195] F. W. Sears, M. W. Zemansky, and H. D. Young, *University physics*, Addison-Wesley Pub. Co., 1982.

[196] K. Tanaka and R. Tamamushi, "A Physico-chemical Study of Concentrated Aqueous Solutions of Lithium Chloride," *Zeitschrift für Naturforschung*, vol. 46a, 141–147, 1991.

[197] Y. Kato, S. Hori, T. Saito, K. Suzuki, M. Hirayama, A. Mitsui, M. Yonemura, H. Iba, and R. Kanno, "High-power all-solid-state batteries using sulfide superionic conductors," *Nature Energy*, vol. 1, 16030, 2016.

[198] R. A. Horne and R. A. Courant, "The electrical conductivity of aqueous electrolytic solutions near the freezing point," *Journal of Physical Chemistry*, vol. 68, 1258–1260, 1964.

[199] C. J. Wen, B. A. Boukamp, R. A. Huggins, and W. Weppner, "Thermodynamic and Mass Transport Properties of "LiAl"," *Journal of The Electrochemical Society*, vol. 126, 2258, 1979.

[200] W. D. Richards, L. J. Miara, Y. Wang, J. C. Kim, and G. Ceder, "Interface Stability in Solid-State Batteries," *Chemistry of Materials*, vol. 28, 266–273, 2016.

[201] A. Sakuda, K. Kuratani, T. Takeuchi, H. Kiuchi, T. Kawaguchi, M. Shikano, H. Sakaebe, and H. Kobayashi, "Cubic Rocksalt Li_2SnS_3 and a Solid Solution with Li_3NbS_4 Prepared by Mechanochemical Synthesis," *Electrochemistry*, vol. 85, 580–584, 2017.

[202] Y. Inaguma, L. Chen, M. Itoh, and T. Nakamura, "High Ionic Conductivity in Lithium Lanthanum Titanate," *Solid State Communications*, vol. 86, 689–693, 1993.

[203] Y. Tian, Y. Sun, D. C. Hannah, Y. Xiao, H. Liu, K. W. Chapman, S. H. Bo, and G. Ceder, "Reactivity-Guided Interface Design in Na Metal Solid-State Batteries," *Joule*, vol. 3, 1037–1050, 2019.

[204] R. D. Armstrong and K. Landles, "Electrochemical behaviour of lithium iodide monohydrate," *Journal of Applied Electrochemistry*, vol. 11, 247–251, 1981.

[205] R. D. Armstrong and K. Landles, "Lithium ion conducting solids for ambient applications," *Journal of Applied Electrochemistry*, vol. 12, 533–535, 1982.

[206] R. Demir-Cakan, M. R. Palacin, and L. Croguennec, "Rechargeable aqueous electrolyte batteries: From univalent to multivalent cation chemistry," *Journal of Materials Chemistry A*, vol. 7, 20519–20539, 2019.

[207] New Jersey Zinc Company, "Private Communication," tech. rep., Palmerton, Pennsylvania, USA.

[208] J. Saha and J. Podder, "Crystallization Of Zinc Sulphate Single Crystals And Its Structural, Thermal And Optical Characterization," *Journal of Bangladesh Academy of Sciences*, vol. 35, 203–210, 1970.

[209] V. Kavun, N. Uvarov, A. Slobodyuk, V. Goncharuk, A. Kotenkov, I. Tkachenko, A. Gerasimenko, and V. Sergienko, "Ionic Mobility, Phase Transitions, and Superionic Conduction in Solid Solutions $(100 - x)\mathrm{PbF_2} - x\,\mathrm{ZrF_4}$ and Crystals $\mathrm{K_2ZrF_6}$, $(\mathrm{NH_4})_2\mathrm{ZrF_6}$, $\mathrm{KSnZrF_7}$, and $\mathrm{M(NH_4)_6Zr_4F_{23}}$ (M = Li, Na)," *Russian Journal of Electrochemistry*, vol. 41, 501–509, 2005.

[210] N. M. Sammes, G. A. Tompsett, H. Näfe, and F. Aldinger, "Bismuth based oxide electrolytes - Structure and ionic conductivity," *Journal of the European Ceramic Society*, vol. 19, 1801–1826, 1999.

[211] O. Alekperov, N. Gasimov, K. Khalilova, Y. Shim, R. Paucar, N. Abdulzade, O. Samedov, Z. Jahangirli, E. Nakhmedov, K. Wakita, and N. Mamedov, "Temperature dependent spectroscopic ellipsometry of $\mathrm{Ag_2Se}$ and $\mathrm{Ag_2S}$ with phase transitions from ionic to superionic conductivity state," *Physica Status Solidi (C) Current Topics in Solid State Physics*, vol. 12, 605–609, 2015.

[212] J. Schneider, T. Schröder, M. Hoelzel, O. Kluge, W. W. Schmahl, and O. Oeckler, "Phase transitions to superionic $\mathrm{Li_2Te}$ and $\mathrm{Li_2Se}$ – A high-temperature neutron powder diffraction study, atom displacements, probability density functions and atom potentials," *Solid State Ionics*, vol. 325, 90–101, 2018.

[213] B. Singh, M. K. Gupta, R. Mittal, and S. L. Chaplot, "Ab initio molecular dynamics study of 1-D superionic conduction and phase transition in β-eucryptite," *Journal of Materials Chemistry A*, vol. 6, 5052–5064, 2018.

[214] V. Sharma, D. Swain, and T. N. Guru Row, "Superionic Behavior and Phase Transition in a Vanthoffite Mineral," *Inorganic Chemistry*, vol. 56, 6048–6051, 2017.

[215] Y. M. Baĭkov and V. M. Egorov, "Solid-hydroxide protonic conductors: Superionic conductivity, phase transitions, isotopic effect, and self-organized microheterogeneity," *Physics of the Solid State*, vol. 51, 33–43, 2009.

[216] D. Swain, V. S. Bhadram, G. K. Pradhan, S. V. Bhat, C. Narayana, and C. N. R. Rao, "Superionic phase transition in $\mathrm{KHSO_4}$: A temperature-dependent raman investigation," *Journal of Physical Chemistry A*, vol. 114, 10040–10044, 2010.

[217] O. S. Hernández-Daguer, H. Correa, and R. A. Vargas, "Phase behaviour and superionic phase transition in $\mathrm{K_3H(SeO_4)_2}$," *Ionics*, vol. 21, 2201–2209, 2015.

[218] A. R. Lim, "Study of superionic phase transition of $(NH_4)_4LiH_3(SO_4)_4$ by ^{1}H MAS NMR," *Solid State Communications*, vol. 160, 22–25, 2013.

[219] A. Pawłowski, L. Szcześniak, M. Połomska, B. Hilczer, and L. Kirpichnikova, "Pretransitional effects at the superionic phase transition of $Rb_3H(SeO_4)_2$ protonic conductor," *Solid State Ionics*, vol. 157, 203–208, 2003.

[220] J. Otomo, T. Tamaki, S. Nishida, S. Wang, M. Ogura, T. Kobayashi, C. J. Wen, H. Nagamoto, and H. Takahashi, "Effect of water vapor on proton conduction of cesium dihydrogen phosphate and application to intermediate temperature fuel cells," *Journal of Applied Electrochemistry*, vol. 35, 865–870, 2005.

[221] L. H. Jones, "Infrared spectrum and structure of the thiocyanate ion," *The Journal of Chemical Physics*, vol. 25, 1069–1072, 1956.

[222] J. Maier, "On the Conductivity of Polycrystalline Materials," *Berichte der Bunsengesellschaft für physikalische Chemie*, vol. 90, 26–33, 1986.

Acknowledgements

Es gibt viel, wofür ich dankbar bin, und nur weniges, wofür nicht. Zu allererst möchte ich natürlich Professor Joachim Maier danken, dass er mich in seine Gruppe mitaufgenommen hat, und mir sein Vertrauen geschenkt hat, in seinem Namen zu forschen. An Herr Maier: *Sie werden mir immer in Erinnerung als großes Vorbild für die Wissenschaft bleiben.*

Als nächstes möchte ich meinen Dank an meine täglichen Betreuer richten, Dr. Rotraut Merkle und Dr. Robert Usiskin. Nur wenige auf der Welt können von sich sagen, unter einer der Koryphäen der ionischen Festkörper gelernt zu haben. Doch in meinem Fall, hatte ich das Vergnügen gleich von Zweien täglich belehrt zu werden; mit dem akkuraten Praktizismus von Rotraut, und dem praktikablen Perfektionsismus von Rob.

Auch bedanken möchte ich mich für das Engagement und die herrovragenden Beiträge meiner Kollaborationspartner: Prof. Thomas Schleid und seinem Doktoranden Maurice Conrad von der Universität Stuttgart, sowie Prof. Bettina Lotsch und ihrem Doktoranden Christian Schneider vom MPI FKF.

Zuletzt, gilt mein größter Dank meiner direkten Familie: mein Vater Friewald Joos, meine Mutter Renate Joos, mein Bruder Armin Joos und meine Partnerin Yuanye Huang. Es gab, und wird es wieder geben, Zeiten, in denen ich an mir gezweifelt habe. Ich kann aber mit wohlen Herzens sagen, dass meiner Familie dies nie widerfahren ist, die immer an mich geglaubt und unterstützt haben.

I dedicate this PhD thesis to my family, my father Friewald Joos, my mother Renate Joos, my brother Armin Joos and my partner, Yuanye Huang, who I love, treasure and cherish.
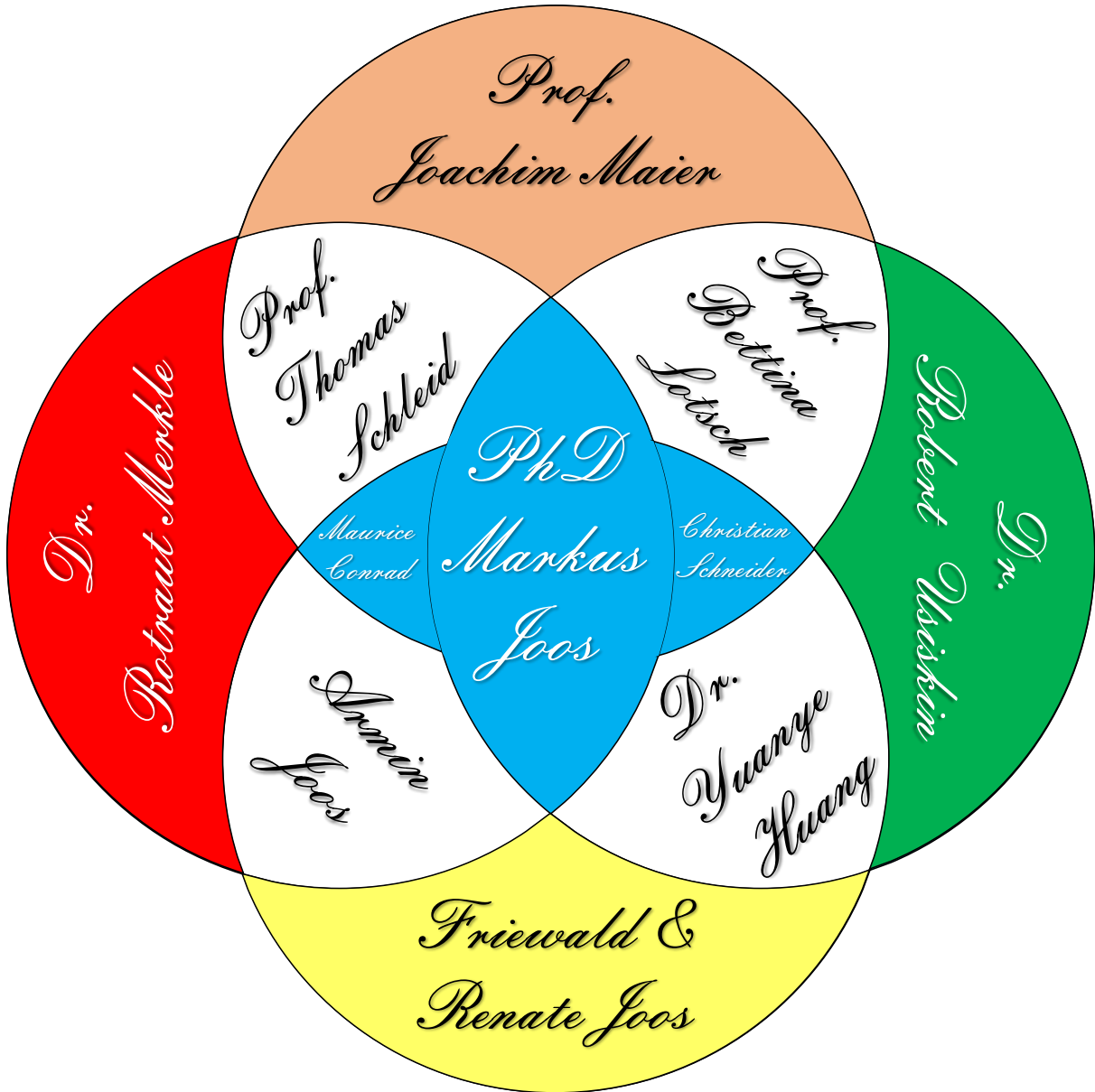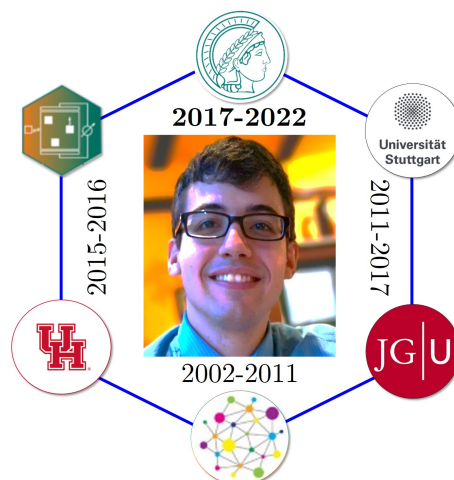
Figure C.1: Venn diagram PhD Markus Joos.

Curriculum Vitae

born 19$^{\text{th}}$ of March 1992, Balingen,
Baden-Württemberg, Germany

- **1998-2002 Elementary School**
  Grundschule am Schlossgarten, Geislingen b. Balingen, Baden-Württemberg,
  Germany

- **2002-2011 Abitur (high school degree)**
  Gymnasium Balingen, Balingen, Baden-Württemberg, Germany

- **2011-2014 Bachelor of Science in Chemistry**
  Johannes Gutenberg University, Mainz, Rheinlandpfalz, Germany

- **2015-2016 Semester Abroad**
  University of Houston, Houston, Texas, USA

- **2014-2017 Master of Science in Chemistry**
  Johannes Gutenberg University, Mainz, Rheinlandpfalz, Germany

- **2017-2018 Internship**
  PFINDER Chemie GmbH, Böblingen, Baden-Württemberg, Germany

- **2017-2022 PhD in Physical Chemistry**
  Max Planck Institute for Solid State Research (University of Stuttgart), Stuttgart,
  Baden-Württemberg, Germany

- **Publications:**

M. Joos, M. Conrad, S. Bette, R. Merkle, R. E. Dinnebier, Th. Schleid, J. Maier, On the Crystal Structures of Lithium Thiocyanate Monohydrate LiSCN $\cdot$ 1 H_2O and the Phase Diagram LiSCN $-$ H_2O, *J. Phys. Chem. Solids*, 2022, **160**, 110299,
https://doi.org/10.1016/j.jpcs.2021.110299

M. Joos, C. Schneider, A. Münchinger, I. Moudrakovski, R. Usiskin, J. Maier, B. Lotsch, Impact of Hydration on Ion Transport in $Li_2Sn_2S_5 \cdot x$ H_2O, *J. Mater. Chem. A*, 2021, **9**, 16532-16544,
https://doi.org/10.1039/D1TA04736A

M. Joos, M. Conrad, R. Merkle, Th. Schleid, J. Maier, R. E. Dinnebier, S. Bette, Synthesis, Characterization and Thermal Behavior of Solid Phases in the Quasi-Ternary System $Mg(SCN)_2 - H_2O - THF$, *Dalton Trans.*, 2021, **50**, 6949-6961,
https://doi.org/10.1039/D1DT00469G

M. Joos, G. Cerretti, I. Veremchuk, P. Hofmann, H. Frerichs, D. H. Anjum, T. Reich, I. Lieberwirth, M. Panthöfer, W. G. Zeier, W. Tremel, Spark Plasma Sintering (SPS)-Assisted Synthesis and Thermoelectric Characterization of Magnéli Phase V_6O_{11}, *Inorg. Chem.*, 2018, **57**, 3, 1259–1268,
https://doi.org/10.1021/acs.inorgchem.7b02669

M. Conrad, **M. Joos**, S. Bette, R. Merkle, R. E. Dinnebier, J. Maier, Th. Schleid, Synthesis and Characterization of two Novel Solvent-Containing Lithium Pseudohalides: Li[SCN] $\cdot$ THF and Li[SCN] $\cdot$ 2 THF, *Dalton Trans.*, 2021, **50**, 12292-12300,
https://doi.org/10.1039/D1DT02124A

A. Hatz, I. Moudrakovski, S. Bette, M. Terban, M. Etter, **M. Joos**, N. Vargas-Barbosa, R. E. Dinnebier, B. V. Lotsch, Fast Water-Assisted Lithium Ion Conduction in Restacked Lithium Tin Sulfide Nanosheets, *Chem. Mater.*, 2021, **33**, 18, 7337–7349,
https://doi.org/10.1021/acs.chemmater.1c01755

J. Kröger, G. Savasci, I. Moudrakovski, A. Jimenez-Solano, M. W. Terban, S. Bette, V. Duppel, **M. Joos**, A. Senocrate, R. Dinnebier, F. Podjaski, C. Ochsenfeld, B. V. Lotsch, Conductivity insights and correlation to photocatalytic activity in ionic 2D carbon nitrides, **submitted to *Adv. Mater.***

M. Joos, M. Conrad, A. Rad, P. Kaghazchi, S. Bette, R. Merkle, R. E. Dinnebier, Th. Schleid, J. Maier, Part I: Conductivity and Defect Chemistry of Anhydrous LiSCN, **in preparation**

M. Joos, M. Conrad, I. Moudrakovski, M. Terban, A. Rad, P. Kaghazchi, R. E. Dinnebier, R. Merkle, Th. Schleid, J. Maier, Part II: Frequency Dependence of the Conductivity in Anhydrous LiSCN; Application of the Jump Relaxation Model, **in preparation**

M. Joos, M. Conrad, S. Bette, R. Merkle, R. E. Dinnebier, Th. Schleid, J. Maier, Part III: Defect chemistry in the Premelting Regime of Anhydrous LiSCN; Application of the Cube-Root Law, **in preparation**

M. Joos, M. Conrad, A. Münchinger, I. Moudrakovski, R. Merkle, Th. Schleid, J. Maier, Ion Transport in H_2O-doped and Hydrated LiSCN $\cdot$ x H_2O, **in preparation**